



Douglas, Fraser J. (2012) Synthesis and nanocharacterisation of magnetic nanoparticles: from cubes and spheres to octapods and wires. PhD thesis.

<http://theses.gla.ac.uk/3740/>

Copyright and moral rights for this thesis are retained by the author

A copy can be downloaded for personal non-commercial research or study, without prior permission or charge

This thesis cannot be reproduced or quoted extensively from without first obtaining permission in writing from the Author

The content must not be changed in any way or sold commercially in any format or medium without the formal permission of the Author

When referring to this work, full bibliographic details including the author, title, awarding institution and date of the thesis must be given.

Synthesis and nanocharacterisation of magnetic nanoparticles: from cubes and spheres to octapods and wires

Fraser J. Douglas

M.Sci

Submitted in the fulfilment of the requirements for the
Degree of Doctor of Philosophy

School of Chemistry
College of Science and Engineering
University of Glasgow

Supervisors: Dr. Mark Murrie & Dr. Donald MacLaren

October 2012

© Fraser J. Douglas 2012

fraserjdouglas@gmail.com

Abstract

This thesis details the chemical synthesis and nanocharacterisation of magnetic nanoparticles (MNPs). Throughout this thesis, solution-based synthesis methods are used to fabricate MNPs with a variety of shapes, from spheres and cubes to wires and octapods.

Chapter 3 assesses the role of polyol solvent in autoclave-based magnetite NP synthesis. It was found that solvents containing functional groups (especially primary alcohols) afforded the greatest control over final MNP morphology and that the presence of additional alkyl substituents could disrupt the packing of surfactant molecules around a particle surface, giving rise to more complex ‘compound’ MNPs. Magnetic measurements show the particles to be superparamagnetic, with saturation magnetisation values close to that of the bulk.

In Chapter 4 It was found that by replacing the polyol solvents used in Chapter 3 with a large excess of bulky surfactant molecules it was possible to form high aspect ratio lanthanide oxide (LnO_x) nanowires and ribbons. It was found that the nanowires formed via an intriguing 3-stage ‘oriented assembly’ mechanism, in which individual NPs form, before aligning anisotropically and recrystallising into a more crystallographically homogeneous product. The magnetic properties of Gd_2O_3 nanowires and Dy_2O_3 nanoribbons are very similar to those of discrete particles, implying that no long-range ordering exists in the nanowires. Optical characterisation of the Eu_2O_3 nanowires showed that there is an increase in fluorescence lifetime going from bulk Eu_2O_3 to the nanoscale.

In Chapter 5 the high temperature reflux approach is used in the synthesis of manganese oxide (as MnO) particles, using manganese-containing polynuclear carboxylate complexes as precursors. It was found that control over MnO NP size and shape is dependent on many factors, such as the carboxylate ligand present in the precursor (which can disrupt particle stabilisation by surfactant molecules) and the heating regime, which

determines if the particles grow under thermodynamic or kinetic growth regimes. The magnetic behaviour of MnO MNPs was found to be dependent on the relative number of surface spins present in the particles.

In Chapter 6 new routes to gadolinium-doped magnetite particles are discussed. It was found that decomposition of a single-source precursor yielded doped magnetite particles which had a gadolinium content of 2–4%. Magnetic characterisation of these particles showed them to be superparamagnetic, with a reduced saturation magnetisation compared to bulk magnetite. Preliminary investigations showed that the gadolinium doped particles (after being rendered water soluble by a ligand exchange reaction) were readily taken up by human fibroblast cells and exhibited low toxicities.

Acknowledgements

I would like to express my gratitude towards my supervisors Dr. Mark Murrie and Dr. Donald MacLaren, without whom this Ph.D would not have been possible. I am grateful for the guidance they gave me and for the time that they spent correcting this thesis.

I would like to thank Dr. Shouheng Sun for allowing me to visit his research labs and for the hospitality I received whilst there. The experience I gained was invaluable, and I wish to thank the members of the Sun research group for their friendship, advice and volleyball coaching during the 3 months I spent in Rhode Island.

I would also like to thank Dr. Catherine Berry and Carol-Anne Smith for their help (and patience!) during my time at the Centre for Cell Engineering. Without their help and supervision the biological studies that make up the latter sections of this thesis would not have been possible.

The microscopes that I depended on were kept in excellent working order by Colin How and Dr. Sam McFadzean, and I am grateful for the training I received within the MCMP group and for the helpful discussions during the colloquia I attended. I would like to thank Dr. Floriana Tuna for performing some of the SQUID measurements that appear in this thesis, and I am grateful to Dr. Rafael Valiente and Dr. Bob Peacock for the optical measurements.

I wish to thank all those who provided much-needed relief: the Murrie Group (past and present) for never needing an excuse to go to the pub, Niall MacLean for his Portal 2 skills and his hard work (sic) during the M.Sci project, my brother for listening to my \LaTeX / writing-up gripes and the rest of my friends (you know who you are!) for making the last 3 and a bit years thoroughly enjoyable. Finally I wish to thank Eilidh for the constant support, patience and encouragement she has given me, and for making writing-up that bit more bearable.

Abbreviations

BE	Benzyl ether
B-DEA	N-butyldiethanolamine
Bis-tris	2-[bis(2-hydroxyethyl)amino]-2-(hydroxymethyl)-1,3-propanediol
Bis-tris propane	1,3-bis(tris(hydroxymethyl)methylamino)propane
BSA	Bovine serum albumin
DEA	Diethanolamine
DEG	Diethylene glycol
E-DEA	N-ethyl-diethanolamine
EDX	Energy dispersive X-ray spectrometry
EELS	Electron energy loss spectroscopy
HDD	1,2-hexadecanediol
M-DEA	N-methyl-diethanolamine
MNP	Magnetic nanoparticle
MPT	3-methyl-1,3,5-pentanetriol
NP	Nanoparticle
OA	Oleic acid
OAm	Oleylamine
PBS	Phosphate buffered saline
SAED	Selected area electron diffraction
STEM	Scanning transmission electron microscopy
TEM	Transmission electron microscopy
Tetrakis	N,N,N',N'-tetrakis(2-hydroxyethyl)ethylenediamine
Tris	2-amino-2-hydroxymethyl-propane-1,3-diol

Contents

1	Introduction	1
1.1	Nanoscale Materials	1
1.1.1	Types of Nanomaterials	3
1.2	Synthesis of Nanoscale Materials	4
1.2.1	Top-down Approach	4
1.2.2	Bottom-up Approach	5
1.2.3	Solution Based Methods	5
1.3	Nucleation and Growth Processes	7
1.3.1	Nucleation	8
1.3.2	Growth Processes	11
1.4	Nanomagnetism	18
1.5	Medicinal Applications of Magnetic Nanoparticles	20
1.5.1	Magnetic Resonance Imaging	20
1.5.2	Magnetic Fluid Hyperthermia	22
1.6	Summary	24
2	Experimental Techniques and Instrumentation	26
2.1	Nanoparticle Synthesis	26
2.2	Other Experimental Techniques	28
2.2.1	Thermogravimetric Analysis (TGA)	28
2.2.2	Infrared Spectroscopy	29
2.2.3	Magnetic Measurements - SQUID	30
2.3	Transmission Electron Microscopy (TEM)	30
2.3.1	The Instrument	33

2.3.2	TEM Imaging	34
2.3.3	TEM Analytical Techniques	40
3	Role of Solvent During Solvothermal Synthesis of Iron Oxide Particles	50
3.1	Introduction	50
3.2	Experimental	52
3.2.1	Materials and Instrumentation	52
3.2.2	Synthesis	52
3.3	Results and Discussion	54
3.3.1	Benzyl Ether	59
3.3.2	Diethylene Glycol	65
3.3.3	Diethanolamine	67
3.3.4	Methyldiethanolamine	69
3.3.5	Ethyldiethanolamine	74
3.3.6	3-methyl-1,3,5-pentane-triol	76
3.3.7	Summary	77
3.3.8	Mixed Solvent Reactions	77
3.4	Magnetic Measurements	80
3.4.1	Introduction	80
3.5	Conclusions	82
4	Synthesis of Lanthanide Oxide Nanowires and Ribbons	85
4.1	Introduction	85
4.2	Experimental	88
4.2.1	Materials and Methods	88
4.3	Results and Discussion	90
4.3.1	Characterisation of Nanowires and Ribbons	90
4.3.2	Nanowire and Ribbon Formation Mechanisms	99
4.3.3	Factors Contributing to Anisotropic Growth	110
4.4	Physical Properties of Ln ₂ O ₃ Nanowires and Ribbons	118
4.4.1	Magnetic Characterisation	118
4.4.2	Optical Characterisation	121

4.5	Conclusions and Further Work	124
5	Metal carboxylate complexes as precursors for metal oxide nanoparticles	126
5.1	Introduction	126
5.2	MnO _x Nanoparticles From Mn-carboxylate Clusters	130
5.3	Experimental	131
5.3.1	Synthesis of [Mn ₃ O(O ₂ CR) ₆ L ₃] Precursors	131
5.3.2	Synthesis of Larger Mn-Containing Complexes	133
5.3.3	Synthesis of Manganese Oxide Nanoparticles	133
5.4	Results and Discussion	134
5.4.1	Optimising MnO NP Synthesis Using Mn ₁₂ -acetate	135
5.4.2	MnO Particle Synthesis Using the Other Precursors	139
5.4.3	The Role of Precursor Ligand	148
5.4.4	The Role of Heating Regime	154
5.4.5	Magnetic Characterisation	161
5.5	Conclusions and Further Work	166
5.5.1	Further work: Iron Complexes as Nanoparticle Precursors	166
5.5.2	Conclusions	167
6	Synthesis of bimetallic magnetic nanoparticles	170
6.1	Bimetallic Particles by the Multi-Source Approach	172
6.1.1	Experimental	174
6.1.2	Results and Discussion	176
6.1.3	Conclusions	187
6.2	Bimetallic Particles by the Single Source Approach	188
6.2.1	Experimental	189
6.2.2	Results and Discussion	192
6.2.3	Conclusions	208
6.3	Biological Studies Using Gd:Fe ₃ O ₄ Particles	209
6.3.1	Experimental	210
6.3.2	Results and Discussion	213
6.3.3	Conclusions	219

6.4 Chapter Conclusions and Further Work	220
7 Conclusions and future work	222

List of Tables

3.1	Overview of solvents used and their physical properties.	53
3.2	Measured and expected d values for a typical nanoparticle electron diffraction pattern.	58
3.3	Comparison of observed and expected d spacings for hematite reflections	63
3.4	Overview of product morphologies obtained for each solvent.	78
4.1	Stability constants for lanthanide a complexation reaction.	104
5.1	Hold temperatures for each manganese precursor.	141
5.2	Overview of product morphologies obtained from the manganese complex precursors.	142
5.3	Magnetism data for spherical MnO nanoparticles.	162
5.4	Magnetism data for the 85 nm octapod MnO particles	164
6.1	Reaction combinations performed to investigate precursor addition. . . .	174
6.2	Outcomes of the eight simultaneous/subsequent reactions	184
6.3	Magnetic data for Gd:Fe ₃ O ₄ NPs.	200

List of Figures

1.1	Relative size of nanomaterials compared to molecules and bulk materials.	2
1.2	Different types of nanomaterial.	3
1.3	Stages of nanoparticle formation.	8
1.4	The LaMer mechanism.	9
1.5	Diagram of the Ostwald ripening mechanism.	12
1.6	Diagram of the oriented attachment mechanism.	13
1.7	Common polyhedral NP shapes	15
1.8	Role of surfactants during NP synthesis	16
1.9	Potential well diagram for two superparamagnetic particles	19
1.10	Hysteresis loops for ferromagnetic and superparamagnetic materials.	19
1.11	Behaviour of proton spins in an MRI experiment.	21
1.12	Diagram of MNPs behaving as MRI contrast agents.	22
1.13	Behaviour of MNPs in an alternating magnetic field.	23
2.1	Diagram of reflux and autoclave reaction setup.	27
2.2	Diagram of TGA apparatus.	28
2.3	Schematic of an electromagnetic lens used in a TEM	34
2.4	Signals generated with interaction of electron beam with matter.	35
2.5	Diagram of main lenses and apertures of an electron microscope.	36
2.6	Main modes of TEM imaging.	37
2.7	Factors affecting TEM image contrast	39
2.8	Example of a HRTEM image.	40
2.9	Schematic showing Bragg reflection of parallel rays from crystal planes	42
2.10	Arrangement of lenses and scan coils for STEM.	44
2.11	Process of X-ray emission from an atom upon exposure to an electron beam.	45

2.12	Low-loss and high-loss EELS spectrum.	47
3.1	TGA plot for Fe(acac) ₃	54
3.2	Particles obtained from autoclave decomposition with no heating hold-step.	55
3.3	Particles obtained from autoclave decomposition with a heating hold-step.	56
3.4	Particle size distributions from autoclave reactions.	57
3.5	Structural formulae showing possible iron/polyol chelates.	59
3.6	TEM images from nanoparticle formation using non chelating solvents.	60
3.7	XRD pattern of the particles obtained using benzyl ether as a solvent.	61
3.8	Particles obtained using dioctyl ether and squalene.	62
3.9	SAED patterns from reactions using dioctyl ether and squalene.	63
3.10	TEM images showing evolution of platelets.	64
3.11	Additional TEM images from DEG reactions	66
3.12	Agglomeration mechanisms for single crystal NPs or compound agglomerated NPs using DEA derivatives.	69
3.13	Electron diffraction from a single compound nanoparticle.	71
3.14	STEM EELS data for a compound cube particle.	72
3.15	Additional TEM images from M-DEA reactions.	73
3.16	TEM images from M-DEA reactions, showing assembly of cubes.	74
3.17	Additional TEM images from E-DEA reactions.	76
3.18	TEM images and ED patterns from a mixed BE/DEG system.	79
3.19	IR spectra of solvents used compared with NP spectra.	80
3.20	Hysteresis loops collected from as-obtained nanoparticles.	81
3.21	Schematic showing alignment of spins in the magnetite lattice.	82
4.1	Literature examples of Ln ₂ O ₃ nanoplates and small Ln ₂ O ₃ particles	87
4.2	TGA analysis of the oleate precursors.	91
4.3	TEM images of nanowires and ribbons.	92
4.4	HRTEM images of nanowires and ribbons.	93
4.5	Additional HRTEM images of nanowires.	94
4.6	Change in nanowire width with increasing atomic number.	94
4.7	SAED patterns from nanowires and ribbons.	95

4.8	IR spectra of the obtained nanowire powders.	97
4.9	EELS spectra from CeO ₂ nanowires.	98
4.10	TEM images from a CeO ₂ 4 hour reaction.	100
4.11	HRTEM images from a 4 and 24 hour CeO ₂ reaction.	101
4.12	BF and DF images from a 4 and 24 hour CeO ₂ reaction.	102
4.13	BF and DF images of Eu ₂ O ₃ nanowires.	103
4.14	3-stage mechanism for nanowire formation.	103
4.15	Additional TEM images of the Dy ₂ O ₃ nanoribbon species.	106
4.16	TEM images of Dy ₂ O ₃ wires from a 4 hour reaction.	108
4.17	Image of the nanoparticle species obtained under stirred reflux conditions.	112
4.18	TEM image of the NP species obtained from an unsealed autoclave.	113
4.19	TEM images of Gd ₂ O ₃ nanowires prepared with additional water added.	114
4.20	TEM pictures of Gd ₂ O ₃ wires obtained using benzyl ether.	115
4.21	Analysis of Gd(OH) ₃ nanorods.	116
4.22	Fe ₃ O ₄ NPs obtained from autoclave decomposition of iron oleate.	117
4.23	Magnetism data for Gd ₂ O ₃ nanowires.	120
4.24	Magnetism data for Dy ₂ O ₃ nanowires	121
4.25	Excitation spectra of bulk and nano Eu ₂ O ₃	122
4.26	Excitation spectra of bulk and nano Eu ₂ O ₃	122
4.27	Emission spectra and luminescence intensities of bulk and nano Eu ₂ O ₃	123
5.1	Structure of the [M ₃ O(O ₂ CR) ₆ L ₃] precursor and the ligands used in MnO NP synthesis.	129
5.2	TGA data for Mn ₁₂ -acetate precursor.	135
5.3	TEM images of cubic NPs obtained from Mn ₁₂ -acetate.	136
5.4	Polydisperse particles obtained using BE.	137
5.5	Effect of heating hold step time on particle morphology.	139
5.6	TGA plots for each manganese containing precursor.	140
5.7	TEM images of NPs obtained using manganese precursors.	143
5.8	XRD pattern showing oxidation of MnO nanoparticles	144
5.9	SAED data for typical octapod particles	145
5.10	HRTEM image of 17 nm spherical particle.	146

5.11	EELS spectra acquired from sample of octapod MnO _x particles.	147
5.12	TEM images of MnO particles obtained by varying the carboxylate precursor.	149
5.13	Additional TEM figures of porous MnO particles.	152
5.14	TEM images of multipod MnO particles.	155
5.15	Tilted TEM series of octapod MnO particle.	156
5.16	TEM image of an octapod particle.	156
5.17	Twinned particles formed using [Mn ₃ O(benz) ₆ (py) ₂ (H ₂ O)].	159
5.18	TEM images of the spherical particles obtained at different reaction temperatures.	161
5.19	Hysteresis loops from spherical MnO nanoparticles.	162
5.20	ZFC-FC scans from spherical MnO nanoparticles.	163
5.21	Surface to bulk atom ratios for spherical nanoparticles.	163
5.22	Hysteresis loops for the 85 nm octapod MnO particles.	165
5.23	TEM images of particles from iron containing precursors.	167
6.1	TGA data for gadolinium precursors.	176
6.2	TEM images from gadolinium precursor control reactions.	177
6.3	TEM images of particles obtained from iron control reactions.	178
6.4	TEM images of simultaneous reactions with Gd(acac) ₃	180
6.5	TEM images of subsequent reactions with Gd(acac) ₃	181
6.6	TEM images of simultaneous reactions with Gd(OAc) ₃	182
6.7	TEM images of subsequent reactions with Gd(OAc) ₃	183
6.8	STEM EELS data for a multi source iron and gadolinium reaction.	186
6.9	Structures of each of the ligands used.	190
6.10	Powder XRD patterns of benzoate precursors.	194
6.11	IR spectra of benzoate precursors.	195
6.12	TGA data of benzoate precursors.	196
6.13	Particles obtained after decomposition of Fe ₂ Gd-benzoate	197
6.14	STEM analysis of NPs obtained using Fe ₂ Gd-benzoate	198
6.15	Magnetic data for Gd:Fe ₃ O ₄ NPs.	201
6.16	ZFC-FC data for Gd:Fe ₃ O ₄ NPs.	202

6.17	TEM analysis Gd-Mn bimetallic NPs.	205
6.18	STEM analysis Gd-Mn bimetallic NPs	207
6.19	Synthesis of the PEG-DPA ligand	214
6.20	Ligand exchange schematic.	215
6.21	Images of water dispersible particles.	216
6.22	MTT toxicity assays of Fe_3O_4 and $\text{Gd}:\text{Fe}_3\text{O}_4$ particles.	217
6.23	Optical fluorescence microscopy of cells exposed to particles.	217
6.24	EM pictures of cells exposed to particles.	218

Chapter 1

Introduction

This thesis relates to the synthesis and characterisation of magnetic nanoparticles (MNPs), a remarkable class of material that has attracted considerable interest within the scientific community due to their interesting properties and potential applications across a range of disciplines. The chemical synthesis of NPs (both magnetic and non-magnetic) is an emergent and diverse area of research, driven by the need to understand the relationship between a particle's morphology and its physical properties. Understanding this often complicated relationship enables researchers to tailor the properties of particles for a specific application, although as we will see it is often far from trivial to synthesise 'high quality' NPs; that is particles which have a narrow size distribution, high degree of shape selectivity and possess a uniform crystallinity throughout the sample. Each of the experimental chapters in this thesis relates to a different aspect or approach to MNP synthesis, although before we examine the synthetic procedures involved in NP fabrication it is important to first discuss nanoparticles in more detail, within the broader context of 'nanoscale materials'.

1.1 Nanoscale Materials

Nanomaterials are materials defined as having at least one dimension between one and a hundred nanometres ($1 \text{ nm} = 1 \times 10^{-9} \text{ m}$). Research interest in nanomaterials has ballooned in recent decades, driven by their potential applications in a large number of fields. The small dimensions of nanomaterials means that they are often considered as the bridge

between molecular and bulk species (Fig. 1.1). What is interesting about nanomaterials is that they often possess unique properties that differ to those of their bulk counterparts, and that these properties (be they physical, optical or magnetic) are often shape or size dependent and can be controlled by varying the dimensions of the nanomaterial. This is not the case for bulk materials, whose properties usually remain fixed, regardless of their dimensions.

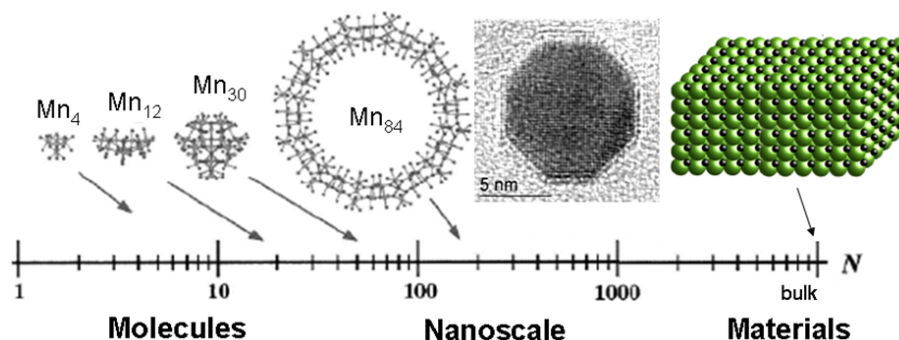


Figure 1.1: Relative size of nanomaterials compared to molecules and bulk materials ($N =$ number of atoms). Nanomaterials are considered the ‘bridge’ between molecular and bulk materials and often possess physical properties not observed in the bulk. Figure adapted from reference [1].

The emergence of improved characterisation techniques (such as the advances made to transmission electron microscopy) have allowed researchers to probe the precise nature of nanomaterials, enabling the relationships between size, shape, elemental composition and physical properties of a material to be investigated. As such, the ability to develop ‘tunable’ nanomaterial syntheses (which can produce a high-quality nanomaterial product with properties pre-determined for a particular application) has emerged as a major research goal for scientists. The last decade alone has seen a dramatic rise in the number of published reports relating to nanoscale science, from 18,000 in 2000 to approximately 130,000 in 2010.[2] Within nanoscale research a number of distinct research branches have emerged, each relating to the study of a particular type of nanomaterial and its applications. It is therefore prudent to first provide an overview of the different types of nanomaterial that can currently be produced, so the work contained within this thesis can be appreciated within the context of nanomaterial synthesis in general.

1.1.1 Types of Nanomaterials

Nanomaterials are usually classified according to their morphologies (see Fig. 1.2). Three dimensional species are known either as nanoparticles or nanocrystals (as they can be synthesised as discrete single crystals). Species with high aspect ratios (defined as the length ratio between major and minor axes) are known as nanowires (or nanotubes if they are hollow). Thin films of material deposited on a surface can also be considered as nanomaterials, provided their thickness is less than 100 nm.

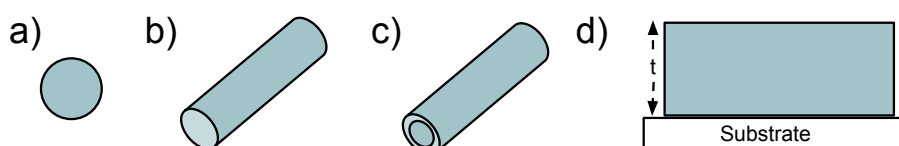


Figure 1.2: Different types of nanomaterial: a) spherical discrete nanoparticle, b) high aspect ratio nanowire, c) hollow nanotube and d) thin film of material, provided thickness (t) is less than 100 nm.

As well as being a variety of different shapes, nanomaterials can have a range of different compositions. Nanotubes of elemental carbon are among the most widely-studied nanomaterial, [3] with potential applications in a range of fields including catalysis, [4] nanomedicine [5] and high mechanical strength materials.[6]

Another area of significant research interest is the synthesis of semiconductor nanoparticles, also known as ‘quantum dots’. Quantum dots have many potential applications in electronics, for example they could be used in transistors [7] and as q-bits for quantum computing.[8] Quantum dots also exhibit size-dependent fluorescence behaviour,[9] and as such have been extensively studied as potential *in vivo* medicinal imaging agents.[10]

Metals and metal oxides represent another significant branch of nanomaterials research. The rich chemistry of the transition metals means that nanomaterials of these metals and their oxides have potential applications across many fields. For example, nano-sized particles of the group 10 elements (nickel, palladium and platinum) can be used as catalysts, and are often found to be more catalytically active than their bulk counterparts. These nanoparticle catalysts have been used in a number of processes including CO oxidation,[11] in fuel cells [12] and even mediating organic reactions, such as the Suzuki cross coupling.[13] Metal nanomaterials make good catalysts due to their in-

creased surface to volume ratios when compared to the bulk (the case of gold nanoparticles is a well-known example — bulk gold is chemically inert, yet gold nanoparticles are catalytically active).[14]

Besides catalysis, transition metal / metal oxide nanomaterials have attracted attention because of their potential uses as new magnetic materials. The *d*-electron configurations of certain metals and their ions render them magnetic, due to the presence of unpaired electrons and nanoscale magnetic materials often exhibit different, size-dependent properties compared to bulk magnetic materials.

The work contained within this thesis relates to the synthesis of magnetic nanomaterials, and as such, detailed sections relating to nanomagnetism (Section 1.4) and the applications of magnetic nanomaterials (Section 1.5) are provided later. The following section outlines the synthetic procedures currently available to synthesise nanomaterials. At present a number of different synthetic protocols are known, which fall into one of two general synthetic strategies as described below.

1.2 Synthesis of Nanoscale Materials

There are two general approaches to fabricating nanomaterials, commonly known as the ‘top-down’ and ‘bottom-up’ methods. The top-down approach uses physical methods and is so-called as it arrives at a nanoscale product by breaking up a bulk material into smaller, nano-sized parts. Conversely, the bottom-up approach ‘builds’ a nanomaterial from atomic or molecular precursors, and is considered the chemical approach.

1.2.1 Top-down Approach

A common top-down approach to fabricating nano materials involves using a high-energy beam to ‘etch’ nanoscale features and patterns onto a substrate. This etching is achieved using a beam of high energy particles (either photons, ions or electrons) to achieve accurate site-specific sputtering and milling of a sample. Patterning of substrates is used extensively by the semiconductor industry when fabricating circuits. This technique is suitable for introducing fine detail onto a surface at the sub micrometer level, though cannot produce discrete nanoparticulate material.

Another commonly used top-down technique is ball-milling. In ball-milling a powder of bulk material is continually circulated in a cylindrical chamber in the presence of a mixing agent (usually steel or stone balls) which grind up the powder to produce fine particles. High-energy ball milling has been used to produce nanoparticles with sizes as low as ~ 9 nm,[15] though the disadvantage of this process is that there is very little control over the final particle shape and size.

1.2.2 Bottom-up Approach

The bottom-up approach involves building a nanomaterial in a step-by-step, atomic approach, fuelled by the decomposition of a molecular precursor or the generation of atomic species. For example, in the pulsed laser decomposition (PLD) method a target material is irradiated by a laser beam, causing the material to vaporise. The vaporised material can be deposited on a nearby substrate, leading to thin film growth. PLD allows precise control over the composition and thickness of a thin film, though the PLD apparatus is expensive and not suitable for producing large quantities of material.

The solution-based synthesis of nanomaterials has been the subject of significant research interest in recent years, as this approach has the ability to produce a range of nanomaterial products with a high level of size and shape control. As this thesis focuses exclusively on the solution-based synthesis of nanomaterials, a thorough discussion is provided below.

1.2.3 Solution Based Methods

Solution based syntheses are one of the most popular methods to create NPs. A variety of different methodologies currently exist, namely co-precipitation, micro-emulsions, micelles and vesicles, reverse micelles, hydro/solvothermal methods and high-temperature thermolysis of metal-containing precursors.

One of the earliest reported nanoparticle synthesis was published by Massart over thirty years ago, and is an example of a co-precipitation reaction.[16] In this synthesis a stoichiometric solution of ferrous and ferric salts are combined in the presence of base, to produce a colloidal solution of magnetite (Fe_3O_4) particles (known as a ferrofluid):



The co-precipitation method is still used today as a straightforward way to produce metal oxide nanoparticles. Unfortunately, the fast nucleation and growth of the particles means that shape control is usually poor and the obtained particles have a wide size distribution.[17] Wide size distributions are undesirable, as many NP properties are size dependent and hence products with a narrow size distribution will have well defined physical properties. Samples with wide size distributions are said to be ‘polydisperse’, and samples with narrow size distributions (where the sample size possess a standard deviation, σ , $< 10\%$ of the mean) are said to be ‘monodisperse’. It should be noted that a sample with a large average particle will also possess a large *range* of particle sizes, unless the size distribution is extremely narrow.

To improve the product quality, new synthetic methods were required that could impart more control over particle nucleation than the co-precipitation method. It was thought that by performing the reaction in a constrained environment, particle growth would be more regulated, and a better quality product could be formed. Using the ‘constrained environment’ approach, microemulsion and micelle based techniques were developed. These techniques rely on the spontaneous formation of nano-sized droplets of surfactant molecules in solution. These nano-sized droplets act as ‘reactors’ which encapsulate aqueous metal solutions, separating them from the surrounding organic-phase solvent. This surfactant-stabilized nanoreactor confines particle nucleation and growth, which can improve particle quality.[18] Micelle-based techniques are popular because factors such as particle size and shape can be easily varied by simple modifications to the reaction conditions, such as metal concentration, surfactant and solvent.[19]

As the microemulsion/micelle technique was developed, reports emerged of a new solution-based method to produce nanoparticles, which involved the decomposition of metal-containing precursors (which were typically simple transition metal carboxylate complexes) at elevated temperature in a high boiling point solvent in the presence of surfactant molecules. [20, 21]. This new ‘thermolysis’ method proved to be a straightforward and versatile way to produce metal, metal oxide and metal alloy nanoparticles with excellent shape and size control. [22, 23] The addition of surfactant molecules to the reaction mixture promoted complex crystal growth kinetics that gave rise to the formation of particles with complex shapes, allowing researchers to investigate the nucleation and

growth mechanisms inherent to solution based nanoparticle synthesis.

The above examples show that solution based methods are popular because they are extremely versatile; there are numerous experimental parameters that can be changed such as reaction time, reaction temperature, solvent, surfactants and precursor — each of which has an impact on the final morphology of the product.

This thesis will look at two closely related techniques — the solvothermal method and the thermolysis of metal-containing precursors. Both methods involve the decomposition of metal-containing species at elevated temperatures, with the only difference between the two methods being the reaction conditions. Solvothermal syntheses involve the reaction occurring within a sealed system known as an autoclave, which can generate large pressures upon heating as any gasses evolved during the reaction are unable to escape. This is interesting as it creates a unique reaction environment not obtainable using conventional glassware, and can give rise to interesting and otherwise inaccessible nanomaterial products.

The ‘thermolysis’ method entails synthesising nanoparticles in a high boiling point solvent, at a reaction temperature above the decomposition point of the metal-containing precursor. The reaction is performed at ambient pressure, meaning standard reflux glassware can be used. The above two experimental techniques are discussed in more detail in Chapter 2.

To understand how NPs can be obtained from a solution based reaction, it is necessary to establish each of the individual steps that comprise the whole nanoparticle growth process, as discussed below.

1.3 Nucleation and Growth Processes

The mechanisms by which colloidal particles grow in solution are still the subject of much research. It is accepted that there are a number of elemental steps that contribute to the overall process; these being precursor decomposition, particle nucleation and particle growth, depicted together in Fig. 1.3.[24] However, the precise nature of the species involved at each stage is not yet fully understood, partly due to experimental limitations. For example, it is not possible to directly observe the species formed immediately follow-

ing precursor decomposition. These species, commonly referred to as ‘monomers’, are taken to be the minimum subunit of a nanocrystal. It is the precipitation of a number of monomers that nucleates a nanoparticle. Nanoparticles in their early stages of growth are known as ‘seed’ or ‘nuclei’ particles. NP nuclei are too small to observe directly (using electron microscopy, for example), though computational simulations suggest that they bear similarities to inorganic ‘magic-number’ metal clusters, as extra stability is derived from such closed-shell systems.[25] The processes by which NPs precipitate and grow from a monomer-containing solution are described below.

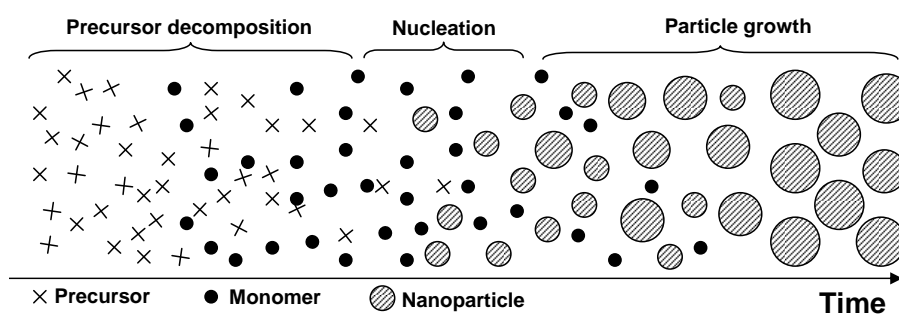


Figure 1.3: Diagram showing the various stages of nanoparticle formation via precursor decomposition. Monomers are formed by precursor decomposition. NP nucleation occurs when monomer concentration is high enough, and NPs consume monomers as they grow. (Adapted from reference [24]).

1.3.1 Nucleation

Nucleation of Particles in Supersaturated Systems (LaMer Mechanism)

The LaMer mechanism was originally developed in the 1950’s to explain the formation of monodisperse colloidal particles in aerosols and sulfur hydrosols.[26] This mechanism describes formation of particles within a concentrated solution (known as a ‘supersaturated’ solution) and has since been used by scientists to explain the formation of nanoparticles from decomposition of metal-containing precursors in solution. The LaMer mechanism is depicted pictorially in Fig. 1.4.

In the LaMer mechanism, decomposition of the precursor (via heat or sonication, for example) produces NP monomers (Stage I). The concentration of monomers increases with continued precursor decomposition, until the solution becomes ‘supersaturated’. In

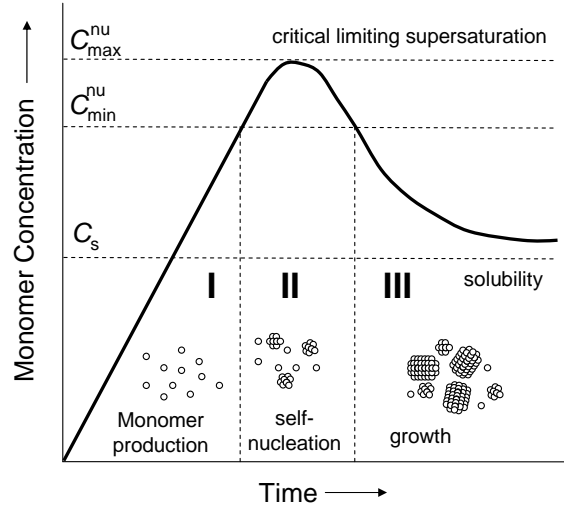


Figure 1.4: Graphic representation of the LaMer mechanism, highlighting the three main stages of nanoparticle formation: I) supersaturation of monomers in solution; II) nucleation of particles; III) particle growth through monomer consumption. Adapted from reference [27].

a homogeneous solution such as this, without a seed for heterogeneous nucleation (such as dust or gas bubbles) the energy barrier to particle nucleation is high. The energy barrier to nucleation can be described thermodynamically as follows. The Gibbs free energy to form spherical crystals of radius r from a solution with supersaturation S is given by

$$\Delta G = 4\pi r^2 \gamma + \frac{4}{3}\pi r^3 \Delta G_v \quad (1.1)$$

where γ is the surface free energy per unit area and ΔG_v is the free energy change between monomers in solution and unit volume of the bulk crystal (i.e: $r \rightarrow \infty$). [25] γ is always positive and since $\Delta G_v = (-RT \ln S)/V_m$ (where V_m is the molar volume of the bulk crystal), ΔG_v is negative provided the solution is supersaturated. Hence a plot of ΔG against r will have a maximum. The value of r where ΔG reaches a maximum is called the ‘critical radius’ (r_c), which is the minimum radius of a NP ‘nuclei’ particle that can grow spontaneously in supersaturated solution. By equating $d\Delta G/dr = 0$, r_c can be calculated: We know from equation 1.1 that

$$\Delta G = 4\pi r^2 \gamma + \frac{4}{3}\pi r^3 \Delta G_v$$

it follows that

$$\frac{d\Delta G}{dr} = 8\pi r\gamma + 4\pi r^2\Delta G_v \quad (1.2)$$

and we know r_c occurs when equation 1.2 is equal to zero, therefore we obtain

$$r_c = \frac{-2\gamma}{\Delta G_v} = \frac{2\gamma V_m}{-RT \ln S}. \quad (1.3)$$

As the solution is supersaturated with monomers (high S), it follows that the value for r_c (which is the size of the NP nuclei) will be small.[25] As mentioned above, the NP nuclei are too small to be observed by any physical methods and their structure can only be estimated by simulation and numerical methods.

Once the energy barrier for nucleation is overcome (when the monomer concentration is above C_{\min}^{nu} , Stage II in Fig. 1.4), particle nucleation begins. After this point, the rate of monomer supply (from precursor decomposition) is exceeded by the rate of monomer consumption (in the nucleation of particles) and eventually the net particle nucleation rate will be zero (C_{\max}^{nu}). After this point, no nucleation events will occur and the system will enter Stage III, where particle growth occurs by aggregation between NP nuclei and monomers for as long as the solution is supersaturated (above C_S). The separation of the nucleation and growth phases is believed to be crucial in obtaining a monodisperse product, as if the two stages overlap, nucleation occurs concurrently with particle growth leading to a product with a range of particle sizes.

There are two experimental methods used in the high-temperature solution based (reflux) synthesis of NPs, called the hot-injection and heating-up processes.

Hot-Injection

An early example of the hot-injection technique was originally reported by Murray et al. for the synthesis of cadmium chalcogenide NPs.[28] Hot injection involves rapidly introducing metal containing precursor into a solution above the decomposition temperature of the precursor. Rapid precursor decomposition causes the solution to rapidly become supersaturated, and nucleation occurs to reduce the free energy of the solution caused by supersaturation. Hot-injection routes have been used to synthesise a variety of NPs including semiconductors [29] and iron oxides.[30]

Heating-Up

In the heating-up process, the metal precursor is mixed at room temperature with surfactants in a high boiling point solvent. The mixture is then heated to the point of precursor decomposition to initiate the nucleation process. For this reason this process is also known as the ‘thermolysis’ route. The heating-up process is popular due to its simplicity and ability to create large quantities of particles with a narrow size distribution. Factors such as heating rate and reflux temperature (determined by the solvent used) have been shown to influence the final morphology of the particle. [31, 32]

1.3.2 Growth Processes

NP growth mechanisms have been widely studied, and a number of different mechanisms have been identified. NP growth processes are of interest to scientists since they influence the final shape of a nanoparticle, which determines the particle’s physical properties.

Ostwald Ripening

Ostwald ripening is a thermodynamically-driven diffusion process that controls the size of particles in solution. Larger particles are energetically favoured, due to the lower proportion of surface atoms they possess compared to smaller particles. The fate of any particular particle is determined by its radius, as there exists a critical radius, r_{cr} , below which the particle becomes thermodynamically unfavourable. This radius is given by

$$r_{cr} = \frac{2\gamma V_m}{RT \ln S} \quad (1.4)$$

with γ the specific surface energy, S the ratio of monomer concentration to the monomer solubility over a flat surface, R the gas constant, T the temperature and V_m the monomer volume.[33] Particles with radius $> r_{cr}$ will experience growth at the expense of those with radius $< r_{cr}$, which experience negative growth (ie: dissolution of atoms into solution.) Dissociation of surface atoms of smaller particles will increase the number of free ions in solution until the solution becomes saturated. At this point free atoms in solution will condense on the surface of the larger particles in solution. The net effect of Ostwald ripening is the growth of larger particles at the expense of smaller ones, as shown in

Figure 1.5.

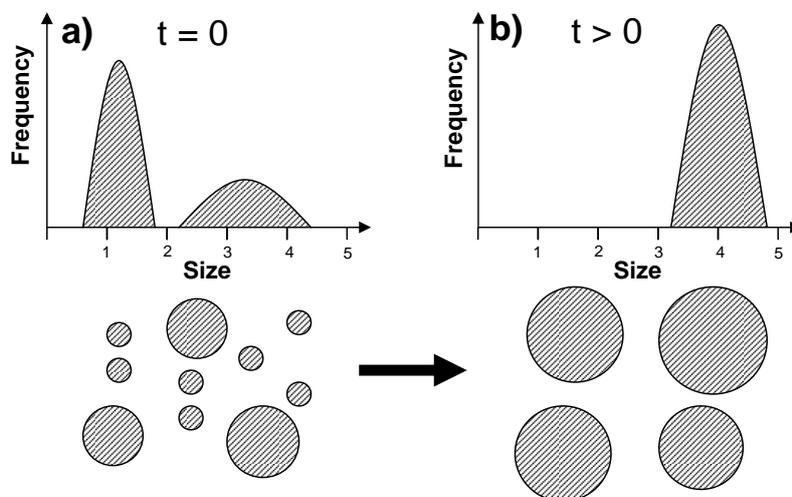


Figure 1.5: Diagram of the Ostwald ripening mechanism for a nanoparticle species at a) $t=0$ and b) $t>0$.[34]

From Fig 1.5 it can be seen that as time increases, the average particle size increases, the number of particles decreases, whilst the total volume of all the particles in the system remains constant. This is characteristic of Ostwald ripening. Ostwald ripening is a slow, diffusion-limited process and usually results in large particle sizes compared to other growth processes.

Oriented Attachment

The oriented attachment mechanism was developed to account for nanoparticle growth behaviour that appeared to deviate from conventional Ostwald ripening. Oriented attachment describes the tendency of some nanoparticulate species to grow by aligning themselves in crystallographic registry with neighbouring particles, meaning that homogeneous crystalline products, often with unusual morphologies can form. For example, Penn reported the synthesis of anisotropic anatase nanowires, which consisted of extended arrays of nanoparticle sub-units aligned in a common crystallographic orientation.[35] This synthesis was developed and more complicated, branched structures could be formed by the same mechanism.[36] This can be depicted graphically as shown in Fig. 1.6, which shows the coalescence of three spherical particles to give a larger, crystallographically homogeneous product.

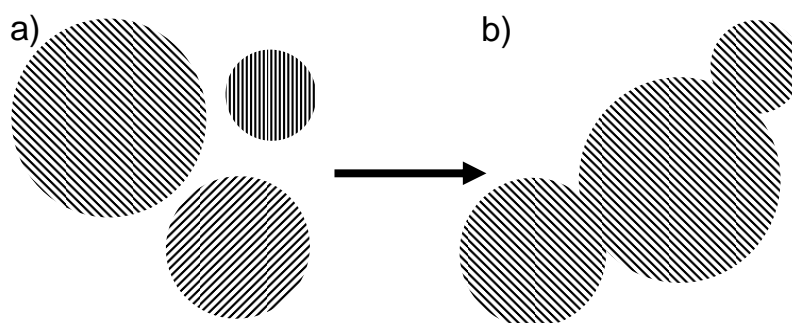


Figure 1.6: Diagram of the oriented attachment mechanism, showing a) a collection of individual and randomly oriented nanoparticles, and b) oriented attachment of these nanoparticles into one species, with a common crystallographic direction.

Whilst capable of giving rise to nanoparticles with complex and branched structures, [37] the oriented attachment process is most commonly observed during the formation of nanowire products, driven by the end-to-end addition of individual subunits. This behaviour has been observed for PbSe,[38] ZnO[39] and CdTe,[40] amongst others. The oriented attachment mechanism and its role in the formation of anisotropic species is discussed further in detail in Chapter 4, which relates to the synthesis of LnOx nanowires.

Van der Waals Interactions

For particles that are not adequately stabilised (by surfactants or ions, for example) then the contribution of van der Waals forces should be considered. These short range interactions have been shown to influence the mechanisms of assembly between particles, with factors such as surface area and polarizability linked to the size of the attractive force between species.[41]

Seed-Mediated Growth

Seed-mediated growth involves decomposing a precursor in a reaction mixture which contains pre-formed nanoparticles. Upon precursor decomposition, the monomers formed precipitate on the surface of the existing NPs since the energy barrier for this processes is lower than that for the nucleation of new particles - ensuring nucleation of new particles is discouraged. Seed-mediated growth is considered a laborious way to produce nanoparti-

cles and requires high quality and monodisperse seeds as starting materials. Furthermore, the heating rate has to be carefully controlled to ensure separate nucleation does not occur.

The advantage of seed-mediated growth is that sequential deposition of layers of different materials can be accomplished, allowing particles with a core-shell morphology to be synthesised — provided there is no mismatch between the seed crystal lattice and that of the incoming material. In the field of nanomagnetism, the nature of the core-shell structure heavily influences the magnetic properties of the product as exchanged-coupled NPs can be synthesised.[42] In nanomedicine, decomposing $\text{Fe}(\text{CO})_5$ in the presence of Au NP seeds gives rise to bi-functional composite materials, which allow the attachment of two different biomolecules, via thiol groups on the Au surface or through covalent bonding to the iron oxide surface.[43] In this thesis we will see seed-mediated growth used in Chapter 6 as a potential route to obtain $\text{Gd}_2\text{O}_3\text{-Fe}_3\text{O}_4$ core-shell particles.

Shape Controlled Growth

The shape of a nanoparticle can be dictated by the difference in growth rates of the various crystal faces (facets) of the particle. Often materials have a preferred crystal growth direction, such as the growth along the c -axis that is observed for materials with hexagonal space groups, such as ZnO[44] and $\text{Ln}(\text{OH})_3$,[45] which yields anisotropic products. Conversely, if particle growth occurs in all directions at an equal rate then a spherical product will form.

The difference in growth rates between crystal faces can be determined by consideration of the free energies of each face. The free energy γ of each face can be calculated by considering the number of broken bonds (i.e.: surface bonds), the bond strength and the density of surface atoms, given by

$$\gamma = 1/2N_b\varepsilon P_a \quad (1.5)$$

where N_b is the number of broken bonds, ε is the bond strength, and P_a is the density of surface atoms.[46] For a crystal with a fcc structure this gives the surface energies $\gamma\{111\} < \gamma\{100\} < \gamma\{110\}$, meaning the final nanoparticle shape should be octahedral or tetrahedral, as these shapes have the most expression of the low energy $\{111\}$ faces. [27] Both the octahedral and tetrahedral morphologies have larger surface area to volume

ratios than a cube of the same volume however, meaning single crystal nanoparticles exist as truncated octahedra which are enclosed by a mixture of $\{111\}$ and $\{100\}$ facets, as shown in Fig. 1.7. The truncated octahedron has a nearly spherical profile and a low surface area to volume ratio, meaning the overall free surface energy is lower than for the octahedral or tetrahedral shapes.

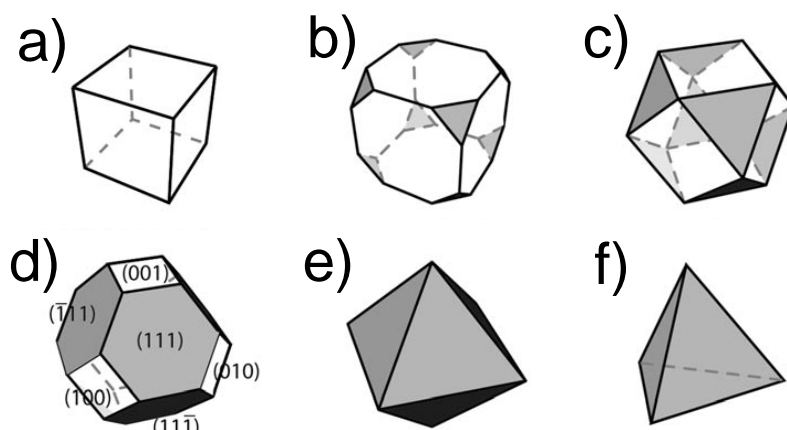


Figure 1.7: Common polyhedral NP morphologies, showing the shapes obtained by increasing the expression of the $\{111\}$ facets (grey) over the $\{100\}$ facets (white). a) Cube, b) truncated cube, c) cuboctahedron, d) truncated octahedron, e) octahedron and f) tetrahedron. Adapted from reference [47].

Shape control can also be achieved during NP growth by the presence of adsorbed species on the NP surface.[47] These adsorbed species are usually surfactant molecules or ions, and they function as ‘molecular capping agents’ that can selectively adsorb onto specific crystal facets during particle growth. Shape control is generally achieved by using reagents that can strongly bind to a particular facet, which causes a reduction in growth at this facet. Conversely, exposed facets where adsorbed species are weakly bound will experience increased growth. The degree to which binding occurs at any given site is determined by the surface energies of each facet, and by the affinity of the capping agent used for a particular material.

Common surfactants used in metal oxide NP synthesis are based on long chain hydrocarbons with either acid or amine moieties, such as oleic acid (OA) and oleylamine (OAm) which contain an unsaturated oleyl ($C_{18}H_{36}$) backbone. Surfactants with long hydrocarbon tails help separate NPs in solution, which prevents agglomeration of adjacent NPs. Acid and amine functional groups have different affinities for the crystal planes of

metal oxides. The acid group is known to bind strongly to iron oxide $\{100\}$ surfaces, whereas the amine group is known to exhibit weak and isotropic binding to metal oxide surfaces. By varying the quantities of OA and OAm present in a reaction, different shapes of NPs can be formed, as shown in Fig. 1.8.



Figure 1.8: Role of surfactants in controlling NP morphology. The weak isotropic binding of OAm on iron oxide surfaces means that particles grown in the presence of excess OAm can be spherical. Increasing the OA:OAm ratio to 1:1 presents enough OA to regulate the competitive growth in the $\langle 100 \rangle$ direction over the $\langle 111 \rangle$ direction, a process leading to the formation of the truncated octahedron. At higher acid concentrations, $\langle 100 \rangle$ growth dominates and a cube is formed.[48]

For example, the decomposition of $\text{Fe}(\text{acac})_3$ with a 1:1.5 excess of OAm to OA yields spherical iron oxide particles, yet increasing the amount of OA to give a 1:1 ratio yields truncated octahedral iron oxide particles.[49] This observation can be explained in terms of the weak isotropic binding of OAm across the particle surface. Hence when OAm is used in excess isotropic (spherical) particles are formed. Increasing the amount of acid in the reaction causes competitive growth in the $\langle 100 \rangle$ and $\langle 111 \rangle$ directions, which causes truncated octahedra to form.[49] Increasing the acid:amine ratio further still results in the formation of iron oxide nanocubes, which form because of the affinity of the acid group for $\{100\}$ surfaces.[48]

OA and OAm are frequently used in NP synthesis, and both reagents were used extensively throughout this thesis. In later chapters we will see the importance of the OA/OAm ratio on particle shape, and also what happens to the final particle morphology when the OA/OAm adsorption at a particle surface is disrupted by either competitive adsorption of solvent molecules (Chapter 3) or by the ligands which comprise the metal containing precursor (Chapter 5).

It is worth noting that the shape of a nanoparticle is not solely determined by the acid/amine ratio, there are many other factors such as the reaction solvent, temperature, heating rate, the crystal structure of the material and type of surfactant that also influence the particle growth mechanism. For example, the length of the hydrocarbon backbone can also control particle shape and size by determining the packing of surfactants on a particle surface. Shorter surfactant molecules will not be able to separate particles in solution as efficiently as longer molecules, meaning that aggregation between particles is more likely to occur, leading to larger particles. An et al. recently showed that decreasing the hydrocarbon length in the acid surfactant from behenic acid ($C_{21}H_{43}COOH$) to decanoic acid ($C_9H_{19}COOH$) resulted in the size of MnO particles increasing from 3 nm to 13 nm.[50]

In addition to enabling shape-controlled NP synthesis by acting as adsorbed species, surfactants can also enable shape-controlled synthesis by acting as templating species. The long chain hydrocarbon tails of surfactants enables them to spontaneously form lamellar species, similar to liquid crystals. These lamellar species can act as nano-reactors in which constrained or anisotropic growth of nanoparticles can occur.[51] The role of surfactant lamellar species in NP synthesis is further discussed in Chapter 4.

The above discussions highlight the considerable number of underlying processes that can contribute to NP formation. It is clear that understanding the complexities of NP synthesis requires thorough and systematic study across a large number of variables, and there is still much work to be done before the nature and role of the species involved in the nucleation and growth processes is fully understood. Understanding the theory behind nanomaterial synthesis represents only one aspect of nano-research. Large numbers of researchers are interested in another equally important aspect, which is finding and implementing applications involving nanomaterials. As this thesis is concerned with the synthesis of magnetic nanoparticles, some discussion of nanomagnetism and the potential applications of MNPs is required, and is given in the following sections.

1.4 Nanomagnetism

The magnetic properties of NPs can differ drastically from their bulk counterparts. A bulk magnetic material will consist of a large number of magnetic domains that form in an attempt to minimise the magnetostatic energy of the material — which is why the structure of a magnetic material plays an important role in determining the magnetic properties. If the material size is reduced to the nanoscale, a single NP can represent a single magnetic domain. Below a critical particle size the formation of domain walls will no longer occur (as the energy required to form them is more than the energy saved should they be formed) and hence stable single domain particles can form.[52] The critical diameter (R_{sd}) for a MNP to reach the single domain limit is given by

$$R_{sd} = \frac{36\sqrt{AK}}{\mu_0 M_s^2} \quad (1.6)$$

where A is the exchange constant, K is the effective anisotropy constant and M_s is the saturation magnetization.[53] For the majority of magnetic nanomaterials R_{sd} will be in the range of 10-100 nm, though for materials with a high magnetic anisotropy (large K value) this value can be higher.

For a single domain particle, the amount of energy required to reverse the magnetization over the energy barrier from one stable magnetic configuration to the other is proportional to $KV/k_B T$, where k_B is Boltzmann's constant, V is the particle volume and T is temperature.[54] If the ambient thermal energy is enough to overcome the anisotropy energy barrier, the magnetisation will no longer be stable and the NP is said to be superparamagnetic. Superparamagnetism can be summarised by a double potential well diagram, as given in Figure 1.9.

In a superparamagnetic regime the magnetisation of the NPs can easily be saturated in the presence of an external magnetic field. Once the field is removed however, the ambient thermal energy is enough to randomise the magnetic moments of the particles, giving a zero net magnetisation — ie: M_r (the remnant magnetisation) and H_c (the field required to bring the net magnetization back to zero, known as the coercivity) are both zero. This can be visualised in the hysteresis loops given in Figure 1.10, comparing the magnetic characteristics of a bulk ferromagnetic material with those of a single-domain superparamagnetic nanoparticulate material.

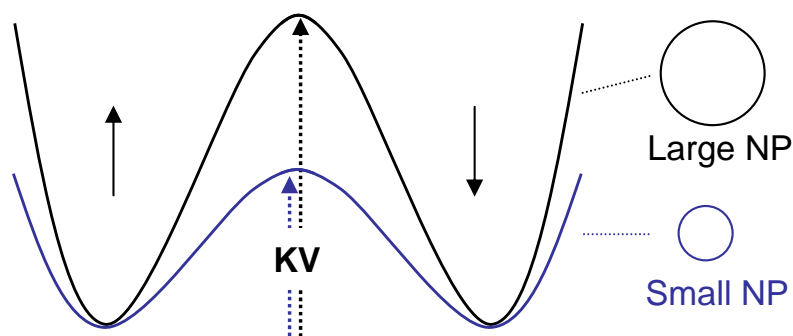


Figure 1.9: Potential well diagram for two superparamagnetic particles of different sizes. The energy barrier separating the two spin states is given by KV , with K the anisotropy constant and V the particle volume. [55]

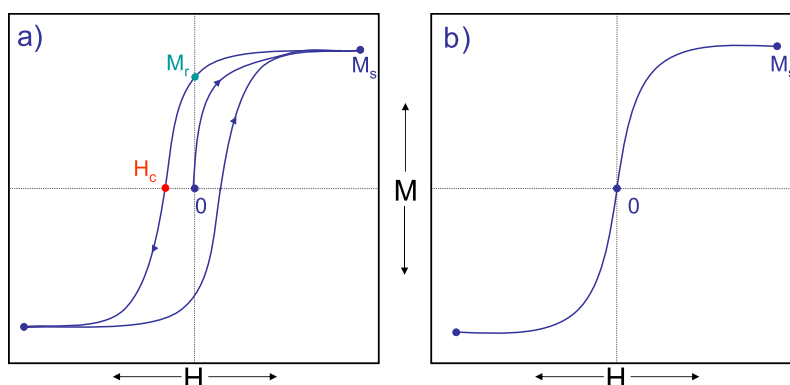


Figure 1.10: Hysteresis loops for a) a ferromagnetic material and b) a superparamagnetic material.[53]

The magnetic properties of superparamagnetic NPs lend them well to certain applications, more so than others. For example, the poor magnetic stability of such particles under ambient conditions has been a constant barrier in developing high density magnetic data storage devices. As such, developing procedures to synthesise NPs with high anisotropy constants that can counteract the thermal fluctuations that are apparent at small particle volumes is currently a high interest area of research. It is interesting to note that much of the earlier magnetic nanoparticle literature was carried out by IBM, as part of their search for high density data storage technologies.[22]

While some magnetic characteristics of superparamagnetic NPs do not lend them well to certain applications, certain properties such as the lack of remnant magnetisation and high saturation magnetisation make them ideally suited for biomedical applications, some of which are described in the following section.

1.5 Medicinal Applications of Magnetic Nanoparticles

The lack of prominent inter-particle interactions due to the absence of remnant magnetisation, which would normally lead to aggregation of particles means that dispersions of magnetic nanoparticles (MNPs) can exhibit high stability under physiological conditions. This stability, combined with the ability to be manipulated by an external magnetic field means MNPs can fulfil both therapeutic and diagnostic roles — which has given rise to a new area of research known as ‘theranostics’. The most studied use of MNPs (and in particular iron oxide nanoparticles) as a diagnostic tool is as potential contrast agents in magnetic resonance imaging.

1.5.1 Magnetic Resonance Imaging

Magnetic Resonance Imaging (MRI) is amongst the most powerful non-invasive imaging methods currently in use. MRI works by observing the behaviour of water protons within biological tissue in the presence of a large external magnetic field.

Protons will align either parallel or antiparallel to the applied field, with slightly more aligning in the parallel (lower energy) configuration. This imbalance leads to a small but detectable remnant magnetisation, conventionally described as being in the z -direction, M_z (Fig. 1.11a,b). To perform an MRI scan, a radiofrequency (RF) pulse is applied to the specimen, which has the effect of tipping the M_z vector (the longitudinal component) from the z -axis and into the transverse (xy) plane. If the RF pulse is of sufficient energy and applied for the correct amount of time the entire M_z component can be tipped by 90 degrees, becoming transverse magnetisation, M_{xy} (Fig 1.11c,d)).

After the RF pulse has been applied, the spins will re-align with the applied field, with the magnitude of the transverse magnetisation in the x - y plane decreasing slowly and the magnitude of the longitudinal magnetisation (M_z) increasing back to the level it was before the RF pulse was applied. The times taken for longitudinal and transverse magnetisation to recover are denoted T_1 and T_2 respectively. The MRI scanner can detect these relaxations in magnetisation, with relaxation rates specific to individual tissues. It is the difference in relaxation rates between types of tissue that generates contrast in the final MR image, and is used to differentiate abnormalities from the surrounding healthy

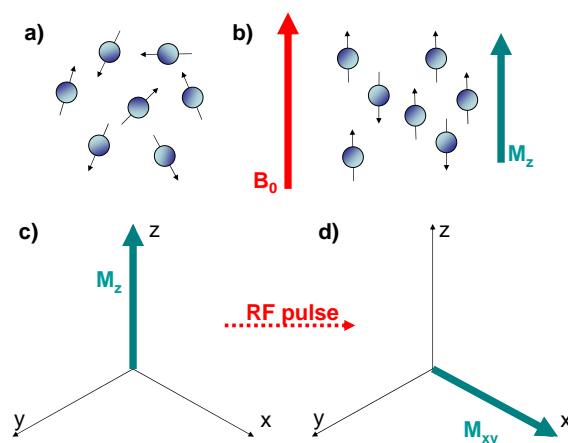


Figure 1.11: Behaviour of protons a) in the absence of an applied field, showing random orientation of magnetic moments and b) in the presence of an external field B_0 , showing parallel and antiparallel alignment of spins, with a slight majority aligning parallel giving a measurable magnetisation, M_z . (c,d) Effect of RF radiation on direction of magnetisation. If an RF pulse is applied at the right frequency for sufficient time, the M_z component of magnetisation can be tipped into the transverse plane, leaving a measurable M_{xy} component. Adapted from [56]

areas.

MNPs can be used as contrast agents because they generate local magnetic fields when placed in an MRI scanner. These localised fields will perturb the magnetisation relaxation rates of nearby water molecules, generating localised contrast specific to the site where the MNP is located, see Fig. 1.12.

The real advantage of using MNPs as contrast agents lies in the scope for functionalising the particle surface with targeting molecules, enabling MNPs to be delivered to specific sites within the body. For example Na et al. showed that manganese oxide particles functionalised with the Herceptin antibody could be used to selectively image breast cancer cells in mice, providing improved image contrast versus the non-functionalised particles.[57]

The above highlights the great potential of MNPs as diagnostic and medical imaging agents. However, MNPs have attracted significant interest as therapeutic agents as well. This is because of the interesting behaviour of magnetic particles when placed in an

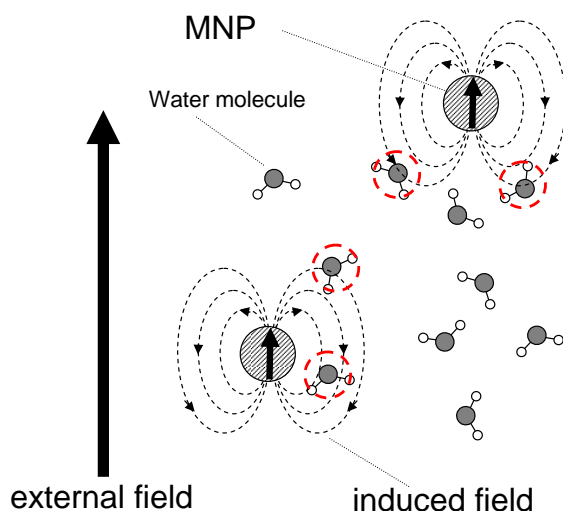


Figure 1.12: An externally applied field will induce a local field within magnetic particles. This induced field will perturb the relaxation of magnetisation of nearby water molecules (highlighted with red circles), giving a noticeable change in contrast in areas where particles are localised. Adapted from [54]

alternating magnetic field, as described below.

1.5.2 Magnetic Fluid Hyperthermia

The physiological conditions present in cancerous tissue (low pH, reduced oxygen levels) render them more susceptible to increases in temperature than healthy tissue.[54] Hyperthermia refers to the class of treatments that involve destroying cancerous tissue by heating to temperatures above normal body temperature where the cancerous tissue is destroyed, but the healthy tissue is unharmed. Dispersions of MNPs can be used in hyperthermia treatments due to the localised heating they experience when placed in an alternating magnetic field, in a technique known as magnetic fluid hyperthermia (MFH). The ability to selectively functionalise MNPs to ‘target’ specific tissues enables excellent spatial control of heating to be achieved, ensuring no healthy tissue is affected.

Heat dissipation from MNPs in an alternating magnetic field occurs when the reversal time of the applied field is far shorter than that of the relaxation time of the magnetic moment of the particles. This results in a lag between the alternating field and rotation of the particle magnetisation. Relaxation of the magnetisation is aided by two relaxation pathways; Néel relaxation, τ_N , which is the rotation of the magnetic moment within the

particle and Brownian relaxation, τ_B , which is the rotation of the entire particle. These pathways are illustrated in Fig 1.10.

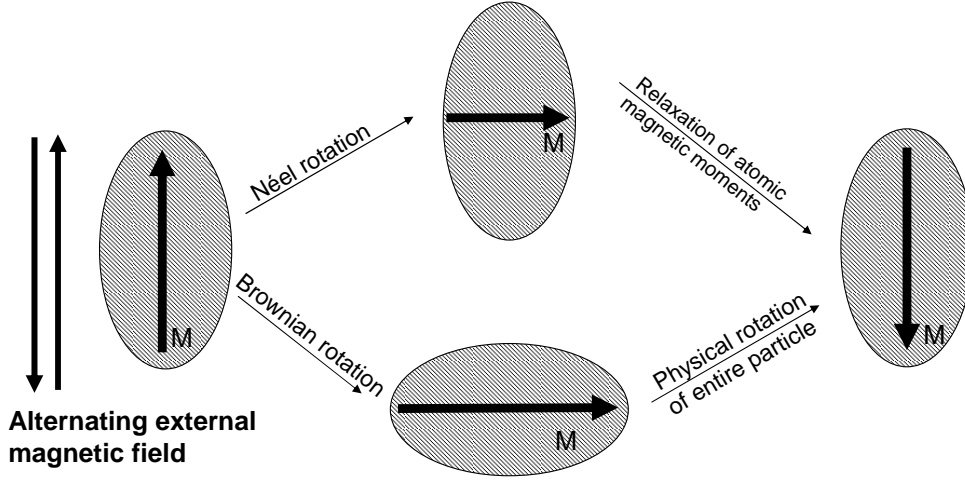


Figure 1.13: Schematic showing behaviour of MNPs in an alternating magnetic field. Néel relaxation (top route) is the rotation of the NP magnetic moment, given by the black arrow. Brownian relaxation (bottom route) is when the entire particle rotates.

These relaxation times are given by

$$\tau_N = \tau_0 \exp\left(\frac{KV_M}{k_B T}\right) \quad (1.7)$$

and

$$\tau_B = \frac{3\eta V_{hyd}}{k_B T} \quad (1.8)$$

with

$$\tau_{eff} = \frac{\tau_B \tau_N}{\tau_B + \tau_N} \quad (1.9)$$

where τ_{eff} is the effective relaxation time (a combination of Néel and Brownian Relaxations), τ_0 is the Larmor time constant (which is an expression of many factors and is equated to 10^{-9} s for simplicity[58]), V_M the particle volume, K is the anisotropy constant, k_B is the Boltzmann constant, T is the temperature, η the viscosity of the medium, and V_{hyd} is the hydrodynamic particle volume.[55] Dissipation of heat from particles is calculated as an average of both these relaxation processes, with the power loss P from a superparamagnetic particle given by the complicated relationship:

$$P = (mH\omega\tau_{eff})^2 / [2\tau_{eff}k_B T \rho V (1 + \omega^2\tau_{eff}^2)] \quad (1.10)$$

where m is the magnetic moment of the MNP, ω the field angular frequency, H the AC magnetic field amplitude and ρ the density of the material.[55]

Equation 1.10 demonstrates that heat dissipation from a MNP is dependent on its physical characteristics; its size and shape (which determine V_M and K), and its chemical properties, such as composition, which determines the magnetic moment m and density ρ of a sample of MNPs. As such, developing syntheses to generate MNPs with high levels of size and shape control underpins most of the current nanoparticle research. Additionally, many researchers are now developing methods to precisely control the elemental composition of a MNP sample, as in both MRI and MFH the elemental composition (and hence the magnetic properties) of a particle directly relate to its effectiveness for that given application. For example, a recent report by Lee et al. highlighted the effect of magnetic exchange in core-shell metal oxide particles. It was found that MNPs comprising a cobalt ferrite core with a manganese ferrite shell ($\text{CoFe}_2\text{O}_4@ \text{MnFe}_2\text{O}_4$) exhibited much higher saturation magnetisations and more efficient magnetic thermal induction than standard iron oxide particles.[42] The improved magnetic properties of these particles makes them promising candidates for future MFH treatments.

1.6 Summary

By achieving high levels of control over all physical and chemical aspects of nanomaterials, researchers will be able to develop truly functional materials that are tuned for a specific purpose. Whilst the field of nanomaterials research is still in its relative infancy, considerable progress has been made in understanding the fundamental processes that contribute to nanomaterial formation and growth mechanisms. Despite this improved understanding, a lot of unknown factors remain, and optimising nanomaterial (especially nanoparticle) synthesis remains largely a trial-and-error process, due to the large parameter space in which nanoparticle syntheses are performed.

This thesis examines different aspects of magnetic nanoparticle synthesis, and examines a number of different synthetic protocols. A variety of magnetic nanoparticles are

investigated, including iron oxide nanoparticles, manganese oxide nanoparticles and lanthanide oxide nanoparticles and nanowires. The effect of other magnetic ions as dopants is also investigated for the iron oxide system.

The MNPs synthesised in this thesis were primarily characterised by transmission electron microscopy (TEM), amongst other techniques. Before we look at the syntheses for individual nanoparticle systems, the following chapter describes the experimental and characterisation techniques that are central to understanding the results given in the later chapters.

Chapter 2

Experimental Techniques and Instrumentation

In the previous chapter an introduction into nanomaterials research was provided. The main synthetic methodologies behind nanomaterial fabrication and their potential applications were introduced, with an emphasis on solution based NP synthesis and applications in nanomedicine. In this chapter we will examine in more detail the protocols used to synthesise the particles contained within this thesis. The main characterisation techniques will also be covered, with a special emphasis on transition electron microscopy (TEM), as the application of TEM is undoubtedly central to nanoparticle research and was certainly the most widely-used characterisation technique in this thesis. To begin with, we shall discuss the two synthetic approaches that were used to synthesise the NPs described in the later chapters.

2.1 Nanoparticle Synthesis

In this thesis two approaches were used to synthesise NPs — the reflux and autoclave methods. These methods were chosen as they allow the greatest degrees of flexibility when performing solution-based NP synthesis, as there are numerous experimental parameters that can easily be changed. Both approaches involve heating a reaction mixture which contains metal-containing precursor, surfactant and a high boiling point solvent. A typical reflux set-up is given in Fig. 2.1a). Reflux experiments can be performed under

inert atmosphere, throughout this thesis N_2 was used as the purge gas. Performing a NP synthesis under an inert gas can prevent unwanted oxidation of the NPs. The reaction mixture is heated with stirring in a round-bottomed flask using a heating mantle, and the reaction temperature monitored using a temperature probe. For each reflux reaction performed in this thesis a purge step was included at $110\text{ }^\circ\text{C}$, in which a flow of nitrogen was allowed to pass over the mixture. This stage was included to remove all the low boiling point impurities (such as residual solvent, water etc.) that are present in the reaction, as well as encouraging complexation between metal ions and surfactants. After 30 minutes at $110\text{ }^\circ\text{C}$, the exit tap is closed and the reaction mixture is said to be under an inert ‘blanket’ of nitrogen. If required, additional reagents can be added during the reaction via syringe, this is known as ‘hot-injection’.

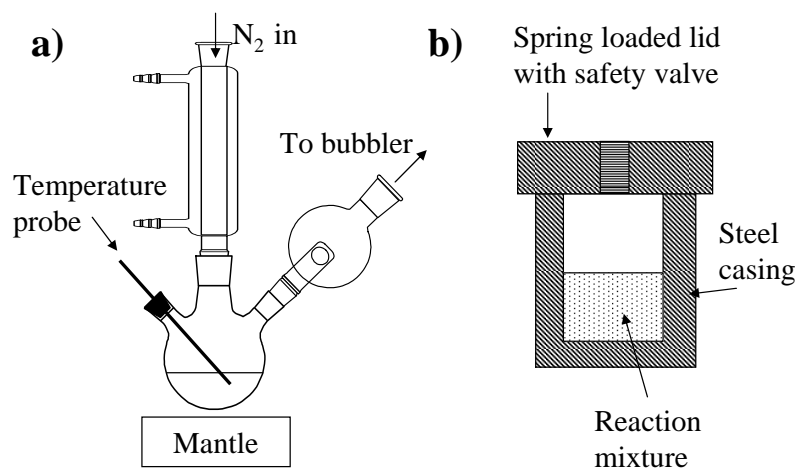


Figure 2.1: a) Reflux reaction setup and b) steel autoclave setup.

The autoclave (or solvothermal) approach involves heating the reaction mixture in a sealed reaction vessel, known as an autoclave (Fig. 2.1b). The autoclave consists of a Teflon liner encased within a steel shell. The reaction mixture is placed in the Teflon liner, the autoclave sealed and then heated in an oven. As the reaction vessel is sealed, high pressures can be achieved. This is the main difference between reflux-based methods, which are performed at ambient pressures. It is also not possible to stir the contents of an autoclave during a reaction. Autoclave methods were used in the following two chapters, and were shown to give rise to interesting particle morphologies. Throughout this thesis, Parr acid digestion bombs with a 12 mL capacity Teflon liner were used.

2.2 Other Experimental Techniques

2.2.1 Thermogravimetric Analysis (TGA)

Thermogravimetric analysis (TGA) is a technique that measures changes in sample weight as a function of temperature. The information obtained from TGA measurements gives insight into the decomposition characteristics of a material. Since weight loss can be expressed as a percentage loss of the sample starting weight it is often possible for users to determine the nature of the decomposition products. A diagram of a typical TGA instrument is given in Fig. 2.2. Throughout this thesis TGA measurements were taken on a TA Instruments Q500 Thermogravimetric Analyzer under a nitrogen atmosphere. The decomposition characteristics of powdered samples were measured in the room temperature to 450 °C range, using a 10 °C / minute ramp rate.

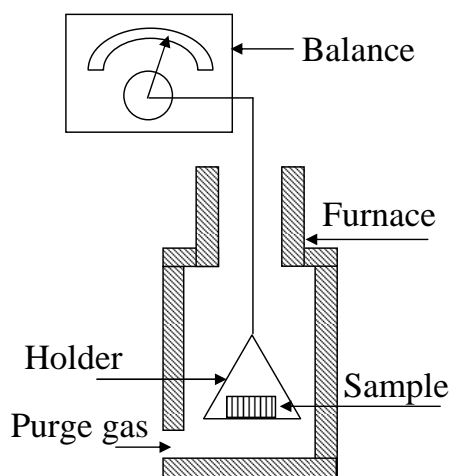


Figure 2.2: Diagram of TGA apparatus. During the measurement, the sample is loaded onto a cradle which is lowered into a furnace. The cradle is attached to a sensitive balance, which measures the change in weight as the temperature is increased.

TGA is a valuable tool in nanoparticle synthesis as it allows the decomposition temperature of the metal-containing precursors to be exactly determined, enabling the rational design of experiments. TGA also determines the suitability of a complex as a precursor for nanoparticle synthesis, as an ideal precursor would exhibit rapid, uniform decomposition — leading to rapid and homogeneous nucleation of particles. A precursor that

decomposes slowly across a broad temperature range will continually nucleate particles over a long period of time, leading to an undesirable polydisperse product. TGA was used extensively in Chapter 5 when assessing the decomposition behaviour of polynuclear manganese complexes, data which allows the rational placing of hold temperatures to ensure complete precursor decomposition.

If bimetallic particles are being synthesised, TGA allows the selection of precursors that will decompose at similar temperatures.[59] This encourages the formation of bimetallic particles as opposed to a mixture of single-metal particles, although as we will see in Chapter 6, simply having two precursors with similar decomposition characteristics does not guarantee the formation of bimetallic particles. Additionally, TGA can be used to determine the reaction temperature when particles are synthesised using the ‘hot-injection’ technique, where precursors are injected directly into a hot reaction mixture at or above their decomposition temperatures.

2.2.2 Infrared Spectroscopy

Infrared (IR) spectroscopy is used to determine the binding modes of molecules within a sample. A standard IR spectrometer irradiates a sample using light in the 4000–1000 cm^{-1} frequency range. Bonds between atoms vibrate in this frequency range, and IR photons produced by the spectrometer will be absorbed by the bonds, provided the frequency of the bond and the incident IR photons are identical. A difference map between a blank background spectrum and a sample spectrum shows which wavelengths of light have been absorbed, and will therefore show which types of bonds are present in the sample. In nanoparticle synthesis, IR spectroscopy is used to determine which surfactants are present on a particle surface. For example, oleic acid (used throughout this thesis) exhibits strong CH stretches from the hydrocarbon tail of the molecule, in addition to the oxygen stretches and bends resulting from oxygen-metal bonds at the point where the surfactant binds to the particle surface.[32] Throughout this thesis IR spectra were obtained using a Shimadzu 8400s FT-IR. IR spectra were collected using the as-obtained nanomaterial powders.

2.2.3 Magnetic Measurements - SQUID

Magnetic characterisation was performed on a superconducting quantum interference device (SQUID). During a SQUID measurement, the sample is moved through superconducting detection coils. The moving magnetic moment of the sample induces a current in the detection coils which is detected by the SQUID, with the size of the current proportional to the magnetic moment of the sample. The SQUID can be cooled to liquid helium temperatures, which allows for temperature-dependent magnetisation data to be collected. To perform SQUID measurements of nanoparticle samples, a known amount of the as-obtained NP powders were sealed in gelatin caps and mounted in eicosane to prevent movement of the sample during measurement. The obtained data was corrected for diamagnetism by subtracting the diamagnetic contribution measured from an empty gelatin capsule. SQUID measurements were performed using a Quantum Design MPMS-XL SQUID (University of Glasgow, UK) or a Quantum Design MPMS-XL7 SQUID (National EPR centre, University of Manchester, UK.)

2.3 Transmission Electron Microscopy (TEM)

Nanomaterials research has reached the level it is at today due to an increased understanding of the factors that influence nanomaterial formation. Understanding the often complex relationships between synthetic procedures and final material morphologies is made easier by direct observation of the obtained products. In nanoparticle research, detailed characterisation of a sample is conducted primarily using transmission electron microscopy (TEM) and associated analytical techniques. As TEM is the main characterisation technique used in this thesis, the following section describes the TEM instrument and the processes that are involved in obtaining meaningful data from TEM.

Before the development of electron microscopy, visible-light microscopy (VLM) was the only technique available to scientists that allowed the observation of species too small to be visible to the naked eye. Unfortunately, there is a fundamental limit to the resolution available using VLM, given by the Rayleigh condition, which states that the smallest distance that can be resolved, δ , is given by

$$\delta = \frac{0.61\lambda}{\mu \sin\beta}, \quad (2.1)$$

with λ the radiation wavelength, μ the refractive index of the viewing medium and β the collection semi-angle of the magnifying lens.[60] $\mu \sin \beta$ is often known as the ‘numerical aperture’ and is often equated to unity for simplicity. From this we can see that the smallest distance that can theoretically be resolved with an ideal optical microscope is approximately $\times 0.6$ the wavelength of visible light (about 300 nm). Unfortunately, the 300 nm limit (although small — around 1000 atom diameters) is insufficient to resolve atomic-scale structure, and in the first half of the 20th century electron microscopy (EM) was developed.

The development of EM as a characterisation tool quickly followed de Broglie’s theory that electrons had wave-like properties, with a wavelength much shorter than that of visible light.[61] His predictions were later proved (independently) by Davisson and Germer, and also by Thompson and Reid whose electron diffraction experiments illustrated the wave-like nature of electrons.[62, 63] With this discovery it became apparent that if electrons were used in microscopy it would be possible to achieve much greater image resolution and the term ‘electron microscope’ was first used by Knoll and Ruska in 1932.[64] de Broglie showed that the wavelength of an electron is related to its energy, E . The de Broglie wavelength is calculated by

$$\lambda = \frac{h}{p} = \frac{h}{mv}, \quad (2.2)$$

where h is Planck’s constant and $p = mv$ are the momentum, mass and velocity of the electron. In TEM the momentum is imparted to the electron by accelerating it through a potential V , giving it a kinetic energy eV . Potential energy must equal kinetic energy, therefore

$$eV = 1/2mv^2, \quad (2.3)$$

so the momentum is

$$p = mv = \sqrt{2meV}, \quad (2.4)$$

and hence by equation 2.2, the electron wavelength is

$$\lambda = \frac{h}{\sqrt{2meV}} \quad (2.5)$$

which can be approximated to

$$\lambda = \frac{1.22}{E^{1/2}} \quad (2.6)$$

with E in electron volts (eV) and λ in nm.[60] From equation 2.6 it can be shown that for a 100 keV electron, $\lambda \approx 0.004$ nm, which is far smaller than the diameter of an atom. This limit represents the theoretical maximum resolution obtainable for an electron at 100 keV, though in practice this resolution is not achieved due to limitations with electron lenses. There are 3 main defects that limit the resolution achieved in TEM. **1)** Spherical aberration (C_S), which occurs when the lens field acts differently for off-axis electrons. The further an electron is off-axis, the more strongly it will be bent back towards the axis upon passing through a lens. The result of this is that a point object is imaged as a finite-sized disk, which limits our ability to magnify detail because the detail is degraded by the imaging process. The most modern TEM instruments are fitted with a C_S corrector, which automatically corrects the spherical aberration and allows for the imaging of individual atoms. Neither of the microscopes used in this thesis were fitted with a C_S corrector, although for satisfactory NP imaging a C_S corrector is not required. **2)** The second defect that limits resolution in TEM images is chromatic aberration (C_C). This relates to the ‘spread’ of energies that the electrons after they interact with the specimen. Due to inelastic scattering the electrons that leave a sample have a slight spread in their energies. Lower energy electrons are bent more strongly by electron lenses than high energy electrons, which means that electrons emerging from a specific point of a sample can be spread into a disk on the image plane, thereby reducing resolution. This effect is more pronounced in thicker samples, meaning C_C is more of an issue in thin film samples (100’s of nanometres) than nanoparticle (10’s of nanometres at most) samples. **3)** The final resolution-limiting lens defect is astigmatism. Astigmatism occurs when electrons experience a non-uniform magnetic field within an electron lens. The non-uniform field arises as it is too difficult to machine the soft iron pole pieces to be perfectly cylindrical. It is also possible that the magnetic field within an electron lens will be affected by micro-structural defects within the soft iron itself. Fortunately, astigmatism can be easily corrected for using the astigmaters, which are octupoles within the microscope that can introduce a compensating field, balancing the inhomogeneities that cause astigmatism.

Since the first transmission electron microscopes were made available commercially, much progress has been made refining these instruments into powerful imaging and analysis tools. The basic principles of how electrons can be used to form an image and the

theory behind some of the analytical methods of EM that are mentioned in this thesis are described in the following sections.

2.3.1 The Instrument

A standard TEM instrument consists of 3 main components; the electron source, the imaging system (which contains the lenses and apertures) and the imaging/spectroscopy hardware. Each of these components will be briefly described in turn.

Electron Sources

There are two main types of electron sources: thermionic and field-emission. These sources operate on different principles and microscopes with each type of source were used throughout this thesis. The Tecnai T20 instrument was equipped with a thermionic LaB₆ source, which produces electrons by heating the LaB₆ source to high temperatures, until the work function is overcome and electrons can leave the material. The Tecnai TF20 was equipped with a Field Emission Gun (FEG), which pulls electrons from a sharp tungsten tip by using a large negative electric potential. The electron source for each microscope is found at the top of the microscope column. Both microscopes were operated at 200 kV (which by equation 2.6 gives $\lambda \approx 0.003$ nm — which is many times smaller than an atom, although as previously stated due to imperfections within electron lenses this resolution cannot be obtained). It is not enough to simply be able to produce a beam of electrons from a source, these electrons must first be focused before they can be used for any analytical purpose. Electron focusing is achieved by using electromagnetic lenses, as described in the following section.

Magnetic Lenses

The magnetic lens of a TEM manipulate the electron beam similar to the effect of placing an imperfect convex glass lens in a beam of visible light. Unlike optical lenses however, TEM lenses focus beams of electrons using electromagnetic fields created by passing a current through copper wires within the lens, as seen in Fig. 2.3.

Electron lenses were first focused using electromagnets by Busch as long ago as 1927,[65] and modern lenses are capable of focusing electrons to achieve atomic reso-

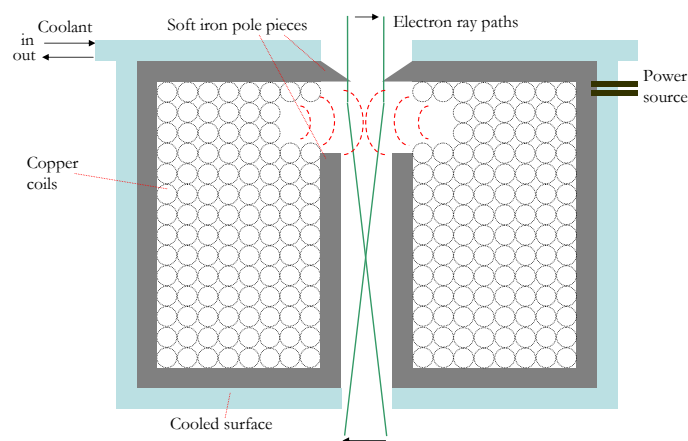


Figure 2.3: Schematic of a cross-section of an electromagnetic lens used in a TEM, showing the bundles of copper coils within a cooled housing. The incoming electron beam is focused when it passes through the magnetic field (indicated by red lines) which exists where there is a gap in the iron pole pieces. [60]

lution. The lenses in a TEM are fixed in position, with their strength depending on the current that is applied to them (this is compared with lenses in visible light microscopes, which can be moved up and down the optic axis). Electrons are focused by these lenses before and after they interact with the sample, and there are a number of different outcomes that are possible after the interaction of the electron beam with the sample, these are shown in Fig. 2.4.

Many of these interactions produce signals that can be detected by probes fitted to the microscope, allowing for detailed characterisation of the sample. These analytical techniques will be summarised in later sections. Generally, it is the electrons that pass through the sample (those which are transmitted — hence the ‘T’ in TEM) that are used to form a typical TEM image or electron diffraction pattern.

2.3.2 TEM Imaging

Diffraction and Imaging

The two most common modes of TEM operation are diffraction and imaging, depicted in Fig. 2.5. Electrons scattered from the specimen are dispersed by the objective lens and a diffraction pattern is created in the back focal plane of the objective lens. In diffraction mode, the back focal plane of the objective lens acts as the *object plane* of the intermediate

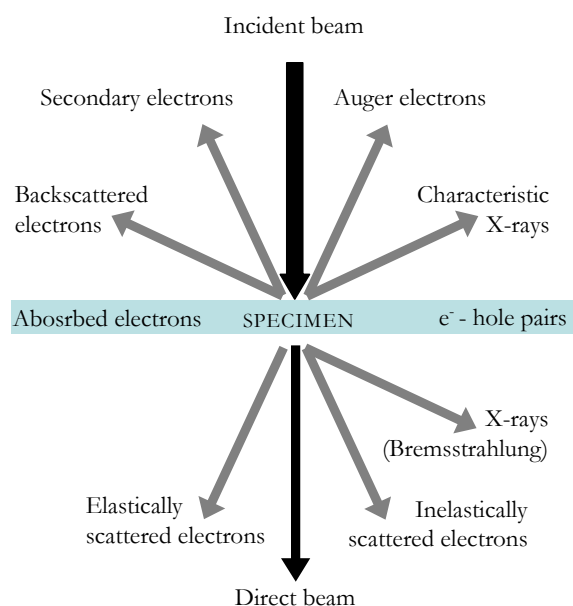


Figure 2.4: Signals generated from interaction of incident electron beam with a thin sample. The arrows indicate the relative direction of the signal. Many of the inelastic processes produce signals that can be detected using probes built in to the TEM column. The characteristic X-rays produced can be analysed using EDX, and the transmitted beam contains electrons which have suffered energy loss and can be analysed using EELS. Both EDX and EELS were used in this thesis and will be discussed in more detail later in this chapter.

lens, meaning a diffraction pattern is projected onto the viewing screen. In imaging mode, the strength of the intermediate lens is adjusted so that its object plane is the *image plane* of the objective lens, which means that an image is projected onto the viewing screen.

Diffraction patterns arise when electrons are scattered from crystallographic planes within the specimen, which are subsequently transmitted at a variety of angles. These scattered electrons are focused by the objective lens, resulting in a diffraction pattern in the back focal plane of the objective lens (Fig. 2.5a). A more thorough look at the principles behind diffraction will be given later in section 2.3.3. When operated in diffraction mode, a selected area aperture can be inserted into the image plane of the objective lens. This has the effect of excluding all the electrons apart from those which pass through the area defined by the selected area aperture. The advantage of selected area electron diffraction (SAED) is that diffraction patterns can be collected from specific regions (or even specific nanoparticles) within the sample, meaning that the diffraction data can un-

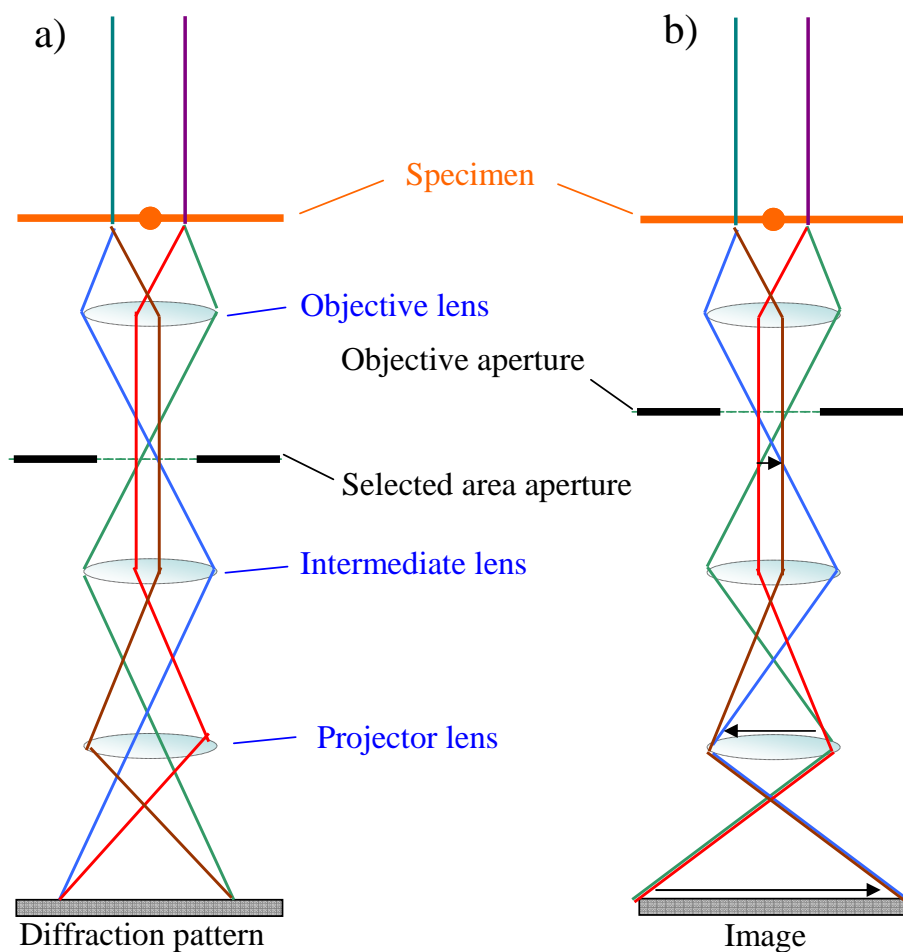


Figure 2.5: Diagram of the a) diffraction and b) imaging modes of TEM operation, showing the paths of the electron beam and how changing the strength of the lenses results in the formation of a diffraction pattern or an image respectively. The lenses are drawn here as convention glass lenses for clarity, though the true structure of an electron lens is different and was explained in more detail in Section 2.3.1

ambiguously be ascribed to the images that we see.

For conventional imaging, the projector lenses below the objective lens magnify the image formed in the objective image plane and project it onto the viewing screen (Fig. 2.5b). To acquire an image, the screen is lifted and the beam is dropped onto a detector. When operated in imaging mode, there are two distinct modes of imaging available: bright field (BF) and dark field (DF). In bright field imaging the image is formed using the direct beam, which contains unscattered electrons and those which have been scattered through very small angles. It is possible to insert an objective aperture into the back focal plane

of the objective lens, which can exclude the scattered electrons and give a higher contrast image (Fig. 2.6a).

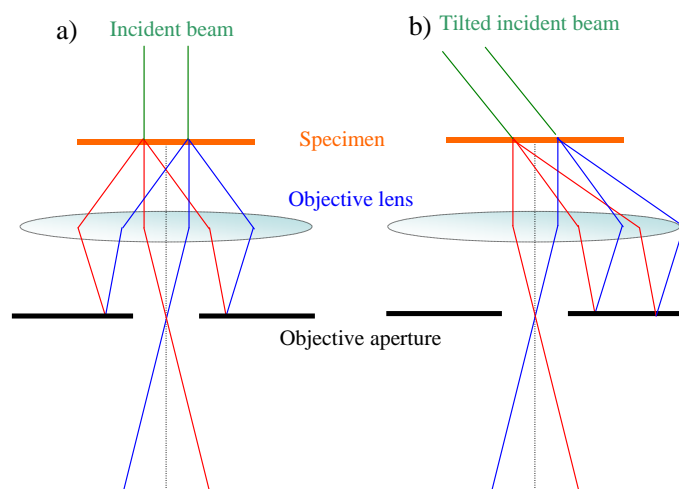


Figure 2.6: Ray diagram showing a) bright-field imaging, using an objective aperture to omit scattered electrons and b) dark-field imaging, where the objective aperture is used to select scattered electrons from a tilted beam.

In contrast, a dark field image is formed by excluding the direct beam, meaning only electrons which have been scattered are used to form the final image. This is achieved by tilting the electron beam prior to contact with the sample, allowing diffracted electrons (rather than the incident beam) to pass into the projector optics and form an image. Inserting an objective aperture allows only electrons from a specific crystallographic reflection to be imaged, as shown in Fig.2.6b). DF imaging is a useful tool as it allows the user to select electrons that have been scattered by a specific angle, meaning regions of a specific crystallographic orientation can be imaged — which provides insight into the crystalline make-up of a material which in turn can give insight to growth mechanisms. Images collected using different electron scattering angles can be false-coloured and superimposed, which is a convenient way of distinguishing regions of varying crystallographic orientation. This is especially useful when dealing with unusual nanoparticle morphologies, as nanoparticle growth cannot be imaged in real-time. DF TEM was used throughout this thesis, to investigate the crystalline nature of the unusual aggregated magnetite NPs we will see in the following chapter, and also to investigate the growth mechanisms of the LnO_x nanowire species we will see in Chapter 4.

Any image can be thought of as a collection of regions of different contrast, and

contrast in BF TEM images is dependent on the number of electrons that hit a particular point on a detector (the microscopes used were all equipped with charged-coupled device (CCD) detectors, discussed in more detail in Section 2.3.2). The more electrons that hit a point on the detector, the brighter that region will be.

The number of electrons that reach the detector depends primarily on two factors: the sample thickness and atomic mass (Z) of the material. It is easier for an electron to pass un-deflected through a thin material than a thick one, as the likelihood of interaction with the nucleus and electron cloud of a sample increases with thickness. This means a thick region of a sample will transmit more scattered electrons, which in bright-field imaging mode leads to fewer counts on the detector and a darker region in the final TEM image. Heavier (high Z materials) will contain larger nuclei and denser electron clouds, which increase the likelihood of scattering electrons from the incident beam. This means regions within a sample containing heavy elements will appear darker than regions containing lighter elements. This is why it is extremely difficult to image isolated organic molecules (such as polymers) using TEM, unless the specimen is stained first (we will cover the staining of biological samples using osmium and uranium stains in Chapter 6) or the support used is exceptionally thin. For this reason graphene has emerged as a new support material for TEM samples, it is possible to fabricate single-layer thick sheets of the material, which can be dropped onto holey-carbon films. The areas where graphene straddles a hole in the carbon are mono or few-layer in thickness, so are effectively electron transparent. A derivative of graphene was recently used as a support to image the iron component of a single molecule of the iron transport protein ferritin. [66]

For this thesis, holey carbon film mounted on copper grids was used as the support during TEM imaging. Samples were prepared by dropping a dilute NP dispersion directly onto the grid, and allowing the solvent to evaporate slowly. Holey carbon grids contain a thin layer (≈ 30 nm) of amorphous carbon support. When imaged, the NPs appear darker than the carbon support, due to the high Z of the metal component of the particle, with respect to the carbon support. So a 5 nm iron oxide (high Z) particle appears dark on a carbon support (low Z), despite the support being many tens of nanometres thicker, as illustrated in Fig 2.7a). Similarly, the Fe core of a Fe-Fe₃O₄ core-shell NP would appear darker than the Fe₃O₄ that surrounds it, (Fig. 2.7b).

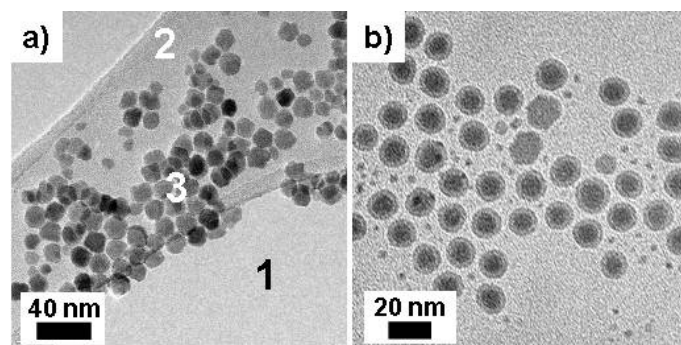


Figure 2.7: a) Effect on material thickness on TEM contrast. The brightest region **1** indicates a hole in the carbon film, the brightness being due to the high number of electrons striking the CCD detector. Region **2** is the 30 nm thick carbon support, which appears slightly darker than the hole due to the scattering of electrons as they pass through the support. Region **3** indicates iron oxide nanoparticles, showing high contrast with the carbon support due to particle thickness and increased Z . b) Effect of Z on TEM contrast, the Fe core of these particles appears darker than the Fe_3O_4 shell.

Capturing an Image

The microscopes used in this thesis are fitted with charge-coupled device (CCD) sensors. A CCD is a metal-insulator-silicon device that can store charge generated by light or electron beams (CCDs are also found in modern digital cameras, not just electron microscopes). A typical CCD sensor will consist of an array of individual capacitors. Each capacitor is electrically isolated from its neighbours and is able to store charge through the creation of a potential well underneath each CCD cell. The charge accumulated by each potential well is dependent on the intensity of the incident radiation. The CCD cells used for TEM are typically 10–15 μm in size, with the frame rate for acquiring an image depending on the image size and the technology used to read the acquired signal. CCD displays exist that are capable of achieving over 10^5 frames per second (for imaging rapid processes in real-time), though for NP imaging such high speeds are not necessary. Indeed, long exposure times were often required to detect diffuse scattering in electron diffraction patterns.

TEM data were obtained and processed using either Digital Micrograph or IMAGEJ 1.41 software. Throughout this text, particle sizes are quoted as mean \pm standard devia-

tion followed by the standard deviation expressed as a percentage of the mean.

2.3.3 TEM Analytical Techniques

TEM was used in this thesis to thoroughly characterise NP samples. Apart from obtaining basic information such as particle size and shape, TEM was also used in a much more analytical capacity to obtain information on particle crystallinity (i.e: phase identification) and elemental quantification such as measuring the variation in oxidation state of metal ions in metal oxide particles (as we will see in Chapters 3 and 5) or looking for the presence of dopant ions within particles (Chapter 6).

High Resolution TEM (HRTEM)

High resolution TEM (HRTEM) requires the microscope to be operated at very high magnifications. When imaging particles at high magnification, it becomes possible to see contrast created by the atomic columns of a material, as shown in Fig. 2.8. The atom columns can be resolved if their orientations are parallel to the incident beam. The space between these columns of atoms relates to the space between atoms of a known atomic plane. By measuring the distance between the atomic columns it is possible to assign the observed spacing to a particular atomic planar spacing of a material. HRTEM is therefore a convenient way of determining the crystallinity of a sample, especially when used in conjunction with electron diffraction. HRTEM was used extensively throughout this thesis, and HRTEM images can be found in every chapter. The use of HRTEM is especially relevant in Chapter 4, where high magnification images were used to investigate the size of crystalline domains within CeO₂ nanowires.

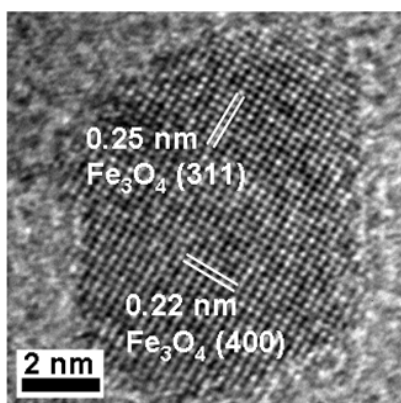


Figure 2.8: HRTEM image of a Fe₃O₄ nanoparticle. The distances between the atomic planes (shown by white lines) were calculated and indexed to the corresponding reflection.

Electron Diffraction

The diffraction of radiation (either X-rays or electrons) from crystalline material is an established method to characterise materials. Information on phase purity, crystalline orientation and crystallite size can be obtained from diffraction. Both electron diffraction and (to a lesser extent) X-ray diffraction were used in this thesis. Within the context of nanoparticle synthesis and characterisation there are a number of advantages to using electron diffraction over X-ray diffraction:

- Because electrons are charged, they interact more strongly with matter than X-rays do. This means intense diffraction patterns (DPs) can be obtained quickly from small amounts of material, whereas an X-ray DP would require a substantial amount of powder and a considerable amount of time to obtain a pattern.
- Switching between TEM imaging and diffraction modes is straightforward, meaning electron DPs can be obtained in the same session as the sample is being imaged, obtaining an acceptable DP takes only a few minutes and no additional sample preparation is required. X-ray DPs require additional preparation and collecting an acceptable pattern (from a nanocrystalline material) can take several hours.
- It is possible within to use selected area electron diffraction techniques (SAED) within the TEM column to collect DPs from *specific* crystallites within a sample, meaning we can relate the crystallography to the images we see. Being able to distinguish multiple phases or different materials within a sample is one of the great advantages of the TEM.

The physical principles behind electron and x-ray diffraction are similar and are discussed briefly below.

Fig. 2.9 illustrates the Bragg conditions for the reflection of electrons by a crystal. P_1 and P_2 indicate a set of parallel planes with Miller indices hkl and interplanar spacing d_{hkl} . The two incident beams R_1 and R_2 are shown being scattered by atoms C and B respectively. Simple geometry shows that

$$AC = CD = d_{hkl} \sin \theta. \quad (2.7)$$

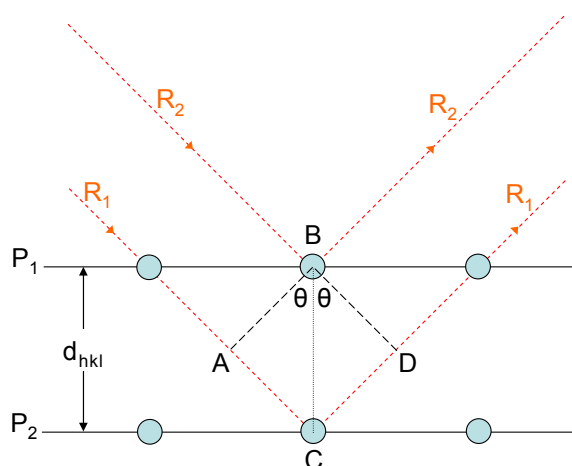


Figure 2.9: Bragg reflection of parallel rays from crystal planes P_1 and P_2

It can clearly be seen that ray R_1 travels a distance $AC + CD$ greater than R_2 , therefore

$$\text{path difference} = AC + CD = 2d_{hkl} \sin \theta. \quad (2.8)$$

If the path difference is an integer ($AC + CD = n\lambda$), then constructive interference of the rays will occur, and the reflection is observed. A non-integer value causes destructive interference between the scattered rays and the reflection is not observed. Equation 2.8 can be simplified to give to give Bragg's law, which states the angles for allowed scattering from a crystal lattice,

$$2d \sin \theta = n\lambda. \quad (2.9)$$

Diffraction from a single crystalline region in TEM will give rise to a spot pattern on the viewing screen, with each spot corresponding to electrons that have been scattered by a particular reflection. Diffraction from a large number of crystalline regions, each with different orientation (ie: a polycrystalline sample or a sample of numerous single crystal nanoparticles) will yield a ring pattern, where each ring is made up of numerous spots. Calculating the radius of these rings gives the d value for each reflection, and the d of each ring correspond to the reflections of a known material that can be looked up in a database.

X-ray powder diffractometers have a different mode of operation. An X-ray pattern is generated by plotting the intensity of radiation for a given value of 2θ , while 2θ is varied by rotating the detector around the sample. The final plot of 2θ vs intensity will look similar to a radial intensity plot of an electron diffraction ring pattern, and can be used to characterise the material. The XRD data in this thesis was collected using either a Bruker

D8 or a PANalytical X'Pert instrument. Samples were prepared for XRD either by sealing the as-obtained powders in glass capillaries or by evaporating a particle dispersion onto a silicon support.

Scanning TEM (STEM) Mode

In STEM mode, the electron beam is converged into a point which scans over the sample in a raster. This is in contrast to conventional TEM (CTEM) where the electron beam is broad and illuminates the large areas of the sample. The beam is converged into a point by the condenser lenses, which are positioned in between the electron source and the sample in the microscope column. Control over the positioning of the beam is achieved using scan coils, as shown in Fig. 2.10

The advantage of STEM is that the user has far greater control over the placement of the electron beam, allowing for nanometre scale precision. When used in conjunction with the analytical techniques EDX and EELS (which are described below), a microscope operated in STEM mode allows for the mapping of the interfaces and boundaries between materials, areas which are of interest to materials scientists. For nanoparticle characterisation, STEM mode allows for the simultaneous imaging and collection of data from a series of points across an individual particle, which allows the user to map elemental distributions and variations in oxidation states for an individual particle. For this thesis, the Tecnai TF20 microscope was used for STEM investigations.

Energy Dispersive X-Ray Spectroscopy (EDX)

EDX is a popular method for performing elemental analysis of a sample. It relies on the principle that when matter is struck with a beam of high energy radiation the electrons within the matter can be promoted to higher energy levels or be ejected completely from the sample, leaving a hole in a lower energy level. Electrons from higher energy levels can drop energy levels to fill these newly-created low-energy holes, in doing so they emit X-rays. The energy of the emitted X-ray is unique for each element, and relates to a specific energy level transfer (Fig. 2.11). As the energy of the emitted X-rays are unique to each element and to each transition, EDX analysis can be used to 'fingerprint' a sample.

The Tecnai TF20 instrument has an EDX detector fitted to the TEM column, meaning

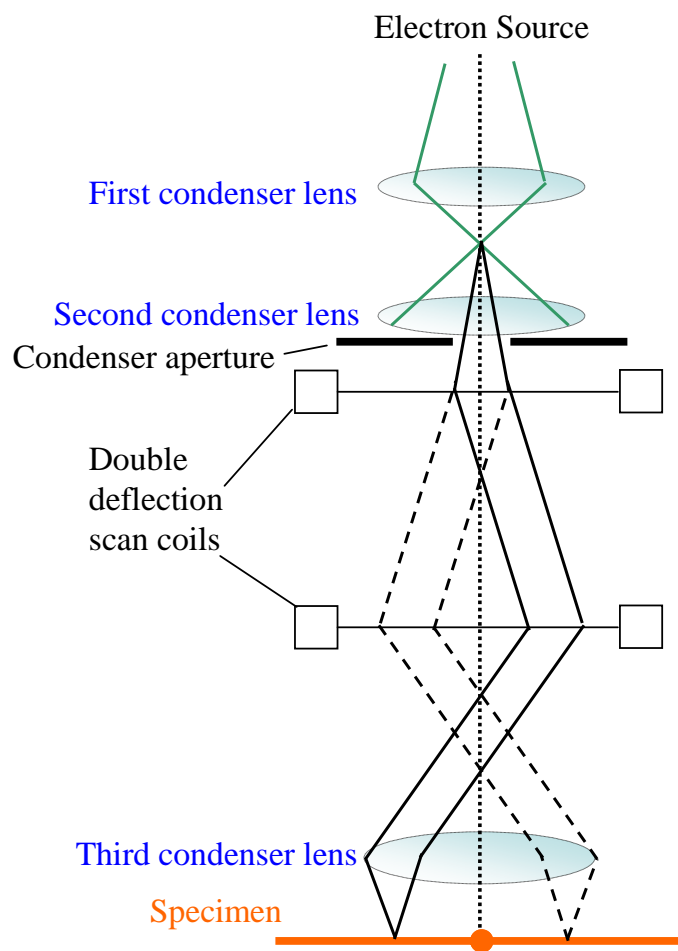


Figure 2.10: Formation of a condensed electron probe for the STEM mode of operation. The beam is condensed into a point by the condenser lenses, and the double deflection scan coils allow for precise positioning of the probe, or for the probe to be scanned over the sample in a raster.

EDX spectra can be obtained easily. These spectra provide information on the elements present within a sample and their relative ratios. When used in STEM mode, EDX spectra can be obtained from specific areas of a sample and can be used to provide information on the elemental distribution of metals within an alloy or core-shell nanoparticle, for example. EDX has been used extensively to investigate nanoparticles, such as determining the extent of doping [59, 67] or confirming the nature of core-shell particles. [68, 69]

With EDX there is the possibility that an emitted X-ray will travel to another part of the sample and cause the emission of another X-ray from a different material. This can lead to spurious peaks in the EDX spectrum, as the detector may pick up X-rays from ma-

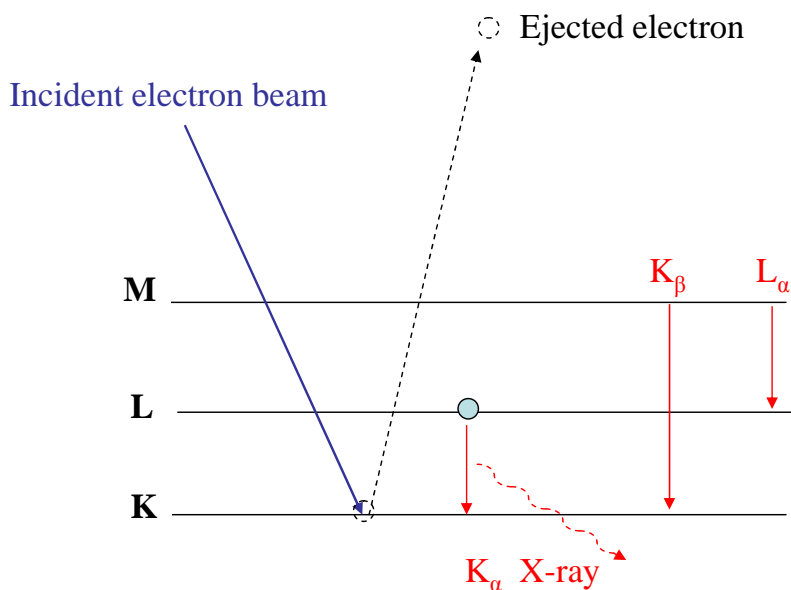


Figure 2.11: Process of X-ray emission from an atom upon exposure to the incident electron beam. Symbols in red indicate the transitions associated with each type of X-ray.

material that is not directly in the path of the electron beam — which can limit the accuracy of EDX spectra. Furthermore, EDX data only provides information on the elements that are present in a sample and the quantities they are present in, and no information relating to the chemistry or electronic structure of atoms at a particular point in a sample is obtained. For these reasons electron energy loss spectroscopy (EELS) can be performed as a complementary technique, as described below.

Electron Energy Loss Spectroscopy (EELS)

EELS is the analysis of the energy distributions of electrons that have passed through the sample, these are electrons that will have lost no energy (ie: have passed straight through) or have suffered inelastic collisions. Energy losses like these can reveal aspects of the chemistry of the sample atoms, which can give us information on their valence states and bonding modes. This is of relevance to this thesis as EELS can be used in conjunction with the STEM operating mode to provide detailed information from a specific nanoparticle within a sample, such as the spatial distribution of elements, or the electronic structure (such as oxidation state of metal ions) of said particle.

We will see throughout this thesis that using EELS to map intra-particle metal oxida-

tion states affords insight into particle formation mechanisms. For example, in Chapter 3 we will see that the formation of a thin maghemite ($\gamma\text{-Fe}_2\text{O}_3$) shell on a magnetite (Fe_3O_4) particle can be observed and the thickness of the shell quantified, and in Chapter 4 the susceptibility of Ce^{3+} to air oxidation into Ce^{4+} in CeO_2 nanowires is discussed. When used in STEM mode the sensitivity of EELS allows for accurate quantification of the composition of specific particles within a sample, which we will see in further detail in Chapter 6 when looking for small quantities of Gd^{3+} dopant in Fe_3O_4 and MnO nanoparticles. In order to understand the EELS data which will be presented in this thesis, it is first important to describe the physical processes which produce EELS spectra.

As was described in section 2.3.3, an electron beam passing through a sample can ionise (remove an electron from a core electron shell) from the atoms within the sample. An electron from an outer shell can drop to fill the hole created by ionisation, and there is the release of an X-ray of a characteristic energy associated with this process — which is the basis of EDX spectrometry. EELS and EDX are related in that they deal with different aspects of the same processes. In EELS, an electron that has ionised an atom within the sample will have lost the energy associated with that ionisation. As the energy required to ionise an electron from an element is unique to that element and also to the shell that the electron was ionised from, analysis of the distribution of energy losses of the electrons that pass through a sample provides key information on the elements that are present in a sample. An ionisation event will be represented by a feature known as an ‘edge’ in the EELS spectrum, and comparison to literature values allows the identification of the elements present in a sample. EELS spectra are usually divided into 2 regions, the low & zero loss regions (with energy losses below ~ 50 eV) and the high loss regions (energy loss > 50 eV). These two regions are shown in Fig. 2.12 a) and b) respectively, which is the EELS spectra of Fe_2O_3 , taken from the Gatan EELS atlas reference library.

It is instantly obvious that the zero loss peak (ZLP) is considerably more intense than the rest of the signal (note the logarithmic scale for the low loss region shown in Fig. 2.12a). This is because for a thin sample (such as a nanoparticle) most electrons will pass through the sample without suffering inelastic collisions, and have retained the energy of the incident electron beam. The ZLP also contains electrons which have suffered small energy losses. The peak occurring after the ZLP is the plasmon peak. In

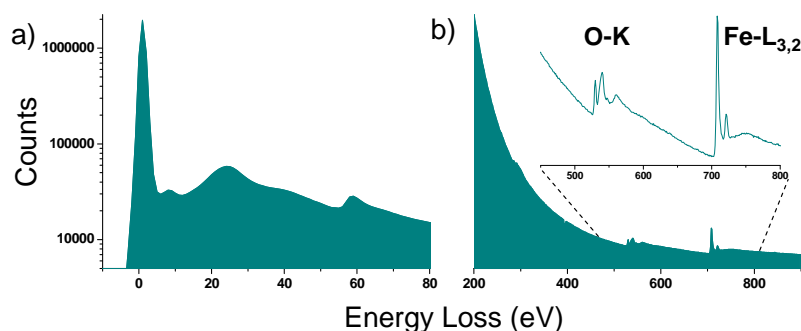


Figure 2.12: EELS spectrum showing a) the low loss and b) high loss regions.

The oxygen and iron edges are indicated inset.

this thesis, elemental analysis was performed exclusively using the high loss regions of the EELS spectra, as the shape of the edges in this region provide information on the chemistry of the sample. The oxygen- K edges and the iron- $L_{2,3}$ edges are shown inset in Fig. 2.12b). The letter associated with each edge represents the shell from which the electron was ionised. So the oxygen K edge at ~ 530 eV represents all the electrons that passed through a sample which lost ~ 530 eV ionising an electron from the K shell of an oxygen atom. The energy required to remove a K shell from a heavier atom (such as a transition metal) would be too great to be detected by EELS, as there is a rapid decay in signal with increasing energy loss. For this reason we generally work with the L edges of transition metals and the M edges for lanthanide elements (as will be seen in Chapter 4). The numbers after the L symbol in the iron case indicate which orbital the electron was ionised from, so the ionisation of a $2s$ electron gives rise to a L_1 edge and a $2p$ electron gives rise to either the L_2 or L_3 edge. The EELS edges can be used for quantification of the elements present within a sample. The atomic percentage composition of a sample can be determined simply by integrating the area under the EELS edges present in the spectra, after removal of the background. All of the EELS data in this thesis was processed using the Digital Micrograph software package. Elemental quantification was performed using Hartree-Slater electron scattering cross-sections and following the removal of a fitted power-law background.

EELS edges like those shown inset in Fig. 2.12b) often contain fine detail, such as additional peaks after the initial edge onset. These features are known as energy loss near edge structures, referred to using the acronym ELNES. The shape of ELNES features is

dependent on the interactions of the energy beam with the lattice of atoms that surround the ionised atom. The underlying physics behind these interactions is complicated and is outwith the scope of this thesis. What is important is to understand that the shape of the ELNES features of an EELS edge depend on factors such as the co-ordination between atoms within a sample (ie: within a nanoparticle) and their oxidation states. Ultimately, analysis of EELS and ELNES features is a very powerful analytical fingerprinting technique.

Whilst it is true that EELS is a more powerful analytical technique than EDX, it is also more challenging to obtain quality information. Acquiring EELS spectra requires careful calibration of the TEM, and thin samples are needed — which can make it difficult to obtain EELS data from larger agglomerated particles. In comparison, EDX spectra can be obtained quickly and thin samples are not required (as EDX uses a back-scattered signal, whereas EELS uses the transmitted electron beam). Sample thinness is not a major concern in this thesis as all of the materials imaged are at most a few tens of nanometers thick. An extra complication is that EELS requires a very clean sample, as sample contamination can lower the intensity of the signal. For example, when acquiring EELS spectra from a NP sample the electron beam can degrade the surfactant molecules that coat the particle, which causes the build-up of a layer of carbon on top of the particle. This carbonaceous layer decreases the signal to noise ratio during EELS acquisition and worsens the data obtained. For this reason, NP samples for EELS have to be thoroughly cleaned prior to TEM imaging and analysis, which is a problem when dealing with materials which are sensitive to oxidation as the particle washing procedure is usually performed in the open air. As the particles examined by EELS in this thesis were primarily prepared using a nonaqueous, surfactant-based technique, sample contamination was a significant problem. To overcome this problem, the dwell time of the electron beam on specific particles was kept to a minimum, which reduced the electron ‘dose’ that each particle received. By manually moving the beam across numerous particles whilst simultaneously acquiring EELS data, it was possible to reduce the contamination and obtain satisfactory datasets.

EELS spectra were collected on the Tecnai TF20 instrument, which is fitted with a post-column Gatan Enfina Electron Energy Loss Spectrometer.

Now that the experimental and characterisation techniques have been described, we will now turn our attention to the remaining chapters which detail the synthesis of magnetic nanoparticles. In the next chapter we will discuss the factors which influence the autoclave synthesis of iron oxide particles.

Chapter 3

Role of Solvent During Solvothermal Synthesis of Iron Oxide Particles

3.1 Introduction

‘Hydrothermal’ is a term first used by geologists in the early 19th century to define naturally occurring subterranean geological conditions. The extremes of temperature and pressure found under the surface of the earth are ideal conditions for the crystallisation of a range of minerals, and it was thought by recreating such conditions in a laboratory, synthetic minerals could be created.

Scientists have since been able to reproduce similar high temperature and high pressure reaction conditions by utilising sealed reaction vessels known as autoclaves. When heated above the boiling point of the reaction solvent, extreme pressures can be generated within the autoclave which mimic geological conditions. When a non-aqueous solution is used as the reaction solvent the general term ‘solvothermal’ synthesis is used. Hydrothermal and solvothermal techniques are now an established method of preparing crystalline materials, from minerals to single crystals of discrete molecules.[70–72]

With the advent of nanotechnology and nanomaterial synthesis, hydrothermal and solvothermal techniques received renewed interest as a route to fabricate nanoparticles. The advantages of solvothermal synthesis over other methods, such as the ease of performing large scale reactions and the simplicity of the equipment required, mean that solvothermal methods represent an appealing alternative to high temperature reflux-based

reactions. However, the simplicity of the solvothermal apparatus means that there are limitations. For example:

- The stainless steel casing of an autoclave does not allow the reaction mixture to be directly observed, meaning any mechanistic insight gained from noting the physical changes in the mixture (such as colour changes and at what temperature they occur at) is lost.
- It is not easy to stir the contents of an autoclave in a conventional oven-based reaction. At best, the contents can be thoroughly stirred manually before being placed in the oven. Lack of stirring may be an issue as it can cause inhomogeneities in reagent levels at individual points throughout the reaction mixture. It is worth noting that although inconvenient, not being able to stir the mixture is not necessarily a drawback, as unstirred conditions can encourage growth of interesting anisotropic species.[73]
- It is not possible to add additional reagents to a reaction mixture midway through a reaction. Sequential and/or controlled addition of reagents is often a key feature of reflux-based experiments, since the temperature at which a reagent is added is a contributing factor to product morphology.[74]

Despite these limitations, autoclave-based methods are a popular and simple method to produce nanomaterials, and a range of materials including carbon nanotubes, quantum dots and metal oxide nanoparticles have been synthesised.[75–77] Iron oxide nanoparticles are amongst the most extensively studied, due to their potential applications in a range of fields, as described in Chapter 1. Experimental parameters such as surfactant choice, iron source, heating rate and heating time have all been examined in the solvothermal synthesis of iron oxide, and a range of morphologies including spherical,[78] cubic,[79] nano-ring,[80] hexagonal prism,[81] and hollow spheres[82] have been previously prepared.

The aim of this chapter is to study the often-overlooked influence of the solvent in the autoclave synthesis of magnetite (Fe_3O_4) NPs, since solvents have a number of potentially exploitable characteristics. For example, the solvent boiling point sets the maximum attainable temperature (or pressure in the case of a sealed system) which determines the

decomposition rate of the metal containing precursor.[31] Additionally, solvent viscosity will determine mobility and diffusion rates of solvated ions, NP nuclei and larger NPs, thereby influencing nucleation and growth rates and the extent of aggregation, which is especially relevant in unstirred systems such as the autoclave. Furthermore, if the solvent has chemical functionality then it may be able to stabilise species through chelation[83] or undergo direct reaction, such as acting as a reducing agent through the presence of hydroxyl groups.[82] This chapter demonstrates that all of the above factors are relevant to the formation of Fe_3O_4 NPs and a family of related solvents are considered that allow competing factors to be distinguished. A solvothermal polyol protocol is employed that is particularly promising for large-scale NP production because it offers a facile, relatively low-temperature route and uses innocuous reagents that would be attractive for a commercially-scalable process. The role of hold times and variable heating rates during thermal processing is examined, which are often not considered in autoclave based protocols but will be shown to profoundly affect NP morphology.

3.2 Experimental

3.2.1 Materials and Instrumentation

Transmission electron microscopy (TEM) and electron diffraction was performed on the FEI Tecnai T20 and FEI Tecnai TF20 instruments, both operated at 200 keV. Samples were prepared for TEM, TGA and IR as described in Chapter 2. Magnetic measurements were conducted at room temperature on a Lakeshore vibrating sample magnetometer using the as-obtained powders.

3.2.2 Synthesis

Reagent quantities were chosen following an established protocol for Fe_3O_4 NPs.[23] In a typical synthesis $\text{Fe}(\text{acac})_3$ (0.5 mmol), 1,2-hexadecanediol (2.5 mmol), oleic acid (1.5 mmol) and oleyl amine (1.5 mmol) were mixed in air with 10 mL of one of the solvents listed in Table 3.1, [84, 85] within in a 12 mL Teflon lined stainless steel autoclave. Two heating protocols were adopted, both using a heating rate of 20 °C per minute: either the

sample was heated in an oven at 230 °C for 6 hours; or was heated to 110 °C for 4 hours, then at 230 °C for 2 hours. We refer to the latter as using a heating hold-step, which is a common protocol in reflux-based nanoparticle syntheses and is used to separate the nucleation and growth phases of particle formation. The hold-temperature of 110 °C was chosen to encourage the formation of coordination complexes between the iron precursor and solvent, to allow the role of solvent during particle growth to be observed. As 110 °C is well below the decomposition temperature of Fe(acac)₃ (which thermogravimetric analysis (TGA) indicated to be ~190 °C (Fig. 3.1)), no NP formation is expected to occur. The maximum temperature of 230 °C was chosen as this is above the decomposition temperature of the Fe(acac)₃ precursor, so full conversion of precursor into nanoparticle is expected. Furthermore, at temperatures above 230 °C the Teflon lining of an autoclave may start to deform, so no temperatures above 230 °C were used.

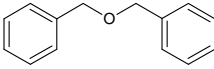
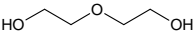
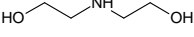
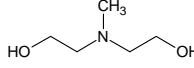
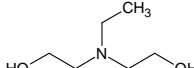
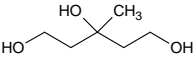
Solvent	BP (°C)	Structure	Viscosity (mPas)
Benzyl ether (BE)	298		-
Diethylene glycol (DEG)	245		35.7
Diethanolamine (DEA)	217		379.3
N-methyldiethanolamine (M-DEA)	247		57.14
N-ethyldiethanolamine (E-DEA)	252		48.27
3-methyl-1,3,5-pentanetriol (MPT)	216		-

Table 3.1: Overview of solvents used and their boiling points (BP), molecular structures and viscosities (where data is available).

After heating, the reaction was left to cool naturally to room temperature and excess ethanol (~100 mL) was added to precipitate the product, which was collected by centrifugation for 10 minutes at 4000 r.p.m. The black precipitate was washed with ethanol and centrifuged at least three times before being air dried at 60 °C overnight. At this temperature no additional oxidation is expected to occur, as conversion from Fe₃O₄ to γ-Fe₂O₃

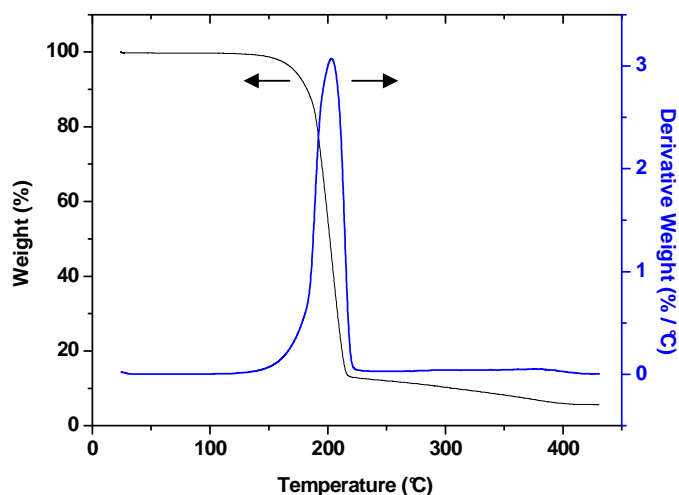


Figure 3.1: TGA decomposition plot and corresponding weight derivative curve for $\text{Fe}(\text{acac})_3$. The TGA data shows rapid decomposition of the complex, with the rate of weight loss peaking at ~ 200 °C.

requires temperatures above 250 °C.[21]

It should be noted that the reaction temperature is above the boiling point of two of the solvents chosen (DEA and MPT, see Table 3.1). For these reactions there is expected to be a contribution from the solvent to the internal pressure of the autoclave. The remaining, higher boiling point solvents are not expected to contribute to the autoclave pressure. In support of this, control reactions using DEA and MPT were performed in un-sealed autoclaves. These control reactions yielded identical products to the sealed autoclave reactions, providing strong evidence that for our system contributions to reaction pressure (where applicable) does not influence product morphology.

3.3 Results and Discussion

Representative TEM micrographs and electron diffraction (ED) patterns for NPs synthesised using each solvent shown in Table 3.1 are presented in Figs. 3.2 and 3.3 for protocols either omitting or including a heating hold-step, respectively. Particle size distributions (measured using at least 100 particles) for each experiment are given in Fig. 3.4.

ED patterns and lattice fringe spacings (Table 3.2) observed in individual nanoparticles are consistent with a cubic (inverse) spinel structure with measured lattice constants

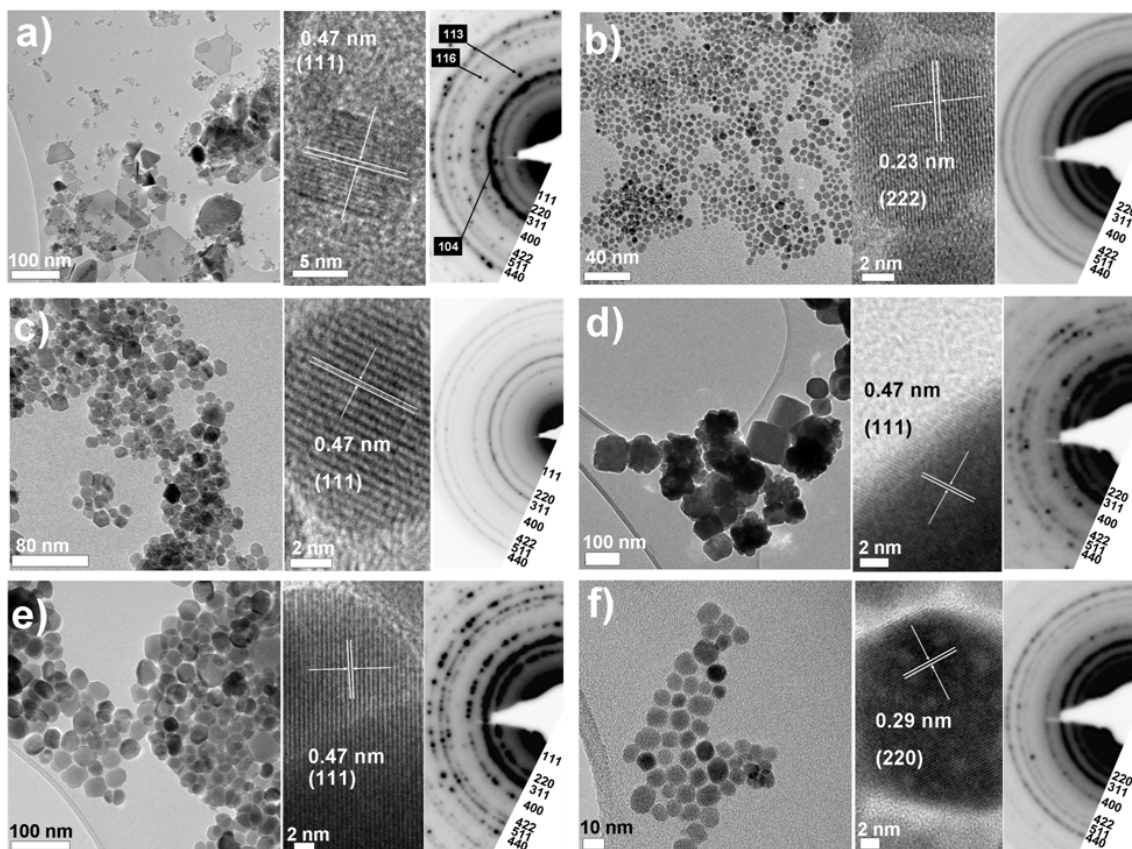


Figure 3.2: Overview of particles obtained using the autoclave based protocol with no heating hold-step. TEM images and electron diffraction patterns are shown for each of the solvents investigated: (a) BE, (b) DEG, (c) DEA, (d) M-DEA (e) E-DEA and (f) MPT (see Table 3.1). Electron diffraction patterns are indexed according to the magnetite structure with additional spots assigned to hematite in the case of BE.

of $8.379 \pm 0.055 \text{ \AA}$ across the data sets, in agreement with the structure of magnetite (JCPDS index card number 19-629). As the diffraction patterns of maghemite ($\gamma\text{-Fe}_2\text{O}_3$) and magnetite (Fe_3O_4) are very similar, O-K and Fe-L_{2,3} EELS edge profiles were used to assess the Fe oxidation state and confirmed the assignment of magnetite (discussed later in Section 3.3.4). Black powders were obtained in each instance, which also suggests that magnetite was formed, since nanoscale maghemite tends to be brown.[23] There was one exceptional case where hematite ($\alpha\text{-Fe}_2\text{O}_3$) is formed, as discussed in Section 3.3.1 below.

As all of the solvents (with the exception of BE) contain functional groups capable of

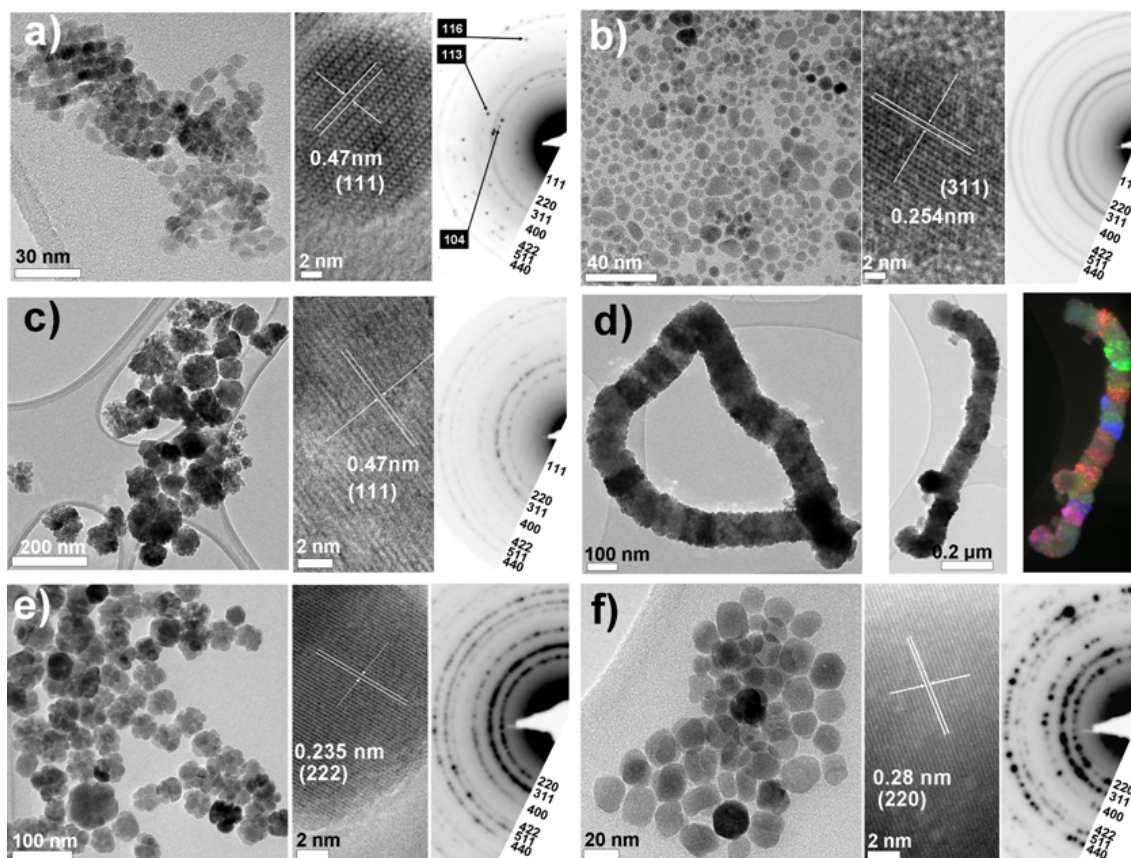


Figure 3.3: Overview of particles obtained using the autoclave based protocol when a 110 °C heating hold-step was used. TEM images and electron diffraction patterns are shown for each of the solvents investigated: (a) BE, (b) DEG, (c) DEA, (d) M-DEA (e) E-DEA and (f) MPT (see Table 3.1). Electron diffraction patterns are indexed according to the magnetite structure, with additional spots assigned to hematite in the case of BE. For particles obtained using M-DEA a bright field TEM image and the corresponding composite dark field TEM image is shown. Particles obtained when a 180 °C step was used are shown in (f), as no particles were obtained using a 110 °C step.

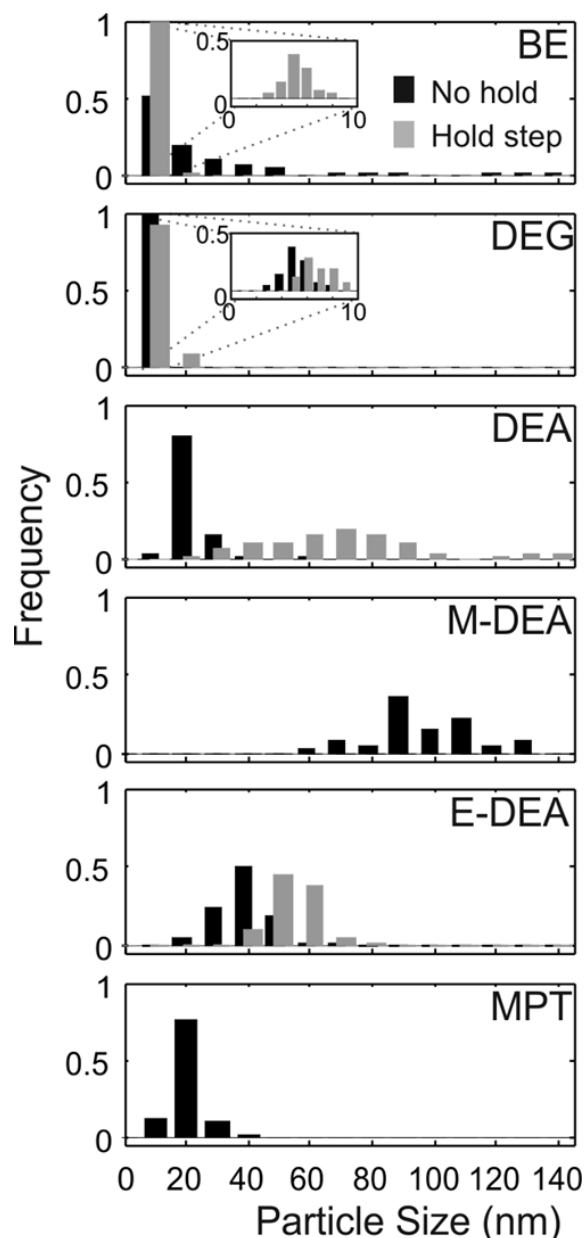


Figure 3.4: Particle size distributions for various reaction conditions. The black histograms show size distributions obtained when no heating step was used. The grey histograms show size distributions obtained when the 110 °C heating step was used. The same scale is used for each distribution.

binding to iron, the possible structures of the solvent-iron chelates formed during the reaction must also be considered. Examples in the literature have shown that coordinating solvent molecules can form iron-chelate complexes in-situ, which assist in the formation of iron oxide nanoparticles. For example, Zhang et al. showed that iron chloride decomposition in the presence of ethylenediamine formed α -FeOOH nanorods.[86] The

Reflection	d_{obs} (nm)	d_{hkl} (nm)
(111)	0.487	0.486
(220)	0.299	0.297
(311)	0.253	0.253
(400)	0.211	0.210
(422)	0.172	0.186
(511)	0.161	0.171
(440)	0.149	0.162

Table 3.2: Measured and expected d values for a typical nanoparticle electron diffraction pattern, showing agreement with Fe_3O_4 literature values.[23] Values were calculated by measuring diffraction ring diameters from a selected area diffraction pattern.

ethylenediamine was believed to form octahedral complexes with the iron, complexes which subsequently decomposed into Fe-OH-Fe assemblies. In a similar report, Zhu et al. showed that magnetite particles could be formed by the autoclave reaction of iron chloride with ethylene glycol and ethylenediamine, via the formation of iron-ethylenediamine complexes.[82] In this report, the chelation of iron and ethylenediamine removed free Fe^{3+} from the reaction mixture which slowed the rate of NP formation, resulting in the formation of a homogeneous product.

It is clear that the polyol solvents used in this Chapter (with the exception of BE) contain functional groups capable of chelation to iron and that the NP formation reactions performed using these solvents may proceed via the formation of an iron-solvent intermediate complex. The possible structures of these iron-solvent complexes are shown in Fig. 3.5.

From the TEM images it is apparent that particle size, shape and homogeneity vary considerably with the solvent used, and so the results for each solvent are addressed in turn.

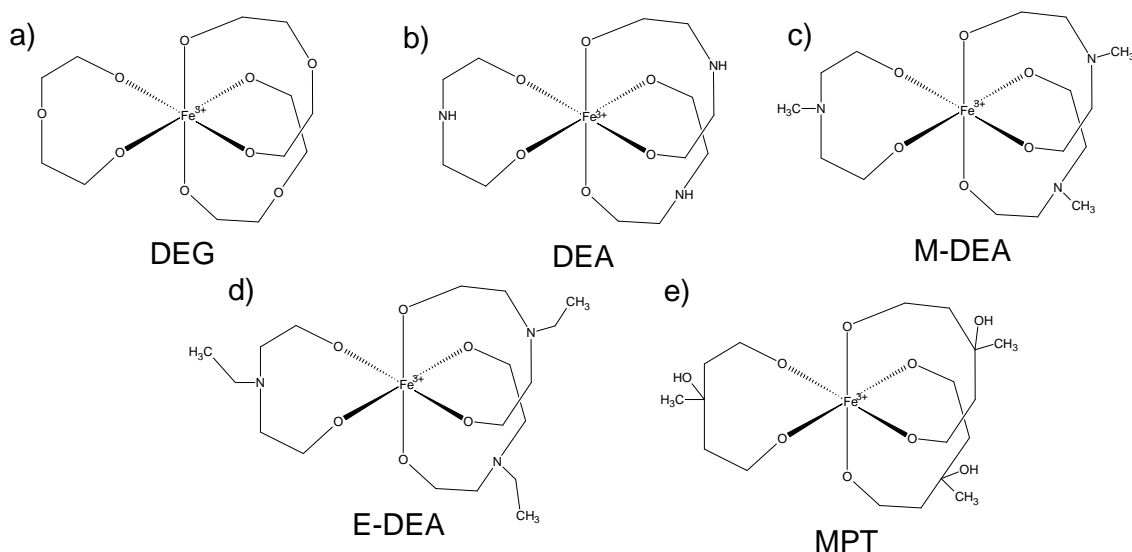


Figure 3.5: Structural formulae showing possible iron/polyol chelate structures for (a) DEG, (b) DEA, (c) M-DEA (d) E-DEA and (e) MPT.

3.3.1 Benzyl Ether

Benzyl ether (BE) was selected because, unlike the other solvents in Table 3.1, it does not contain hydroxyl groups to chelate to iron and therefore provides a useful benchmark as an inactive, spectator solvent. Binding to iron may be possible through the central ether oxygen, though this is sterically hindered by the two benzyl groups and should therefore be weak. The absence of hydroxyl groups also means that the only reducing agent present is 1,2-hexadecanediol (HDD). In an unstirred reaction vessel like the autoclave, uneven distribution of HDD may hinder the reduction of Fe^{3+} to Fe^{2+} that occurs during the formation of Fe_3O_4 , potentially leading to the formation of other iron oxide phases.

In terms of physical characteristics, the boiling point of BE is 298 °C, which is above the reaction temperature, so there will be negligible solvent contribution to the reaction pressure. The relatively low viscosity of BE (as determined by visual comparison with the other solvents in lieu of published data) could also be expected to aid the mobility of NP seeds and reactive intermediates, thereby favouring larger product NPs compared to other, more viscous solvents.

TEM images for the particles obtained using BE are given in Figs. 3.2(a) and 3.3(a). Additional TEM images are given in Fig. 3.6. When no heating hold-step is used, poly-disperse and inhomogeneous particles are formed (Fig 3.2a). The TEM images reveal at

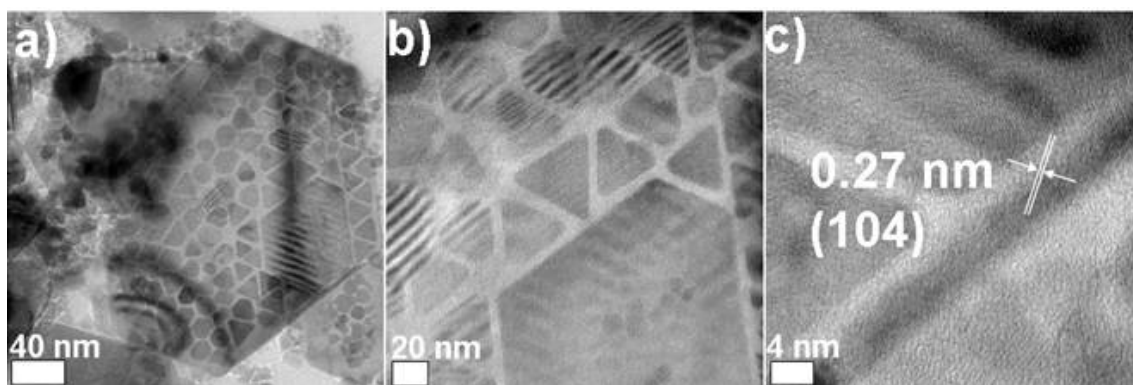


Figure 3.6: TEM images from nanoparticle formation using non chelating solvents with no heating step. (a-c) Images from benzyl ether, showing (a) a large hexagonal platelet, (b) alignment of smaller triangular particles underneath the platelet and (c) the fringe spacing at the particle edge, the distance 0.27 nm corresponding to γ - Fe_2O_3 (104) reflections.

least two NP populations: small, roughly spherical particles, 10.2 ± 5.0 nm (49 %) in diameter; and large hexagonal and triangular plates with edges up to 100 nm long. Analysis of electron diffraction patterns reveals the presence of a mixture of iron oxide species — magnetite (Fe_3O_4) and hematite (α - Fe_2O_3 , PDF card number 34-664). Formation of this mixture suggests that some NPs were able to grow without reduction by HDD and is indicative of an absence of strong driving forces to select a particular morphology. Analysis of the diffraction fringes within the smaller particles identifies them as magnetite (Fig. 3.2a) whilst the lattice fringes evident in the image of the platelets (with a spacing of 0.27 nm), Fig. 3.6(c), are consistent with the (104) reflection of hematite.

Additionally, X-ray diffraction (XRD) of a powdered sample of particles obtained using BE also shows strong reflections consistent with hematite, see Fig. 3.7. Differentiation of the magnetite and hematite reflections from a mixed sample such as this is difficult, given the overlap of reflections between the two phases. Fortunately, the hematite (104) reflection does not coincide with any magnetite reflections and its presence confirms the presence of hematite. Whilst HRTEM studies of lattice fringes confirm the smaller particles in the sample to be magnetite, the XRD pattern also hints at the presence of small magnetite particles. Scherrer's equation shows that XRD peak broadening occurs as the crystalline domain size decreases. A typical benzyl ether sample will consist of

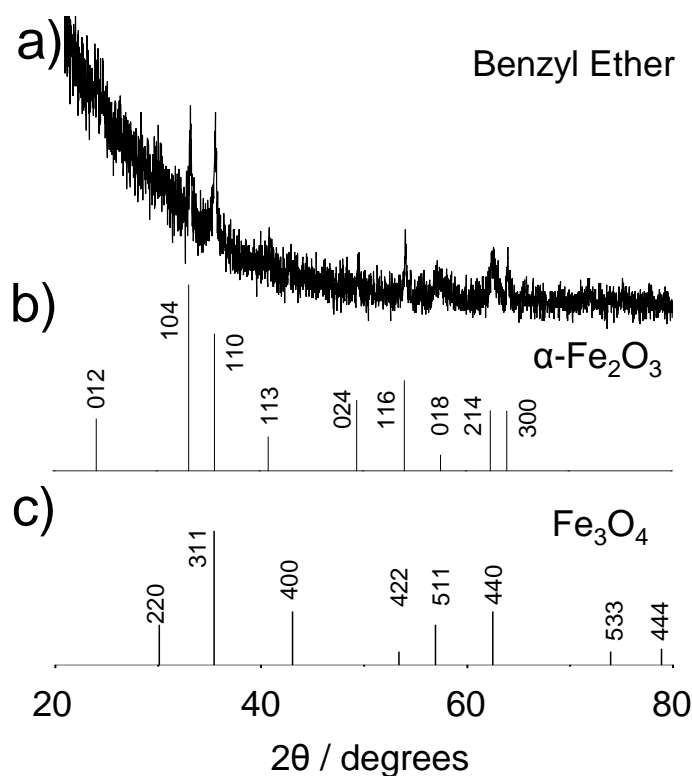


Figure 3.7: (a) XRD pattern of the particles obtained using benzyl ether as a solvent. Reference patterns for a) $\alpha\text{-Fe}_2\text{O}_3$ and b) Fe_3O_4 are provided for comparison. The ‘sloping’ intensity visible at low angles is believed to be scattering from amorphous carbon present in the glass capillary.

large hematite hexagonal plates and small magnetite samples, hence the XRD pattern should therefore consist of sharp hematite peaks and broader magnetite peaks. Analysis of Fig. 3.7 confirms that hematite peaks are sharp — like the (104) peak for example. Given the similarities between the two patterns, spotting broad magnetite peaks is difficult, however examination of the magnetite (311), (511) and (440) shows them to be broader than would be expected for sharp hematite peaks, inferring the presence of small, single-crystal particles of magnetite.

The formation of hexagonal platelets agrees with the crystal habit of hematite [87] and similar hexagonal platelets of iron oxide (albeit magnetite) have been observed in previous syntheses using non-chelating solvents, such as super critical CO_2 . [88] To test the assumption that platelet growth is encouraged by using BE as a non-coordinating, non-reducing solvent, additional reactions were performed with similar solvents. It was

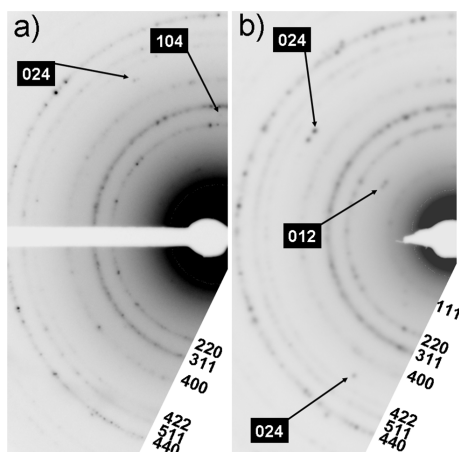


Figure 3.9: Electron diffraction patterns from the additional reactions using non-coordinating solvents a) diethyl ether and b) squalene. Similar to the particles obtained using BE, these solvents give a mixture of small magnetite particles and larger hematite platelets.

Reflection	d_{obs} (nm)	d_{hkl} (nm)
(012)	0.3676	0.3684
(104)	0.2717	0.2700
(024)	0.1830	0.1841

Table 3.3: Agreement between observed and expected d spacings for various hematite reflections from particles synthesised with non-coordinating solvents. Values were calculated by measuring diffraction spot distances from a selected area diffraction pattern.

action was repeated, this time including a 110 °C hold step. The inclusion of a heating hold-step resulted in small magnetite NPs of 5.35 ± 0.88 nm (17%) diameter: a relatively narrow particle size distribution and much more like the NPs produced when using BE within a reflux-based protocol.[21, 23] Also present were easily-separable, micron-sized agglomerated particles. Importantly, no platelets were observed, implying that their formation, or the formation of their precursors, is hindered at lower temperatures and is fuelled directly by $\text{Fe}(\text{acac})_3$ decomposition at elevated temperatures.

To further investigate the growth mechanisms of the platelets, time dependent reactions were performed, (Fig. 3.10). Time dependent reactions show platelet growth to be

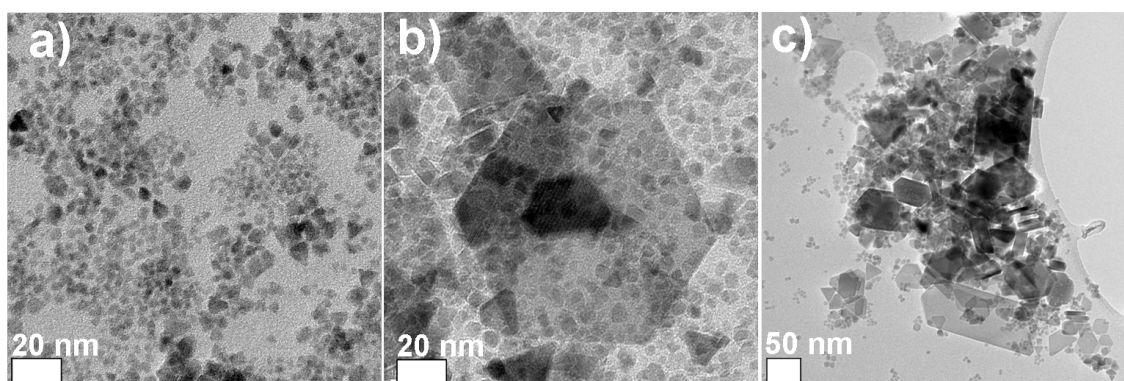


Figure 3.10: TEM images showing evolution of platelets for various reaction times (a) 30 minutes (b) 2 hours and (c) 6 hours.

initially relatively slow, as after 30 minutes only small ~ 5 nm particles are visible. However, after 2 hours large platelets are visible, and after 6 hours heating many platelets can be seen.

Using the TEM data for the hold-step and no hold-step reactions, in addition to the time dependent reactions, it is possible to propose a mechanism for particle formation using BE as a solvent. When no hold step is used, the reaction is heated rapidly to above the $\text{Fe}(\text{acac})_3$ decomposition temperature. The rapid decomposition of $\text{Fe}(\text{acac})_3$ releases Fe^{3+} and carboxylate decomposition products into the reaction mixture. The Fe^{3+} ions are stabilised through complexation with oleic acid, oleylamine and HDD. It is conceivable that inhomogeneities in HDD distribution will exist within the unstirred reaction mixture, leading to areas where Fe^{3+} is unreduced to Fe^{2+} . The high temperature means that particle nucleation occurs rapidly, soon after $\text{Fe}(\text{acac})_3$ decomposition. At this point, two species will nucleate, either a mixed $\text{Fe}^{3+}/\text{Fe}^{2+}$ containing oxide (which will grow into Fe_3O_4 particles) or a species containing Fe^{3+} only (which will give either $\gamma\text{-Fe}_2\text{O}_3$ or $\alpha\text{-Fe}_2\text{O}_3$ particles). The oxygen content of iron oxide particles is believed to arise from the fact that the reagents were pre-mixed in air prior to being heated in the oven.

On the other hand, holding the reaction for an extended period of time at a lower temperature (110°C for 4 hours) allows ligand exchange between surfactants and (acac) to occur. The viscosity of BE at 110°C will be low enough to allow diffusion of HDD through the mixture, allowing reduction of Fe^{3+} to Fe^{2+} to occur. This ensures the formation of a large number of exclusively magnetite seed particles, which explains the absence

of hematite platelets in the final reaction mixture under hold-step conditions. The formation of a large number of seeds during the hold step also explains the smaller magnetite particle size seen versus the non-hold step sample (~ 5 and ~ 10 nm respectively). Forming a large number of seeds means there is less iron present in the reaction mixture (as iron oleate/olyelamine/HDD complexes) for particle growth. The narrow size distribution of the small NPs highlights the crucial role of the hold-step in forming NP nuclei that grow uniformly.

3.3.2 Diethylene Glycol

Derivatives of ethylene glycol (EG) have long been considered versatile reagents to use in NP synthesis since the hydroxyl groups allow for both chelation to, and reduction of, reaction intermediates and growing NPs (Fig. 3.5).[78, 83, 89] In other words, EG is influential as it can mediate both stages of the LaMer mechanism. It was found in the present autoclave system that the ability of diethylene glycol (DEG) to influence the key stages of nanoparticle growth was crucial to obtaining high-quality particles with a narrow size distribution.

TEM images for the particles obtained using DEG are given in Figs. 3.2(b) and 3.3(b). The images show that small, spherical particles have been generated in each instance, with diameters of 4.9 ± 1.1 nm (22%) and 6.7 ± 2.0 nm (30 %) (without and with the heating hold-step, respectively).

Spherical NPs can be rationalised if DEG adsorbs isotropically on the growing magnetite, in direct comparison to the cases of BE (Section 3.3.1), where little adsorption is expected, and M-DEA (Section 3.3.4), where the product morphology indicates anisotropic adsorption. In the context of the LaMer mechanism, a well-defined burst of nucleation events is essential for product monodispersity and the inclusion of a hold-step should encourage the formation of NP seeds during the nucleation stage, thereby increasing the number but reducing the size of product NPs (as was the case when BE was used). Interestingly, the results show the reverse: slightly larger and more polydisperse NPs are formed; the relative particle size distribution, which would remain constant if the process is self-similar, increases from 22% to 30%. The increases of size and relative polydispersity that arise with the inclusion of a heating step suggest either an ill-defined nucle-

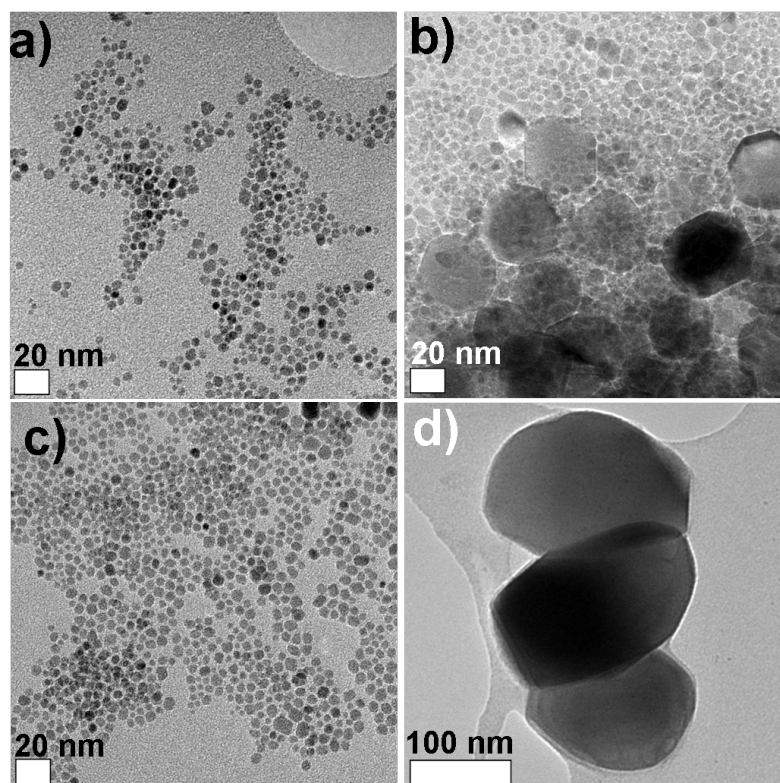


Figure 3.11: Additional TEM images from DEG reactions: (a,b) from the reaction without a heating step when the heating rate was slowed to 5 °C/minute. (c) Particles obtained using a 180 °C hold step, in comparison with (d) species obtained under reflux.

ation/growth threshold or a poorly chosen hold-step. To investigate this, two variables were altered: the heating rate and the hold-step temperature. Firstly, the heating rate was reduced from 20 °C/min to 5 °C/min to increase the time between NP nucleation and growth stages. This resulted in a broader size distribution, with particles up to 30 nm diameter evident (see Fig. 3.11 a,b). Secondly, the hold-step temperature was increased to 180 °C. The particles obtained at this elevated hold-step temperature remain similar to those observed for the 110 °C hold-step, with a size distribution of 4.8 ± 1.1 nm (23%) (Fig. 3.11c). The results from these two reaction conditions strengthen the theory that the nucleation/growth threshold for synthesis using DEG is poorly defined.

The small size of the NPs derived using DEG under the present standard reaction conditions implies that the iron-DEG chelate is labile, since a large number of NP nuclei are formed early on in the reaction. A large number of nucleation events will then limit the

amount of iron-DEG chelate available in the reaction mixture to contribute to NP growth, resulting in smaller particles.[83] The lack of stirring in an autoclave seems ideal for NP synthesis using DEG, since we find that using the same reagents under stirred reflux conditions produces large, poorly defined micron-sized particles (representative results are presented in Fig. 3.11d). In the autoclave case, interactions between Fe-DEG chelates and NP nuclei are minimised — meaning that NPs grow slowly and independently. In contrast, stirring during reflux increases collisions and interactions between species, as seen by the poor-quality particles obtained using reflux conditions. Under reflux, the labile DEG chelate does not protect NP seeds from coalescence and they readily combine to produce large, poorly-defined NPs.

3.3.3 Diethanolamine

DEA presents an interesting comparison with DEG since the two molecules are structurally similar and have the same number of hydroxyl groups, so can be expected to undergo similar chemical interactions with NP species. However, changing the ether linkage for a secondary amine enhances intermolecular hydrogen bonding and substantially increases solvent viscosity, by an order of magnitude, whilst reducing from 245 °C to 217 °C the boiling point (Table 3.1). TEM images show that this slight structural change in the solvent results in a marked difference when comparing particles obtained using DEG and DEA.

TEM images for the NPs obtained using DEA as a solvent are given in Figs. 3.2(c) and 3.3(c). It was found that the large change in viscosity between DEG and DEA does not affect NP shape, at least when no hold-step was used, in agreement with the similar chelation properties expected from these two solvents. However, particle size has increased considerably, with the DEA reaction yielding mostly spherical particles with rounded octahedral particles also present. The particles are 16.6 ± 6.4 nm (39 %) diameter, over 10 nm larger than those obtained using DEG. The emergence of a mixture of spherical and rounded octahedral particles suggests that DEA perturbs the adsorption dynamics of oleic acid, oleylamine and HDD at the particle surface, since previous reflux-based studies have shown that the production of cuboidal over spherical NPs can be manipulated through the ratio of adsorbed oleic acid and oleylamine.[49] The increase in particle size between use

of DEG and DEA suggests that the amine group does not contribute substantially to the initial reduction of precursor, since this would manifest as a larger number of smaller NPs. Conversely, the increase in particle size is consistent with the increase in solvent viscosity, since greater viscosity limits species mobility and hence favours slow nucleation of NP nuclei, which rely on iron-DEA chelate–chelate collisions to grow. Slow seed nucleation means that fewer nuclei form, leaving more iron-DEA chelates in solution for subsequent particle growth.

A more interesting comparison is between Figs. 3.2(c) and 3.3(c). The inclusion of a heating hold-step drastically broadens the size distribution and results in the formation of ‘compound’ NPs, where compound particles are defined as particles that do not exist as discrete single crystals but rather as fused agglomerations comprising several crystalline sub-units. The average agglomerate size was 75.0 ± 26.5 nm (35 %) with sub-units of varying shape and with diameters typically ranging between 10 and 20 nm, which is similar to the size of individual particles obtained when no heating step was used. This dramatic difference in NP morphology is rationalised as follows. The inclusion of a hold-step exhausts iron-DEA chelate supplies in the formation of a larger number of nuclei, which subsequently coalesce during the elevated temperature phase. Gao et al. recently reported that lowering the reaction temperature in solvothermal Fe_3O_4 particle synthesis limits the diffusion of active species and therefore induces disproportionation and aggregation.[78] In our system, the final temperature has not changed but the use of a heating hold-step extends the time that the reaction is held at a lower temperature, again decreasing the reaction rate and slowing diffusion, thus broadening the size distribution. The observed agglomeration may occur because competitive adsorption of DEA, oleylamine, oleic acid and HDD destabilises the protective coordinating shell on the NP surface, so that collisions lead to fusion of individual NPs (similar trends are seen for both methyl-DEA and ethyl-DEA, discussed below). This is plausible since the formation of compound NPs is known to be favoured when surfactant concentration is low,[90] and particles in solution can fuse together to minimise their surface energies.[91] The formation mechanisms behind each of the two products obtained using DEA (with and without heating steps) are summarised in Fig. 3.12.

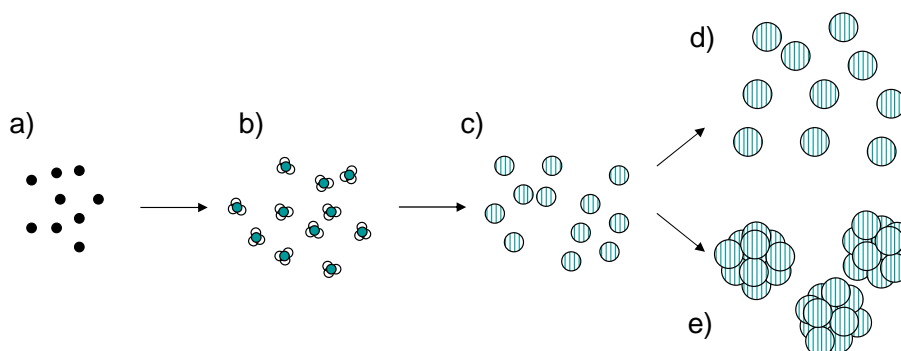


Figure 3.12: The different mechanisms that give rise to either discrete single crystal nanoparticles or compound agglomerated particles using DEA and its derivatives. (a) Initial reaction mixture, black dots represent $\text{Fe}(\text{acac})_3$. (b) ligand exchange between $\text{Fe}(\text{acac})_3$ and DEA to give an intermediate iron-DEA chelate (the possible structure of which is given in Fig. 3.5). (c) Nucleation of Fe_3O_4 nanoparticles (seed particles here not shown to scale). When no hold step is used, reaction mixture is less viscous and diffusion of surfactants to stabilise the particle surface readily occurs, giving discrete particles (d). At the lower, hold-step temperature, diffusion of reactive species and inadequate nanoparticle stabilisation occurs. Particles agglomerate together (e) to reduce their surface energies, to give a stable product.

3.3.4 Methyldiethanolamine

M-DEA differs from DEA by the inclusion of a methyl group on the central N atom, which reduces the solvent viscosity by limiting the amount of hydrogen bonding. Although the presence of two hydroxyl units suggests the chemical activity to be similar to that of DEA and DEG, it is worth noting that the bulkier M-DEA molecules may not pack as densely in an adsorbed layer, thereby affecting lability of the solvent and, indeed, of the other surfactants present in the reaction mixture. Perturbations in surfactant concentrations near a particle surface would be expected to hinder particle growth kinetics and stabilisation, and it was found that in the M-DEA case interesting particle morphologies are readily obtained.

TEM images for the particles obtained using M-DEA as a solvent are given in Figs. 3.2(d) and 3.3(d). Changing the solvent from DEA to M-DEA causes a dramatic change in particle morphology. Comparison between Fig. 3.2 (c) and (d) reveals that the

particles formed using M-DEA are larger (98.4 ± 19.6 nm (20%)) and are a mixture of single crystalline and ‘compound’ particles, with a preference for cuboid morphology. Compound particles dominate, although the proportion of large single crystal cubes increased when the heating rate was increased, and no single crystal cubes were obtained when the rate is reduced to 5 °C / min. Analysis of the fringes observed by TEM, ED data and EELS data (discussed below) confirms that all the particles in Fig. 3.2(d) are magnetite. The sub-units that combine to form the assembled, compound cubes were themselves typically pseudo-cubic particles ~ 20 nm in side-length, similar to the sub-units seen when DEA was used with a hold-step.

The more cuboid character of these NP subunits is interesting as previous studies have shown that cuboid NPs can be produced when the ratio of oleyl amine to oleic acid is perturbed towards increased acid, as over expression of the $\{100\}$ crystal faces occurs.[48] Our results therefore suggest that M-DEA adsorption perturbs the balance of oleylamine and oleic acid adsorption. The comparison with DEA is then of particular interest since it implies that the methyl side chain of M-DEA has a profound effect on the competitive adsorption of other species onto growing NPs and that such functionalisation of the solvent provides a new route to NP optimisation.

We also find there to be a preferred orientation of sub-units within each compound cube assembly. There was consistency in the number of sub-units — approximately 5 — comprising the edge of each compound cube. This suggests that oriented attachment of cuboid sub-units proceeds until enough surfactant is present to stabilise the exposed NP surfaces, that is until a sufficiently large particle is formed that the surface-to-volume ratio becomes low enough to be favourable. Preferred orientation was also revealed through selected area ED (SAED) measurements. SAED of a single compound particle revealed a distinct spot pattern (Fig. 3.13a,b) which indicates a preferred crystalline orientation — since randomly-oriented sub-units would yield a ring pattern. This ‘oriented assembly’ can be rationalised in terms of the fusion of subunits to reduce surface energy, in which subunit recrystallisation will be easier if adjacent crystals share a common crystal facet.[91, 92] The formation of compound particles of defined shape and uniform intraparticle crystallinity is interesting, since it implies anisotropic self-assembly is occurring. Anisotropic self-assembly was found to be specific to M-DEA, and similar self-assembly

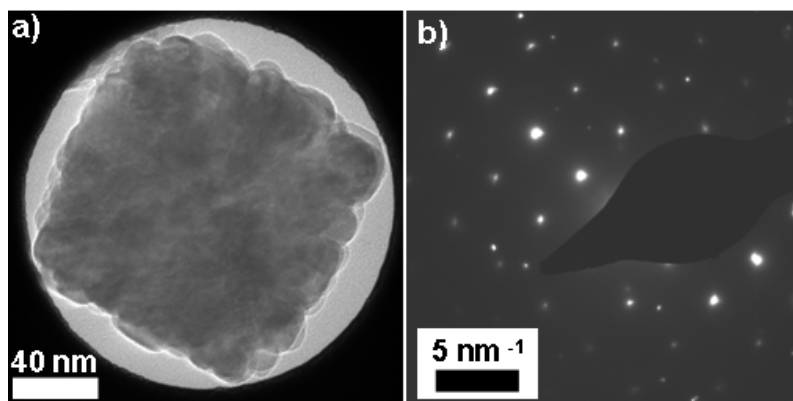


Figure 3.13: (a) Bright field TEM image of a single compound cube particle and (b) corresponding selected area electron diffraction pattern, showing distinct spot pattern.

was not observed for any of the other solvents tested.

To investigate the chemical composition of the compound particles, scanning TEM electron energy loss spectroscopy (STEM EELS) experiments were performed, as EELS is a very sensitive technique and is often used to differentiate areas of varying oxidation state within metal oxide samples.[93–95] To perform the EELS analysis, measurements were taken at various points across a typical particle, by scanning the electron beam across the NP. The scan area comprised a line of 22 pixels with a 5 nm separation, giving a total scan length of 110 nm, chosen to encompass an entire particle. EELS spectra were collected at each pixel with a dwell time of 10 seconds. Automatic drift correction was performed automatically by the Digital Micrograph software after every 3rd pixel.

The data from this line scan are given in Fig 3.14, showing the chosen particle and area of scan, elemental composition plots for iron and oxygen and an average EELS spectrum from the particle. The elemental composition of a typical particle was calculated by taking the average elemental compositions (as determined by the intensities of O and Fe edge features of an EELS scan) across a number of points within a particle. A typical spectrum, yielding an elemental composition of Fe:O = 41.9 : 58.1, is shown in Fig. 3.14(c). The composition is close to that of magnetite (Fe_3O_4 , Fe:O = 42.9:57.1) but suggests the presence of a thin shell of maghemite (Fe_2O_3 , Fe:O = 40:60). As we will see in later chapters, mild oxidation of metal oxide particles can occur as a consequence of the repeated washing cycles required to ensure the samples are clean enough for STEM experiments.

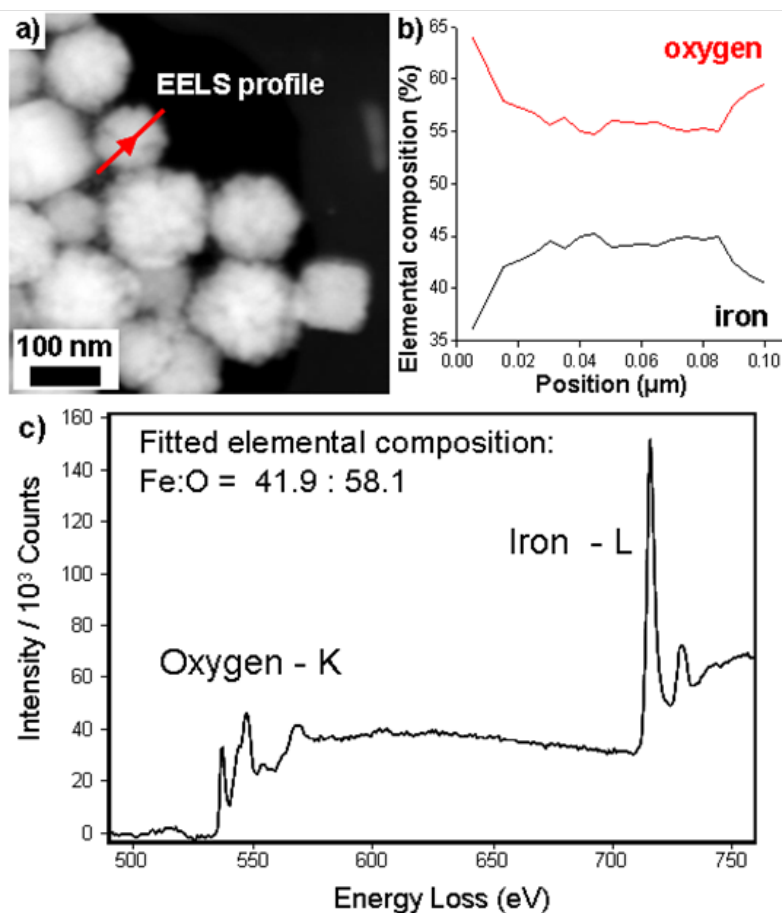


Figure 3.14: (a) Dark field STEM image showing line trace used for collection of EELS data. (b) Variation in elemental composition of particle indicated in (a) for different points across the particle. (c) Averaged EELS spectra from several points across the particle.

Repeated washings remove surfactants from the particle surface, allowing oxidation upon exposure of the sample to air. Furthermore, a thin shell of maghemite would be insufficient to yield distinguishable diffraction features in Fig. 3.13(b). The sensitivity of iron and iron oxide particles to mild surface oxidation is well documented, and is usually only avoidable by performing experiments and handling products in a sealed glovebox.[96]

For the M-DEA protocol the inclusion of a 110 °C heating hold-step yields compound particles of similar size to those described above, but also induces a remarkable, second level of self-assembly. The compound cubes form into chains, as shown in Fig. 3.3(d). The fact that the cubes obtained are consistently the same size, regardless of the reaction conditions, implies that the iron precursor is completely converted to NP nuclei during the

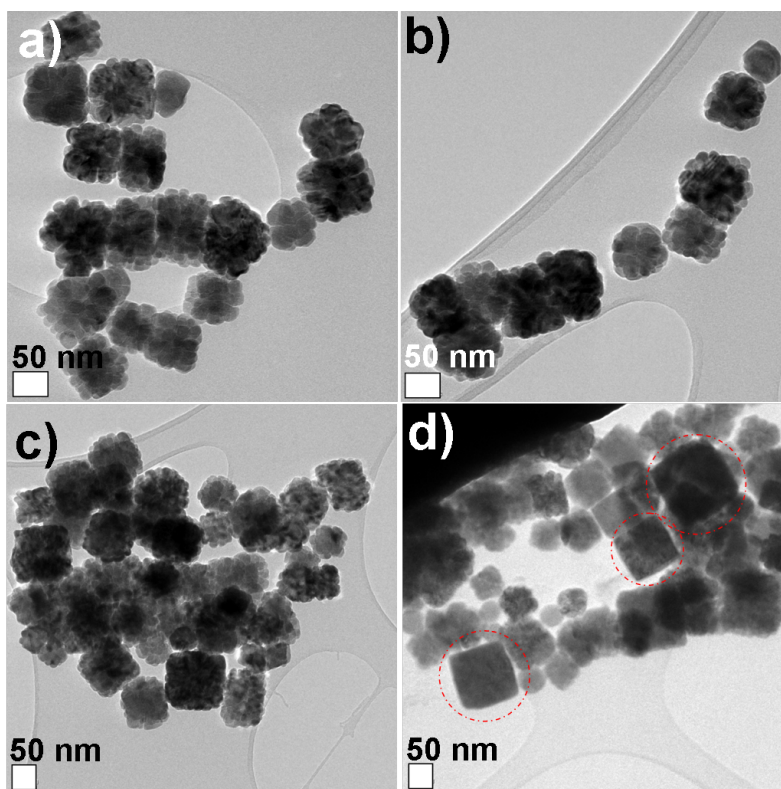


Figure 3.15: (a-d) Additional TEM images from M-DEA reactions, showing the compound cubes obtained when the heating step was set to 180 °C. Although the majority of particles existed as compound cubes, some single crystalline cubes could also be seen (d). These were present as a minority species, comprising ~ 5 % of the total cube population.

early, low-temperature, stages of the reaction. If a higher temperature hold-step (180 °C) was used, a mixture of single crystalline and compound cubes were obtained, though self assembly was minimal (see Fig. 3.15). Thus, chain formation is favoured by a slow reaction rate at a low temperature.

As mentioned above, SAED of the compound cube NPs obtained in Fig. 3.2(d) revealed that there is alignment of individual sub-units within a compound cube. To determine the nature of attachment of these compound cubes within a larger self-assembled chain, dark-field (DF) TEM imaging was used, as illustrated in Figs. 3.3(d) and 3.16.

The DF TEM image has been false-coloured to highlight variations in crystallographic orientation within the chain, with each colour representing an image collected under unique diffraction conditions and therefore indicating different crystal orientation. That

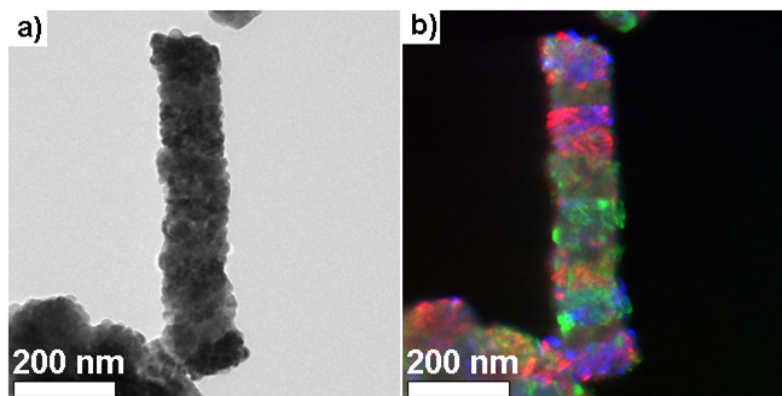


Figure 3.16: Additional a) bright-field and b) dark-field TEM images from M-DEA reactions, showing assembly of cubes into linear hierarchical assemblies.

the colour varies in sections along the chain implies that these hierarchical assemblies form by face-to-face alignment of individual pre-formed compound cubes, as opposed to continuous chain growth along a specific crystal axis at an end of one cube.

Similar ‘hierarchical assembly’ of NPs has been observed previously, including formation of supercrystals [97] and helical chains.[38] Literature examples [98, 99] of chain growth suggest the alignment of magnetic dipoles are a viable anisotropic driving force towards chain formation. This is because dipole interactions could encourage end-to-end addition of sub-units and still allow the rotational disorder evidenced by the colour variation along the chain in Fig. 3.3(d). Face-to-face contact of cuboids provides a greater van der Waals force to direct assembly than that between two spherical NPs and so facilitates self assembly, perhaps explaining why no hierarchical structures are observed between the particles obtained using DEA. Additionally, the rotation of particles into low-energy configurations that lead to hierarchical assemblies will be easier in less-viscous solvents, and as such is more likely to occur in M-DEA than in DEA.

3.3.5 Ethyldiethanolamine

The TEM images for those particles obtained using E-DEA as a solvent are given in Figs. 3.2(e) and 3.3(e). E-DEA has a similar boiling point and viscosity to M-DEA, and differs structurally only by the length of the alkyl chain, meaning E-DEA is a useful indicator of the effect of steric hindrance contributions from solvent on particle morphology.

When no hold-step was present, rounded particles of size 34.2 ± 8.5 nm (25%) were

formed. These particles are different to those obtained from M-DEA and in fact are more similar to those obtained using DEA. Thus, there is no simple trend between N-substituent chain length and final NP morphology. The lower viscosity of E-DEA compared to M-DEA means that iron/E-DEA chelates and the subsequent NP nuclei are slightly more mobile. The number of hydroxyl groups is the same for all the DEA derivatives, so the reductive power of each solvent (and hence its ability to form Fe_3O_4) should be similar. The longer alkyl substituent will sterically hinder chelate packing between E-DEA and iron seed particles, worsening the ability of E-DEA to stabilise NP nuclei — which could explain why larger and more polydisperse particles are obtained using E-DEA than DEA.

The inclusion of a 110 °C heating hold-step resulted in the formation of popcorn-like compound particles of size 49.2 ± 7.0 nm (14 %), shown in Fig. 3.3(e). These particles bear resemblance to other oxide ‘nano-flower’ species reported previously, in which radial growth of material occurs from a central nanoparticle core. For example, Choi et al. showed that iron oxide could be grown epitaxially on a metal (Pt or Ni) core.[100] A recent report by Song et al. described the synthesis of star-shaped hematite particles, in which growth of the particle arms was ascribed to oriented attachment.[101] In our system, TEM and lattice spacing analysis reveal each sub-unit of the compound particles is a single crystalline ~ 20 nm magnetite particle. Dark field TEM studies reveal that sub-units of an individual particle have coherent crystallinity, in a similar fashion to the compound cubes obtained when M-DEA was used. Formation of these popcorn-like agglomerates can be rationalised in terms of the fusion of subunits to reduce surface energy, in which subunit recrystallisation will be easier if adjacent crystals share a common facet.[91, 92] The observed shape of the compound particles (popcorn-shaped as opposed to the cubic morphology seen using M-DEA) may be due to the extra steric hindrance of E-DEA perturbing the adsorption of surfactants to an extent where isotropic agglomeration of sub-units occurs, giving the more spherical appearance of the final compound particle.

If the temperature of the heating hold-step was raised to 180 °C, no compound particles and only spherical particles were obtained, implying that popcorn-like particles only seed at low temperatures. At lower temperatures viscosity will be increased and diffusion of surfactants to exposed particle surfaces will be reduced. Furthermore, if E-DEA is unable to fully stabilise NP nuclei due to more labile chelation as a result of increased steric

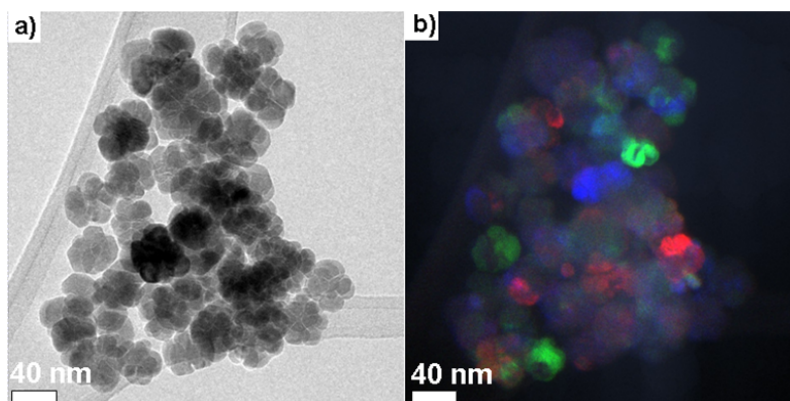


Figure 3.17: Additional a) bright-field and b) dark-field TEM images from E-DEA reactions, showing a group of ‘popcorn’ particles. The dark-field image shows that particles and their sub-units have the same crystalline orientation.

hindrance from the N-ethyl group then agglomeration will occur. The radial nature of the sub-units suggests that agglomeration followed by further growth of these sub-units, i.e.: epitaxial overgrowth is responsible for the popcorn-like morphology.

3.3.6 3-methyl-1,3,5-pentane-triol

MPT was included in this study to ascertain the effects of a triol chelating agent. Based on the number of hydroxyl groups a triol would be expected to possess a greater reducing ability than a diol, which may promote formation of Fe_3O_4 seeds and in turn facilitate the growth of well-defined Fe_3O_4 NPs. This assumption was based on the observation that long-chain monoalcohols worsen NP yield and quality compared with long-chain diols.[23] Hence, a triol could improve the quality of the NP product.

The TEM images obtained for MPT are given in Figs 3.2(f) and 3.3(f). When no heating step was present, mostly spherical Fe_3O_4 particles were obtained with sizes 12.0 ± 6.6 nm (54 %). The majority of particles were small, though some larger, poorly defined particles were also present. No NPs were obtained using a 110 °C hold-step, only micrometer sized agglomerates. It was only after increasing the hold temperature to 180 °C that spherical $14.7 \text{ nm} \pm 4.6$ (31 %) particles were obtained. This represents a slight increase in size but a marked narrowing of the size distribution compared to when no hold-step was used. The spherical NPs are similar to those seen when using DEG, DEA and E-DEA; slightly larger than for DEG but smaller than those obtained using

DEA derivatives. This implies that the NP nucleation is easier using MPT than it is using DEA derivatives and therefore suggests that the ether link of DEG contributes more to the reductive power of the solvent than the amino links of DEA derivatives.

3.3.7 Summary

An overview of particle morphologies and size distributions is provided in Table 3.4.

3.3.8 Mixed Solvent Reactions

The above sections demonstrate that the choice of solvent in autoclave-based nanoparticle synthesis reactions plays an important role in determining the final product morphology. It is clear that certain solvents offer clear synthetic advantages, such as the narrow size distribution of particles obtained using DEG or the interesting platelets obtained using BE. Additional test reactions were performed to see if mixed solvent systems were a viable route towards particles with ‘tunable’ morphologies, as it was previously shown by Caruntu et al. that tuning solvent ratios particle size could be controlled.[102] In Caruntu’s report magnetite particles prepared by the co-precipitation method, with the particle size controllable by the solvent used. Neat DEG yielded 6.6 nm particles, and M-DEA gave 17.8 nm particles. It was shown that using a 1:1 mixture of DEG and M-DEA yielded intermediate 11.6 nm particles. For the NPs synthesised in this Chapter, TEM images of particles obtained using 5 mL each of BE and DEG (with and without hold-step) are given in Figure 3.18. The TEM images show that small, pseudo-spherical particles have been formed for each reaction condition, with sizes 5.6 ± 0.8 nm (9%) and 7.1 ± 1.2 nm (17 %) respectively. Importantly, the particles bear a striking similarity with those obtained using only DEG — nearly mono-dispersed small particles were obtained and no platelets could be seen (regardless of whether a hold-step was used or not). This observation confirms that DEG plays far more influential role during NP nucleation and growth than BE, and highlights the importance of solvent functionality on nanoparticle growth in general.

Given the ability of the polyol solvents tested in this chapter to help stabilise nanoparticles, additional control reactions were performed to determine if solvent molecules alone were capable of stabilising nanoparticles without the addition of extra surfactants. There are already some reports of simple reactions involving only $\text{Fe}(\text{acac})_3$ and polyols, which

Solvent	No Hold Step		Hold Step	
	Morphology	Particle Size	Morphology	Particle Size
BE	spherical, hexagonal platelet	10.2 ± 5.0 nm (49 %)	spherical	5.35 ± 0.88 nm (17%)
DEG	spherical	4.9 ± 1.1 nm (22%)	spherical	6.7 ± 2.0 nm (30 %)
DEA	spherical, rounded octahedral	16.6 ± 6.4 nm (39 %)	compound	75.0 ± 26.5 nm (35 %)
M-DEA	compound cubic	98.4 ± 19.6 nm (20%)	linear assemblies	Multiple subunits
E-DEA	spherical	34.2 ± 8.5 nm (25%)	popcorn	49.2 ± 7.0 nm (14 %)
MPT	spherical	12.0 ± 6.6 nm (54 %)	spherical	14.7 nm ± 4.6 (31 %)

Table 3.4: Overview of product morphologies obtained for each solvent from different reaction conditions.

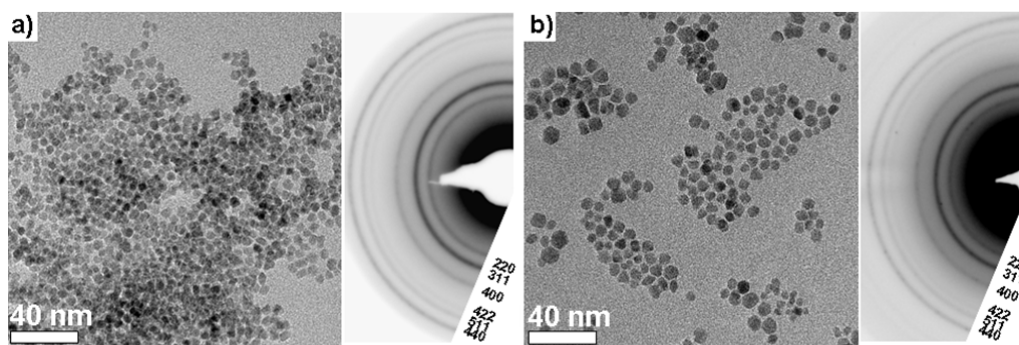


Figure 3.18: TEM images and corresponding ED patterns for particles obtained from a mixed BE/DEG system (a) with and (b) without a heating hold-step.

are shown to produce iron oxide particles. For example, solvothermal decomposition of $\text{Fe}(\text{acac})_3$ in benzyl alcohol yielded magnetite particles,[103] and Cai et al. reported the decomposition of $\text{Fe}(\text{acac})_3$ in DEG, which was shown to yield particles.[104] At the time of writing there were no published studies investigating the decomposition of $\text{Fe}(\text{acac})_3$ (or any iron precursor for that matter) using only DEA, M-DEA, E-DEA or MPT as both solvent and surfactant. Control reactions performed using these solvents failed to yield any nanoparticulate product, with TEM investigations showing either large, multi-micron sized agglomerates or no discernible precipitate at all. So it is apparent that only DEG is capable producing particles without additional surfactants,[104] presumably due to its low viscosity, reductive power and minimal steric hindrance. This observation is further supported by IR, in which particles prepared using DEG appear to have DEG on their surface, in addition to oleic acid and oleylamine, see Fig 3.19.

Compared to DEG, particles obtained using the other solvents do not appear to have any broad features in the $\sim 3200 \text{ cm}^{-1}$ region, where OH stretches would be expected to appear. This suggests that whilst reaction solvent contributes to the growth process of a particle, the final product is ultimately stabilised by the long-chain surfactants added (as shown by IR). Furthermore, the fact that the as-prepared powders are dispersible in hexane implies that they are coated in non-polar hydrocarbons, as opposed to exposed hydroxyl groups.

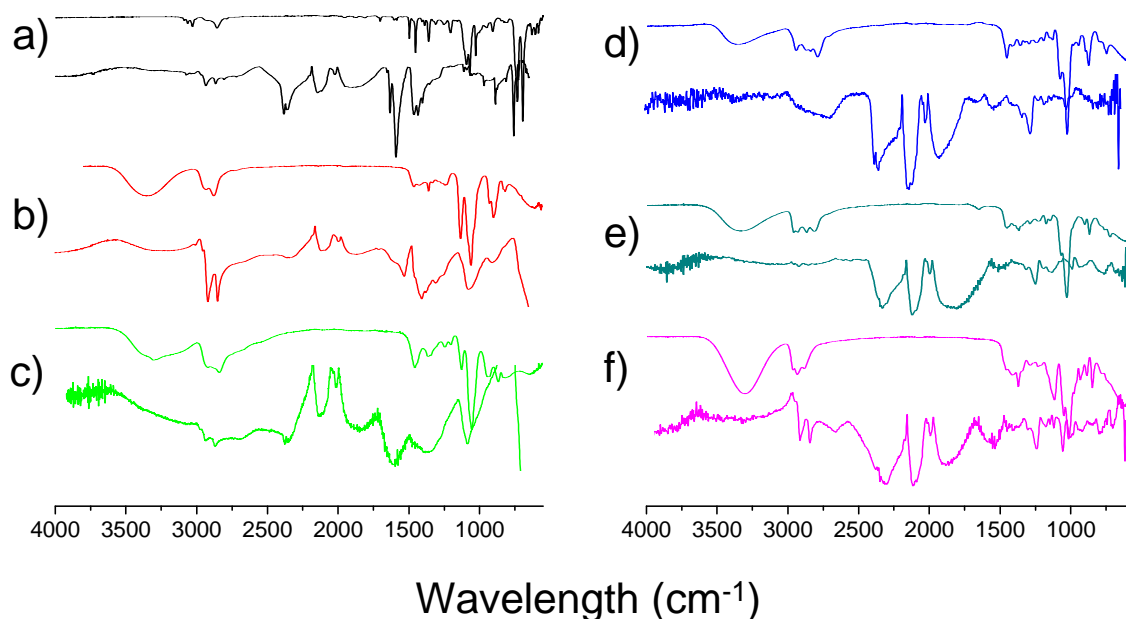


Figure 3.19: IR spectra of solvents used in particle synthesis (upper line) compared with the resultant particles (lower line) for (a) BE, (b) DEG, (c) DEA, (d) M-DEA (e) E-DEA and (f) MPT.

3.4 Magnetic Measurements

3.4.1 Introduction

Significant progress has been made in the study and understanding of the magnetic properties of iron oxide particles. The majority of syntheses for magnetite create well defined, single crystalline particles. Provided the particle size is below the single domain limit, the sample will be expected to be superparamagnetic, with negligible or zero coercivity. For the polyol samples described in this chapter, hysteresis curves were recorded from the as-obtained powders at room temperature, for samples prepared where no heating step was present (Fig. 3.20).

The hysteresis curves show each sample tested to be superparamagnetic, with negligible coercivity and saturation magnetisation (M_{sat}) values slightly below the bulk value of 96.4 emu/g.[105] This slight decrease in saturation magnetisation is due to a finite size effect present in small magnetic domains. As nanoparticles have a much higher surface atom to volume ratio compared to bulk materials, they have a higher proportion of surface spins. The decrease in M_{sat} values is due to the canting of surface spins, which

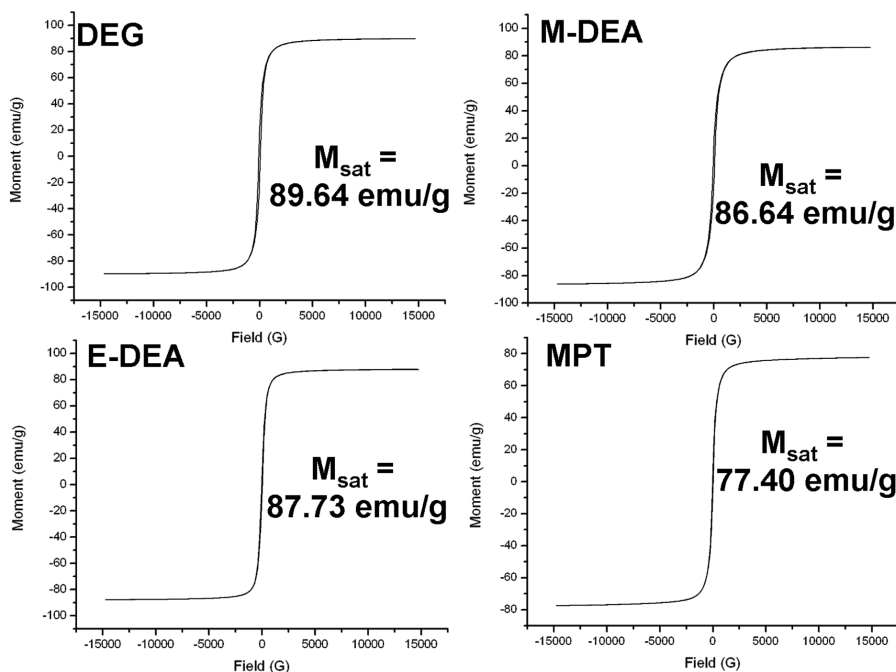


Figure 3.20: Hysteresis loops collected from nanoparticles synthesised using different solvents and without a heating holdstep.

renders them unaligned with the remaining spins present in the rest of the domain.[106] This layer of canted surface spins is often said to be magnetically inert, and does not contribute to the magnetic properties of the particle. For a nano-sized magnetic domain the proportion of canted spins per discrete magnetic domain is large enough to cause a noticeable decrease in the observed magnetisation, with the effect more pronounced for smaller particles.[48, 107] We will see in Chapter 5 the pronounced effect that surface spin canting has on the magnetism of small particles, when the size dependent magnetism of 7, 11 and 17 nm MnO particles will be discussed.

An alternative explanation for decreases in saturation magnetism was described by Wang et al., who proposed that decreases in saturation magnetisation could be attributed to uneven cation distribution in a poorly crystalline sample.[83] Consider the unit cell of magnetite (Fe_3O_4), which can be written as



showing that the tetrahedral sites (Td) are occupied by Fe^{3+} , and the octahedral sites (Oh) are filled with an alternating mixture of Fe^{3+} and Fe^{2+} (Fig 3.21).[108]

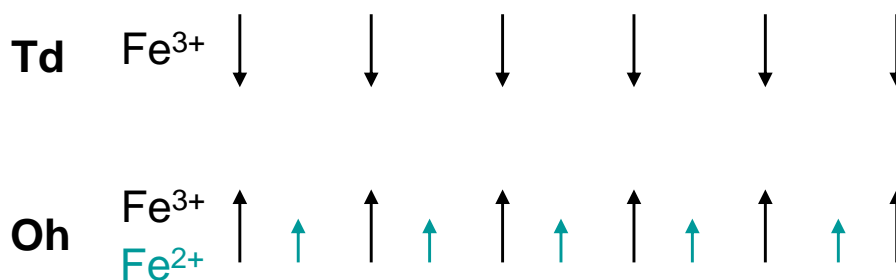


Figure 3.21: Schematic showing alignment of spins in the tetrahedral (Td) and octahedral (Oh) sites in the magnetite lattice.

The magnetic moments of Fe³⁺ ion pairs in octahedral and tetrahedral sites are coupled anti-ferromagnetically, and as such their spins cancel. The observed magnetic properties are due to the remaining parallel Fe²⁺ (S=2) spins, giving a saturation magnetization of $4\mu_B$ per formula unit.[109] In a poorly crystalline sample, defects will exist within the Fe₃O₄ lattice which will disrupt the ordering of spins, reducing the overall magnetic moment. However, experimental evidence shows our particles to be highly crystalline, evident by lattice fringes visible in TEM and the strong diffraction patterns obtained by both electron and x-ray diffraction. For this reason, the decreased M_{sat} values are more likely a consequence of surface spin canting.

3.5 Conclusions

In this chapter a systematic study of the often-overlooked role of solvent in the autoclave-based decomposition of Fe(acac)₃ to synthesise iron oxide nanoparticles is provided. The results demonstrate that the solvent is active and as influential as all other reagents in determining NP product characteristics. It should therefore not be overlooked in experimental design: its functionality can determine the decomposition rate of precursors; its viscosity determines the diffusion rate of reaction intermediates; its structure can profoundly alter product morphology and assembly. The sequential variations in solvent structure studied in this chapter allow some general observations to be drawn.

Firstly, choosing a solvent with functionality — particularly primary alcohols in the case of magnetite NP synthesis — will lead to far greater control over the NP product and is far more important than the physical characteristics of the solvent. For example, al-

though solvent viscosity will influence the number of interactions and collisions between reactive species, the concentration of those reactive species depends strongly on the solvent's ability to reduce the precursor in the first place. Thus, unstirred BE was shown to produce large, heterogeneous NPs because the increased collision rate arising from a relatively low viscosity is unimportant if formation of reaction intermediates has been limited by slow decomposition of the precursor.

A second observation considers the molecular packing of adsorbates on growing NPs. This observation has previously been made in the context of competition just between oleyl amine and oleic acid,[49] where NP shape selectivity is driven by the adsorption dynamics of oleic acid on specific crystallographic surfaces. Throughout this chapter, the ratio of these surfactants is unchanged yet the product morphology, including the production of cuboidal NPs, can still be manipulated via the solvent. A useful conceptual image (and one which would merit a further detailed theoretical study) is that of monodentate adsorption and parallel alignment of the hydrocarbon chains of surfactant and solvent molecules about growing NPs, forming a densely packed solvation sphere. This image helps to explain why there is no simple trend with an increase in the the number of hydroxyl units of a solvent: although additional hydroxyl units may increase the rate of formation of seeds during the first stages of reaction, only the terminal group is in physical contact with the growing NP during NP growth phase. Similarly, changes to secondary functionality — for example, changing from DEG to DEA — have little effect during the growth phase and the differences observed in NP morphology seem more consistent with changes in solvent viscosity. Moreover, the addition of bulky side-chains on the solvent backbone will disrupt the densely packed adsorption layer, with two results. Disrupted packing will render the growing NP more susceptible to attack and coalescence and therefore facilitate the formation of compound structures (as seen using M-DEA and E-DEA). Steric effects will also alter the competitive adsorption kinetics of surfactants, as seen in production of cuboidal particles using M-DEA. Prediction of specific changes to NP morphology for a particular side chain is difficult, because morphology arises from a delicate balance of several factors, but it has been demonstrated that it merits further study as a new means of control of NP morphology and self-assembly.

In conclusion, a simple, reliable protocol for the production of monodisperse spheres,

hexagonal platelets and compound cubes has been demonstrated. Within this chapter the versatility of autoclave-based protocols was demonstrated, particularly with the inclusion of hold-temperatures, and it is anticipated that the more general conclusions above will have relevance to other protocols. Careful tuning of the reaction heating conditions and solvent functionality permits the formation of self-assembled, hierarchical structures, all tuned through subtle variations in solvent chemistry.

In the next chapter, we will again use the autoclave protocol to synthesise nanomaterials, although this time a different class of nanomaterials will be made. We will see once again that product morphology is sensitive to the reaction conditions, as we investigate the synthesise of lanthanide oxide nanowires and ribbons.

Chapter 4

Synthesis of Lanthanide Oxide

Nanowires and Ribbons

4.1 Introduction

The previous chapter introduced a simple autoclave-based method to synthesise Fe_3O_4 NPs. The unique reaction conditions afforded by the autoclave reaction vessel were seen to give rise to unusual particle morphologies, such as compound cube particles. In this chapter we will see that the range of materials that can be synthesised using the autoclave can be extended to include an interesting class of material — lanthanide oxide (LnO_x) nanowires and ribbons. We will see that by changing the synthetic protocol used in chapter 3 to include a greater number of long-chain surfactants, liquid-crystalline phases can be invoked and the growth mechanisms of particles can be altered, leading to the formation of novel nanowire and ribbon species. The procedures for synthesising CeO_2 and Ln_2O_3 nanowires and ribbons and the discussion into their formation mechanisms are given below in sections 4.2–4.3.3, though we will begin with an overview of lanthanide-containing materials and their potential applications.

The lanthanide (or rare-earth) elements have long been of interest to scientists, because of the unique physical properties that arise with the filling of the 4f electron shell. Exploitation of the optical and magnetic phenomenon that arise as a consequence of f-electron chemistry is key to many technological applications of lanthanide-containing materials, such as MRI contrast agents which utilise the high magnetic moment of Gd^{3+} -

chelates,[110] or electronic displays which use Eu^{3+} as the red emitter.[111] Within the last decade, lanthanide research has expanded to include the study of lanthanide-containing nanomaterials. Exploiting the magnetic and optical properties of the rare-earth elements has underpinned much research, with a focus on potential applications. For example, the large numbers of unpaired electrons present on the Gd^{3+} and Dy^{3+} ions gives them large magnetic moments (7.94 and 10.65 μB respectively).[56] This large magnetisation combined with small particle size means that nanoparticles of Gd_2O_3 and Dy_2O_3 are ideally suited to use as MRI contrast agents. The processes by which magnetic NPs enhance contrast in MRI scans was described in Chapter 1. Lanthanide nanoparticle contrast agents were found to exhibit longer r_1 relaxivities than conventional Gd-containing chelates.[112–114] Longer r_1 times improve contrast in T_1 weighted MRI images, providing better diagnostic clarity to physicians. Medical imaging is arguably the most studied application of lanthanide nanomaterials, as in addition to the aforementioned magnetic properties, the rare earth elements also exhibit desirable optical properties, such as sharp line-like emission bands, large Stokes shifts and long fluorescence lifetimes.[115] The luminescent properties of a given lanthanide ion are determined by the nature of their host matrix, and the shielded nature of the f-electron shell means factors such as particle size have little bearing on optical properties, compared to factors such as crystal structure and dopant levels.[116] This is in contrast to other luminescent nanomaterials such as quantum dots, which exhibit size dependent fluorescent behaviour.[9] This means the fluorescent properties of lanthanide nanomaterials can be altered whilst keeping the particle size small, which is a major advantage when using nanomaterials for medicinal and molecular imaging. Furthermore, lanthanide nanomaterials were found to be non-toxic even at high concentrations, which is an advantage over quantum dots which often contain heavy metals such as cadmium.[117] These advantages (high magnetic moments, tunable luminescent properties and low toxicity) have fuelled research interest in this area. As such, there is a wealth of literature available studying the applications of rare-earth nanomaterials, and a number of in-depth reviews are available.[116, 118]

The most popular route to rare-earth nanomaterials is solution-based synthesis, due to experimental flexibility and the range of materials that can be prepared. To date, a host of rare earth containing materials have been synthesised using solution based

methods including rare earth oxides,[119] sodium rare-earth fluorides,[120] lanthanide hydroxides,[117] garnets,[121] perovskites,[122] and rare earth orthovanadates.[123] Of the solution based methods, the two most popular are co-precipitation and thermolysis. In co-precipitation, Ln^{3+} is reacted with OH^- to yield either $\text{Ln}(\text{OH})_3$ or Ln_2O_3 , depending on the reaction temperature and solvent.[124] If an alcohol is used as the solvent at elevated temperatures the oxide is formed, due to the the dehydrating properties of the alcohol.[125] At ambient temperature it is difficult to form Ln_2O_3 by precipitation with OH^- , due to the high dehydration activation energies for $\text{Ln}(\text{OH})_3$. [114] The thermolysis method typically employs the decomposition of metal carboxylate compounds under refluxing solvent conditions to yield Ln_2O_3 particles. To date, a range of Ln-containing carboxylates have been used, including acetates,[119] acetylacetonates,[126] benzoylacetates[127] and oleates.[128] Du and co-workers showed it was possible to use chloro- and fluorinated carboxylate precursors to obtain LaOCl and EuOF nanoplate and nanowire products.[129, 130] Typically, lanthanide oxide nanomaterial products usually fall into one of two categories; thin nanoplates[119, 126, 131] or small (~ 3 nm) discrete particles[128] — as shown in Fig. 4.1 The thin nanoplate species obtained often have edge lengths extending into tens of nanometres, yet will retain a thickness of only a few nanometres. Some nanoplates were even shown to be as thin as one unit cell of the material.[119, 131] This ‘restricted dimensionality’ is a recurring theme in LnO_x nanoparticle synthesis, and the nanowires and ribbons described in this chapter can be included in this group of materials.

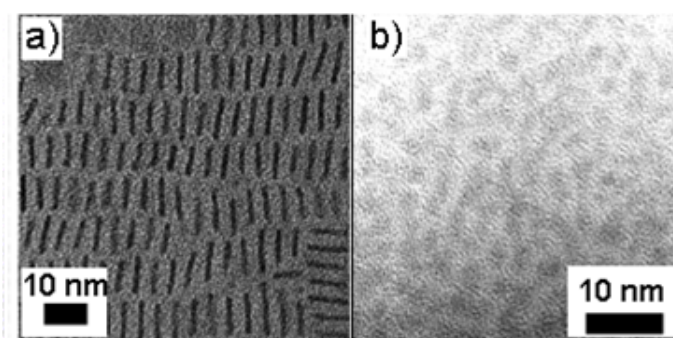


Figure 4.1: Literature examples of Ln_2O_3 particles, showing the ‘restricted dimensionality’ of a) 8 nm Gd_2O_3 nanoplates and b) ~ 3 nm small Gd_2O_3 particles. Images taken from references [119] and [132].

As we saw in Chapter 3, the high pressure, autoclave-based approach is a simple and effective way to produce interesting nanomaterial products. In the current chapter we will see that variations to the polyol methodology described previously for Fe_3O_4 NPs result in the formation of unexpected nanowire and ribbon nanomaterial products. As was described above, solution-based Ln_2O_3 NP syntheses usually result in small particles or thin nanoplates. Small Ln_2O_3 particles usually form when a polyol solvent is used, and the anisotropic nanoplate species are usually formed when long-chain hydrocarbon solvent and surfactants are used under reflux conditions.[119] It is postulated that anisotropic species sometimes form when bulky solvents are used due to the in-situ formation of lamellar phases which can act as templating species.[51] The formation of lamellar liquid-crystalline surfactant phases and their potential role as templates for anisotropic materials is a key aspect of this chapter, and will be discussed in more detail in section 4.3.3. As this thesis relates to the synthesis of magnetic nanoparticles and their properties, anisotropic species are potentially more interesting as they may have unusual magnetic properties as a consequence of their shapes and constrained dimensions. For this reason, the polyol solvents used in the previous chapter were exchanged for a mixture of long-chain surfactant and solvents, in the hope that the autoclave environment may produce unusual anisotropic nanomaterials as opposed to small and spherical particles. The acetylacetonate starting material used in chapter 3 was exchanged for a lanthanide oleate precursor, as it was hoped that the presence of bulky carboxylate ligands in close proximity to the Ln^{3+} ion would facilitate the formation of liquid crystalline phases. Ultimately, it was found that a combination of the solvent and the elevated pressure, unstirred reaction conditions of the autoclave are essential to the formation of nanowires and ribbons. Experimental details, thorough product characterisation, and the factors leading to wire formation and their growth mechanisms were investigated and will be discussed below.

4.2 Experimental

4.2.1 Materials and Methods

Transmission electron microscopy (TEM) and electron diffraction were performed on the FEI Tecnai T20 and FEI Tecnai TF20 instruments, both operated at 200 KeV. Samples

were prepared for TEM, TGA, IR and SQUID characterisation as described in Chapter 2.

Synthesis of the Oleate Precursor ($\text{Ln}(\text{oleate})_3 \cdot n\text{H}_2\text{O}$)

Lanthanide chloride hexahydrate (6 mmol) was mixed with sodium oleate (18 mmol) in a mixture of hexane (21 mL), ethanol (12 mL) and water (9 mL). This mixture was refluxed at 70 °C for 4 hours then allowed to stir for a further 16 hours at room temperature. The upper organic layer containing the lanthanide oleate was separated in a separating funnel, washed twice with deionised water and the hexane was removed under vacuum (with mild heating at ~35–40 °C) to yield lanthanide oleate as a waxy, gum-like solid. Care should be taken during the final vacuum drying step, as prolonged drying or excessive heating can degrade the lanthanide oleate precursor. The oleate precursor should be isolated as a viscous, gum-like solid. Excessive heating will degrade the waxy solid into a powdery form, from which it is not possible to obtain nanowires.

Synthesis of Lanthanide Oxide Nanowires and Ribbons

To make the nanowires, the lanthanide oleate precursor (0.5 mmol) was mixed in air with oleylamine (4 mL, 13.7 mmol), oleic acid (3 mL, 9.5 mmol) and dioctyl ether (2 mL) before being transferred to a 12 mL Teflon lined steel autoclave. The autoclave was then heated at 10 °C per minute to 200 °C and maintained at this temperature for 24 hours. After allowing the autoclave to cool naturally, ethanol was added to the mixture to precipitate the particles which were collected by centrifugation at 4,000 rpm for 10 minutes. To clean the particles, the residue collected after centrifugation was dispersed in 5 mL of hexane, re-precipitated with ethanol and centrifuged. This procedure was repeated at least 5 times to ensure the sample was clean enough for HRTEM experiments. Lanthanide oleates were prepared using cerium, neodymium, europium, gadolinium, dysprosium and ytterbium chlorides as starting materials. These starting materials were chosen so as to obtain a range of oleate precursors from across the lanthanide series.

4.3 Results and Discussion

4.3.1 Characterisation of Nanowires and Ribbons

The obtained nanowire and nanoribbon species were primarily characterised by TEM and electron diffraction (ED), which provided insight into their morphology and crystallinity. EELS and EDX analysis were also performed to examine the elemental compositions and oxidation states of the nanowires, to determine the LnO_x stoichiometry, and the nature of the adsorbed species on the nanowire and ribbon surface was confirmed using IR spectroscopy. The oleate precursors were characterised using TGA and CHN analysis, and the results of all of the above measurements are provided in the following sections.

Characterisation of the Oleate Precursor

A combination of TGA and CHN microanalysis were used to determine the precursor composition and hydration levels. TGA plots for each precursor are given in Fig. 4.2. Examination of TGA data for each of the oleates tested reveals variation in initial hydration levels, observable by different weight losses upon heating to $\sim 100^\circ\text{C}$ (Fig. 4.2). Variation in water content between lanthanide oleates is probably due to inadequate drying of the precursor during the separation phase of the oleate synthesis. During synthesis of the lanthanide oleate precursor, the thick hexane layer containing the product is washed with water repeatedly to remove the NaCl by-product. It is conceivable that some water may persist in the hexane layer, despite care being taken during the separation.

The europium oleate precursor ($\text{Eu}(\text{oleate})_3 \cdot n\text{H}_2\text{O}$) was determined to be the ‘driest’ according to TGA, and so the water loss observed by TGA should relate only to water of crystallisation, and not to any water that persists from the separation phase. Fig. 4.2b) inset shows a weight loss of 5.08% weight loss up to 200°C (the reaction temperature), which is in good agreement with the predicted percentage change assuming the loss of 3 waters from the $\text{Eu}(\text{oleate})_3$ complex, which would equate to a weight change of 1050.55 g/mol to 996.49 g/mol (5.15%). We can therefore conclude that the formula for a dry oleate precursor can be written as $\text{Ln}(\text{oleate})_3 \cdot 3\text{H}_2\text{O}$. The variation in oleate water content was not found to be detrimental to nanowire synthesis, as reactions performed using different batches of precursor were found to yield identical products. Furthermore,

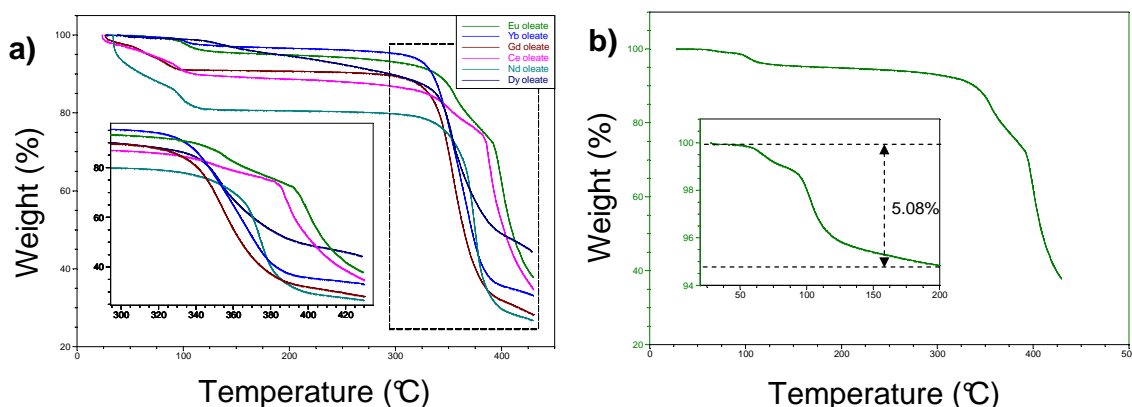


Figure 4.2: a) TGA analysis for the each of the oleate precursors in the RT to 450 °C temperature range. Inset is an expansion from to 300 to 450 °C region. b) TGA analysis for the Eu-oleate precursor, showing a 5.08 % weight loss corresponding to the loss of 3 waters from the $\text{Eu}(\text{C}_{18}\text{H}_{33}\text{O}_2)_3 \cdot 3 \text{H}_2\text{O}$ complex.

reactions performed with additional water added yielded identical products, as will be discussed later.

The $n = 3$ level of hydration was also confirmed through CHN microanalysis. CHN analysis for $\text{Eu}(\text{C}_{18}\text{H}_{33}\text{O}_2)_3 \cdot 3 \text{H}_2\text{O}$: Calculated (found); C: 65.08(60.28); H: 10.03(9.55); N: 0(0). Slightly lower C and H content than expected were obtained, which suggests impurities in the sodium oleate precursor, possibly as variation in hydrocarbon chain length (the sodium oleate starting material is sold at >82 % purity, and the 99% purity sodium oleate was prohibitively expensive). To test this hypothesis CHN analysis was obtained for the sodium oleate precursor, which also gave a lower than expected C and H content. This suggests that there is indeed an impurity in hydrocarbon chain length. CHN for sodium oleate ($\text{C}_{18}\text{H}_{33}\text{O}_2\text{Na}$) calculated (found); C: 71.01(68.09); H: 10.92(10.66); N: 0(0).

TEM Characterisation of Nanowires and Ribbons

Representative TEM pictures are given in Fig. 4.3, showing the nanowire and ribbon species obtained for each of the oleate starting materials used. It can be seen that for each of oleates, anisotropic products were obtained, with slight variations between each lanthanide oxide. For example, nanowires were obtained for each precursor with the exception of $\text{Dy}(\text{oleate})_3$, which yielded nanoribbons. Furthermore, where nanowires were

obtained, the morphology of the nanowires varies slightly from lanthanide to lanthanide, with the earlier series lanthanide oxides CeO_2 and Nd_2O_3 yielding thicker and better-defined wires than the mid series (Gd_2O_3 and Eu_2O_3) and late series Yb_2O_3 nanowires. Indeed, at the magnification used in Fig. 4.3f), it is not possible to clearly see the Yb_2O_3 nanowires. It was also possible to see larger isolated Ln_2O_3 particles on the TEM in some cases (Fig. 4.3e,f), though these particles were present as a minority species.

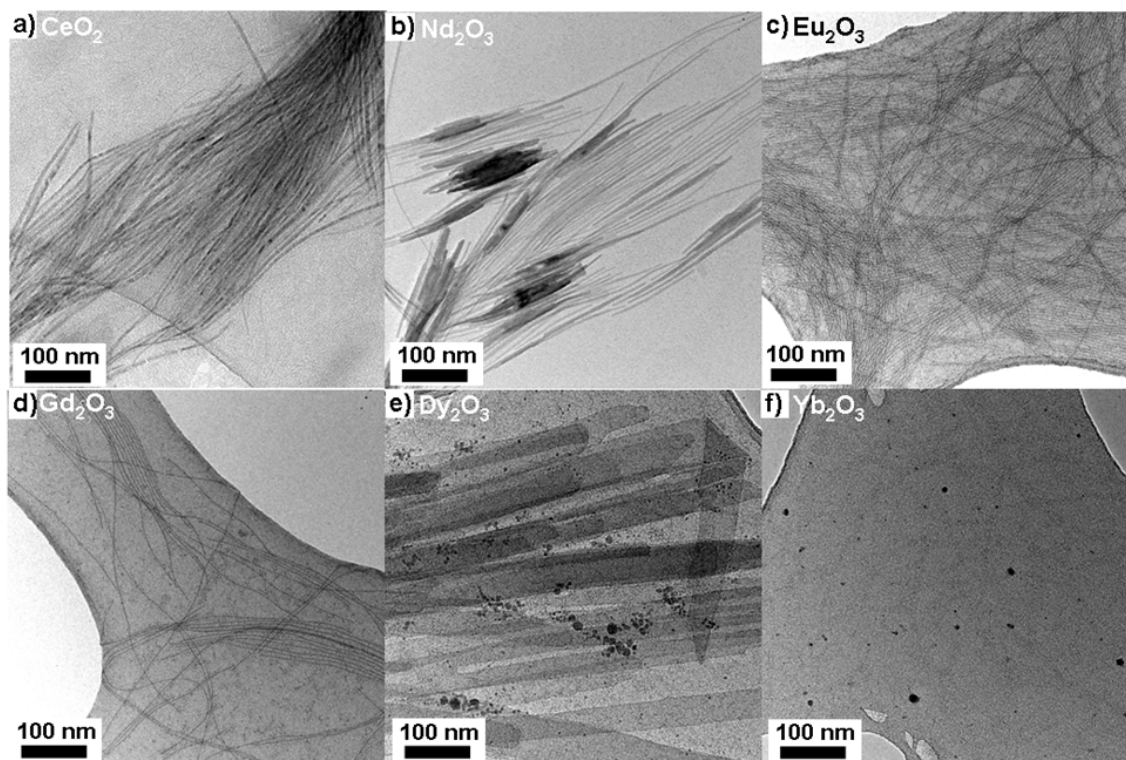


Figure 4.3: TEM images of (a) CeO_2 (b) Nd_2O_3 (c) Eu_2O_3 (d) Gd_2O_3 nanowires and (e) Dy_2O_3 nanoribbons (the latter of which also shows a minority population of Dy_2O_3 nanoparticles, evident as dark spots) and (f) Yb_2O_3 , which also shows minority population of Yb_2O_3 particles. The thin Yb_2O_3 nanowires are not easily visible at this magnification.

Rare-earth oxides in the bulk phase exhibit polymorphic modifications classified as A, B or C type for hexagonal, monoclinic, and cubic structures, respectively.[133] The distinct radii of the Ln^{3+} ions and the type of thermal treatment used promote one of the three structural types. The C-type structure has been observed for Sm–Lu inclusive, whereas the A-type structure is observed for Ce–Nd.[133] For some thermal treatments Sm, Eu and Gd can adopt either B- or C-type structures. In our experiments, electron

diffraction, together with an analysis of TEM lattice fringes, indicate that the materials are, contrary to the behaviour observed in the bulk, all cubic ($Fm\bar{3}m$ for CeO_2 and $Ia\bar{3}$ for Ln_2O_3), with lattice constants corresponding to PDF card numbers 43-1002 (CeO_2), 21-0579 (Nd_2O_3), 34-0392 (Eu_2O_3), 43-1014 (Gd_2O_3), 86-1327 (Dy_2O_3) and 18-1463 (Yb_2O_3). The formation of cubic LnO_x nanoparticles across the lanthanide series has been previously reported, and would seem to be favoured by the thermolysis of carboxylate containing precursors.[126, 127]

High resolution TEM was used to further characterise the nanowires and ribbons. These images are given in Figs. 4.4 and 4.5. The HRTEM figures show that each of the nanowire and ribbon products is polycrystalline, comprising numerous randomly oriented crystalline regions, which are linearly aligned into wire or ribbon morphologies.

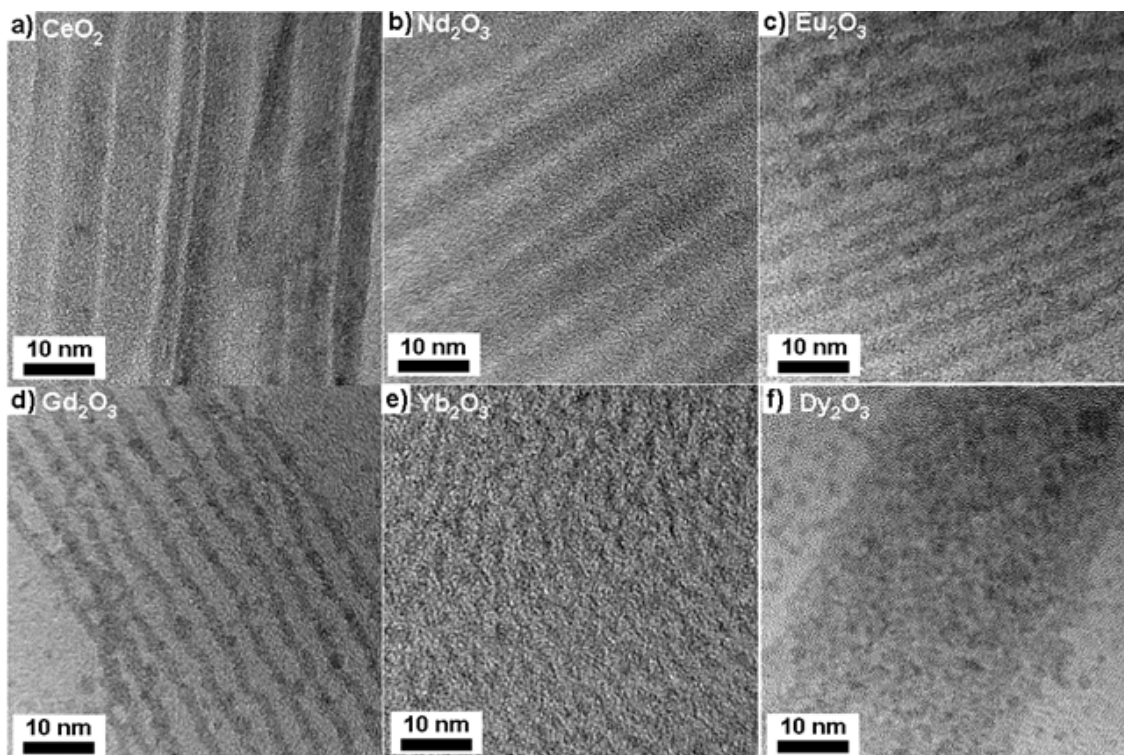


Figure 4.4: HRTEM images of (a) CeO_2 (b) Nd_2O_3 (c) Eu_2O_3 (d) Gd_2O_3 , (e) Yb_2O_3 nanowires and (f) Dy_2O_3 nanoribbons, with discrete nanoparticles also visible in some cases.

The HRTEM images in Fig. 4.4 confirm that the width of the nanowire species decreases with increasing lanthanide atomic number (i.e: from left to right across the f -block). The observed widths decrease from 5.0 nm for CeO_2 to 1.8 nm for Yb_2O_3 . Aver-

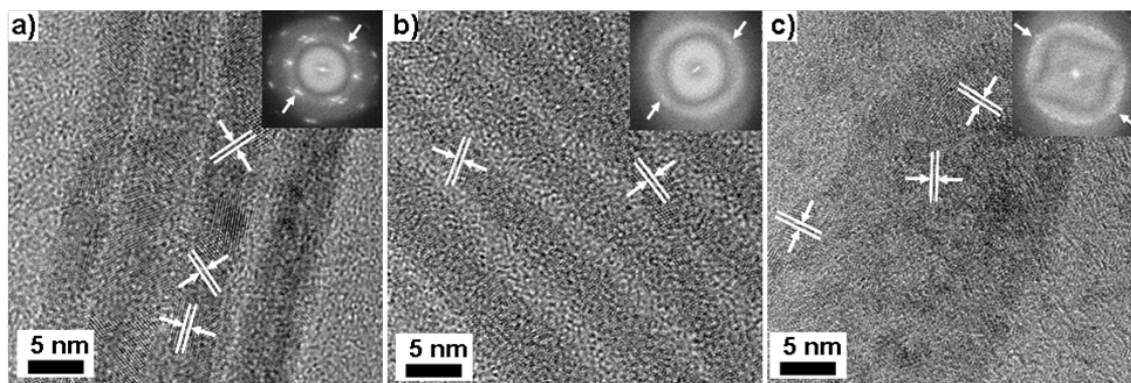


Figure 4.5: Additional HRTEM images for (a) CeO₂ nanowires, (b) Nd₂O₃ nanowires and (c) Dy₂O₃ nanoribbons. Inset are the corresponding fast Fourier transforms (FFTs). The images highlight the material polycrystallinity. Interplanar distances for each of the crystalline regions examined were determined to be (a) 0.28 nm, (b) 0.27 nm and (c) 0.26 nm, consistent with cubic CeO₂ (200) and cubic Ln₂O₃ (400) reflections. Lattice constants were determined from (200) or (400) FFT spot distances (indicated with arrows) as (a) 0.528 ± 0.015 nm, (b) 1.094 ± 0.006 nm and (c) 1.056 ± 0.030 nm, which are in agreement with the reference cards previously mentioned.

age wire widths were calculated from HRTEM images and are shown in Fig. 4.6.

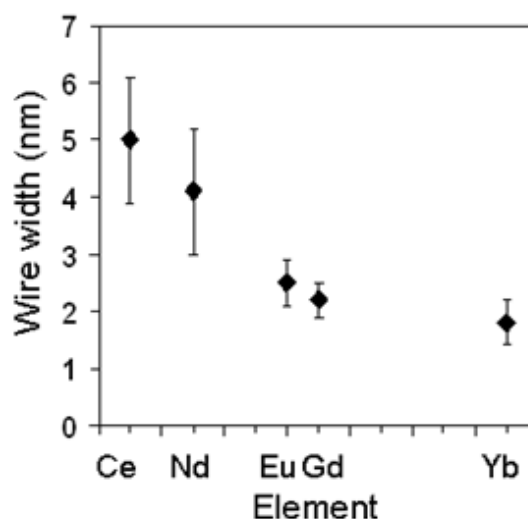


Figure 4.6: Decrease in wire width with increasing atomic number across the lanthanide series.

In addition to decreasing wire width across the lanthanide series, it can also be seen that the length of the individual single crystalline regions which comprise each nanowire varies from lanthanide to lanthanide. For the early series lanthanides such as CeO_2 and Nd_2O_3 the observed crystalline regions often extend into tens of nanometres and are typically oriented with a $[100]$ axial direction (see Fig. 4.4a,b). Selected area electron diffraction from CeO_2 gave ‘textured’ diffraction patterns as opposed to distinct rings due to the reduced number of individual crystalline domains, shown in Fig. 4.7a). Conversely, the mid and later series lanthanide oxide wires (which comprise much smaller, randomly orientated crystalline regions ~ 3 nm in diameter) yielded only diffuse ED patterns Fig. 4.7c-f). The presence of ring patterns confirms the presence of a large number of randomly aligned particles as opposed to large regions of uniform crystallinity (which would yield spot patterns). It should also be noted that it was not possible to obtain satisfactory X-ray powder diffraction patterns for any sample, as each was too weakly diffracting to give observable peaks in the collected X-ray patterns.

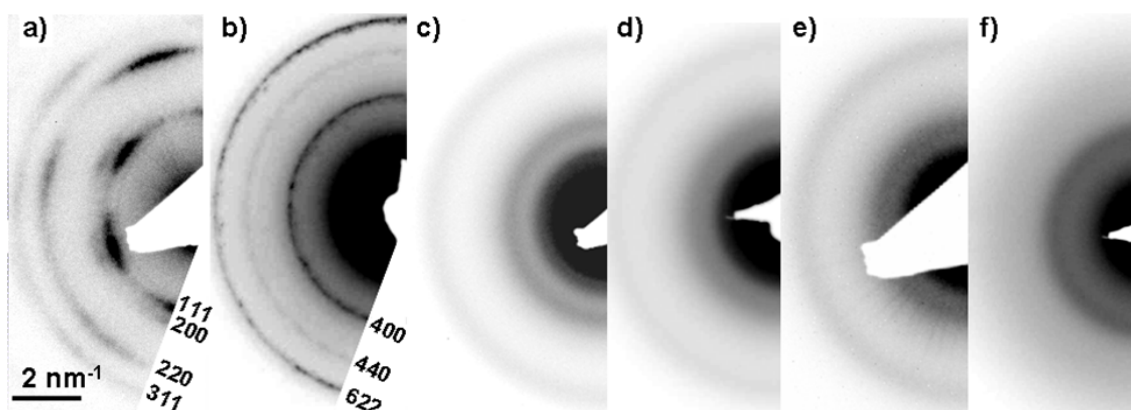


Figure 4.7: ED patterns from (a) CeO_2 (b) Nd_2O_3 (c) Eu_2O_3 (d) Gd_2O_3 , (e) Dy_2O_3 and (f) Yb_2O_3 , showing the characteristic weak diffraction expected for thin nanowire species.

The TEM and HRTEM images show that the nanowire species are well dispersed on the TEM grids and that agglomeration is minimal. The even spacing seen between nanowires on the TEM grids (such as in Fig. 4.4) implies that the nanowires and ribbons must be well coated with surfactants, which minimise inter-particle interactions and prevent agglomeration. IR spectroscopy was performed to investigate the nature of the species adsorbed to the wire and ribbon surfaces, as described below.

Nanowire and Ribbon Surface Characterisation

IR spectroscopy was performed on each of the samples to determine the nature of the adsorbed surface species. The spectra for each of the nanowire samples obtained and the surfactants used are given in Fig. 4.8. The peaks at 2926 cm^{-1} and 2854 cm^{-1} are assignable to the antisymmetric and symmetric methylene stretches ($\nu_{\text{as}}(\text{CH}_2)$ and $\nu_{\text{s}}(\text{CH}_2)$) of oleic acid (g) and oleylamine (h). The antisymmetric methyl stretch, $\nu_{\text{as}}(\text{CH}_3)$, is observable as a shoulder on the 2926 cm^{-1} peak. These peaks show little difference to their counterparts on pure oleylamine and oleic acid. The $\nu(\text{C}=\text{O})$ stretch for pure oleic acid (g), appears at 1710 cm^{-1} . This peak is absent in the infra-red spectrum of the CeO_2 and Ln_2O_3 nanowires (a–f), confirming that the carbonyl present in the product exists bound to the surface. The 1710 cm^{-1} stretch is replaced with two characteristic bands at 1545 cm^{-1} and 1432 cm^{-1} , which are assignable to the antisymmetric ($\nu_{\text{as}}(\text{COO}^-)$), and symmetric, ($\nu_{\text{s}}(\text{COO}^-)$) stretches, respectively. The difference in wavenumber of these two (COO^-) stretches can be used to determine the mode of co-ordination of the carbonyl group of oleic acid to the lanthanide oxide nanowire surface. For a monodentate ligand a separation of $>200\text{ cm}^{-1}$ is expected, $<110\text{ cm}^{-1}$ for a bidentate and $140\text{--}200\text{ cm}^{-1}$ for a bridging ligand.[134] For our system the separation is 113 cm^{-1} , which suggests oleic acid on the particle surface is acting as a bidentate ligand in agreement with literature observations.[135] It is harder to comment unambiguously on the presence of OAm on the particle surface, as the peaks for OA and OAm overlap. It has been previously reported that when OAm is used as the sole stabilising agent for Fe_3O_4 particles the IR spectra of the particles is nearly identical to the IR spectrum of pure OAm, so it is anticipated that there is OAm on the particle surface.[136]

IR confirms the presence of an oleate stabilising layer on the particle surface, which is formed during the particle synthesis procedure. There is a large excess of surfactant molecules present in the reaction mixture (4 mL of oleylamine and 3 mL of oleic acid) which ensures the nanowires and ribbons are well stabilised. The presence of hydrocarbon surfactant molecules on the particle surface could also be inferred through the stability of dispersions of the nanowire and ribbon powders in non-polar solvents, such as hexane and toluene. In addition to preventing agglomeration of nanoparticles, surfactant molecules also help protect against oxidation. The susceptibility of CeO_2 nanowires to ambient

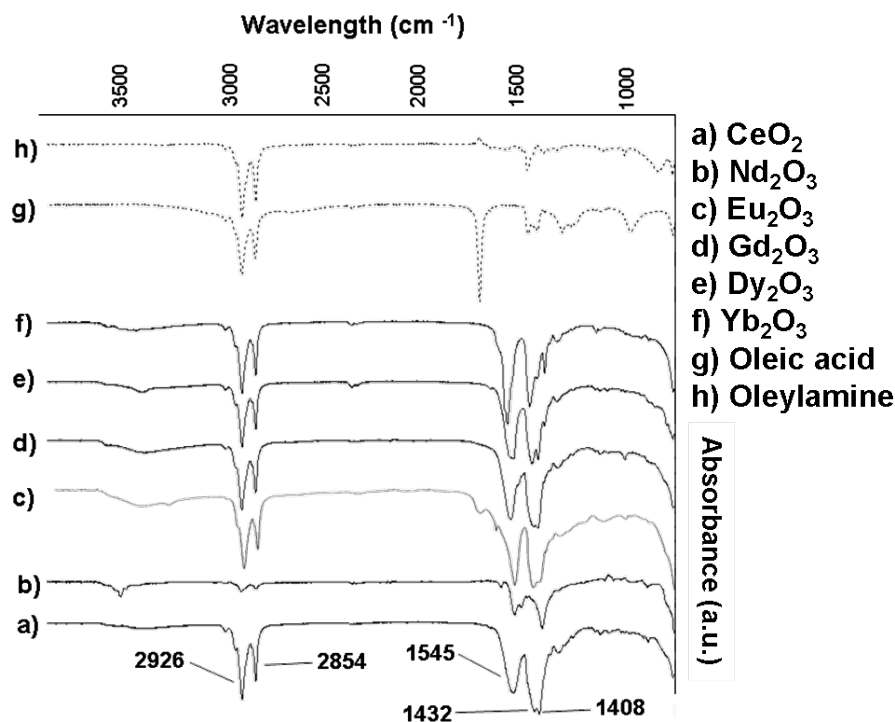


Figure 4.8: IR spectra of the obtained lanthanide oxide nanowire powders (a-e), oleic acid (f) and oleylamine (g). The powders are (a) CeO_2 (b) Nd_2O_3 (c) Eu_2O_3 (d) Gd_2O_3 (e) Dy_2O_3 and (f) Yb_2O_3 .

oxidation was assessed by using EELS, as described below.

Variation of Cerium Oxidation State in CeO_2 Nanowires

All of the nanowires with the exception of those obtained using cerium oleate have the cubic $Ia\bar{3} \text{Ln}_2\text{O}_3$ structure. Cerium oleate did yield nanowires with a cubic space group, though CeO_2 ($Fm\bar{3}m$) was formed. Whilst the Ln^{3+} oxidation state is the most stable for the majority of the lanthanides and no variation in oxidation state is expected, the Ce^{3+} ion has only one f electron which is readily lost to form Ce^{4+} , and hence CeO_2 is formed. It should be noted that C-type $Ia\bar{3} \text{Ce}_2\text{O}_3$ cannot be easily prepared, and harsh synthetic conditions are required (such as reduction of CeO_2 at 1170 K).[137] The SAED patterns obtained from the cerium oxide nanowires (Fig. 4.7) are consistent with the expected pattern for cubic CeO_2 , and no additional reflections associated with other phases of CeO_2 or Ce_2O_3 were observed.

Ceria nanoparticles have previously been studied using nanoanalytical techniques

such as EELS due to the interesting bi-stability of the oxidation state of the cerium ion. It was recently shown that CeO_2 nanoparticles, if small enough (<15 nm), can contain significant amounts of Ce^{3+} at their surfaces.[138, 139] The presence of increased levels of Ce^{3+} at the particle edge was attributed to the migration of oxygen vacancies in the CeO_2 unit cell towards the particle surface.[140] The spatial variation in $\text{Ce}^{3+}/\text{Ce}^{4+}$ across CeO_2 particles was recorded by Wu et al. using STEM EELS techniques, and it was shown that it is more accurate to describe ceria nanoparticles as CeO_{2-x} , with x increasing to 0.5 towards the particle edge.[139]. This means that small particles (3 nm and below) can have a stoichiometry approaching Ce_2O_3 , whilst retaining the cubic CeO_2 structure, as the $Ia\bar{3}$ and $Fm\bar{3}m$ space groups are closely related. The CeO_2 nanowires in the present study were characterised using STEM EELS both immediately after synthesis and following ambient oxidation, the results are presented in Fig. 4.9.

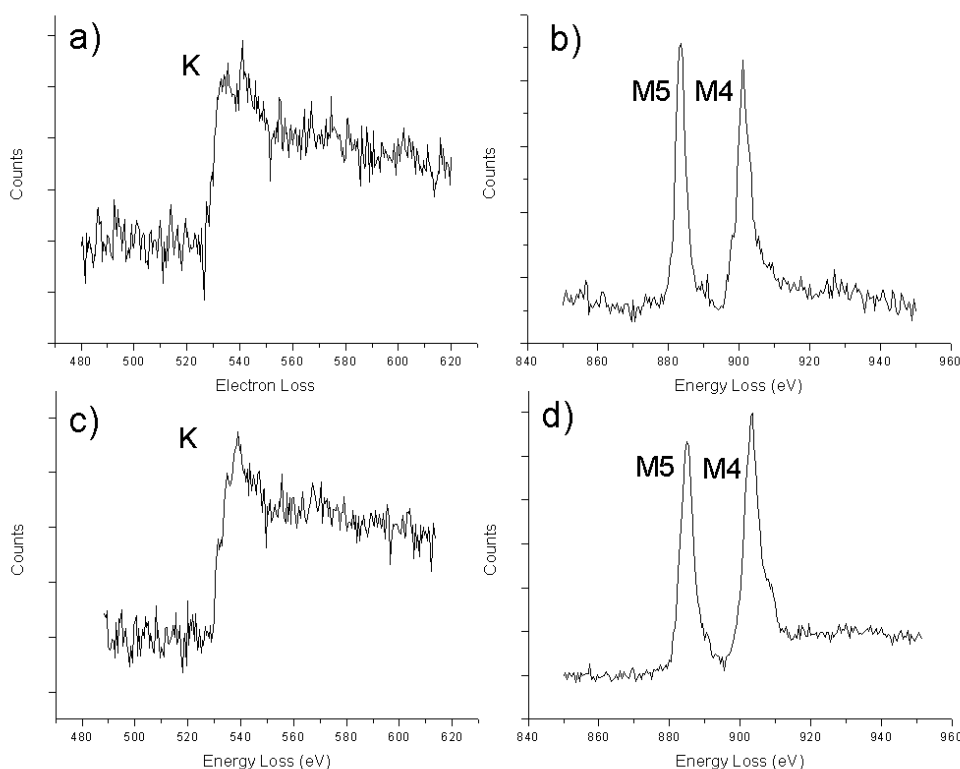


Figure 4.9: EELS spectra of the oxygen K and Ce $M_{5,4}$ edges of nanowires (a,b) immediately after synthesis and (c,d) following atmospheric oxidation to CeO_2 . The Ce $M_{5,4}$ edge ratio increases from (a) to (b), which is consistent with increasing oxidation state from Ce^{3+} to Ce^{4+} . [141, 142]

Elemental compositions were determined using the Gatan Digital Micrograph software package, using Hartree-Slater electron scattering cross-sections and following removal of a fitted power-law background. The elemental compositions were calculated as Ce: 40.8%, O: 59.2% and Ce: 36.7%, O: 63.3% before and after oxidation, respectively. These calculated values show an increase in the oxygen content of the obtained cerium oxide nanowires after exposure to air and are consistent with oxidation of Ce_2O_3 to CeO_2 . However, the SAED patterns were consistent with cubic CeO_2 both before and after oxidation. It is therefore possible to conclude that the as-obtained cerium oxide nanowires are cubic CeO_2 , which contain a significant amount of Ce^{3+} (due to the increased number of surface atoms) though oxidation to Ce^{4+} occurs readily upon exposure to air.

Nanowire and Ribbon Characterisation Conclusions

The key point that should be taken from the characterisation of the nanowire and ribbon species is that they are structurally very interesting. Whilst a number of materials have been synthesised as nanowires before, a versatile approach to LnOx nanowires has not previously been reported and at the time of writing only one brief communication relating to the synthesis of samarium oxide wires was available.[131] We have seen from the TEM and ED characterisation that the nanowires comprise linear assemblies of randomly oriented crystalline regions, which is unusual as nanowire growth usually results in single-crystalline products in which wire growth proceeds via uniform growth at an end. The polycrystalline assemblies described here point towards a fundamentally very different, attachment-based mechanism. Additional experiments were performed to determine the growth mechanisms of the nanowires, as described in the following section.

4.3.2 Nanowire and Ribbon Formation Mechanisms

There are a number of different mechanisms believed to be responsible for nanowire growth, the most common of which is the growth of a continuous and anisotropic single crystal directly from solution. Another mechanism is the oriented attachment (OAT) mechanism, whereby constituent sub-units of a wire attach and organize in crystallographic registry with their neighbours. The OAT mechanism was discussed in Chapter 3 to describe the face-to-face attachment of compound cubic magnetite particles into larger,

anisotropic forms. Surveying the literature revealed that variations of the OAt mechanism exist. For example, Ribeiro et al. reported the in-situ rotation of a SnO_2 particle on a TiO_2 tip, where particle rotation was followed in real time by TEM and showed the smaller SnO_2 particle rotating to align with the TiO_2 tip.[143] There are few literature examples of oriented attachment occurring for lanthanide containing nanomaterials. The three-dimensional assembly of preformed CeO_2 nanoparticles into nanoflower species was reported by Zhou et al., where oriented agglomeration was promoted by a sudden and rapid decrease in surface ligand coverage caused by decomposition of the $(\text{NH}_4)_2\text{Ce}(\text{NO}_3)_6$ precursor above 220°C .[144] Bao et al. reported the self-assembly of NdF_3 plates into ordered chains, which coalesced via oriented aggregation.[145] Comparison with our wire species suggests that a similar ‘imperfect’ OAt mechanism is behind nanowire and ribbon growth. To investigate the formation mechanisms further, additional experiments were devised and performed as described below.

Initially, time-dependent reactions were performed using CeO_2 as a model system. The other Ln_2O_3 species are expected to behave in a similar manner. The reaction time was reduced from 24 to 4 hours. This produced shorter, less uniform wires and an abundance of ~ 3 nm spherical particles on the TEM grid (Fig. 4.10).

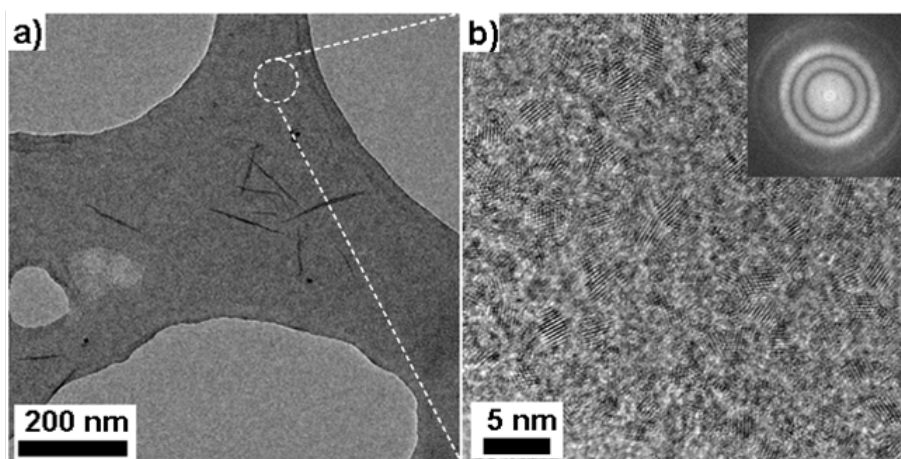


Figure 4.10: TEM images from a 4 hour reaction showing (a) short CeO_2 wires and (b) an abundance of small ~ 3 nm CeO_2 particles. Inset is the corresponding FFT, the presence of rings indicating the presence of a large number of randomly oriented particles.

HRTEM studies show the shorter wires to comprise numerous ~ 3 nm crystalline sub-

units, randomly oriented along the length of a wire which is typically only one nanoparticle wide, (Fig. 4.11a,b). This is in contrast to the CeO_2 wires obtained from a 24 hour reaction, which were crystallographically more uniform and contained larger crystalline regions than the shorter wires obtained from a 4 hour reaction (Fig. 4.11c,d).

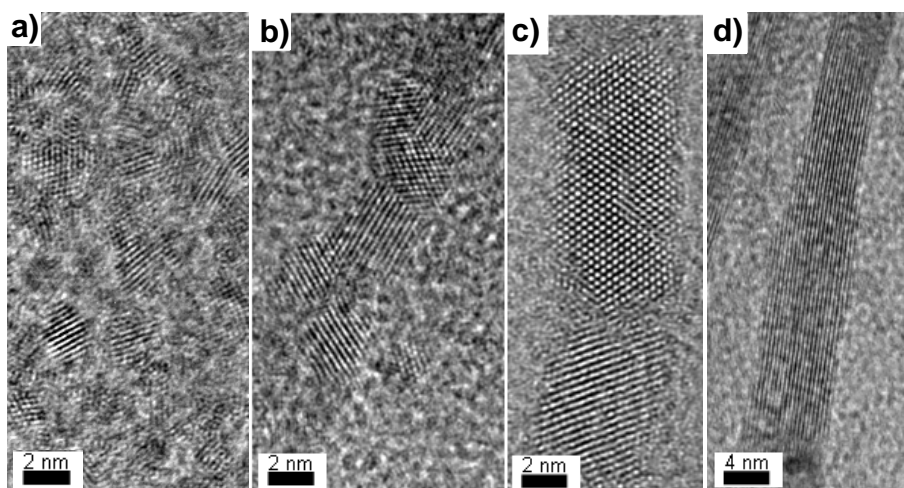


Figure 4.11: a,b) HRTEM images from a 4 hour reaction CeO_2 showing a) abundance of small particles and b) random orientation of smaller crystalline regions along a short wire. Comparative HRTEM images from a 24 hour reaction c,d) showing larger, more uniform regions of CeO_2 .

The crystallinity of the short and long CeO_2 wires was further assessed using dark-field TEM imaging, in which 3 DF TEM images were collected at different scattering angles and then combined into a false-coloured composite. The false-coloured images for the short and long wires are given in Fig. 4.12, in which each colour represents a different crystalline orientation. It can clearly be seen that the shorter wires contain numerous randomly aligned ~ 3 nm sub-units, whereas the larger wires (whilst still polycrystalline) have a smaller number of much larger crystalline domains. This is in agreement with the HRTEM bright-field images given in Fig. 4.11.

The time-dependent studies show that nanowire growth is considerably less organised than the conventional oriented attachment mechanism, where crystallographic registry of successive nanoparticles arises either during attachment or via subsequent nanoparticle rotation.[146, 147] Conversely, these LnO_x nanowires grow seemingly independent of the orientation of their constituent nanoparticles. Comparison between the long and

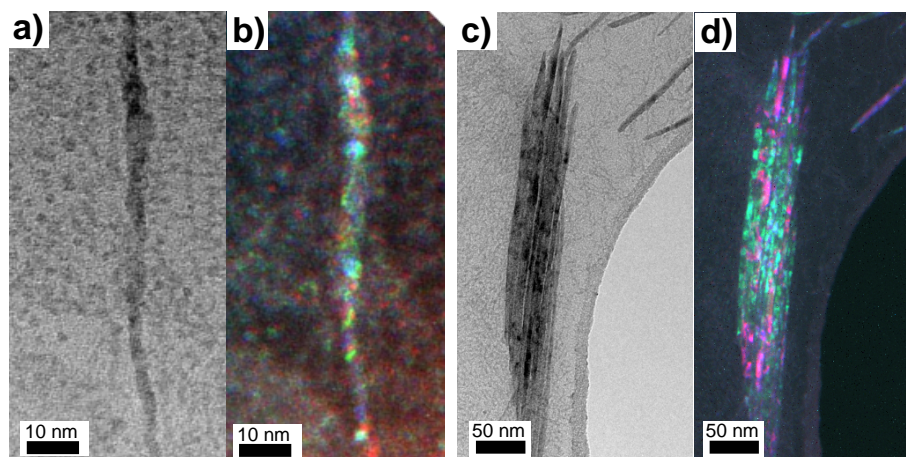


Figure 4.12: Bright field and corresponding dark field TEM images from a,b) 4 hour and c,d) 24 hour CeO_2 reactions. The dark field images show small crystalline domains when the reaction time is 4 hours, compared with the extended crystalline regions when the reaction time is increased to 24 hours.

short CeO_2 wires (Figs. 4.11 and 4.12) clearly shows that the longer wires have smoother and more uniform edges than the shorter wires obtained from the 4 hour reaction. Additionally, the density of isolated ~ 3 nm particles visible on the TEM grid is reduced significantly on increasing the reaction time, which implies that the small particles are consumed during wire growth. For a 24 hour Eu_2O_3 reaction, only a few isolated particles could be observed alongside the micron-long nanowires (Fig. 4.13), providing evidence that the smaller particles are consumed to fuel the growth of the nanowires. The above observations provide strong evidence that nanowire growth proceeds by a mechanism different to conventional nanowire growth mechanisms. A new, three-stage growth process can be proposed, which is best described as ‘imperfect’ oriented attachment.

The 3-stage growth mechanism is depicted in Fig. 4.14. The first stage of the wire formation process is the formation of discrete spherical particles, which are typically ~ 3 nm in diameter (Fig. 4.14a). Thermal decomposition of Ln oleates in the presence of oleic acid or oleylamine is known to produce similarly sized LnO_x particles under reflux conditions.[128] The second step is the assembly of these small LnO_x particles into polycrystalline, one dimensional chains (Fig. 4.14b). Self-assembly is usually driven by the reduction in free surface energy upon recrystallisation,[146] though in this case the observed polycrystallinity implies that there is another force driving self-assembly, which

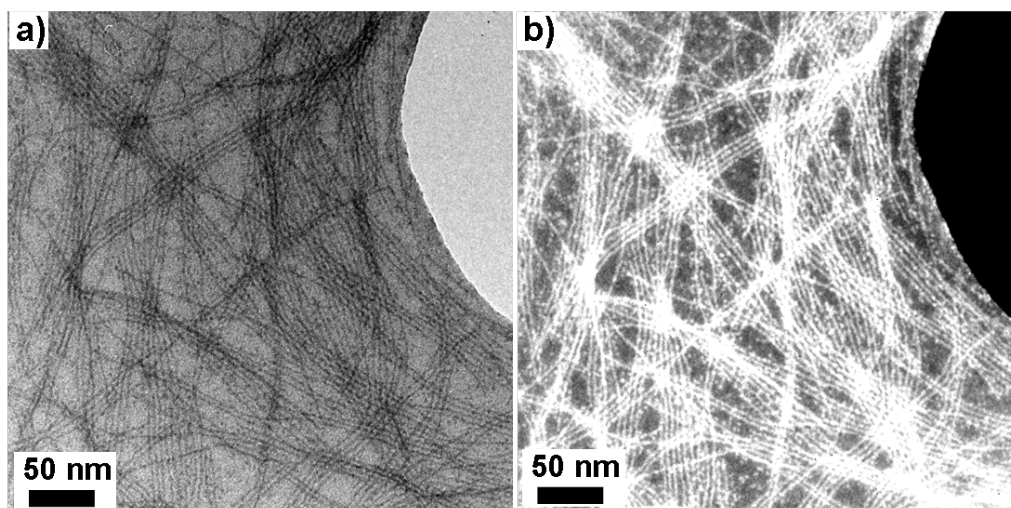


Figure 4.13: Bright field (a) and corresponding dark-field (b) images of Eu_2O_3 nanowires obtained from a 24 hour reaction. The images clearly show small ~ 3 nm particles (as a minority species) alongside the wires.

will be discussed later. The final stage of the process is recrystallisation of individual assembled particles into longer, crystallographically aligned and more uniform materials (Fig. 4.14c). This is evident by comparing the CeO_2 particles obtained from 4 hour and 24 hour reactions (Fig 4.11).

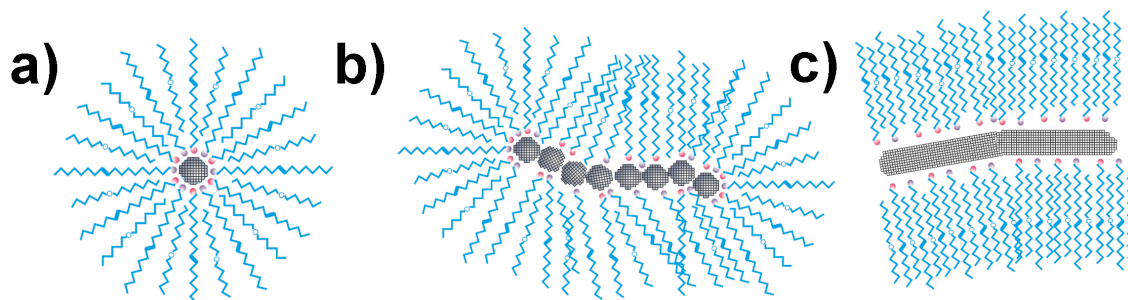


Figure 4.14: TEM evidence strongly suggests a 3 stage mechanism: **a)** Formation of individual ~ 3 nm particles. **b)** Sequential self assembly of small particles into polycrystalline chains (4 hours). **c)** Recrystallisation into longer and more crystallographically aligned uniform materials (24 hours).

The above 3-stage mechanism can also be used to account for the observed decrease in wire width with increasing atomic number. The stability constants of Ln complexes are known to increase with increasing atomic number, as shown in the literature data for

Metal ion	$\log K_{ML}$	Metal ion	$\log K_{ML}$
La ³⁺	14.72	Dy ³⁺	17.57
Ce ³⁺	15.39	Ho ³⁺	17.67
Pr ³⁺	15.75	Er ³⁺	17.98
Nd ³⁺	16.06	Tm ³⁺	18.59
Sm ³⁺	16.55	Yb ³⁺	18.68
Eu ³⁺	16.69	Lu ³⁺	19.06
Gd ³⁺	16.7	Y ³⁺	17.38
Tb ³⁺	17.25		

Table 4.1: Increase in stability constant across the lanthanide series for the reaction $M + L \rightleftharpoons ML$, where M is the lanthanide metal, L is ligand and $K_{ML} = \frac{[ML]}{[M][L]}$. Although these values are for the complexation where L = EDTA, similar trends are seen for other carboxylates, and can be expected for lanthanide oleates. Note that no data for promethium (Pm) is available. [148]

Ln-EDTA complexes given in Table 4.1. This means that the heavier, less reactive lanthanide oleates react slowly during the first stage and will produce smaller nanoparticles. Furthermore, the size of the nanoparticles obtained from oleate decomposition would be expected to decrease with increasing atomic number, due to a decrease in unit cell size as a consequence of the lanthanide contraction.[148]

As most wires appear to be one particle wide, the reactivity and size contraction trends immediately reduce wire width with increasing Ln atomic number. The increased stability of the mid and late series lanthanides means that during the third stage, recrystallisation of adjacent particles will be slow. This observation explains the noticeable decrease in edge uniformity (i.e. wires become less smooth and more irregular in appearance) with increasing atomic number (Figs. 4.4 and 4.11). For example, wires obtained after 4 hours lack the smooth edges of those seen after 24 hours, as the 3 nm crystallites have not yet had time to coalesce into more uniform species (compare Fig. 4.11b and d). Furthermore, the heaviest and least reactive oleate tested (ytterbium) yielded very thin wires which were difficult to image with TEM (as can be seen by the poor contrast of Yb₂O₃ nanowires in

Figs. 4.3f) and 4.4e).

Whilst the 3 stage mechanism and above discussion of wire thickness with respect to oleate stability may be true for the cases where nanowires were obtained, it is clear that the generic mechanism does not account for the unusual Dy_2O_3 nanoribbon species. The formation of Dy_2O_3 nanoribbons as opposed to nanowires is both unprecedented and intriguing. The reasons behind the deviation of Dy_2O_3 ribbons from the observed Ln_2O_3 nanowire trend are unclear. Wang et al. previously reported that the morphologies of lanthanide oxide nanomaterials can vary depending on the atomic number of the lanthanide starting material, as different products were obtained for early (La–Gd), mid (Tb), and late (Dy–Yb) starting materials.[149] It should be noted that in the system used by Wang et al. the reaction starting material is $\text{Ln}(\text{NO}_3)_3 \cdot x\text{H}_2\text{O}$, and the obtained product is $\text{Ln}(\text{OH})_3\text{NO}_3$, which is calcined to the corresponding oxide, which limits the validity of comparisons drawn between this and the current lanthanide oxide nanowire system. The authors offer no explanation of the observed trends. Investigating the products obtained in the present Ln oleate system reveals that there is a ‘late’ series oleate, $\text{Yb}(\text{oleate})_3$, that produces the thinnest wires of the series (see Fig. 4.6). By the classification of Wang et al., ytterbium oleate would be expected to yield the same product as $\text{Dy}(\text{oleate})_3$, yet this is obviously not the case in the present work. This observation suggests that the nanoribbons must form through a different mechanism to other nanowire species. TEM and HRTEM investigations were performed to investigate the differences between the Ln_2O_3 nanowires and Dy_2O_3 nanoribbons, these additional nanoribbon images are given in Fig. 4.15.

The major difference between the wires and ribbons is their width; the ribbons are considerably wider, with widths of around 50 nm. The ribbon thickness was determined by EELS to be ~ 4 nm, which is comparable to the thickness of the nanowire species. The thinness of the Dy_2O_3 nanoribbons is also evident in the poor contrast between the ribbons and the carbon support. Fig. 4.15 shows that the ribbons retain a polycrystalline character, which implies that the assembly/recrystallisation mechanism seen for the lanthanide oxide nanowires also underpins ribbon growth. However, the increased width of the ribbons is consistent with the lateral recrystallisation of between 15 and 20 individual nanoparticles (or nanowires), whilst still retaining one particle thickness. The thinness of the Dy_2O_3 nanoribbons enables them to be as flexible as the other Ln_2O_3 nanowires, as shown in

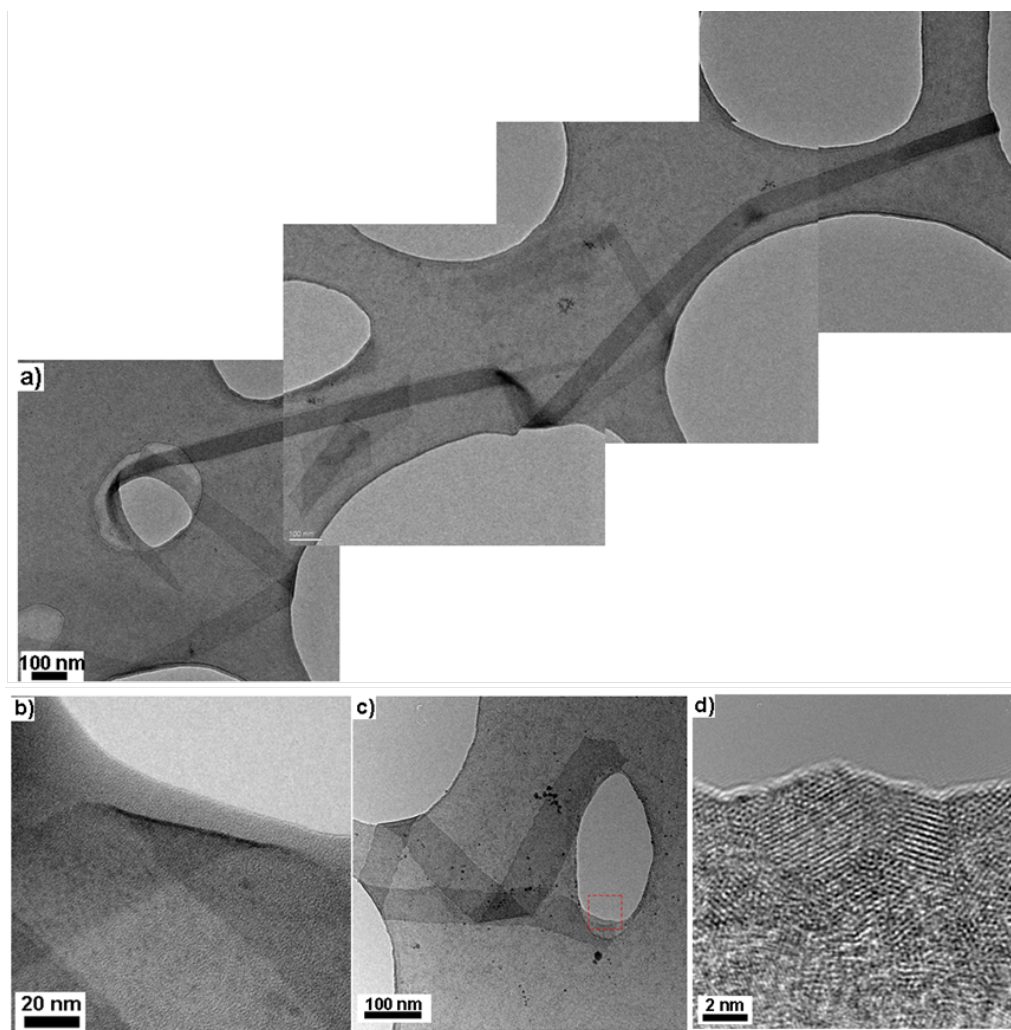


Figure 4.15: Additional TEM images of the Dy_2O_3 nanoribbon species. (a) The length of this particular ribbon is over 3 microns (~ 3150 nm). (b) HRTEM image showing a fold in the thin nanoribbon, illustrating its flexibility and mechanical stability under deformation. (c) TEM image of a shorter nanoribbon, also displaying a high degree of flexibility. The red box shows a fragment of nanoribbon that overhangs a hole in the underlying holey carbon film, corresponding to the area of HRTEM image, (d), which clearly shows the random orientation of crystallinity within a nanoribbon. The interplanar distance was determined to be 0.26 nm, consistent with cubic Dy_2O_3 (400) reflections.

Fig. 4.15(a–c). The Dy_2O_3 ribbons bear similarities to other lanthanide-containing ‘belt-like’ species reported in the literature, although in these reports the obtained nanobelts are single crystalline and thicker than our nanoribbon species. For example, Hu et al. reported

the synthesis of single-crystal $\text{La}(\text{OH})_3$ nanobelts by solvothermal precipitation between $\text{La}(\text{CH}_3\text{COO})_3$ and NaOH / KOH . This surfactant-free approach produced belts up to 30 nm thick, and with widths of up to 200 nm.[150] Han et al. reported the synthesis of Ln_2O_3 ($\text{Ln} = \text{Y}, \text{Dy}, \text{Ho}, \text{Er}$) nanobelts in a stirred biphasic system. The reaction between $\text{Ln}(\text{NO}_3)_3 \cdot x\text{H}_2\text{O}$ with dodecylamine in 1-octadecene at 320 °C produced single crystal nanobelts 30–250 nm wide and 15–60 nm thick.[151] In both of these examples nanoribbons were thought to grow by ordered monomer deposition on a nanowire nuclei particle, which results in a continuous single crystal, as is evident in the HRTEM images contained within these references. Hence it is clear that just as the Ln_2O_3 nanowires in the present work grow by a different mechanism to other lanthanide-containing nanowires seen in the literature, the Dy_2O_3 nanoribbons in this thesis also grow by different mechanisms to lanthanide-containing nanoribbons currently seen in the literature.

To investigate the nanoribbon growth mechanisms, time-dependent reactions were performed. TEM images of these reactions are given in Fig. 4.16. When the reaction time was reduced to 4 hours, shorter polycrystalline ribbons (Fig. 4.16a) and poorly-defined fibrous, plate-like species (Fig. 4.16b) were obtained. Both the shorter ribbons and the fibrous plate-like species were typically $\sim 300\text{--}500$ nm in length. The plate-like particles were present as a minority species, as most of the observed material on the grid was of a ribbon morphology. The ribbons obtained from the 4 hour reaction look similar to those obtained from a 24 hour reaction, the only obvious difference is that the 4 hour ribbons are much shorter. This is similar to the difference seen between the CeO_2 nanowires obtained from time dependent reactions previously in Fig. 4.11, and would suggest that the ribbons grow via random addition of individual particles at the end of an existing nanoribbon. The presence of the secondary species (the plate-like particles) is interesting, as it appears as though the plate-like particles could represent ribbons during the early stage of ribbon formation. The ‘frayed’ edges of the plate-like species appear to represent the edges of a ribbon that have not had sufficient time to coalesce into a more uniform material. Fig. 4.11c) shows a HRTEM image from the end of a short nanoribbon, showing the polycrystalline character. Additionally, gaps could be seen in the short nanoribbon, implying that 4 hours is not long enough for complete coalescence to occur.

It should also be noted that the small, ~ 3 nm spherical particles which were abundant

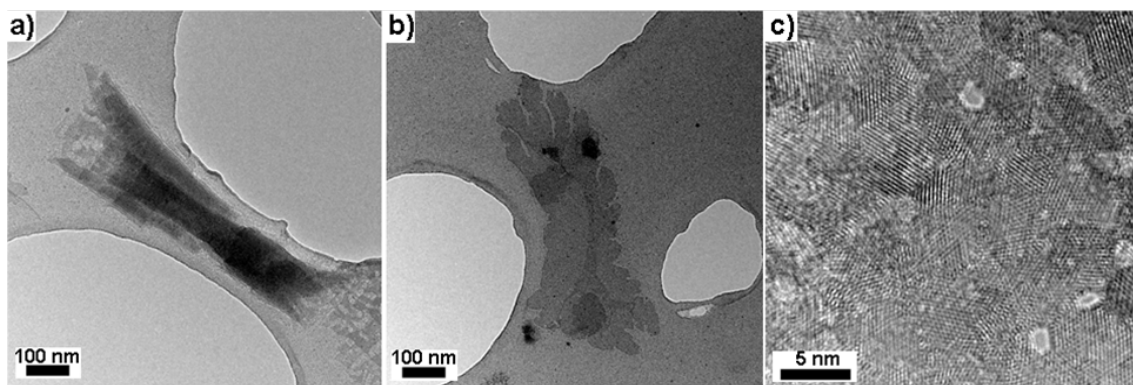


Figure 4.16: TEM images of Dy_2O_3 wires from a 4 hour reaction. a) A stack of ~ 500 nm nanobelts. b) Less well formed platelet species were found as a minority species, featuring ‘frayed’ ends. c) HRTEM image from a short nanobelt, highlighting the polycrystalline nature. Observed lattice fringes were consistent with Dy_2O_3 .

in the 4 hour CeO_2 reactions (Fig. 4.10a) were not observed for Dy_2O_3 , which would suggest that $\text{Dy}(\text{oleate})_3$ decomposition does not form isolated spherical particles, favouring instead the formation of small polycrystalline plates. However, no small polycrystalline plates were observed on the TEM grid from the 4 hour reaction, which implies that their formation and subsequent coalescence must be rapid. A formation mechanism can be proposed, based on this assumption. The first stage is the formation of small polycrystalline plates formed by $\text{Dy}(\text{oleate})_3$ decomposition. The second stage involves the rapid coalescence of these plates into the intermediate 300–500 nm species seen in Fig. 4.16b). The final stage is coalescence of the intermediate plate-like particles into the more uniform nanobelt species seen in Fig. 4.16a). Increasing the reaction time to 24 hours results in longer nanoribbon species, like those seen in Fig. 4.15. The formation and subsequent recrystallisation of polycrystalline platelet species rather than isolated spherical particles upon $\text{Dy}(\text{oleate})_3$ decomposition would account for the formation of ribbons rather than wires.

The proposed 3-stage mechanism for nanoribbon growth is different to the mechanisms cited earlier, which described single crystal growth of lanthanide containing nanobelts.[150, 151] Broadening the literature search to include non-lanthanide nanobelts reveals new formation mechanisms which should be discussed in relation to the Dy_2O_3

nanoribbons contained in this thesis. For example, Deng et al. described the formation of Sb_2O_3 nanobelts by the parallel alignment and subsequent coalescence of adjacent nanowires.[152] The coalescence of side-by-side Dy_2O_3 nanowires *could* account for the formation of Dy_2O_3 nanoribbons, although the time dependent studies (Fig. 4.16) provide no evidence to suggest that nanoribbon first proceeds by the formation of discrete Dy_2O_3 nanowires, as no isolated nanowires were observed on the TEM grid.

Another area of materials research where thin nanobelts are frequently observed is in the area of inorganic/organic composite synthesis. Composite materials such as these involve using organic molecules as spacers or scaffolds, upon which inorganic moieties can be grown. For example, Chen et al. recently described the formation of tungstate-based hybrid nanobelts by the reaction between $\text{H}_2\text{W}_2\text{O}_7 \cdot n\text{H}_2\text{O}$ and a large excess of *n*-alkylamines of various lengths ($\text{C}_m\text{H}_{2m+1}\text{NH}_2$ where $4 < m < 14$).[153] The bulky alkyl groups formed an intercalated lamellar template in which W–O layers grew. The presence of a lamellar phase was confirmed by small angle XRD, which revealed an inter-layer distance of 2.59 nm. A similar approach was taken by Gao et al., who synthesised CoSe_2 nanobelts using bulky amines as templates, again the presence of a highly-ordered lamellar phase was detected by small angle XRD.[154]

It is possible to draw comparisons with these inorganic/organic composite nanobelt examples and the lanthanide oxide species (both the nanowires and the nanoribbons) described in this Chapter. In the current system, the presence of the bulky, long-chain surfactant molecules and hydrated oleate precursors may result in the spontaneous formation of similar extended lamellar species. The channels of these mesophase species could function as constrained ‘nanoreactors’ in which anisotropic growth can occur.

The in-situ formation of constrained reaction environments is one often-cited mechanism responsible for the growth of anisotropic species, although there are numerous other mechanisms known. In the following section, some of the factors commonly believed to contribute to the growth of anisotropic species are described and their relevance to the present lanthanide oxide nanowire and nanoribbon species are assessed.

4.3.3 Factors Contributing to Anisotropic Growth

In the previous section HRTEM and time-dependent studies were used to establish that LnO_x nanowires and ribbons grow by anisotropic assembly of discrete LnO_x nanoparticles, giving rise to a unique polycrystalline product. It is now important to look at the factors responsible for this unusual mechanism. There are a number of known mechanisms by which anisotropic species form. For example, anisotropic growth of single crystal species is often rationalised in terms of an underlying anisotropy in the crystal space group. Materials with hexagonal crystal structures are commonly found to exhibit anisotropic growth. For example, the tendency of zinc oxide to form well-defined hexagonal nanorods is well documented, with preferential growth occurring along the c axis. [39, 155] Furthermore, Wang and Li demonstrated the facile synthesis of single crystalline $\text{Ln}(\text{OH})_3$ nanowires directly from solution.[45] $\text{Ln}(\text{OH})_3$ also has a hexagonal crystal structure and since Wang's initial report other examples have appeared describing anisotropic growth of single-crystal $\text{Ln}(\text{OH})_3$ structures.[156] However, our products were identified as being cubic ($Fm\bar{3}m$) CeO_2 or ($Ia\bar{3}$) Ln_2O_3 , and at present there are far fewer reports of cubic lanthanide oxides forming anisotropic species,[131] with the vast majority of literature relating to the synthesis of small particles or nanoplates.[119, 126] Furthermore, our LnO_x wires and ribbons are clearly polycrystalline, and as such the anisotropy cannot derive from crystallographic alignment of successive nanoparticles or from single-crystal growth.

An alternative explanation for the observed anisotropy is ligand-assisted templating. As we saw earlier this mechanism has been used to explain the formation of nanobelts, whereby organic molecules added into the reaction mixture acted as spacer and scaffold species, providing a template for anisotropic growth.[153, 154] It is believed that during the formation of lanthanide oxide nanowires and ribbons an analogous process occurs, involving the assembly of the bulky oleic acid and oleylamine surfactant molecules into extended lamellar species, the channels of which act as 'nanoreactors' for anisotropic growth. As oleic acid and oleylamine are two of the most common surfactants used in solution-based nanomaterial synthesis, there is already some literature evidence describing the role of surfactant assembly in non lanthanide-containing systems.

For example, Huo et al. used small angle x-ray diffraction to confirm the presence of

an oleylamine ‘mesostructure’, in which Au^+ ions were assembled in channels 4.7 nm wide. These channels acted as nanosized reactors for single-crystal growth of thin Au nanowires.[157] These remarkable nanowires were formed simply by standing a mixture of HAuCl_4 and oleylamine at room temperature for a number of days. A similar reaction was also reported by Lu et al., where Au nanowire growth was rationalised in terms of the formation of ‘polymeric strands’ of an Au-oleylamine complex.[158] Interestingly, Chen et al. reported that the shape of surfactant micelles in aqueous or organic solvent changed from spherical to cylindrical if the surfactant concentration was high enough. The cylindrical nature of these micelles was found to promote growth of FePt nanorods.[159] In Chen’s paper, 0.5 mmol of $\text{Fe}(\text{CO})_5$ and 0.25 mmol of $\text{Pt}(\text{acac})_2$ were reacted with 5 mmol OA and 15 mmol OAm — which represents a metal:OA:OAm ratio of 1:6.66:20. In the present LnO_x nanowire system the metal:OA:OAm ratio is 1:19:27, meaning that the surfactant concentration is certainly high enough to promote the formation of cylindrical surfactant micelles. In a separate study, Lacroix et al. demonstrated anisotropic growth of metallic iron nanoparticles was the result of particle nucleation and growth within a lamellar palmitic acid / hexadecylamine ‘organic superstructure’, which was generated in-situ under elevated pressure (3 atm.).[96] Mixtures of oleate and long-chain hydrocarbon solvents were shown to polymerise to give lamellar liquid crystal structures in the presence of water,[160] and Liu et al. reported the ability of lanthanide oleates to form lamellar bilayer structures.[161] Despite the range of terminology used (mesostructures, polymeric strands, organic superstructures, liquid crystals and lamellar species), it is clear that the above literature evidence is describing the same phenomenon, which is the in-situ formation of lamellar species, and the subsequent growth within these species of anisotropic nanomaterials.

Given the structural similarities between the long-chain molecules used as surfactants and solvents in nanoparticle synthesis and the long-chain molecules used in the formation of liquid crystal displays and detergents, it is not surprising that the in-situ formation of lamellar species has been used to explain anisotropic nanomaterial growth. In our nanowire system, it is proposed that the pressurised, un-stirred conditions of the autoclave encourage similar organization of water, oleylamine, oleic acid, free oleate and octyl ether into extended lamellar structures that act as constrained reactive pockets that promote

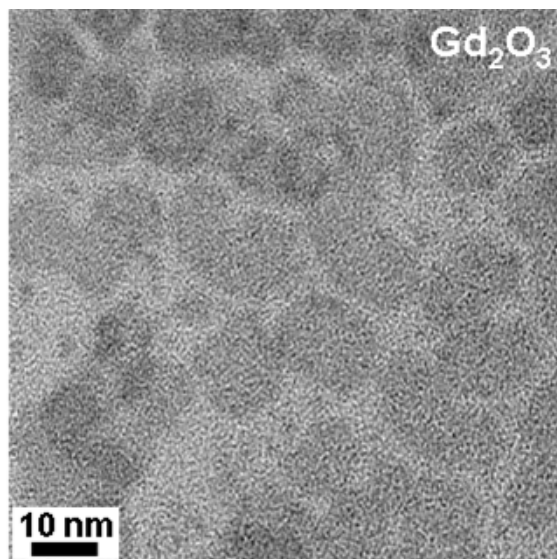


Figure 4.17: TEM image of the nanoparticle species obtained under stirred reflux conditions.

anisotropic self-assembly.

Additional reactions were performed to test the above hypothesis. These experiments were designed to evaluate to what extent the contributions of the autoclave reaction environment and the solvent/surfactants had on the final product morphology, as it was anticipated the lack of stirring and pressurised reaction vessel were the most important factors. To examine the effect of pressurisation on product morphology, the reaction was repeated in an unsealed flask, maintained at ambient pressure. The reaction was performed with and without stirring. It was found that stirred conditions produced thin nanodisks (Fig. 4.17) similar to those seen elsewhere.[119] Un-stirred conditions failed to produce nanoparticles, forming instead micron-sized agglomerates (not shown).

These results suggest that elevated pressures are necessary to form and maintain lamellar structures within the reaction vessel, and that unstirred conditions at ambient pressure are unable to sufficiently stabilise the species formed with Ln oleate decomposition. Similarly, it was found that reactions performed in an unsealed autoclave (so as to prevent pressurisation) did not produce nanowires, and only small particles were formed, Fig. 4.18.

At this point it is important to note that the autoclave pressure during nanowire synthesis is modest, since none of the principal reagents boil below the reaction temperature

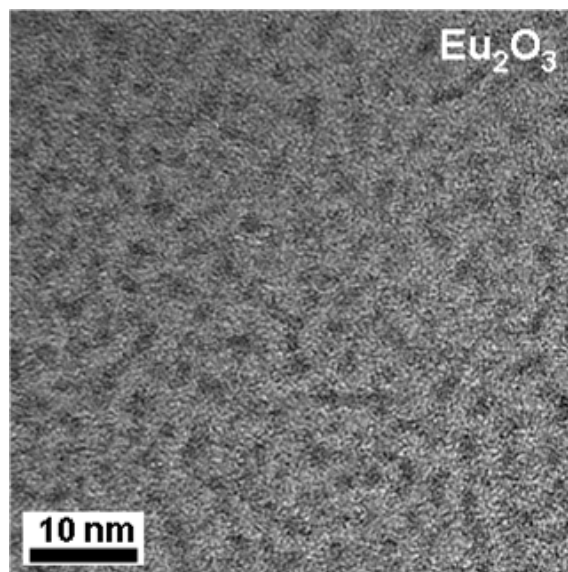


Figure 4.18: TEM image of the nanoparticle species obtained under unsealed autoclave conditions.

of 200 °C. However, as we saw in section 4.3.1 thermogravimetric analysis data indicate that the oleate precursors include small quantities of water of crystallization, typically of order $\text{Ln}(\text{oleate})_3 \cdot 3 \text{H}_2\text{O}$ in addition to residual water not removed during the separation phase of oleate synthesis (Fig. 4.2). Furthermore, it was reported by Wu et al. that a condensation reaction between oleylamine and oleic acid will result in the formation of the amide (*N*-(*cis*-9-octadecenyl)oleamide) and water.[162] As the nanowires and ribbons are formed in a sealed system at 200 °C, the presence of water in the autoclave, (either residual or crystallisation water from the oleate precursor or from the condensation between oleic acid and oleylamine), will contribute to the internal pressure of the autoclave as well as potentially causing the spontaneous assembly of the hydrophobic solvent/surfactant molecules into lamellar species.

The van der Waals gas equation (Eq. 4.1) was used to estimate the internal pressure of the autoclave during nanowire synthesis. The minimum and maximum pressures were calculated assuming either:

- Only the water of crystallisation contributes to pressure (1.5 mmol water, based on using 0.5 mmol of $\text{Ln}(\text{oleate})_3 \cdot 3 \text{H}_2\text{O}$ per reaction).
- Both the water of condensation and crystallisation contribute to pressure (11 mmol water, 1.5 mmol from oleate precursor plus 9.5 mmol from acid and amine conden-

sation).

Then using:

$$P = \frac{nRT}{V - nb} - \frac{n^2V}{a^2}, \quad (4.1)$$

and assuming: $n = 0.0015$ moles for the crystal water only contribution, or $n = 0.011$ moles for the combined crystal and condensation water contributions, $V = 0.003$ L (derived from 12 mL autoclave volume minus 9 mL solvent volume, assumes solvent is non-compressible), $R = 0.08206$ L atm K⁻¹ mol⁻¹, $T = 473$ K, $a = 5.459$ L² atm mol⁻² and $b = 0.03049$ L mol⁻¹, we obtain minimum and maximum reaction pressure values of 18 atm and 86 atm respectively.

Further control reactions were performed to determine the effect of additional water on nanowire formation. An additional 2 mL H₂O (111 mmol) was added to the autoclave prior to reaction, which would substantially increase the reaction pressure. These reactions also yielded nanowires (Fig. 4.19), thereby indicating that the presence of water and even higher pressures are not detrimental. Hence the hydration level of the initial oleate precursor is not a significant factor.

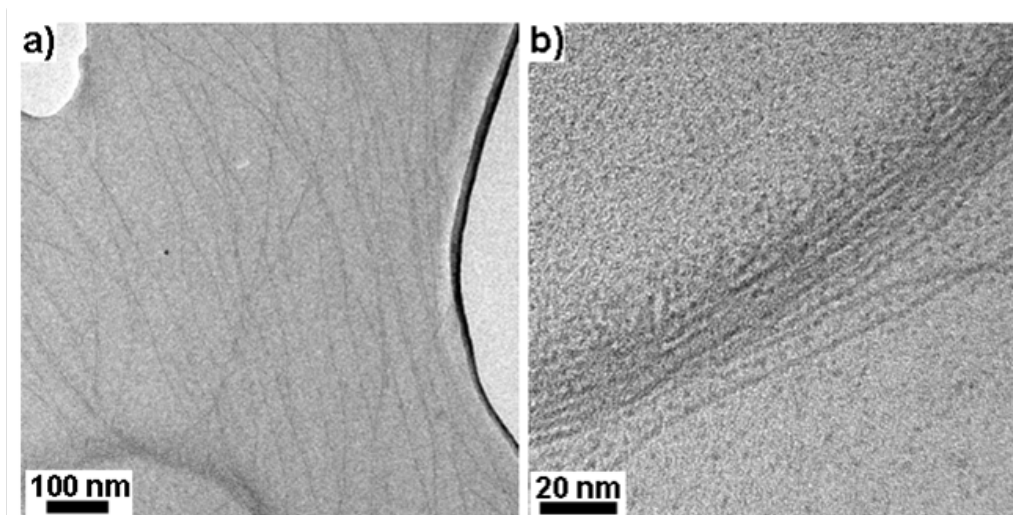


Figure 4.19: Low magnification (a) and high magnification (b) TEM images of Gd₂O₃ nanowires from a reaction performed with 2 mL additional water added.

It was also found that replacing dioctyl ether with a bulkier solvent such as benzyl ether worsened wire quality, and a mixture of wires and ‘necklace’ agglomerates were formed instead, Fig. 4.20. This is presumably since bulky benzyl ether molecules will

disrupt the packing of oleic acid and oleylamine, resulting in disrupted lamellar species. Anisotropic growth will be hindered in these poorly-defined surfactant complexes, resulting in the poorly defined nanowires seen in Fig. 4.20. The necklace agglomerates bear similarities to those seen elsewhere, which are formed in the early stages of growth of FePt and CdTe nanowire growth. [40, 51]

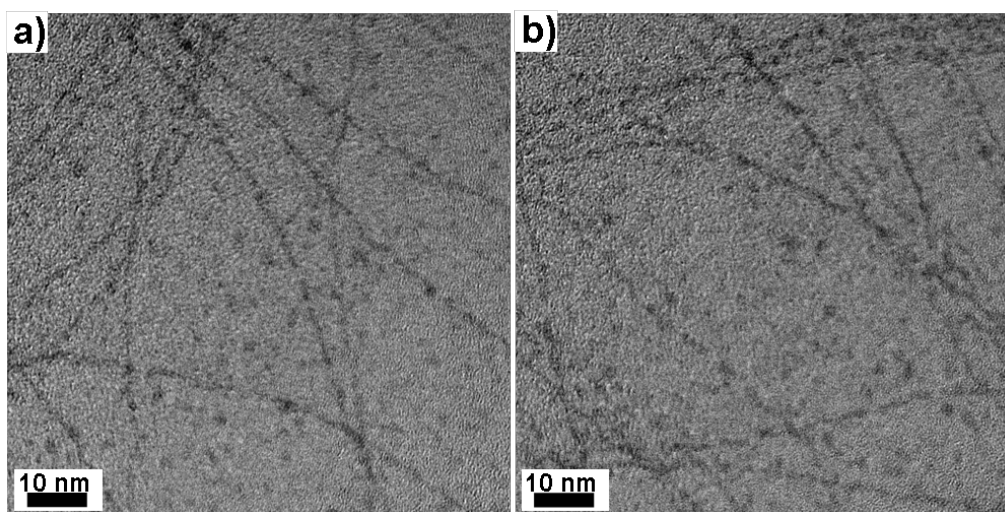


Figure 4.20: Additional TEM pictures of Gd_2O_3 wires obtained when benzyl ether was used instead of dioctyl ether. Broken and crooked regions in the wires can be seen, indicative of a poorly defined reaction environment in which coalescence between adjacent particles is inadequate.

Together, these observations indicate unambiguously that the combination of elevated pressure, unstirred reaction conditions and logical solvent choice is essential to the formation of templating superstructures and subsequent assembly of discrete nanoparticles into nanowires. It was also found that the precursor plays an important role in forming anisotropic Ln_2O_3 species, as the use of any precursor apart from an *f*-block oleate did not produce Ln_2O_3 nanowires, as described below.

The Use of Non- $Ln(\text{oleate})_3$ Precursors

Additional reactions were performed to determine if nanowires could be obtained using other precursors. However, it was found that nanowire formation is unique to lanthanide oleates. Decomposition of other lanthanide containing precursors under autoclave conditions did not produce nanowires. For example, exchanging $Gd(\text{oleate})_3$ for

$\text{Gd}(\text{NO}_3)_3 \cdot 6\text{H}_2\text{O}$ yielded large single-crystal nanorods, which XRD confirmed to be hexagonal $\text{Gd}(\text{OH})_3$ (space group $P63/M$), Fig. 4.21. These nanorods were considerably larger than the Gd_2O_3 wires obtained using the oleate precursor, with thickness of 150–200 nm, two orders of magnitude larger than the Gd_2O_3 wires. These $\text{Gd}(\text{OH})_3$ nanorods are very similar to those reported by Hemmer et al.[117] In this instance, anisotropic growth is rationalised in terms of the hexagonal crystal structure which, as explained earlier, is a contributing factor to nanorod and wire growth.

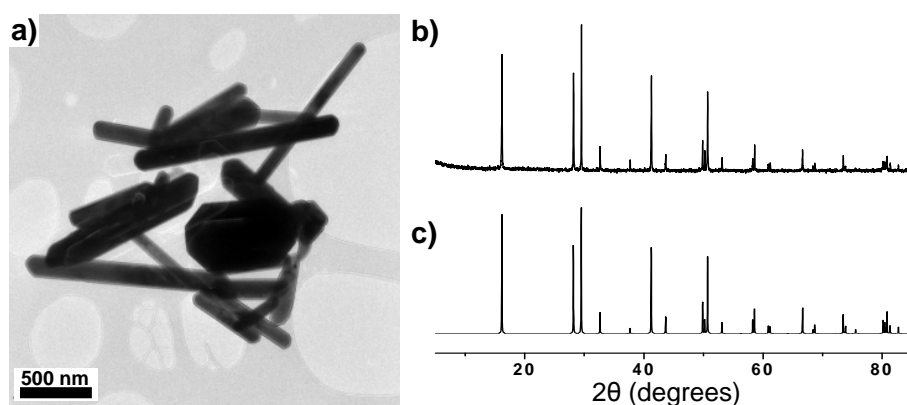


Figure 4.21: a) TEM image of gadolinium hydroxide nanowires obtained from autoclave decomposition of $\text{Gd}(\text{NO}_3)_3 \cdot 6\text{H}_2\text{O}$. (b) Obtained and (c) expected XRD spectra for $\text{Gd}(\text{OH})_3$ (PDF card number 83-2037).

The formation of $\text{Gd}(\text{OH})_3$ instead of Gd_2O_3 can be explained in terms of the ligands surrounding the two lanthanide-containing precursors. The carboxylate oleate group which surrounds the $\text{Gd}(\text{oleate})_3$ precursor forms Gd-oxide monomers upon decomposition (the formation of oxide nanospecies by carboxylate decomposition was discussed in Chapter 1), yet the $\text{Gd}(\text{NO}_3)_3 \cdot 6\text{H}_2\text{O}$ precursor forms Gd-OH subunits, due to the proximity of the 6 H_2O molecules surrounding every Gd^{3+} ion.

Attempts to form anisotropic species using non lanthanide precursors were unsuccessful. For example, a d-block oleate precursor reacted under identical reaction conditions yielded spherical particles. Autoclave decomposition of an iron oleate complex resulted in 9.3 ± 2.2 nm (24%) spherical iron oxide particles, shown in Fig. 4.22.

The rapid growth of large $\text{Fe}_2\text{O}_3/\text{Fe}_3\text{O}_4$ particles is reported routinely [31] and compares with the general observation that lanthanide oxide nanoparticles are small, such as the 3 nm diameters reported here, and slow to grow.[128, 132] The most likely reason

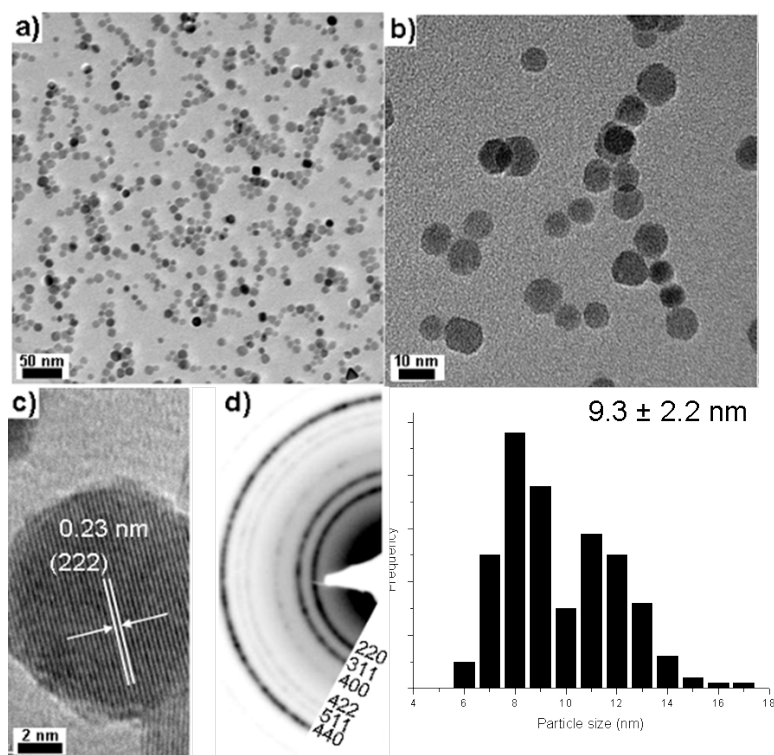


Figure 4.22: (a,b) TEM images of Fe_3O_4 nanoparticles obtained from the autoclave decomposition of Fe oleate under otherwise identical conditions to those used for lanthanide oxide nanowire synthesis. (c) A HRTEM image of a single Fe_3O_4 NP, with (d) the corresponding ED pattern for a sample of the particles. (e) Corresponding size distribution.

why self-assembly is not observed when using iron oleate is that larger particles have a lower proportion of surface atoms, hence the overall free surface energy of the system will be lower for the larger iron oxide particles than the smaller lanthanide oxide particles. As such, coalescence of small LnO_x particles is favoured as the proportion of surface atoms will be reduced, i.e.: the driving force towards self-assembly reduces as the size of individual nanoparticles increases and they become better stabilized by surfactants. Furthermore, the rapid growth of large iron oxide particles may occur on a time-scale shorter than that of the formation of templating superstructures, meaning stable iron oxide particles are formed before the architecture required for anisotropic growth has been formed.

The above discussions show that there are many factors which contribute to the formation of lanthanide oxide nanowires and nanoribbons, which can be rationalised in terms of anisotropic growth within lamellar species which form spontaneously in the reaction vessel. The interesting ‘imperfect oriented attachment’ mechanism by which the nanowires and ribbons grow yields an interesting polycrystalline product. As these polycrystalline assemblies are inherently different to their single crystalline counterparts, magnetic and optical studies were performed on selected Ln_2O_3 samples to determine if they possessed unusual physical properties. The data from these measurements are provided in the following section.

4.4 Physical Properties of Ln_2O_3 Nanowires and Ribbons

4.4.1 Magnetic Characterisation

Magnetic measurements for Gd_2O_3 nanowires and Dy_2O_3 nanoribbons were collected on a Quantum Design superconducting quantum interference device (SQUID) in the 2–290 K temperature range. Samples were prepared as described in Chapter 2.

Gd_2O_3 Magnetic Data

Bulk monoclinic and cubic gadolinium oxides are paramagnetic at room temperature, and become antiferromagnetic on cooling with a Néel temperature (T_N) of around 17.2 K. [163] Nanoscale Gd_2O_3 is reported to be essentially paramagnetic, showing neither remnant magnetisation or coercivity in hysteresis measurements nor evidence for the blocking temperature (T_B) in field cooled measurements.[112] One exceptional report by Huang et al. showed that the presence of trace carbon residue could render hollow Gd_2O_3 nanospheres superparamagnetic, with $T_B = 135$ K.[164] However, after removing the carbon residue, the hollow spheres became paramagnetic.

Magnetic measurements for the Gd_2O_3 nanowires are given in Fig. 4.23. The field cooled curve is given in Fig. 4.23(a). Field cooled and zero-field cooled curves are essentially super imposable, with no divergence at low temperature. Hence there is no evidence of a blocking temperature down to 2 K. The inverse susceptibility ($1/\chi$) plot is shown inset, showing Curie-Weiss behaviour of the Gd_2O_3 nanowires. The sample is

weakly antiferromagnetic with $\theta \approx -3.2$ K, which is below that of the bulk material (reported as being between -17 ± 2 K and -16 K), [165, 166] though θ tending to zero has previously been reported for nanocrystalline Gd_2O_3 . [112] A recent report by Mutelet et al. examined the effect of Gd_2O_3 particle size on the Néel temperature, T_N . In this paper it is shown that T_N is strongly dependent on particle size. For example, for particle sizes < 4 nm, the Néel temperature is close to 2 K, whereas for larger particles (≈ 60 nm) T_N is 18.2 K. [163] These findings are consistent with our observations. From HRTEM measurements we know the Gd_2O_3 nanowire sub-unit particle size is ≈ 3 nm (Fig 4.4), which would mean $T_N < 2$ K, which is lower than the minimum temperature attainable for SQUID measurements. From this we can conclude that the Gd_2O_3 nanowires have similar magnetic properties to the isolated ~ 3 nm Gd_2O_3 particles previously reported in the literature.

The magnetisation versus field curve of the Gd_2O_3 nanowires at 5 K is given in Fig. 4.23(b). The Gd_2O_3 nanowires display little or negligible coercivity and remnant magnetisation, confirming that the nanowires are paramagnetic. Saturation magnetisation (M_{sat}) was calculated to be 77 emu g^{-1} , which is in agreement with the $70\text{--}75 \text{ emu g}^{-1}$ values reported previously. [112] The magnetic data show that despite the unusual morphology of the Gd_2O_3 nanowires, no significant deviation from the previously reported magnetic behaviour of small Gd_2O_3 nanoparticles is observed. This is perhaps due to the random orientation of sub-units within a nanowire, so that any benefit gained from an ordered, linear assembly of nanoparticles is lost. It is possible that annealing the nanowires at high temperatures may force the complete recrystallisation of Gd_2O_3 nanowires into micron-long single crystal nanowires, which may show more interesting magnetic behaviour due to their structural anisotropy.

Dy_2O_3 Magnetic Data

The field cooled (FC) curve for Dy_2O_3 is given in Fig. 4.24. The FC curve shows that the Dy_2O_3 nanoribbons are paramagnetic down to 2 K, which is in agreement with literature observations that nanoscale Dy_2O_3 is paramagnetic. [114, 167–170] Inset is the inverse susceptibility, showing the Curie-Weiss behaviour of the sample. The Weiss constant was calculated to be $\theta \approx -0.56$ K, which is smaller than that of the bulk ($\theta = -17$ K). [171,

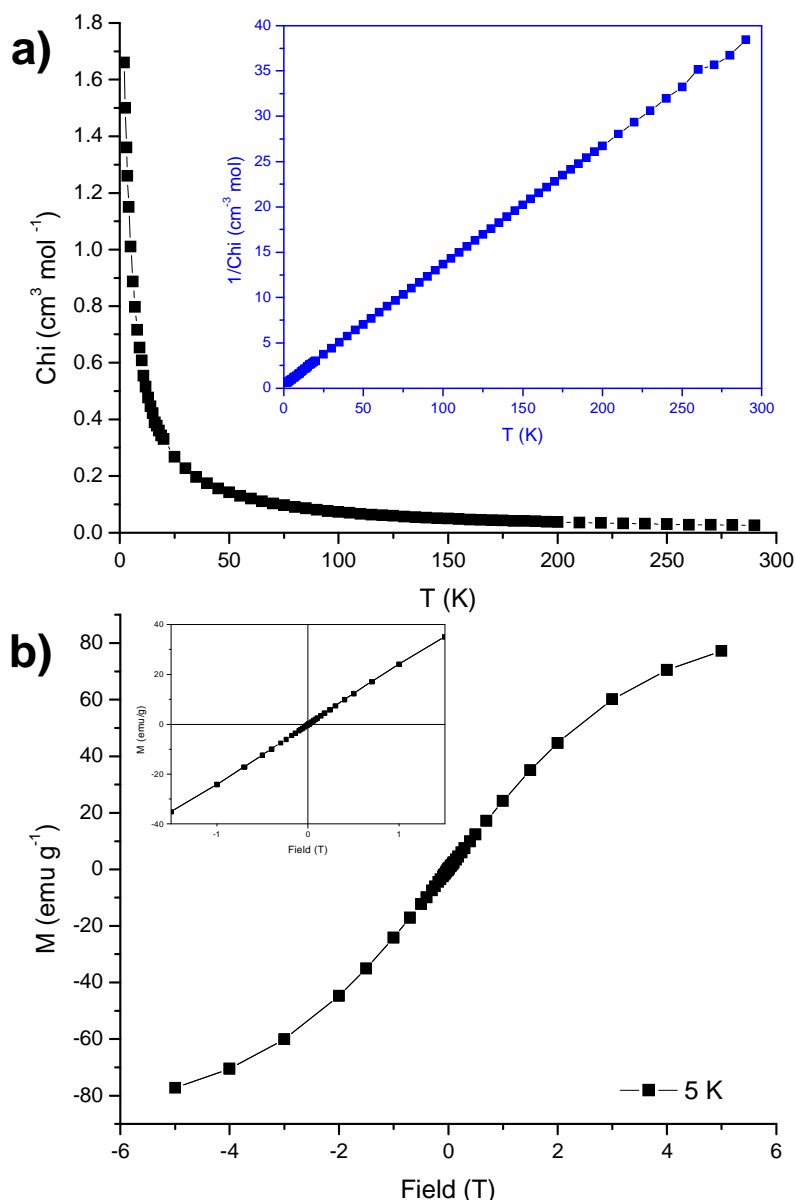


Figure 4.23: (a) FC curve for Gd_2O_3 nanowires (2–290 K). Inset is the inverse susceptibility, from which the Weiss constant was calculated to be $\theta \approx -3.2$ K. (b) Magnetization (emu g^{-1}) versus Field (T) for Gd_2O_3 nanowires collected at 5 K. Inset is a magnification of the region near the origin.

172] It is thought that the value of θ close to zero is a consequence of the small particle size, mirroring the trend seen for the Gd_2O_3 nanowires above. Unfortunately, due to insufficient liquid helium it was not possible to record magnetisation versus field curves for this sample.

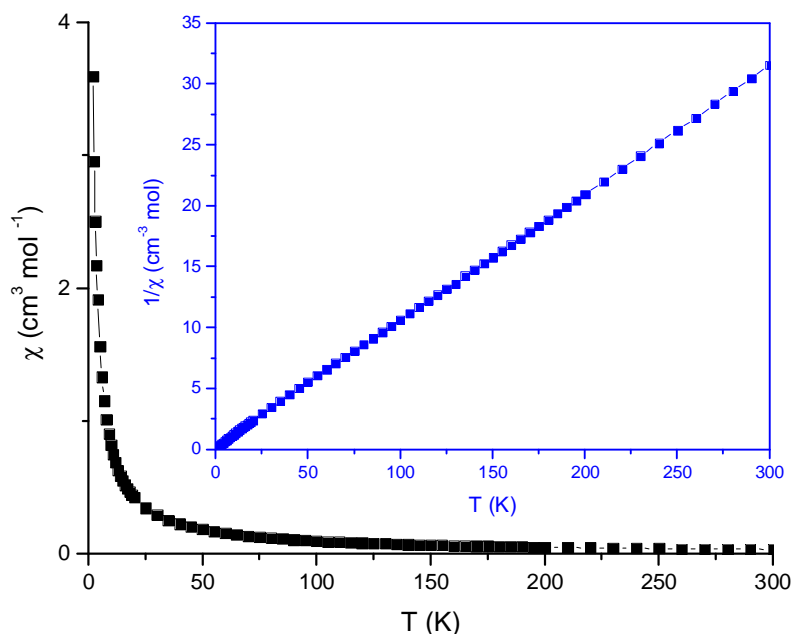


Figure 4.24: FC curve for Dy_2O_3 nanowires (2–290 K). Inset is the inverse susceptibility, showing the Curie-Weiss behaviour of the sample. The Weiss constant was calculated to be $\theta \approx -0.5$ K.

4.4.2 Optical Characterisation

Eu_2O_3 Optical Data

Room temperature photoluminescence measurements were recorded on a Edinburgh Instrument FLS920 spectrofluorometer by Dr. Rafael Valiente (Universidad de Cantabria). The spectra were corrected for the response of the detection system. Excitation spectra for the Eu_2O_3 nanowires and bulk Eu_2O_3 are provided in Figs 4.25 and 4.26. The main difference between bulk and nanoscale Eu_2O_3 is the pronounced broad absorption/excitation band at ≈ 330 nm, the origin of which is not completely understood. This band was not observed in the excitation spectra of commercial, surfactant free Eu_2O_3 nanoparticles,[173] yet is present in Eu^{3+} -doped SiO_2 glasses and is indicative of a disordered crystal structure.[174] A similar peak was previously observed in $\text{Gd}_2\text{O}_3:\text{Eu}^{3+}$ doped particles, and was designated a O^{2-} to Eu^{3+} charge transfer band.[156, 175] In our system, the band could arise from d–f transitions of small traces of Eu^{2+} , or from the surfactants used in the synthesis route. The broad band at 330 nm mostly blocks the absorption edges seen for the bulk sample in the 350–410 nm region, which are the

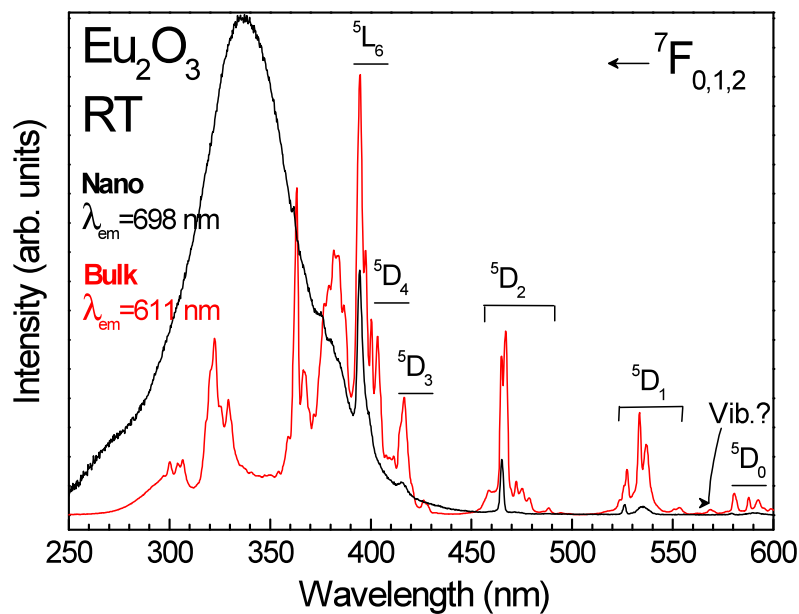


Figure 4.25: Excitation spectra of bulk (red) and nanowires (black) Eu_2O_3 at room temperature.

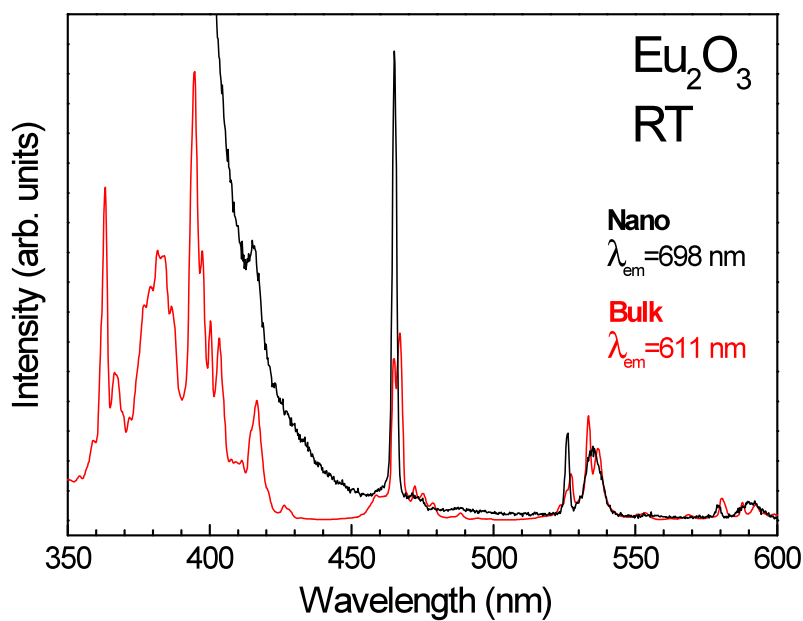


Figure 4.26: Expansion of the 350–600 nm region of Fig. 4.25 — the excitation spectra of bulk (red) and nanorods (black) Eu_2O_3 at room temperature.

${}^7\text{F}_J \longrightarrow {}^5\text{L}_6$ transitions.[176]

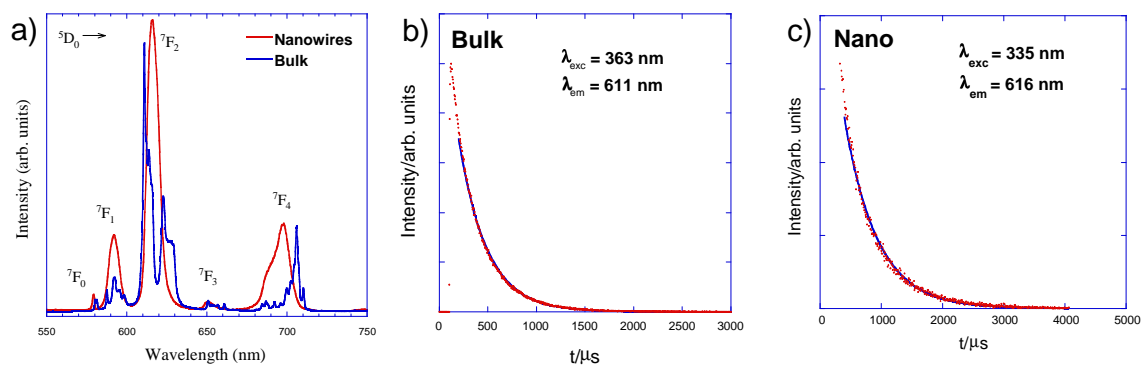


Figure 4.27: a) Emission spectra of Eu_2O_3 nanowires (red) compared with that of bulk Eu_2O_3 (blue). The emission peaks correspond to transitions from the $^5\text{D}_0 \rightarrow ^7\text{F}_J$ ($J = 0-4$). b,c): Temporal decay of the luminescence intensity for Eu_2O_3 in the bulk (b) and nanowires (c). The solid lines correspond to the least square fittings to the experimental data to the equation: $I(t) = I_0 \exp(-t/\tau)$ with $\tau = 290 \mu\text{s}$ and $533 \mu\text{s}$ for bulk and nanowires, respectively.

The emission spectra (Fig. 4.27a) contains several distinct peaks, which can be assigned to the $^5\text{D}_0 \rightarrow ^7\text{F}_J$ transitions, for $J = 0, 1, 2, 3, 4$. Our nanowire PL spectra are consistent with those previously recorded for nanoscale cubic ($Ia\bar{3}$) Eu_2O_3 species,[111, 125, 127, 176] and the cubic crystal phase of the bulk Eu_2O_3 was confirmed by XRD (data not shown). The most noticeable difference between both spectra is that the emission lines of the nanowires are broader than those of the bulk material, which is consistent with the presence of the disordered crystalline regions comprising the nanowire. Another salient feature is that the lifetime associated with the $^5\text{D}_0 \rightarrow ^7\text{F}_2$ Eu^{3+} emission, which is very sensitive to energy transfer mechanisms between ions located in crystal sites with different local symmetry, is significantly larger in the nanowires ($\tau = 533 \mu\text{s}$) than in the bulk ($\tau = 290 \mu\text{s}$), shown in Fig. 4.27b,c). An increase of lifetime upon reducing particle size was previously observed in Eu^{3+} -diluted samples.[177, 178] An increase in lifetime was observed in nanocrystals smaller than the emission wavelength and it is attributed to the change of the refractive index of the medium around emitting Eu^{3+} ions (which is air in the present nanowire system). A reduction of decay lifetime was reported upon increasing the Eu^{3+} concentration;[179] at high concentration, the interaction mechanisms that depend on the distance between Eu^{3+} ions increases the migration of the excitation energy between them, which leads to energy transfer quenching impurities[180] that decrease the

emission intensity and shortening the measured lifetime.[181] The high disorder observed in the polycrystalline nanowires prevents the energy migration and the consequent transfer to killer impurity traps, thus increasing the emission lifetime when compared to the bulk. The increase of the lifetime has previously been attributed to confinement of the excitation within the nanocrystal.[176]

4.5 Conclusions and Further Work

A versatile method for the fabrication of ultra-thin lanthanide oxide nanowires and ribbons with high aspect ratios is presented. The method involves the autoclave decomposition of a pre-formed lanthanide oleate precursor at elevated temperatures in the presence of a high boiling point solvent (dioctyl ether) and surfactant molecules (oleic acid and oleylamine). The obtained nanomaterials are interesting due to their unique morphologies: high aspect ratio CeO_2 and Ln_2O_3 nanowires and ribbons have rarely previously been seen in the literature. HRTEM reveals the obtained nanowires (or nanoribbons, in the case of Dy_2O_3) to be predominately polycrystalline, with constituent sub-units randomly orientated along the length of each wire. HRTEM also revealed a clear decrease in wire thickness with increasing lanthanide atomic number, which is attributed to an increase in stability of the oleate precursor for the later series lanthanides, and also a decrease in unit cell parameters as a consequence of the lanthanide contraction. Time dependent studies reveal the wires to form in a three-stage decomposition/assembly/recrystallisation process, whereby the small particles formed by initial precursor decomposition assemble into linear chains which subsequently recrystallise into nanowires and nanoribbons. This process is described as ‘imperfect oriented attachment’ — a modification of the established oriented attachment mechanism. Anisotropic self assembly is explained in terms of wire growth within constrained lamellar species that form *in-situ* in the autoclave, which can be disrupted by using bulky solvents, stirring the reaction mixture or performing the reaction at ambient pressure.

There is plenty of scope for further work in the present nanowire system. It may be possible to create nanowires of mixed lanthanide oxides, simply by using a mixture of oleates in the reaction vessel. In turn, the optical and magnetic properties of these doped

materials could be studied and compared with their un-doped counterparts. The distribution of dopant ions could in turn be measured and mapped using STEM techniques. As the magnetic data for the Gd_2O_3 nanowires is similar to literature data for discrete Gd_2O_3 nanoparticles, annealing of the wires should be considered as a way of extending the crystalline regions of the nanowire. Decreasing the polycrystallinity may have an impact on the magnetic properties of Gd_2O_3 nanowires and the Dy_2O_3 nanoribbons.

Chapter 5

Metal carboxylate complexes as precursors for metal oxide nanoparticles

5.1 Introduction

As demonstrated in Chapters 3 and 4, solution-based syntheses are a robust and versatile way to produce NPs with a variety of different morphologies and physical properties. We have seen that the sensitivity of NP syntheses is such that even modest changes in reaction protocol can have significant impact on the particle nucleation and growth processes, meaning wildly different product morphologies can arise as the result of relatively minor changes to the synthetic procedure. For example, in Chapter 3 we saw that subtle changes to the structure of the solvent (such as increasing the length of an alkyl side chain) yielded ‘compound’ particles that grew by completely different mechanisms to those obtained for structurally similar solvents. In Chapter 4 the importance of the reaction environment on particle growth mechanisms was discussed, with the conditions enabled by using an autoclave yielding a product that was unobtainable using a conventional reflux set-up. In the present Chapter another aspect of solution based NP synthesis will be investigated, which is the role of the carboxylate precursor in the reflux synthesis of metal oxide NPs.

As described in Chapter 1, the reflux method (also known as the ‘heating-up’ or thermolysis method) is similar to the autoclave approach as it arrives at a nanoparticulate

product by decomposing a metal containing precursor in a solution of high boiling point solvent and surfactant molecules. However, the reflux method differs to the autoclave approach in that the reaction mixture can be magnetically stirred, and higher temperatures can be reached (the Teflon liner of an autoclave cannot safely be heated above 220 °C, whereas a reflux reaction is limited only by the boiling point of the solvent).

These relatively minor differences are advantageous because; firstly, a stirred reaction mixture will have a homogeneous reagent distribution, and so it is easier to synthesise a uniform population of particles (the difficulties associated with creating uniform iron oxide particles by the autoclave method were discussed in Chapter 3, for example). Secondly, being able to access higher reaction temperatures can allow one to control the NP growth rate — which is dependent on monomer consumption and is proportional to the reaction temperature.[31] As this chapter relates to using various carboxylate precursors as starting materials in the synthesis of metal oxide NPs this second point is particularly advantageous, as accessing temperatures above 220 °C means that hold steps can be used for precursors which do not decompose at or below 220 °C — which is true for some of the precursors we will discuss in this Chapter.

It was decided that the role of the carboxylate precursor in NP synthesis would be investigated as it is clear after searching the available literature that there are many reports which study the role of variables such as surfactant type, reagent ratios and reaction heating profiles on the morphology of metal oxide NPs, yet there is considerably less research which investigates the impact that the precursor has on the final particle morphology. Indeed, in the field of metal oxide NP synthesis there is a surprisingly small repertoire of metal-containing precursors that are used, with choices limited largely to mononuclear (with respect to metal nuclei) and structurally simple carboxylate complexes such as formates,[182] acetates,[119] acetylacetonates,[23, 183] and fatty-acid complexes. [31, 57] This limited range is surprising, given that the precursor plays an important role in NP synthesis, and is more than just a source of metal atoms. This is because particle nucleation is influenced by the decomposition characteristics of the precursor, as NP nuclei and monomer production is dependent on factors such as the rate and temperature at which a precursor decomposes.[24, 31, 32] These are physical properties that are dependent on the molecular structure of the precursor, and are determined by the

surrounding ligands and the size of the precursor molecule.

Furthermore, the coordinating ligands present in the precursor may be able to impart new growth kinetics to the particles. As we saw in Chapter 3, the final shape of magnetite particles obtained using the autoclave route was heavily dependent on the solvent used, since solvents capable of chelating to the particle surface could perturb the adsorption dynamics of the surfactants present in the reaction mixture. It was shown that subtle variations to the molecular structure of the solvent yielded significantly different particle morphologies. By extension, it is possible that the ligands present in a metal containing precursor may be able to coordinate to the surfaces of particles — perturbing surfactant adsorption or acting as molecular capping agents — thereby giving rise to new growth mechanisms or particle morphologies. It has been shown previously that the presence of small carboxylate molecules in the reaction mixture can result in different particle growth kinetics. For example, Kim et al. recently showed that large (80–160 nm) magnetite nanocubes could be obtained by the decomposition of $\text{Fe}(\text{acac})_3$ in a mixture of BE and OA. The authors showed that by adding the small carboxylate molecule 4-biphenylcarboxylic acid into the reaction mixture, cube growth could be curtailed and smaller 22 nm magnetite cubes were obtained.[184] The formation of smaller cubes implies that fast growth in the $\langle 111 \rangle$ direction is occurring, which may be due to competitive adsorption between 4-biphenylcarboxylic acid and OA binding to the $\{100\}$ surfaces (as the affinity of the acid group for these surfaces is well-known). If the small 4-biphenylcarboxylic acid molecules bind to the particle surface in place of OA then the $\{111\}$ surfaces are less sterically hindered by large OA molecules, and it is easier for monomers to approach and precipitate on the $\{111\}$ surfaces. Rapid, kinetically controlled growth of the $\{111\}$ surfaces will result in smaller cubes. Conversely, the larger cubes obtained in the absence of 4-biphenylcarboxylic acid implies that growth of the $\{111\}$ surfaces is slower, due to the larger number of OA molecules on the $\{100\}$ faces, which hinder the approach and precipitation of monomers on the particle surface.

The work of Kim et al. shows that small carboxylate molecules can have a significant impact on the final morphology of a particle and provides justification for the work contained in the present Chapter, which investigates the role of the ligands present in the compounds used as NP precursors. The role of the carboxylate ligand and secondary pre-

cursor ligands in NP growth has been largely overlooked by the nanoparticle community, so the present work represents an interesting addition to the field.

In this Chapter a series of polynuclear metal-carboxylate complexes are examined as precursors for metal oxide particles. A number of trinuclear manganese and iron complexes with the general formula $[M_3O(O_2CR)_6L_3]$ (where $M = Mn, Fe$) were prepared, which featured different ligands surrounding the metal centres, see Fig. 5.1. The complexes were chosen so that coordinating ligands not commonly used in NP synthesis such as pivalate (piv), pyridine (py), imidazole (HIm), benzoate (benz) and 2-phenoxybenzoate (phbenz) could be used alongside more 'traditional' ligands, such as acetate (OAc), thereby allowing the role of each ligand to be investigated systematically. These ligands are capable of binding to the particle surface during particle growth, and like 4-biphenylcarboxylic acid used by Kim et al. (as described above), may be able to impart new growth kinetics and give rise to new particle shapes. Additionally, larger hexanuclear and dodecanuclear carboxylate complexes were prepared to ascertain how larger molecules behaved during NP synthesis. The chosen complexes are ideal candidates for this study as they are structurally more complicated than the mononuclear molecules conventionally used as NP precursors yet can easily be prepared using inexpensive, innocuous and readily available starting materials.

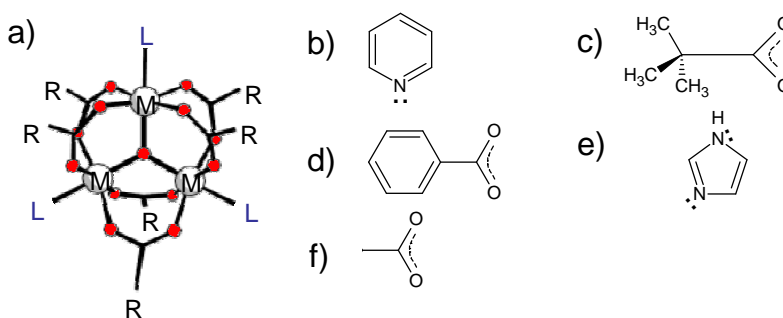


Figure 5.1: a) Generic structure of the $[M_3O(O_2CR)_6L_3]$ precursor, showing the positions of the metal centres (M), carboxylate ligands (O_2CR), secondary ligands (L) and oxygen atoms (red). The ligands used were b) pyridine, c) pivalate, d) benzoate, e) imidazole and f) acetate. Structure in a) adapted from reference [1].

The majority of the work reported in this Chapter relates to the preparation of manganese oxide NPs from manganese carboxylate precursors. There is a brief discussion at

the end of this Chapter which describes the preliminary results of iron oxide NP synthesis using iron carboxylate precursors, which is included as a proof of concept that polynuclear complexes containing other transition metals can be used in NP synthesis. The preparation of the manganese carboxylate precursors and their subsequent decomposition into manganese oxide nanoparticles is discussed in the following section.

5.2 MnO_x Nanoparticles From Mn-carboxylate Clusters

Nanoscale manganese oxides represent an interesting sub-class of nanomaterial, as MnO_x NPs have range of potential applications. For example, the redox chemistry associated with manganese means MnO_x NPs have applications in catalysis.[185, 186] The magnetic moment associated with the Mn²⁺ and Mn³⁺ ions means that MnO_x NPs also have applications in MRI, MFH and as bio-labelling agents.[42, 57] Recently, there has been a surge of interest in manganese oxide NPs due to the unusual exchange-bias magnetic behaviour observed in MnO/Mn₃O₄ core/shell particles.[187, 188] The magnetic properties of MnO_x particles will be discussed in more detail in section 5.4.5. Previous solution-based MnO_x NP syntheses have utilised mononuclear Mn complexes such as formates,[189] acetates,[190] acetylacetonates[23] and fatty acids[37, 50] as precursors. At the time of writing there are only a few low-key reports which examine the possibility of using larger Mn-containing molecules as precursors in MnO_x NP synthesis. The well known polynuclear cluster [Mn₁₂O₁₂(OAc)₁₆(H₂O)₄] · 2 AcOH · 4 H₂O (Mn₁₂-acetate [191]) and its derivatives were recently used to prepare MnO nanoparticles in solid-state decomposition reactions.[192] Large MnO agglomerates were obtained, with the shape and size of the agglomerates dependent on the reaction conditions. Interestingly, the morphology of the product could be changed by varying the carboxylate ligand used when synthesising the precursor. The authors showed it was possible to synthesise micron-sized spherical, pseudo-cubic and rhombic dodecahedral particles by using the corresponding Mn₁₂-acetate, Mn₁₂-phenylformate and Mn₁₂-phenoxyacetate clusters as starting materials, with the different particle morphologies arising as a consequence of the different thermolysis environments.[192] This shows that the ligands that surround metal atoms can directly influence the particle growth mechanisms, at least in the solid

state. Mn_{12} -acetate was again used as a precursor in a solid state reaction by Folch et al. who synthesised Mn_3O_4 particles by calcination of an ordered silica template that had been functionalised with Mn_{12} -acetate molecules.[193] The same group also reported the autoclave-based decomposition of Mn_{12} -acetate in basic solution, to yield MnOOH rods several microns in length.[194] These few examples show that polynuclear complexes are flexible precursors to NP synthesis, and that the final morphology of the product can be influenced by the ligand structure of the complex. Despite these compelling observations, there has been a surprising lack of interest into the possibility of using similar molecules as precursors during the solution-based reflux synthesis of metal oxide NPs, which the following sections aim to address. In the present work the MnO_x precursor repertoire was expanded to include a number of trinuclear complexes based on the $[\text{Mn}_3\text{O}(\text{O}_2\text{CR})_6\text{L}_3]$ motif, synthesised using a host of different ligands. Larger hexanuclear and dodecanuclear complexes were also studied as potential precursors, to determine the effect of cluster size on NP formation mechanisms. The precursors and particles were prepared as described in the following section.

5.3 Experimental

5.3.1 Synthesis of $[\text{Mn}_3\text{O}(\text{O}_2\text{CR})_6\text{L}_3]$ Precursors

The synthetic protocols and relevant references for each precursor and the tetrabutylammonium permanganate (TBAMnO_4) starting material are outlined below.

Synthesis of tetrabutylammonium permanganate (TBAMnO_4)

To a stirred solution of KMnO_4 (2.5g, 15.8 mmol) in 75 mL H_2O was added a solution of tetrabutylammonium bromide (6.00 g, 18.6 mmol) in 50 mL H_2O . The resulting purple precipitate was collected by filtration and washed with H_2O (25 mL) and Et_2O (100 mL) and refrigerated.[195]

Synthesis of $[\text{Mn}_3\text{O}(\text{OAc})_6(\text{py})_3] \cdot \text{py}$

To a solution of $\text{Mn}(\text{OAc})_2 \cdot 4\text{H}_2\text{O}$ (2 g, 8.15 mmol) in acetic acid (10 mL) and pyridine (20 mL) was added TBAMnO_4 (0.6 g, 1.65 mmol) slowly, with the solution agitated by hand. The solution was then left to slowly evaporate overnight before the resulting crystals were collected by filtration and washed with Et_2O (50 mL). Air-dried crystals analyse as $[\text{Mn}_3\text{O}(\text{OAc})_6(\text{py})_3] \cdot \frac{1}{2}\text{py}$, analysis (%) calc. (found): C, 43.64 (43.38); H, 4.41 (4.41); N, 6.04 (5.91).[195]

Synthesis of $[\text{Mn}_3\text{O}(\text{piv})_6(\text{py})_3] \cdot \text{py}$

To a stirred solution of $\text{MnCl}_2 \cdot 4\text{H}_2\text{O}$ (4.4 g, 17.5 mmol) in H_2O (10 mL) and pyridine (20 mL) was added pivalic acid (26.67 g, 30ml, 0.261 mol) and KMnO_4 (0.4 g, 2.5 mmol). The solution was heated at 55 °C for 4 hours to give a black solid. This solid was dissolved in dichloromethane (50 mL) and the resulting solution filtered. This filtrate was then evaporated in the fume cupboard to yield crystals after 1 week. Air-dried crystals analyse as $[\text{Mn}_3\text{O}(\text{piv})_6(\text{py})_3] \cdot \text{py}$, analysis (%) calc. (found): C, 52.74 (52.09); H, 6.78 (7.46); N, 4.10 (2.69).[196]

Synthesis of $[\text{Mn}_3\text{O}(\text{benz})_6(\text{py})_2(\text{H}_2\text{O})]$

To a solution of $\text{Mn}(\text{OAc})_2 \cdot 4\text{H}_2\text{O}$ (2 g, 8.15 mmol) and benzoic acid (7.5 g, 61.4 mmol) in pyridine (3 mL) and ethanol (10ml) was added solid TBAMnO_4 (1.14 g, 3.15 mmol) slowly with stirring to give a brown solution. After 24 hours the precipitate was collected by filtration. The crude product was purified by recrystallisation from MeCN. Air-dried crystals analyse as $[\text{Mn}_3\text{O}(\text{benz})_6(\text{py})_2(\text{H}_2\text{O})]$, analysis (%) calc. (found): C, 57.63(57.07); H, 3.97 (3.91); N, 2.58(1.78).[195]

Synthesis of $[\text{Mn}_3\text{O}(\text{OAc})_6(\text{HIm})_3][\text{OAc}]$

To a solution of $\text{Mn}(\text{OAc})_2 \cdot 4\text{H}_2\text{O}$ (2 g, 8.15 mmol) and imidazole (2.5 g, 36.7 mmol) in acetic acid (12 mL) and DMF (25 mL) was added solid TBAMnO_4 (1.14 g, 3.15 mmol) in DMF (5 mL) slowly with stirring to give a red-brown solution. The resulting microcrystalline material was collected after 30 minutes and washed with ether. Air-dried crystals

analyse as $[\text{Mn}_3\text{O}(\text{OAc})_6(\text{HIm})_3][\text{OAc}]$, analysis (%) calc. (found) C, 34.60(34.10); H, 4.17(4.33); N, 10.53(10.82).[195]

5.3.2 Synthesis of Larger Mn-Containing Complexes

The synthetic protocols and relevant references for each precursor are outlined below.

Synthesis of $[\text{Mn}_6(\text{O})_2(\text{O}_2\text{CCMe}_3)_{10}(\text{THF})_4] \cdot \text{THF}$ (**Mn₆-pivalate**)

$\text{MnCl}_2 \cdot 4 \text{H}_2\text{O}$ (7.75 mmol) was reacted with excess $\text{Na}(\text{O}_2\text{CCMe}_3)$ (16.3 mmol) in MeOH (70 mL) for 24 h. The solution was evaporated to dryness, the product dried *in vacuo* and crystallised from THF as brown blocks. Air-dried crystals analyse as

$[\text{Mn}_6(\text{O})_2(\text{O}_2\text{CCMe}_3)_{10}(\text{THF})_4] \cdot 2 \text{THF}$, analysis (%) calc. (found) C, 48.50(48.67); H, 7.55(7.63); N, 0(0).[197]

Synthesis of $[\text{Mn}_{12}\text{O}_{12}(\text{OAc})_{16}(\text{H}_2\text{O})_4] \cdot 2 \text{AcOH} \cdot 4 \text{H}_2\text{O}$ (**Mn₁₂-acetate**)

KMnO_4 (1g, 6.25 mmol) was dissolved in 60% acetic acid solution (25 mL) and added dropwise to $\text{Mn}(\text{acetate})_2 \cdot 4 \text{H}_2\text{O}$ (4.04 g, 16.5 mmol) dissolved in 15 mL 60% acetic acid solution and stirred for 15 minutes. The resulting mixture was filtered through a sinter and the filtrate was left to stand in a sealed flask. After 1 day ~1.5 g of shiny black crystals were obtained and washed with $3 \times 100 \text{ mL}$ portions of acetone. Air-dried crystals analyse as $[\text{Mn}_{12}\text{O}_{12}(\text{OAc})_{16}(\text{H}_2\text{O})_4] \cdot 2 \text{AcOH} \cdot 4 \text{H}_2\text{O}$, analysis (%) calc. (found) C, 20.99(20.65); H, 3.52(3.35); N, 0(0).[198]

5.3.3 Synthesis of Manganese Oxide Nanoparticles

Particles were formed by decomposition of the precursors under high-temperature reflux conditions. The following synthetic protocols were optimised using Mn₁₂-acetate, and were then applied to the other Mn-containing precursors. Particles were synthesised either with or without a hold-step in their heating profile. The hold temperature was set as the decomposition temperature of the precursor as determined by TGA (as discussed in the results and discussion below (Section 5.4).

Synthesis of particles with a hold step

Mn precursor (0.5 mmol with respect to Mn) was mixed with 10 mL ODE, 1 mL OA (3 mmol) and 1 mL OAm (3 mmol) in a 3 necked flask. The mixture was heated to 110 °C under a nitrogen flow for 30 minutes, resulting in a clear yellow-orange solution. The nitrogen flow was then reduced and the mixture was slowly heated to the required hold temperature (as determined by TGA and given in Table 5.1) and then held at this temperature for 2 hours. During this time the reaction colour darkened to a deep orange-brown. The reaction was then slowly heated to 300 °C for 1 hour, after which a brown-black solution was obtained. The heat source was removed and the solution allowed to cool naturally to room temperature. The particles were precipitated by adding excess acetone and collected via centrifugation at 4,000 r.p.m. for 10 minutes. The waxy brown precipitate obtained was dispersed in 10 mL hexane and re-precipitated with excess ethanol. This procedure was repeated at least 5 times to remove excess surfactants. Hexane dispersions of the particles showed excellent colloidal stability, with no precipitation visible even after weeks of storage at room temperature.

Synthesis of particles without a hold step

Reagent quantities were used as above. After the 110 °C step the reaction mixture was heated slowly to 300 °C for one hour, without being held at an intermediate temperature. The heat source was then removed and the reaction mixture was allowed to cool to room temperature before the particles were collected by centrifugation as described above.

5.4 Results and Discussion

The synthetic protocol described in the experimental section was originally optimised using Mn_{12} -acetate, as this precursor could be made simply, reproducibly and in good yield. Optimisation of any solution-based synthesis requires careful tuning of a number of variables, and is, to a certain extent, a trial-and-error process. The experiments performed in the optimisation process are briefly described below, as these preliminary reactions provide insight into understanding the growth processes of the MnO particles which is relevant to later discussions.

5.4.1 Optimising MnO NP Synthesis Using Mn₁₂-acetate

As we have seen in the previous Chapters, for solution-based synthesis of NPs it is important to understand the decomposition behaviour of the precursor. TGA can be used to determine the temperature and rate at which a precursor decomposes, which can aid the logical placement of hold-steps in the reaction heating profile. TGA data was obtained for each precursor, with the plot corresponding to Mn₁₂-acetate given in Fig. 5.2.

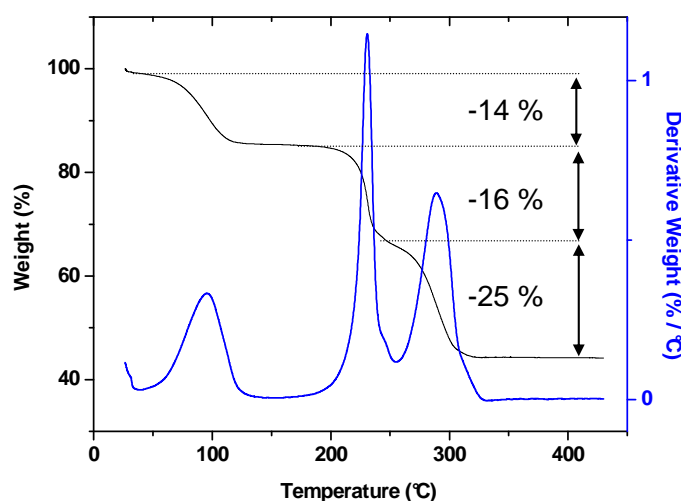


Figure 5.2: TGA plot (black, left abscissa) and corresponding derivative weight-loss plot (blue, right abscissa) for Mn₁₂-acetate. Numbers indicate percentage weight losses from the original weight over the indicated regions.

Fig. 5.2 shows distinct steps in the cluster decomposition. The first of these occurs at ~ 100 °C and corresponds to a weight loss of 14%. This initial weight loss corresponds to the loss of solvent molecules of crystallisation from the parent complex. The 14% loss is higher than would be expected assuming the loss of the two acetic acid and four water molecules from the original cluster (which would give $\sim 9\%$) and probably arises from the presence of residual water or acetic acid not removed during the washing stage of precursor synthesis. Larionova et al. also reported a higher than expected initial loss during TGA analysis of Mn₁₂-acetate.[199] The second (16%) and third (25%) weight losses correspond to the subsequent decomposition of the cluster core.[194] All organic moieties are removed by 330 °C, and the complex undergoes no further decomposition. The remaining 45% of the initial weight agrees with the expected weight corresponding to the formation of 4 formula units of hausmannite (Mn₃O₄) per Mn₁₂-acetate molecule

(44%). The formation of Mn_3O_4 by the solid-state thermal decomposition of Mn_{12} -acetate in inert atmosphere has been recorded previously.[194, 199].

The TGA data for Mn_{12} -acetate reveals more complex decomposition than observed in other NP precursors such as $\text{Fe}(\text{acac})_3$, which decomposes uniformly at $\sim 200^\circ\text{C}$ (as was discussed in Chapter 3). However, the presence of well-defined ‘steps’ in the TGA plot indicate that the temperatures at which these steps occur (where there are maxima in the corresponding derivative weight loss plot) are suitable temperatures for holding the reaction during decomposition. From Fig. 5.2 it is apparent that for Mn_{12} -acetate the strongest decomposition feature occurs at $\sim 230^\circ\text{C}$, which was designated to be the hold step temperature for future experiments using this precursor.

Having determined the decomposition profile of Mn_{12} -acetate, it was then necessary to optimise the synthesis of MnO particles. A number of variables were examined during the optimisation processes, including the type and volume of solvent used, surfactant ratio, length of hold step and reaction temperature. Initially, a similar solvent mixture was used as in the previous chapter for the synthesis of Ln_2O_3 nanowires. When Mn_{12} -acetate was heated directly to reflux in 4.5 mL OAm, 3 mL OA and 2.5 mL benzyl ether, large (70–150 nm) pointed cubes of MnO were formed (Fig. 5.3a). It was found that including a 230°C hold step in the reaction heating regime had no effect on the particle morphology, and similar large particles were formed (Fig. 5.3b).

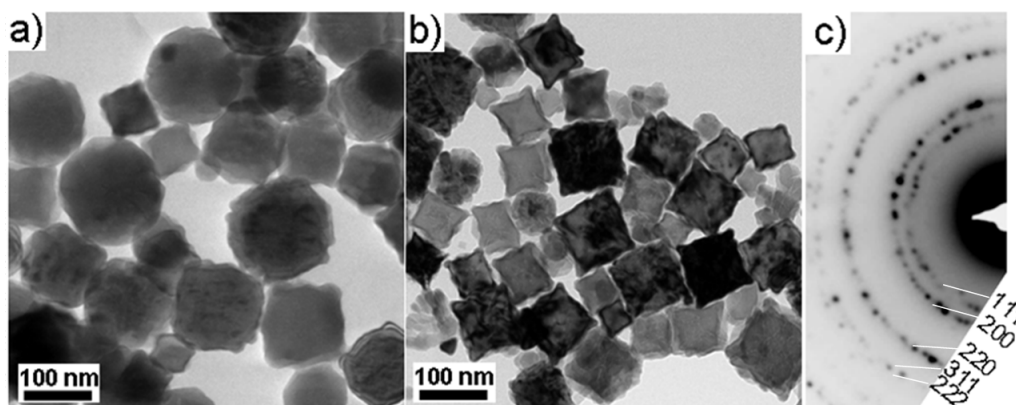


Figure 5.3: TEM images of the large cubic particles obtained by decomposition of Mn_{12} -acetate by decomposition in 4.5 mL OAm, 3 mL OA and 2.5 mL benzyl ether a) without and b) with a hold step. c) The electron diffraction pattern for the particles was indexed to fcc MnO.

Given that there is a large excess of surfactant in the reaction mixture (4.5 mL OAm and 3 mL OA), it was thought that by reducing the surfactant volume it may be possible to access smaller particles or different shapes. This is because it is was previously shown for iron oxide particles that a high concentration of surfactants increases the energy barrier to particle nucleation, meaning that in a surfactant-rich solution only a few NP nuclei will form. Forming few nuclei leaves more monomers available for particle growth, hence larger particles are formed.[200] Therefore, lowering the surfactant concentration should result in the formation of a larger number of smaller particles. By reducing the total surfactant volume to 2 mL (1 mL each of OAm and OA) and increasing the benzyl ether volume to 10 mL, it was possible to synthesise a polydisperse mixture of spherical and star-shaped particles when a hold step was used (Fig. 5.4a). To try and improve the size and shape selectivity, the OA:OAm ratio was altered, whilst keeping the total surfactant volume at 2 mL. No particles could be precipitated when the OA:OAm ratio was increased to 3:1, implying that an excess of acid inhibits particle formation. When the amine content was increased and the OA:OAm ratio changed to 1:3, a mixture of rounded and square platelet species was obtained (Fig. 5.4b,c).

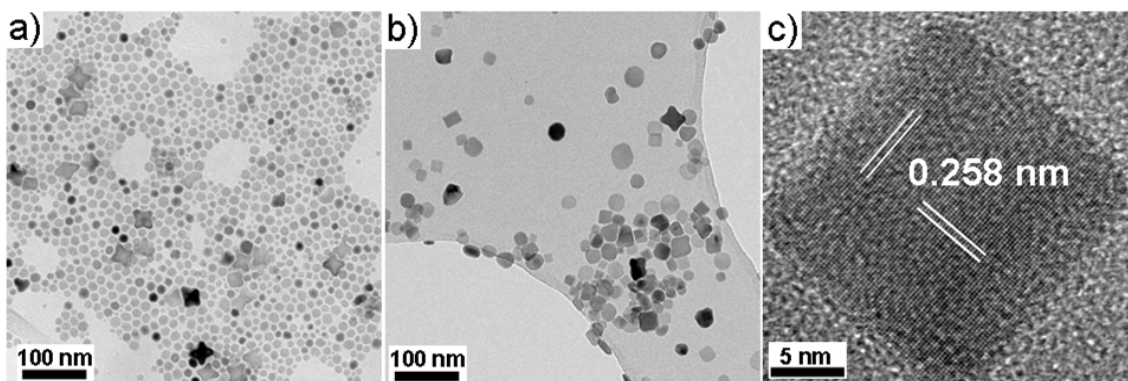


Figure 5.4: TEM images of a) the polydisperse particles obtained using 10 mL BE and 1 mL each of OA and OAm. b) TEM image of the rounded and square platelet species obtained when the OA:OAm ratio was changed to 1:3. c) HRTEM image of a single square platelet particle, lattice spacings of 0.258 nm are consistent with MnO (111) reflections.

It should be noted that although the interplanar spacings in the HRTEM image (5.4c) are consistent with MnO, the electron diffraction patterns for the samples synthesised

with BE as the solvent show that, in reality, a mixture of phases including Mn_3O_4 and Mn_2O_3 are obtained. The formation of numerous manganese oxide phases can be explained in terms of the poor reducing power of the reaction mixture. The particles formed with 4.5 mL OAm were unambiguously MnO (by the ED pattern given in Fig. 5.3c), as this large excess of OAm can act as a reducing agent, reducing the Mn^{3+} and Mn^{4+} ions present in Mn_{12} -acetate to Mn^{2+} . [136] By reducing the OAm volume to 1 mL and using a non-reducing solvent like benzyl ether, a mixture of MnO_x phases will form, as not all manganese ions will be reduced. These observations show that particle nucleation and growth is susceptible to slight variations in the surfactant mixture used, with a 1:1 acid:amine mixture giving the best particles (albeit far from perfect) in terms of size and shape selectivity. To improve upon the particles seen in Fig. 5.4a), the solvent was changed from benzyl ether to 1-octadecene (ODE), a long chain hydrocarbon with a high boiling point of 315 °C. ODE can also act as a reducing agent,[201] which may help improve the crystalline homogeneity of the product, as using BE resulted in a range of MnO_x phases being formed. It was found that the length of time spent at the hold temperature was crucial in obtaining high quality particles. Decomposition of Mn_{12} -acetate in ODE with a 2 hour hold step and one hour of heating at 290 °C yielded monodisperse 7 nm spherical particles (Fig 5.5 a). A two hour hold step followed by one hour at 290 °C was required to form monodisperse particles, as shorter heating hold times of 1 hour at 230 °C and 1/2 hour at 290 °C yielded larger polydisperse particles (Fig. 5.5b).

It is therefore possible to conclude that nucleation of MnO particles in ODE is a slow process, as after one hour at the hold temperature particle nucleation continues with further heating, giving rise to the observed polydisperse product. A longer hold time of 2 hours ensures that the precursor has completely decomposed (the reaction mixture continues to darken, implying the formation of NP seed particles). Increasing the hold time produces a large number of nuclei and ensures that additional nucleation does not occur on further heating. Furthermore, no particles were obtained if the reaction was stopped after the 2 hour hold step, implying that at 230 °C particle growth does not occur, and further heating at higher temperatures is required for particle growth. In this way, separation of the nucleation and growth stages is achieved, and a high quality product was obtained. The precise temperature of the hold step was also found to be important, as

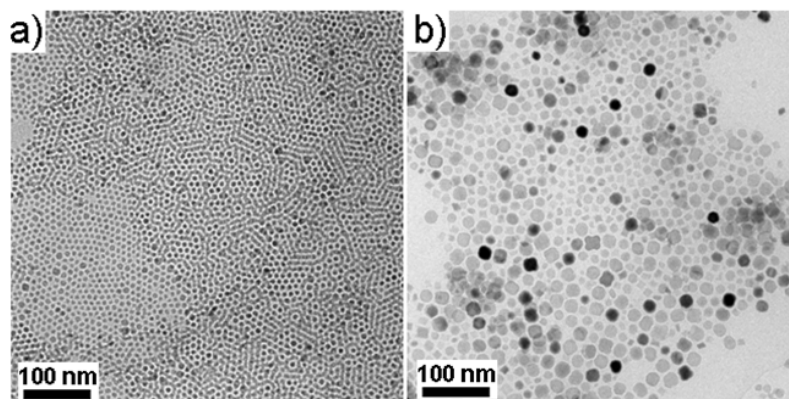


Figure 5.5: TEM images of a) the monodisperse particles obtained by heating in ODE at 230 °C for 2 hours, followed by 290 °C for one hour and b) particles obtained using the shorter heating times of 1 hour at 230 °C and 1/2 an hour at at 290 °C. Long hold steps are evidently required to obtain monodisperse particles.

slight deviations from 230 °C (such as 225 °C or 235 °C) yielded a polydisperse product.

The high quality particles obtained using the OA:OAm:ODE 1:1:10 mL ratio meant that this solvent mixture was designated the ‘standard’ ratio, and was subsequently used in the synthesis of MnO particles using the remaining manganese containing precursors that were mentioned previously in Sections 5.3.1–5.3.2.

5.4.2 MnO Particle Synthesis Using the Other Precursors

In this section the particles obtained from each of the six Mn-containing precursors will be presented and the factors that determine the particle shape (such as the heating regime and the structure of the ligands present) will be discussed.

Investigating Precursor Decomposition Behaviour

As was shown previously for Mn₁₂-acetate, TGA analysis reveals the decomposition behaviour of a compound, which enables the logical placing of heating hold steps which can narrow the size distribution of particles obtained using the thermolysis route. TGA data were obtained for the remaining precursors, and the corresponding weight-loss plots are given in Fig. 5.6.

The observed decomposition features are associated with the loss or decomposition of the carboxylate and secondary ligands for each precursor. By plotting the derivative

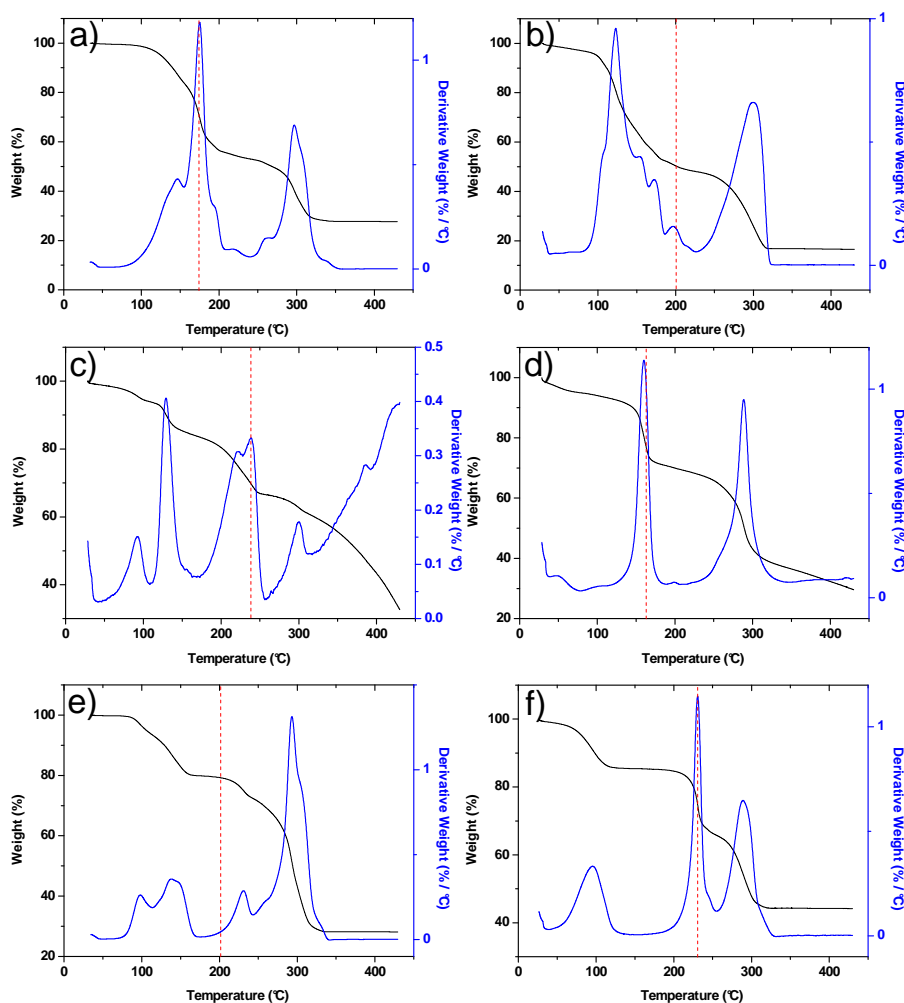


Figure 5.6: TGA plot (black, left abscissa) and corresponding derivative weight-loss plot (blue, right abscissa) for a) $[\text{Mn}_3\text{O}(\text{OAc})_6(\text{py})_3] \cdot \frac{1}{2} \text{py}$; b) $[\text{Mn}_3\text{O}(\text{piv})_6(\text{py})_3] \cdot \text{py}$; c) $[\text{Mn}_3\text{O}(\text{benz})_6(\text{py})_2(\text{H}_2\text{O})]$; d) $[\text{Mn}_3\text{O}(\text{OAc})_6(\text{HIm})_3][\text{OAc}]$; e) Mn_6 -pivalate and f) Mn_{12} -acetate. Dotted red lines indicate the chosen hold temperatures for each precursor.

weight-loss curves (the blue plots in Fig. 5.6), the temperatures at which the rate of precursor decomposition reached a maximum were determined. The hold temperature for each precursor was determined as the point where the first significant weight loss was observed or shortly thereafter (not counting the $\sim 100^\circ\text{C}$ weight losses which are ascribed to loss of adsorbed species such as H_2O and solvent molecules). At the hold temperature the loss of ligands from the precursor and the nucleation of NP seeds is expected to occur. It was anticipated that dissociation of the ligands from the precursor molecule into the reaction mixture would enable the newly-dissociated ligands to act as stabilising molecules

and influence NP growth. The hold temperatures for each precursor are summarised in Table 5.1.

Precursor	Mn Oxidation State	Hold Temperature (°C)
$[\text{Mn}_3\text{O}(\text{OAc})_6(\text{py})_3]$	II/III	175
$[\text{Mn}_3\text{O}(\text{piv})_6(\text{py})_3]$	II/III	200
$[\text{Mn}_3\text{O}(\text{benz})_6(\text{py})_2(\text{H}_2\text{O})]$	II/III	240
$[\text{Mn}_3\text{O}(\text{OAc})_6(\text{HIm})_3][\text{OAc}]$	III	160
Mn_6 -pivalate	II/III	200
Mn_{12} -acetate	III/IV	230

Table 5.1: Hold temperatures chosen for each precursor (on basis of TGA data) for the reactions where hold steps were used.

For the majority of the precursors, the hold temperature corresponds to the the temperature where there is a maxima in the derivative weight loss plots. For the precursors $[\text{Mn}_3\text{O}(\text{piv})_6(\text{py})_3]$ and Mn_6 -pivalate (Fig. 5.6b and e) however, the precursor decomposition was deemed too slow and extended over too large a range of temperatures to find a maxima in the derivative weight loss that did not correspond to the loss of solvent. For these precursors, the hold step was set as the temperature immediately following a broad decomposition feature in the TGA plot. Fig 5.6 shows that the precursors, whilst structurally similar, possess quite different decomposition characteristics. The particles obtained from each of these precursors are discussed in the following section.

Manganese Oxide Nanoparticle Synthesis

Representative low magnification TEM images obtained using each precursor under hold step and no hold step conditions are given in Fig. 5.7, and the results are summarised in Table 5.2. We find that both the precursor choice and reaction heating regime influence the final particle morphology, and a variety of NP shapes such as spherical, rounded cube, porous and octapod are readily obtained.

Product crystallography was confirmed using electron diffraction (ED) and X-ray diffraction (XRD). Diffraction data show that the as-synthesised particles are cubic MnO

Precursor	Hold Step		No Hold Step	
	Morphology	Particle Size	Morphology	Particle Size
$[\text{Mn}_3\text{O}(\text{OAc})_6(\text{py})_3]$	spherical	19.4 ± 2.7 nm (14%)	spherical	16.5 ± 2.4 nm (15%)
$[\text{Mn}_3\text{O}(\text{piv})_6(\text{py})_3]$	porous octahedral	74 ± 24 nm (32%)	porous octahedral	103 ± 18 nm (17%)
$[\text{Mn}_3\text{O}(\text{benz})_6(\text{py})_2(\text{H}_2\text{O})]$	rounded cubes	26.7 ± 3.3 nm (12%)	poorly defined	52.0 ± 10.2 nm (20%)
$[\text{Mn}_3\text{O}(\text{OAc})_6(\text{HIm})_3][\text{OAc}]$	spherical, peanut	26.9 ± 7.2 nm (25%)	octapod	86.8 ± 12.9 nm (15%)
Mn_6 -pivalate	octapod	30.5 ± 4.6 nm (15%)	octapod, cubic	51.2 ± 12.4 nm (24%)
Mn_{12} -acetate	spherical	10.7 ± 1.5 nm (14%)	spherical, octapod	30.8 ± 7.4 nm (24%)

Table 5.2: Overview of product morphologies obtained from the manganese complex precursors for different reaction conditions

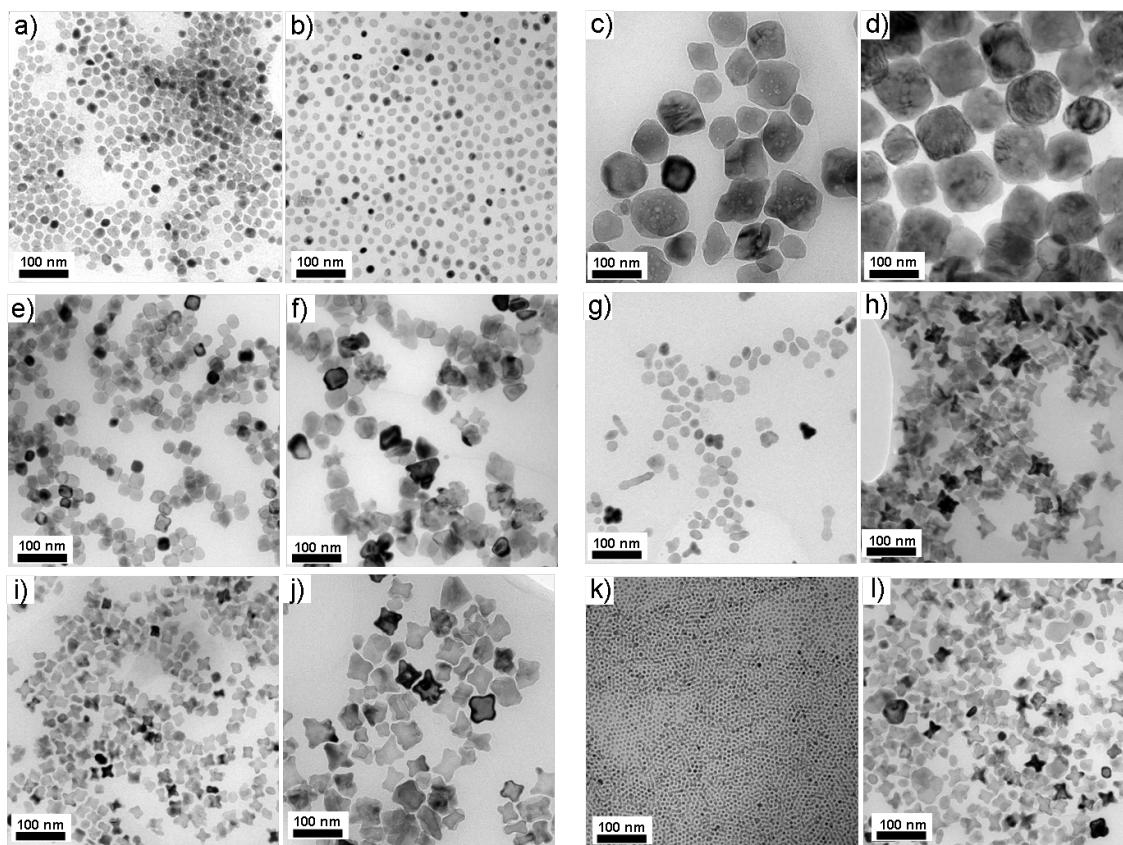


Figure 5.7: TEM images of the particles obtained using a),b) $[\text{Mn}_3\text{O}(\text{OAc})_6(\text{py})_3]$; c),d) $[\text{Mn}_3\text{O}(\text{piv})_6(\text{py})_3]$; e),f) $[\text{Mn}_3\text{O}(\text{benz})_6(\text{py})_2(\text{H}_2\text{O})]$; g),h) $[\text{Mn}_3\text{O}(\text{OAc})_6(\text{HIm})_3][\text{OAc}]$; i),j) Mn_6 -pivalate and k),l) Mn_{12} -acetate. The two images for each precursor correspond to the products obtained with and without hold-steps, respectively.

(JCPDS card number: 07-0230), though upon washing of the samples (to remove excess surfactants) mild oxidation to tetragonal Mn_3O_4 (JCPDS:24-0734) is seen to occur (Fig. 5.8). As the TEM images in Fig. 5.7 show that for each sample only one population of particles is formed, the presence of two manganese oxide phases is indicative of a core/shell morphology. The oxidation of MnO to Mn_3O_4 NPs under ambient conditions is well-known and has been reported previously. [202] A thin layer of Mn_3O_4 will form on the surface of MnO particles upon exposure to air (such as during the washing cycle); this thin layer protects the MnO core of the particle from further oxidation. It was found that the intensity of Mn_3O_4 diffractions peaks varies with particle size, with smaller particles exhibiting stronger and more numerous Mn_3O_4 reflections compared with larger particles

(Fig. 5.9). This is entirely in keeping with a core/shell structure of particle, as smaller particles will have a greater proportion of surface (shell) species compared to larger particles.

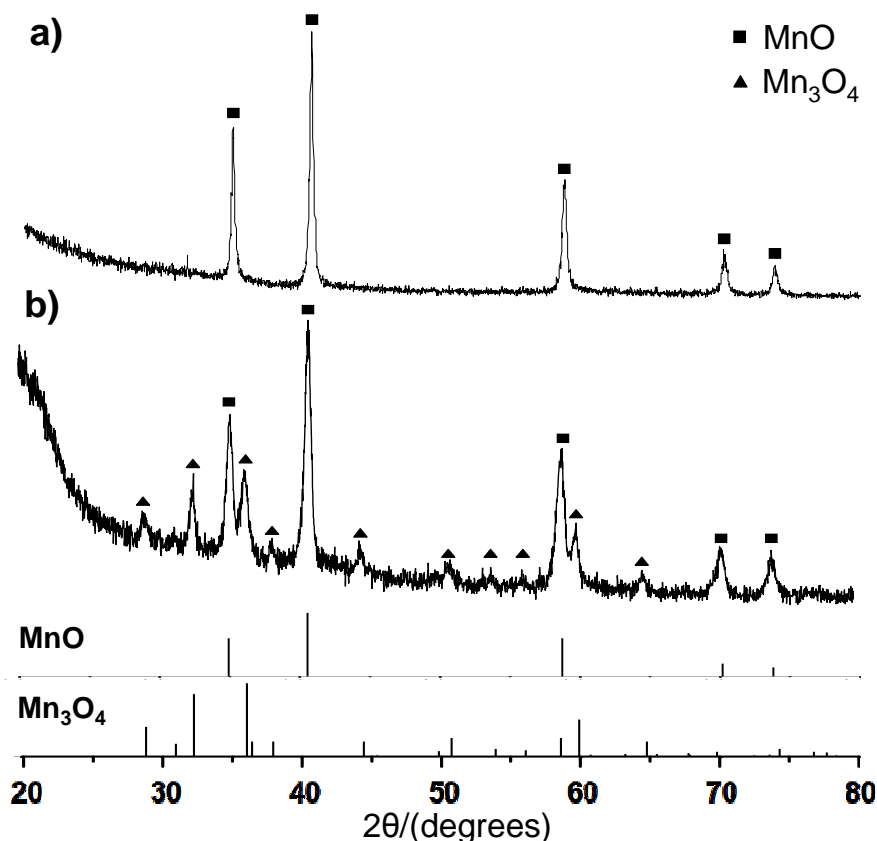


Figure 5.8: X-ray diffraction data for a typical sample a) immediately after precipitation b) after 5 washing cycles. After washing, mild oxidation to Mn_3O_4 is seen to occur.

As MnO particles are formed for each precursor, it is possible to conclude that the oxidation state of manganese in the precursor (given in Table 5.1) has no bearing on final product crystallography. Reduction of Mn(III) or Mn(IV) to Mn(II) is consistent with having excess oleylamine in the reaction, which is known to act both as a reducing agent and stabilising surfactant molecule.[136] It is possible that the vinyl group of the unsaturated hydrocarbon solvent (1-octadecene, ODE) can act as a source of electrons and hence lower the oxidation state of precursor manganese ions, as ODE has been shown to act as a reducing agent elsewhere.[201] Similar unsaturated hydrocarbon solvents such as squalene ($C_{30}H_{50}$) have also been shown as capable of reducing transition metal ions

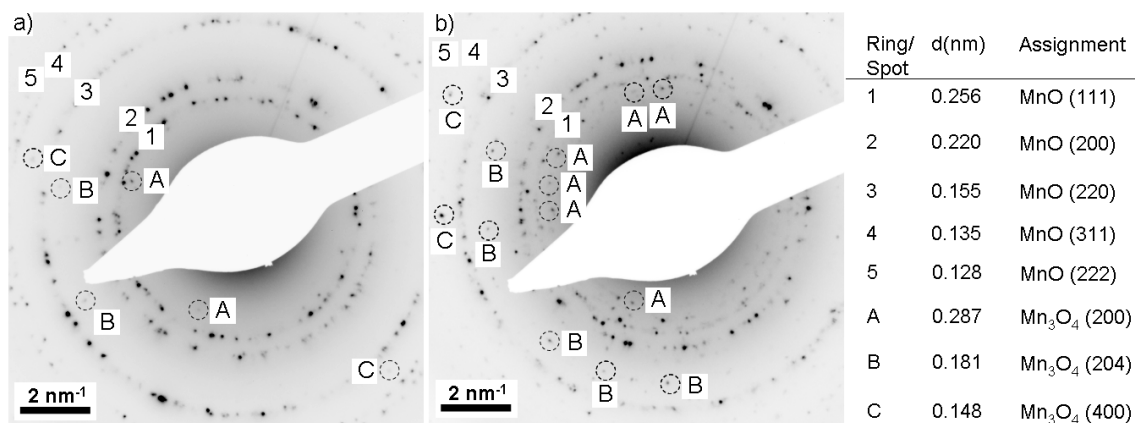


Figure 5.9: Electron diffraction data for typical octapod particles: a) 85 nm and b) 35 nm. Rings (1-5) are assignable as MnO, and it was possible to identify discrete spots (A-C) which could be assigned to Mn₃O₄. The intensity and number of the Mn₃O₄ spots increased with a decrease in particle size, which is consistent with a core/shell morphology, since a smaller particle will have a greater proportion of surface (shell) species.

(such as Fe³⁺) during NP formation.[203]

The colour of the reaction mixture during NP formation can also provide insight into the change in Mn oxidation state during the reaction. In nature MnO exists as the green mineral manganosite. Some MnO NP literature preparations describe the reaction mixture becoming green on NP formation, and suspensions of MnO particles as being green in colour.[57] Other reports describe the reaction mixture turning brown on particle formation, forming brown suspensions of NPs which were unambiguously MnO.[183, 204, 205] Ould-Ely et al. discussed the importance of thoroughly de-gassing the reaction mixture under vacuum before heating, which removed all traces of air and moisture from the reaction vessel, with reactions performed without vacuum de-gassing were found to turn brown on cooling.[189] It seems a brown MnO product indicates the presence of a small amount of additional oxide or hydroxide material, though not sufficiently enough to provide additional diffraction features in the MnO diffraction pattern.[189] For the precursors used in this Chapter, the reaction mixtures turned brown on heating, eventually yielding dark brown NP dispersions. The brown colour is likely due to trace amounts of air or moisture in the reaction vessel that were not removed during the 110 °C purge step in particle synthesis. It is hypothesised that vacuum de-gassing may remove trace impurities

and yield a green product.

Attempts to quantify the thickness of the oxidised shell via HRTEM and STEM EELS were unsuccessful, due to the sample contaminating quickly under the electron beam, due to the presence of residual hydrocarbons on the TEM grid. This meant that during HRTEM imaging, it was often difficult to obtain satisfactory lattice-resolved images as lattice fringes were only briefly visible before becoming obscured by sample contamination. A typical HRTEM image of a spherical MnO particle is given in Fig. 5.10, which shows the partially-obscured lattice fringes.

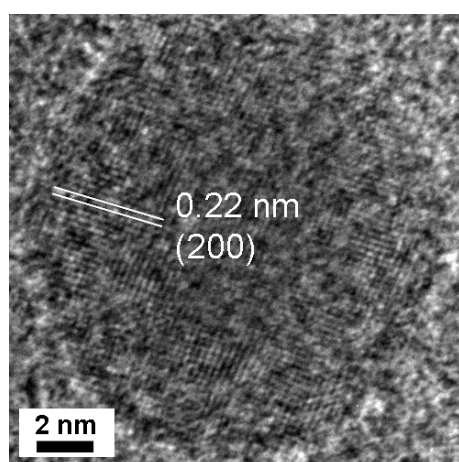


Figure 5.10: HRTEM image of 17 nm spherical particle. The lattice fringes are faintly visible, and where possible have been indexed to MnO (200) reflections. These fringes were only visible for a few moments before they became obscured.

Sample cleanliness was a considerable issue when using ODE as a solvent, and the product obtained was noticeably more ‘oily’ than the products obtained if benzyl ether was used. This meant extra washing cycles were required before a product pure enough for HRTEM or EELS analysis could be obtained. Repeated washing is problematic because NPs are readily oxidised upon exposure to air, hence washing the particles contributes significantly to an increase in oxidation state. However, not washing the particles leaves them too dirty to perform even basic TEM imaging and risks damaging the TEM instrument. The effect of the washing procedure on metal oxidation state has been discussed in both Chapters 3 and 4, where mild oxidation of Fe_3O_4 to Fe_2O_3 and Ce^{3+} to Ce^{4+} was observed, respectively. For the MnO particles, EELS samples were prepared by washing the particles between 8 and 10 times. Significant contamination was still observed despite extensive washing. This meant that satisfactory EELS data could not be obtained through long beam dwell times on a single particle, as after a few seconds enough carbon had built up to completely obscure the particle. Two different acquisition

methods were used: **i)** the electron beam was rastered over the whole field of view, and an average EELS spectra was collected for this whole raster. An average was taken of two 5 second rasters. **ii)** The electron beam was manually ‘hopped’ from particle to particle during a long EELS acquisition, thus minimising the length of time spent on an individual particle. An average of 10×2.5 seconds scans was obtained. The resulting EELS spectra for each of these methods are given in Fig. 5.11.

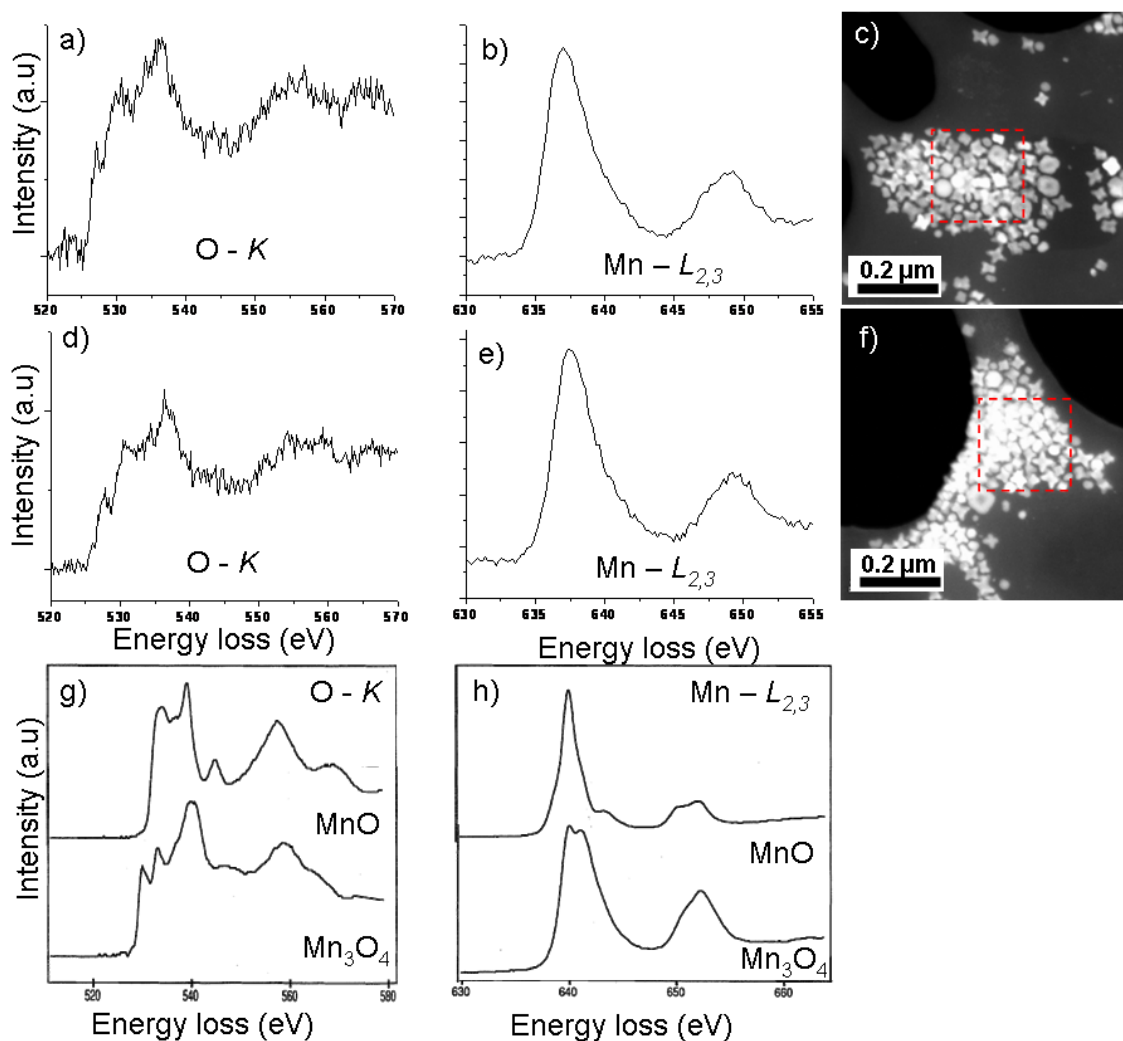


Figure 5.11: a,d) Oxygen K edge and b,e) Mn $L_{-2,3}$ edge EELS spectra acquired from a sample of octapod particles by the averaging and hopping techniques, respectively. c,f) The corresponding STEM DF images showing the regions where the data was collected (highlighted in red boxes). Literature values for the g) Oxygen K edge and h) Mn $L_{-2,3}$ edges of MnO and Mn₃O₄. [206]

The contamination of the sample meant that it was difficult to obtain a meaningful

EELS data, as the oxygen edge was somewhat obscured by a large background signal. This meant that elemental composition analysis (obtained by calculating the areas under the O and Mn peaks) did not provide a sensible result. The Mn composition was determined to be in the region of 50–55%, which is not consistent with either MnO (50%) or Mn₃O₄ (42.9%). However, analysis of the oxygen and manganese edge lineshapes afforded some indication as to the true composition of the particles. Comparison with literature data (shown in Fig. 5.11g,h) shows that the O and Mn edges are in good agreement with the previously observed shapes for Mn₃O₄. [206, 207] The literature data shows that there exist clearly differentiable features between the MnO and Mn₃O₄ oxygen edge shapes, and the oxygen edge obtained for the octapod particles is clearly more similar to the Mn₃O₄ edge. It is therefore possible to conclude that the as-synthesised MnO particles are sensitive to oxidation during the washing procedure, a feature which has been observed numerous times thus far in this thesis. Unfortunately, the presence of a core-shell morphology could not be confirmed using EELS, as the sample contaminated too quickly to perform a line scan across a particle.

We have seen from Fig. 5.7 that it is possible to use the [Mn₃O(O₂CR)₆L₃] and larger Mn₆-pivalate and Mn₁₂-acetate molecules as precursors for MnO NPs, and that a number of different product morphologies can be obtained which are seemingly dependent on both the heating regime that is used and the precursor itself. In the next sections each of these factors will be assessed and the contributions from each on nanoparticle nucleation and growth kinetics will be discussed in turn.

5.4.3 The Role of Precursor Ligand

Figure 5.7 clearly shows that particle morphology can be varied simply by varying the precursor, and shapes such as spherical, rounded cube, porous and octapod are readily obtained. Precursors were chosen so that combinations of precursor ligands not commonly used in NP synthesis (such as pivalate (piv), pyridine (py) and imidazole (Im)) could be used alongside more traditional ligands (acetate (OAc) and benzoate (benz)), enabling the role of ligand combination on particle morphology to be systematically investigated.

Role of the carboxylate ligand

For example, it was found that the structure of the carboxylate ligand (Fig. 5.1) in the precursor influenced the product morphology. 19.4 and 16.5 nm spherical particles were obtained when $[\text{Mn}_3\text{O}(\text{OAc})_6(\text{py})_3]$ was used as the starting material (sizes are for with and without a hold-step respectively, Fig. 5.7a,b). Changing the carboxylate ligand to pivalate (but keeping the secondary ligand as pyridine) yields the $[\text{Mn}_3\text{O}(\text{piv})_6(\text{py})_3]$ precursor, which gave large, irregular octahedral particles of up to 100 nm in size upon decomposition, which featured pores 10–15 nm in diameter on their surfaces (Fig. 5.7c,d). When a third carboxylate ligand, benzoate, was used the $[\text{Mn}_3\text{O}(\text{benz})_6(\text{py})_2(\text{H}_2\text{O})]$ precursor was obtained, which gave 27 nm rounded cubic or ~ 50 nm poorly defined particles (with and without a hold-step respectively, Fig. 5.7e,f). Higher magnification images of the particles obtained by varying the carboxylate precursor are shown in Fig. 5.12.

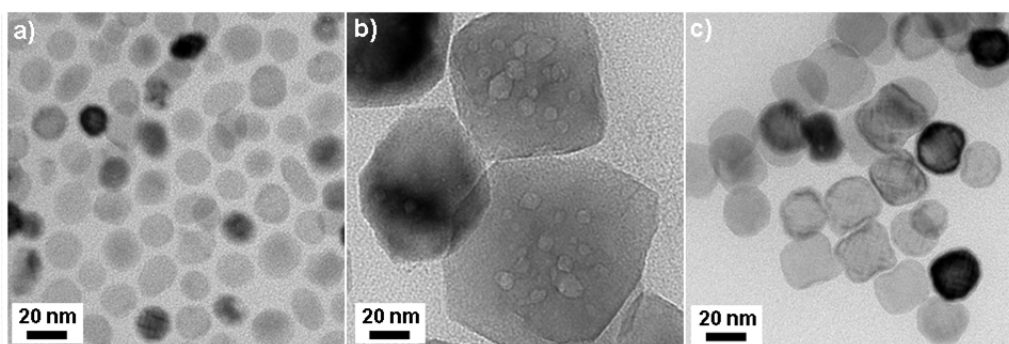


Figure 5.12: TEM images of the particles obtained by varying the carboxylate ligand in the precursor a) $[\text{Mn}_3\text{O}(\text{OAc})_6(\text{py})_3]$ b) $[\text{Mn}_3\text{O}(\text{piv})_6(\text{py})_3]$ and c) $[\text{Mn}_3\text{O}(\text{benz})_6(\text{py})_2(\text{H}_2\text{O})]$.

The difference between the small, regular particles obtained using $[\text{Mn}_3\text{O}(\text{OAc})_6(\text{py})_3]$, the slightly larger rounded cubic particles obtained using $[\text{Mn}_3\text{O}(\text{benz})_6(\text{py})_2(\text{H}_2\text{O})]$ and the much larger, irregular species obtained using $[\text{Mn}_3\text{O}(\text{piv})_6(\text{py})_3]$ provides evidence that the ligands present in a precursor can mediate NP formation mechanisms. In the above comparison, exchanging small acetate molecules for larger benzoate or pivalate molecules yields larger particles, with an apparent worsening of control over the particle shape. The reduction in shape and size control implies that having larger ligand molecules in the precursor hinders the stabilisation of the growing particles, with destabilisation more pronounced for pivalate than for benzoate. This observation can be rationalised in

terms of the steric bulk and relative binding strengths of the pivalate and benzoate groups.

Firstly, the steric bulk of both benzoate and pivalate (which are considerably larger than the simple acetate molecule) will affect the packing of the OA and OAm surfactants on the particle surface. Upon precursor decomposition, NP nuclei will form and begin to grow. The close proximity of the precursor ligands to the metal centres in the starting material means that the precursor ligand molecules will likely be adsorbed to the surfaces of the nascent particles. Having bulky benzoate and pivalate molecules on the particle surface will inhibit the adsorption and packing of OA and OAm on the particle surface. Long chain molecules such as OA and OAm are good surfactants because their long hydrocarbon tails can physically separate particles in solution, which limits the rate of monomer addition to particles and also prevents inter-particle agglomeration. For the benzoate and pivalate precursors, the close proximity of benzoate and pivalate molecules to the manganese metal centres means that upon precursor decomposition, the surface of the nascent particles will be covered by a layer of benzoate and pivalate molecules, bound through their carboxylate groups. The steric bulk of the benzene ring of benzoate and of the $C(CH_3)_3$ tail group of pivalate restricts approach of OA and OAm to the particle surface, meaning that OA and OAm do not pack as efficiently on the particle surface. Benzoate and pivalate, on the other hand, are relatively short molecules (compared to OA and OAm) and so will not be able to control monomer condensation on the particle surface (resulting in larger particles), nor can they as efficiently prevent particles in solution from coming into close contact with one another. Particles brought in close proximity to one another will coalesce (via Ostwald ripening, for example) in order to reduce their surface energies, which results in larger and less well defined particles — such as those seen when pivalate was used. This trend is similar to the formation of the ‘compound’ magnetite particles seen in Chapter 3, in which the alkyl side-arms of polyol solvents were believed to be responsible for hindering OA and OAm from adsorbing on the particle surface, which resulted in inter-particle agglomeration and the formation of compound particles.

It is clear from Fig. 5.7 that the pivalate precursor yields the largest and most poorly-defined particles when compared to the acetate and benzoate-containing precursors (at least when a hold step is used), yet the by the argument of the previous paragraph both benzoate and pivalate should inhibit the adsorption and packing of OA and OAm on the

particle surface and yield similar particles. However, comparison of Fig. 5.7 c) with e) shows that the shape and size control of the particles obtained with benzoate is much better than that of the particles obtained using the pivalate precursor. This observation can be rationalised in terms of the relative binding strengths of the benzoate and pivalate groups to the surface of the nanoparticle. The benzene ring of the benzoate molecule is electron withdrawing, and hence benzoic acid is more acidic than pivalic acid — relative pK_a values: 4.2 (benzoate) and 5 (pivalate). The binding strength of a carboxylate group to a metal centre depends on the pK_a of the conjugate acid, with a higher pK_a (weaker acid) resulting in a more stable complex with a higher stability constant.[208] Hence, the weakly acidic pivalate molecule will bind more strongly to the particle surface than the more acidic benzoate molecule, which will be easily removed and replaced by OA and OAm (the pK_a of OA is 9.85, hence it will be more strongly bound than both benzoate and pivalate).[209] The particles obtained using $[\text{Mn}_3\text{O}(\text{benz})_6(\text{py})_2(\text{H}_2\text{O})]$ therefore have an improved level of size and shape control compared to the particles obtained using $[\text{Mn}_3\text{O}(\text{piv})_6(\text{py})_3]$, due to the greater amount of OA and OAm on the particle surface. In contrast, the particles obtained using the strongly bound pivalate molecule have a lower degree of size and shape control, due to the reduced amount of OA and OAm on the particle surface. Analogously, the small acetate ligands of $[\text{Mn}_3\text{O}(\text{OAc})_6(\text{py})_3]$ allow OA and OAm to approach close to the particle surface and are easily replaced by OA and OAm, which leads to well-stabilised particle growth and a high degree of shape and size selectivity.

Whilst the size and shape control of the particles obtained using $[\text{Mn}_3\text{O}(\text{piv})_6(\text{py})_3]$ is worse than for the other precursors, these 100 nm particles are interesting because they appear to feature pores on their surfaces, see Fig. 5.13. The porous nature of the particles (which are porous without requiring additional processing) is interesting since porous species were not obtained for any of the other precursors examined.

Porous transition metal oxide NPs are of interest as the pores enable applications as molecular sieve materials and in drug storage/delivery.[210, 211] The exact cause of pore formation is unknown, though it could be that the pores are simply artefacts left over from imperfect coalescence between particles, since pores are not observed for any of the other NP samples, and growth by coalescence is only expected for the $[\text{Mn}_3\text{O}(\text{piv})_6(\text{py})_3]$ pre-

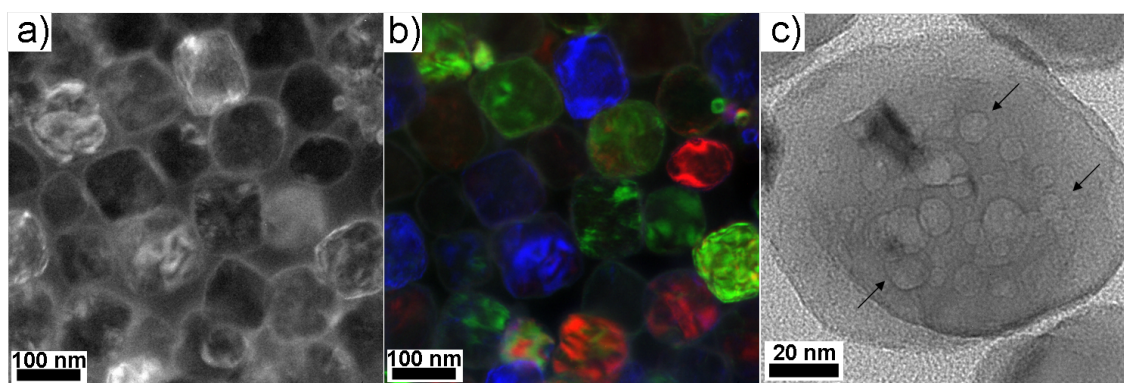


Figure 5.13: Additional TEM figures for the $[\text{Mn}_3\text{O}(\text{piv})_6(\text{py})_3]$ precursor. Images show a) dark-field (DF) TEM image, b) false-coloured DF composite and c) TEM image of a NP, pores marked by arrows.

cursor. The crystalline nature of these porous particles was investigated using dark-field (DF) TEM imaging (Fig. 5.13a,b), which revealed the edges of the particles to show subtle contrast variations in the DF image (or colour variations in the false-coloured image), indicating that the particles are surrounded by a thin layer of material of a different crystallographic nature to the bulk of the particle. This is indicative of a core-shell morphology, and corroborates the diffraction findings (Figs. 5.8 and 5.9) which show the particles to be predominately MnO , with surface Mn_3O_4 present in small amounts.

Role of the secondary ligand

As discussed in the previous section, spherical particles were obtained using $[\text{Mn}_3\text{O}(\text{OAc})_6(\text{py})_3]$ (Fig. 5.7a,b), regardless of the heating regime. Modifying this precursor to $[\text{Mn}_3\text{O}(\text{OAc})_6(\text{HIm})_3][\text{OAc}]$ (interchanging pyridine and imidazole) gives rise to two different morphologies, depending on the heating regime used. Inclusion of a heating step yields a polydisperse product, containing both spherical and elongated particles, whereas bypassing the heating step yields nearly monodisperse octapod particles (Fig. 5.7g,h). The difference in product morphology that arises simply by exchanging pyridine and imidazole is remarkable, given the structural similarity between these two ligands and the similar decomposition profiles of the two precursors (Fig. 5.6a and d). It was anticipated that similar NP morphologies would be obtained for each precursor since both imidazole and pyridine are both small molecules and are expected to adsorb only

weakly to the particle surface, and therefore should be quickly replaced by strongly-bound OA and OAm which are present in excess in the reaction mixture (the Mn:OA:OAm ratio is 1:6:6).

It is clear that the heating regime has a significant impact on the particle morphology for each precursor, as removing the hold step results in isotropic spherical particles for $[\text{Mn}_3\text{O}(\text{OAc})_6(\text{py})_3]$ and anisotropic octapod particles for $[\text{Mn}_3\text{O}(\text{OAc})_6(\text{HIm})_3][\text{OAc}]$. As we will see in section 5.4.4 the presence or absence of a hold step determines if particles experience slow, thermodynamically controlled growth or rapid, kinetically controlled growth. Isotropic species (such as spheres) are favoured by thermodynamic control and the formation of anisotropic species such as octapods suggests that kinetically controlled growth is dominant, and it would appear that, for these two precursors, the growth process is dependent on the secondary ligand. The formation of spherical particles upon the rapid decomposition of $[\text{Mn}_3\text{O}(\text{OAc})_6(\text{py})_3]$ compared with the formation of octapod particles upon the rapid decomposition of $[\text{Mn}_3\text{O}(\text{OAc})_6(\text{HIm})_3][\text{OAc}]$ suggests that kinetically-controlled crystal growth is perhaps impeded by the presence of pyridine molecules, and instead the isotropic (thermodynamic) product is favoured. The exact processes is unknown, though it is clear that ligand-mediated control of NP formation can be induced via the precursors chosen.

Larger molecules as precursors to MnO particles

It was also found that the nuclearity of the precursor (that is, the number of metal centres per molecule) could be increased without detriment to the ability of a precursor to form particles. For example, high quality particles were obtained for both the hexanuclear and dodecanuclear complexes Mn_6 -pivalate and Mn_{12} -acetate (which were synthesised as described previously in section 5.3.2). Large molecules like these have the potential to incorporate a number of different ligands into their structures (indeed, many derivatives of Mn_{12} -acetate are known [192]) and can therefore be seen as flexible precursors to obtaining high-quality particles.

The spherical particles obtained using Mn_{12} -acetate as a precursor with no hold step in the heating regime are consistent with the spherical particles obtained using the smaller acetate containing compounds $[\text{Mn}_3\text{O}(\text{OAc})_6(\text{L})_3]$ (for $\text{L} = \text{py}$ and HIm) and suggests

that the small acetate ligand is labile and is easily replaced by OA and OAm to ensure growth of uniform particles. Keeping the reaction at the hold temperature ensures that the precursor is completely decomposed and the nuclei are well-stabilised by the long hydrocarbon surfactants. Clearly, the heating regime has a significant effect on the growth mechanisms of the particles and these will be discussed in the following section.

Interestingly, Mn_6 -pivalate produced octapod particles regardless of the heating regime, particles which are different from those obtained using the other pivalate containing precursor $[\text{Mn}_3\text{O}(\text{piv})_6(\text{py})_3]$, which yielded porous octahedral particles 70–100 nm in diameter. The difference in particle shapes obtained from the two pivalate-containing precursors suggests that the particle growth mechanism may be sensitive to the Mn:pivalate ratio (in Mn_6 -pivalate this is 1:1.67, whereas for $[\text{Mn}_3\text{O}(\text{piv})_6(\text{py})_3]$ this is 1:2), or that the hold step chosen for Mn_6 -pivalate was incorrect, and at the given hold temperature (200 °C) the precursor may have been decomposing rapidly and experiencing kinetically controlled growth. Indeed, the hold temperature of 200 °C was chosen as this temperature immediately follows a broad decomposition feature in the TGA data (previously shown in Fig. 5.6), though selecting a lower hold temperature may encourage thermodynamic particle growth.

The above discussions highlight that it is possible for the ligands present in a precursor to influence particle growth mechanisms that ultimately determine the final shape of the particle. The ligand molecules can disrupt the adsorption of surfactants on the particle surface, which can result in larger particles. The particle shape can be influenced by the extent of adsorption of the ligand molecules to the particle surface, as strongly-adsorbing molecules hinder particle stabilisation by OA and OAm, resulting in larger, more poorly defined particles. It is clear that the heating regime also has a significant contribution to particle growth mechanisms, which will be discussed in detail in the following section.

5.4.4 The Role of Heating Regime

Comparison of the particles obtained from each precursor in the presence or absence of a heating hold-step (the left and right hand image of each pair in Fig. 5.7) shows that, for the majority of the precursors, the heating regime has a significant influence on par-

ticle morphology. Only the particles obtained using $[\text{Mn}_3\text{O}(\text{OAc})_6(\text{py})_3]$ show no significant change, with spherical particles of similar size forming irrespective of the heating regime ($19.4 \text{ nm} \pm 14\%$ and $16.5 \text{ nm} \pm 15\%$ respectively.) When no hold step was used $[\text{Mn}_3\text{O}(\text{piv})_6(\text{py})_3]$ yielded similar ‘porous’ particles to when a hold step was used, although the particles were clearly larger and had better-defined size and octahedral shape than those obtained when a hold step was used ($74 \text{ nm} \pm 32\%$ and $103 \text{ nm} \pm 17\%$ respectively). Size and shape control was worsened for the particles obtained using $[\text{Mn}_3\text{O}(\text{benz})_6(\text{py})_2(\text{H}_2\text{O})]$, which gave $\sim 27 \text{ nm}$ rounded cubes when a hold-step was used and larger ($\sim 50 \text{ nm}$), polydisperse particles with no clear shape specificity when the hold step was bypassed. The three remaining precursors $[\text{Mn}_3\text{O}(\text{OAc})_6(\text{HIm})_3][\text{OAc}]$, Mn_6 -pivalate and Mn_{12} -acetate all yielded pseudocubic particles when no hold step was used. Representative TEM images of the particles obtained using these three precursors are given in Fig. 5.14, and appear to show ‘pseudo-cubic’ particles, which have elongated corners.

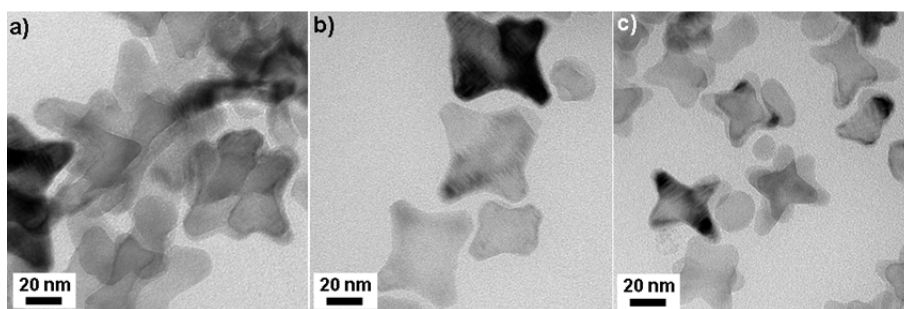


Figure 5.14: TEM images of multipod particles obtained using a) $[\text{Mn}_3\text{O}(\text{OAc})_6(\text{HIm})_3][\text{OAc}]$, b) Mn_6 -pivalate and c) Mn_{12} -acetate, under no hold-step conditions.

To determine the three dimensional shape of the particles, TEM tilting experiments were performed, which confirm that the particles have eight elongated protrusions emerging from their surfaces. This shape can be thought of as a cube with overgrown corners, though the term ‘octapod’ is commonly used in the literature (such as for CdS/CdSe octapods).[212] The TEM tilting experiments were performed by tilting the sample from -45° through to $+45^\circ$ in 15° increments, and the images are presented in Fig. 5.15.

Furthermore, the TEM images of the particles when viewed from the $[100]$ zone axis (i.e.: looking straight down on top of a particle) reveal the particle’s top 4 protrusions

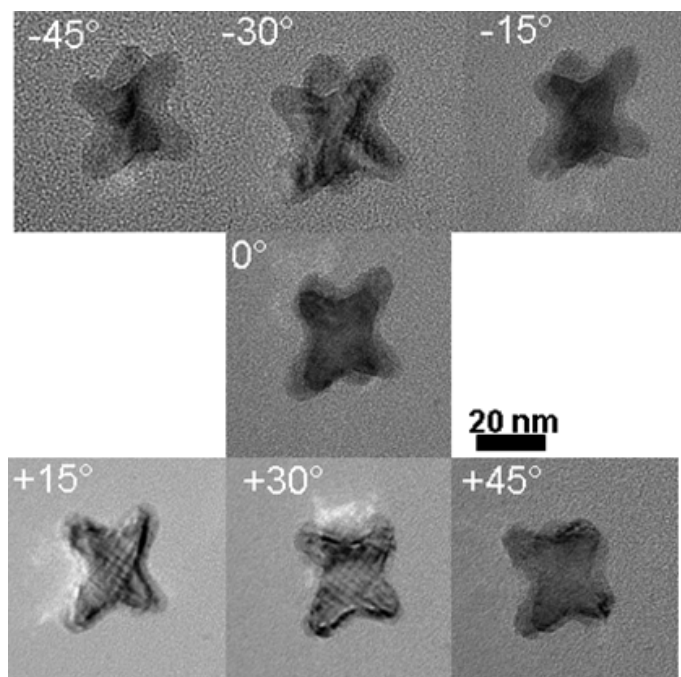


Figure 5.15: TEM images of octapod particles obtained using Mn_{12} -acetate with no heating step. The images were collected at tilt angles of -45° through to $+45^\circ$ in 15° increments. The 8-pronged nature of the particles is visible upon tilting.

to be slightly darker than the centre of the particle (Fig. 5.16), which is consistent with the octapod shape — since each top protrusion will have an equivalent lower protrusion directly beneath it. This means the for the $[100]$ zone axis, the electron beam has to pass through two regions of material and hence will appear darker than the octapod core.

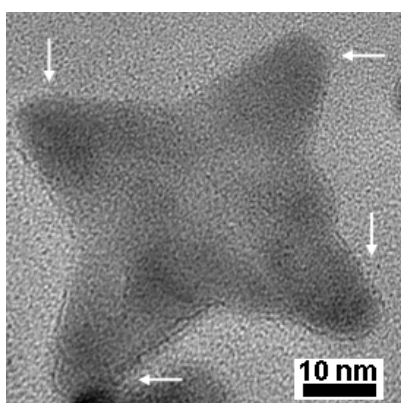


Figure 5.16: TEM image of an octapod obtained using $[Mn_3O(OAc)_6(HIm)_3][OAc]$, viewed from the $[100]$ zone axis. Arrows indicate darker contrast at particle corners, confirming the octapod morphology.

The formation of MnO octapod particles is at odds with other ‘multipod’ MnO parti-

cles that have previously been reported, which usually feature 4–6 branches. For example, Zitoun et al. reported the synthesis of MnO multipods by the decomposition of Mn oleate in trioctylamine and oleic acid.[37] In this paper the authors showed that multipod particles grew through oriented attachment of MnO monomers to a MnO seed particle, resulting in growth in the $\langle 100 \rangle$ direction. Growth by oriented attachment resulted in the formation of predominately hexapod particles, though tetra- and pentapod species were also obtained.[37] In a similar publication, Ould-Ely et al. reported the synthesis of large MnO hexapod and MnO cross-shaped particles by the decomposition of $\text{Mn}(\text{OAc})_2$ again in trioctylamine and oleic acid.[189] In this publication the authors rationalised the growth of multipod particles in terms of the cubic crystal structure of MnO. The authors postulated that the octahedral arrangement of atoms within the MnO rock salt crystal structure would promote the growth of crystals derived from the octahedron, such as hexapods.[189] Indeed, the formation of hexa-branched species has been seen for other materials bearing cubic crystal structures, such as PbS which has the rock salt structure,[213, 214] and hexa-branched dendrites of magnetite (which has a cubic inverse spinel structure) were recently reported by Wang et al.[215]

It is clear from the TEM images in Figs. 5.7h,j,l)–5.14 that the MnO octapod particles are different to the MnO hexapod species that have previously been reported, and that the growth of the octapod particles must proceed by a mechanism not yet observed for MnO — a mechanism which is also clearly dependent on the heating regime used during particle synthesis. A possible explanation for the formation of octapod particles is that the presence or absence of a hold step results in crystal growth occurring under thermodynamic or kinetic control, respectively. Kinetic control of NP growth is often used to rationalise the growth of ‘unusual’ particle morphologies, such as multipod species. For example, in a recent review Jun et al. discussed that the growth of anisotropic nanocrystals is facilitated by a kinetic growth regime, promoted by a large influx of monomers such as when a precursor is rapidly heated above its decomposition temperature. Conversely, isotropic crystal growth is favoured by a thermodynamic growth regime, and is promoted by a low influx of monomers such as when a precursor is held at its decomposition temperature.[216] Kinetic control favours the growth of high-energy facets and concave surfaces, whereas thermodynamic control of growth will result in NPs with simple

polygon shapes with flat edges, such as cubes, octahedra and truncated variants thereof.

It is possible that the growth of MnO NPs under kinetic control may result in the formation of octapod particles, as the growth of similar octapod particles through kinetic NP growth was recently reported for rhodium particles. Zhang et al. showed that the morphology of rhodium particles could be controlled through carefully tuning the precursor decomposition rate. It was shown that the rate at which a rhodium containing precursor was hot-injected into a mixture containing rhodium NP seeds determined the final shape of the particle. Slow injection of precursor resulted in the formation of nanocubes, whilst rapid precursor injection resulted in the formation of octapod particles, which grew due to rapid addition of monomers to the $\{111\}$ surfaces, causing the growth of eight protrusions in the $\langle 111 \rangle$ direction.[217]

Evidence for the thermodynamic/kinetic control of NP growth in the current MnO system can be seen when examining the morphologies of the products obtained under hold step or non hold step conditions (see Fig. 5.7 and Table 5.2 for a reminder of the product morphologies obtained for each precursor). It was anticipated that the inclusion of a hold step would encourage slow decomposition of precursor, and the formation of thermodynamic products — which would be particles with either flat edges (such as cubes or octahedra) or isotropic spheres. Inspection of the left-hand (hold-step) image from each precursor in Fig. 5.7 reveals that all precursors agree with this expectation, with the exception of Mn₆-pivalate which yields octapods irrespective of the heating regime (suggesting that the hold-temperature for Mn₆-pivalate was poorly chosen, as previously discussed).

The picture is more complicated when no hold step was used, and the products obtained are dependent on the precursor used. This indicates (as was discussed earlier in section 5.4.3) that the crystal growth kinetics can be influenced by ligands that are present in the starting material. For [Mn₃O(OAc)₆(py)₃], spherical particles were formed regardless of the heating regime, which implies that these particles grow via isotropic monomer addition to the particle surface and that there is no surface specificity for growth. For [Mn₃O(piv)₆(py)₃], bypassing the hold step narrows the size distribution and results in larger particles. This indicates that particle growth using this precursor most likely proceeds via Ostwald ripening, in which larger particles grow at the expense of smaller par-

ticles. The mechanism of Ostwald ripening was previously discussed in Chapter 1. As was discussed in the previous section, Ostwald ripening may be facilitated if the particle surfaces are covered with short pivalate molecules, which cannot physically separate particles in solution as well as the long chain surfactants OA and OAm are able to. For $[\text{Mn}_3\text{O}(\text{benz})_6(\text{py})_2(\text{H}_2\text{O})]$, bypassing the hold step resulted in the formation of polydisperse and poorly defined particles (Fig. 5.7 f). In this NP sample there was no clear shape preference and some multipod particles were formed. Twinning of particles was also visible (Fig. 5.17), implying that rapid and uncontrolled growth of particles was occurring. Such uncontrolled growth could be a consequence of having weakly-bound benzoate molecules near the particle surface, which will inhibit stabilisation by OA and OAm.

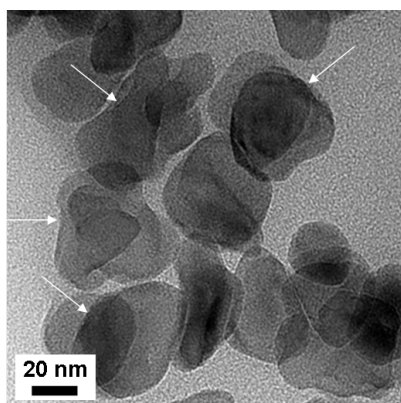


Figure 5.17: TEM image of twinned MnO particles (highlighted by arrows) formed when using $[\text{Mn}_3\text{O}(\text{benz})_6(\text{py})_2(\text{H}_2\text{O})]$ and no hold-step.

For $[\text{Mn}_3\text{O}(\text{OAc})_6(\text{HIm})_3][\text{OAc}]$, Mn_6 -pivalate and Mn_{12} -acetate, bypassing the hold step resulted in the formation of octapod particles, implying that preferential growth in the $\langle 111 \rangle$ direction is occurring, which can be rationalised as follows. In the current system, the presence of strongly-binding OA and weakly binding OAm will influence the growth of the MnO NPs. OA has a high affinity for the $\{100\}$ surfaces, whereas OAm exhibits weaker and non-specific binding to surfaces. This will leave the $\{111\}$ facets exposed, and during particle growth monomers will arrive at the $\{111\}$ facets, as the $\{100\}$ are capped by OA. Under thermodynamic conditions (such as the extended time spent at a reduced temperature hold-step) monomers that arrive at the particle surface will have sufficient time to diffuse evenly across the particle surface, giving rise to particles with thermodynamically favoured morphologies, such as the spheres observed for $[\text{Mn}_3\text{O}(\text{OAc})_6(\text{HIm})_3][\text{OAc}]$ and Mn_{12} -acetate. Conversely, under kinetic conditions (such as when the hold-step is bypassed) there is a rapid influx of monomers arriving at

the {111} facets of a particle's surface, and there is insufficient time for monomer diffusion across the particle surface to occur. As the rate of monomer arrival at the {111} facets is greater than the rate of monomer diffusion away from the {111} facets, growth in the $\langle 111 \rangle$ direction occurs, and octapod particles form.

Role of reaction temperature on particles obtained using Mn₁₂-acetate

The above discussions show the importance of the heating regime during the reflux synthesis of MnO NPs, as the reaction heating profile can determine the growth mode of nanoparticles. Furthermore, it was found that the morphology of nanoparticles was also susceptible to subtle changes in the reaction temperature. The use of a hold step in the synthesis of particles using Mn₁₂-acetate as a precursor was found to be a prerequisite in the formation of monodisperse spherical particles (Fig. 5.7k), and it was found that the size of the spherical particles could be varied (whilst keeping the size distribution narrow) simply by heating the reaction to higher temperatures after the hold step. For example, following a 2 hour hold step at 230 °C, heating the reaction to 290 °C gave 7 nm particles, and heating to higher temperatures of 300 °C and 310 °C yielded 11 nm and 17 nm particles respectively (Fig. 5.18a–c). The size distributions of these particles were very narrow, with mono- and multi-layer assemblies readily formed on the TEM grid, as shown in Fig. 5.18d,e).

The increase in particle size is most probably caused by increased monomer reactivity at higher temperatures.[31] This is a promising result, as the narrow size distribution of these particles makes them good candidates for further magnetic characterisation, as they may exhibit size dependent magnetic behaviour.

The above discussions show that through careful tuning of the reaction conditions it is possible to optimise NP synthesis. It is therefore important to examine all possible variables thoroughly, as often relatively subtle changes to the reaction protocol can have pronounced effects on the product morphology. Both spherical and octapod particles were synthesised with narrow size distributions, and these particles are excellent candidates for magnetic characterisation, as they may show interesting size or shape dependent properties. Magnetic characterisation was performed and the results are given in the following

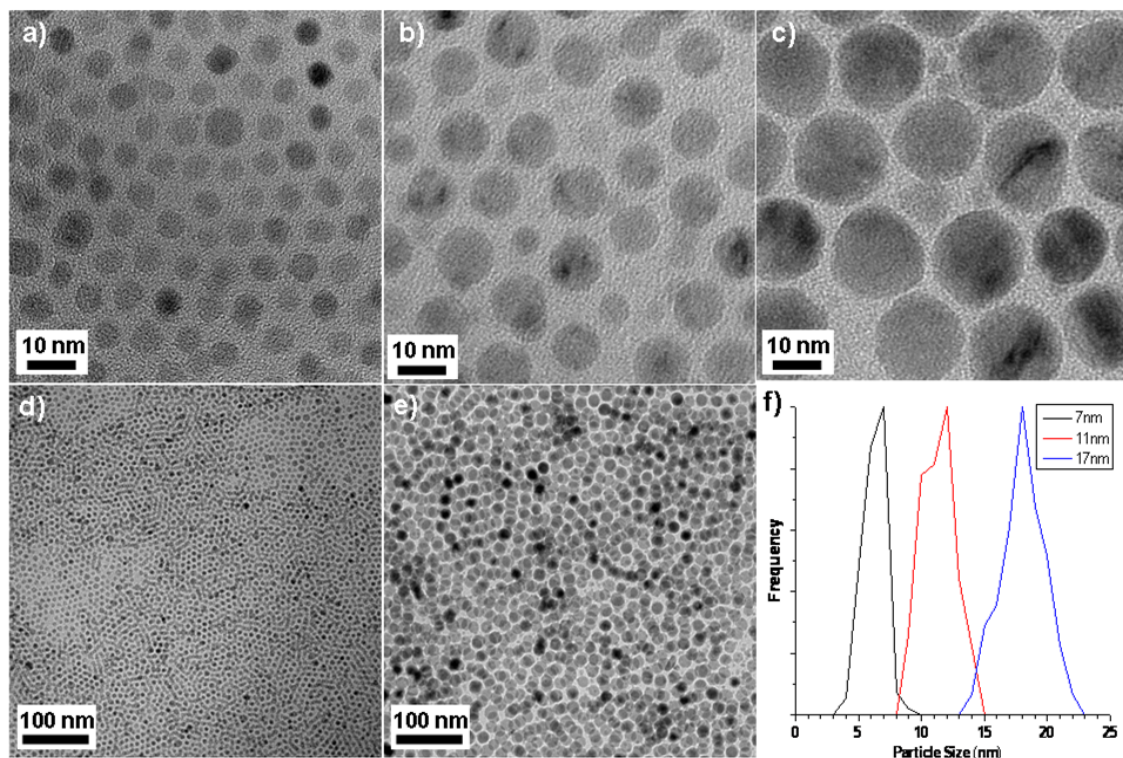


Figure 5.18: TEM images of the spherical particles obtained at different reaction temperatures a) 290 °C, b) 300 °C and c) 310 °C. Superlattices obtained from the d) 7 nm and e) 17 nm particles and f) the corresponding size distributions for each sample.

section.

5.4.5 Magnetic Characterisation

Manganese oxides are common magnetic materials, due to the magnetic moments of the Mn^{2+} and Mn^{3+} ions. Bulk MnO is antiferromagnetic, containing Mn^{2+} ions with a $3d^5$ electron configuration. The high number of unpaired electrons enable MnO NPs to be used as MRI contrast agents, enhancing contrast in T_1 -weighted images.[57] Samples were prepared for magnetic measurements as described in Chapter 2. Data was collected for the spherical 7 nm, 11 nm and 17 nm spherical particles synthesised using Mn_{12} -acetate, and the 85 nm octapod particles synthesised using $[\text{Mn}_3\text{O}(\text{OAc})_6(\text{HIm})_3][\text{OAc}]$. The obtained data was corrected for diamagnetism and the corresponding plots are given in Figs. 5.19 and 5.20 (for the spherical particles) and Fig. 5.22 (for the octapod particles).

The data is summarised in Tables 5.3 and 5.4 (for the spherical and octapod particles, respectively).

Particle size	M_r (emu/g)	M_s (emu/g)	H_c (T)
7 nm	1.53	2.62	0.54
11 nm	0.33	1.06	0.49
17 nm	0.09	0.18	0.00

Table 5.3: M_r (remnant magnetisation), M_s (saturation magnetisation), and H_c (coercivity) values of spherical MnO nanoparticles at 5 K.

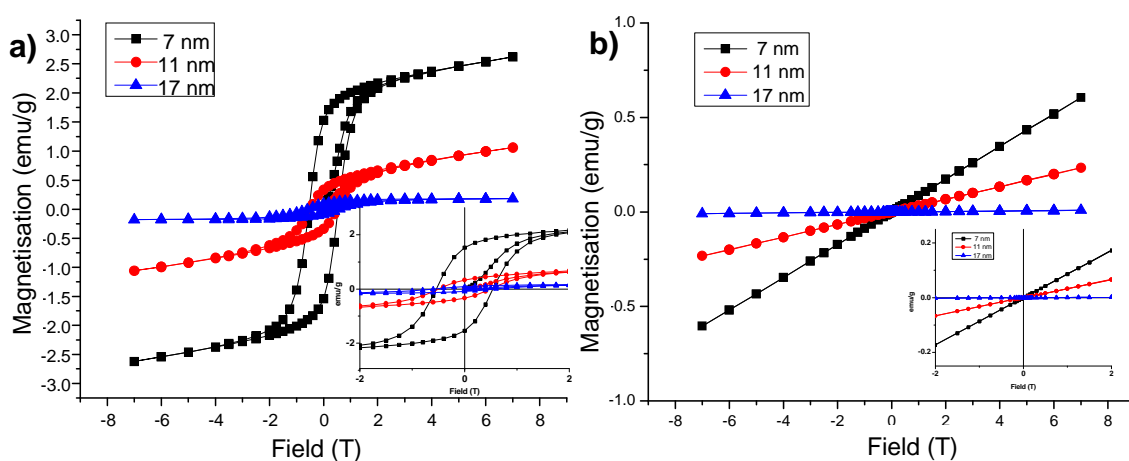


Figure 5.19: Hysteresis loops for spherical MnO particles of various sizes recorded at a) 5 K and b) 100 K. Inset for each is an expansion of the region near the origin.

For the spherical particles a clear decrease in magnetisation can be seen with increasing particle size, with M_r , M_s and H_c values decreasing as the particles get bigger. The behaviour of the small particles is interesting, and contradicts the expected behaviour of bulk MnO, which is antiferromagnetic with $T_N \approx 125$ K.[183] The anomalous properties of nanoparticles (be they optical, catalytic or magnetic) are often explained in terms of the increased number of surface atoms compared to bulk materials, as shown in Fig. 5.21.

For magnetic nanoparticles, the spins of the surface atoms are believed to be misaligned with the spins of the particle core.[106] This ‘canting’ of surface spins is believed to be responsible for the non-linear size dependence of magnetic properties seen for mag-

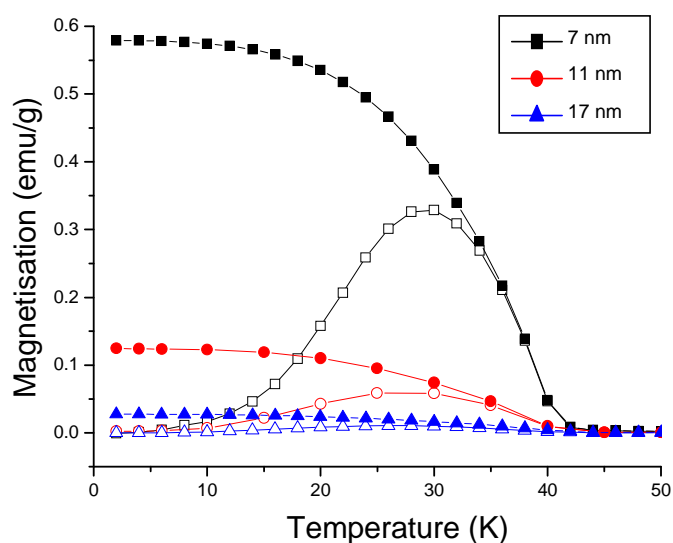


Figure 5.20: Zero field cooled (open symbols) and field-cooled (closed symbols) magnetisation of spherical 7, 11 and 17 nm MnO particles in an applied field of 100 Oe. The blocking temperature was determined to be ~ 30 K for each sample.

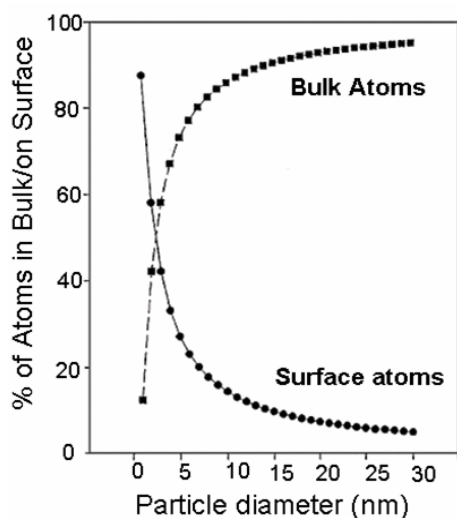


Figure 5.21: Calculated surface to bulk atom ratios for spherical nanoparticles. Adapted from ref [218].

netic nanoparticles. For ferromagnetic and ferrimagnetic materials (like Fe_3O_4), canting of surface spins means that smaller particles will exhibit reduced magnetisation, as misaligned surface spins disrupt the ferro- or ferrimagnetic ordering of core spins.[107] This effect is less pronounced for larger particles as they have a lower proportion of surface spins. In contrast, antiferromagnetic materials (such as MnO) will experience an increase in magnetisation with decreasing size, due to the larger number of non-compensated surface spins. This means smaller antiferromagnetic particles contain a greater proportion of non-antiferromagnetically aligned spins, and so behave more like a ferromagnet. It would

appear that in the current example, the spherical MnO NPs follow the same trend, since there is a clear increase in M_r , M_s and H_c as the particles get smaller — indicating that the contribution from canted surface spins is more pronounced for the small 7 nm particles compared with the larger 11 and 17 nm particles.

If the anomalous magnetic properties are in fact due to canting of surface spins, then the octapod particles provide an interesting model as their branched shape allows for a greater number of surface atoms versus spherical particles. Hence, non-zero values of M_r , M_s and H_c are expected, despite the fact that the particle size (~ 85 nm) is much greater than the largest of the spherical particles (17 nm). The contribution of surface spin canting in the largest of the spherical particles (17 nm) was negligible, and small M_r , M_s and H_c values were obtained (Table 5.3). If the magnetic properties of the large octapod particles (~ 85 nm) followed the inverse size-dependence trend observed for spherical particles then even smaller M_r , M_s and H_c values would be expected. However, this was found not to be the case, as shown in the magnetic data from the octapod particles given in Fig. 5.22 and summarised in Table 5.4.

Temperature (K)	M_r (emu/g)	M_s (emu/g)	H_c (T)
5 K	0.34	2.69	0.34
20 K	0.26	2.25	0.26
300 K	0.00	0.77	0.00

Table 5.4: M_r (remnant magnetisation), M_s (saturation magnetisation), and H_c (coercivity) values of ~ 86 nm octapod MnO nanoparticles obtained from $[\text{Mn}_3\text{O}(\text{OAc})_6(\text{HIm})_3][\text{OAc}]$ with no hold step at 5, 20 and 300 K.

It can clearly be seen that the magnetic properties of octapod MnO particles do not follow the same trend observed by spherical MnO particles. Despite their large size, the octapod particles exhibit greater M_r , M_s and H_c values than the 17 nm spherical particles. In fact, the magnetic properties of the octapod particles are more similar to the 7 and 11 nm spherical particles. It is therefore possible to conclude that surface spin canting contributions in antiferromagnetic NPs depend strongly on the particle morphology. Branched structures (such as octapods) possess a greater number of surface atoms than

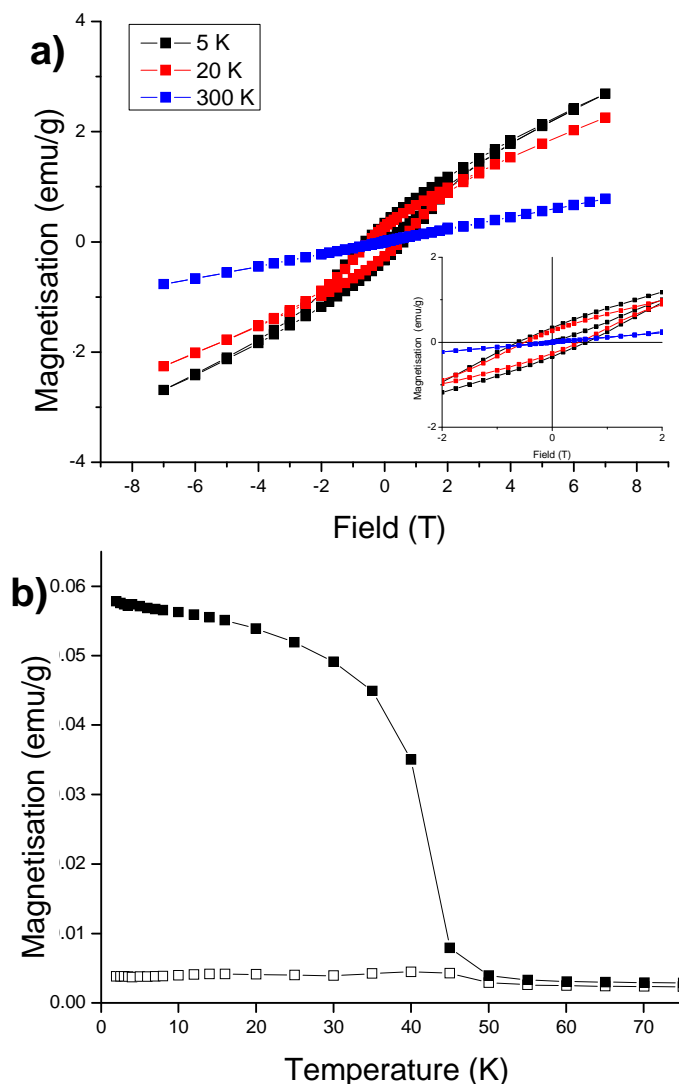


Figure 5.22: a) Hysteresis loops for the 85 nm octapod MnO particles recorded at various temperatures. Inset is an expansion of the region near the origin. b) Zero field cooled (open symbols) and field-cooled (closed symbols) magnetisation from the same sample in an applied field of 100 Oe.

their isotropic counterparts and MnO octapods can exhibit weak ferromagnetic properties, despite their large size.

It should be noted that the above discussion of the anomalous magnetic properties of MnO particles has been in terms of canted surface spins, although the diffraction data presented in Section 5.4.2 indicated that small amounts of tetragonal Mn_3O_4 exist in the particles, which may give rise to MnO- Mn_3O_4 core-shell particles. The MnO- Mn_3O_4 core-shell system has received considerable attention due to the potential exchange inter-

actions between the antiferromagnetic MnO core and ferrimagnetic Mn₃O₄ shell. Systems possessing highly crystalline MnO-Mn₃O₄ particles show exchange bias, evident as a shift in the hysteresis loop.[187, 188] In our system no loop-shift is visible, implying there is no well defined exchange bias mechanism in place and that the MnO particles do not contain a well defined Mn₃O₄ shell. This is probably due to the thinness of the Mn₃O₄ shell present in our particles, which arises during the washing procedure as discussed earlier in Section 5.4.2. Furthermore, if there was a significant contribution from Mn₃O₄ then much higher saturation magnetisation values would be expected. Literature values of M_s for Mn₃O₄ nanoparticles are much higher than the M_s values given in Tables 5.3 and 5.4, which are much more similar to the M_s literature values given for MnO.[183]

5.5 Conclusions and Further Work

5.5.1 Further work: Iron Complexes as Nanoparticle Precursors

In the present chapter we have seen that polynuclear manganese complexes can be used as precursors for manganese oxide particles in a range of different sizes and shapes, which were shown to exhibit morphology-dependent magnetic properties. This is a promising result, and would suggest that other transition metal carboxylate precursors could be used to synthesise metal oxide NPs. Within the Murrie research group there is considerable research experience into the synthesis of transition metal complexes, and a number of preparations for polynuclear iron complexes have been established. Given the technological importance of iron oxide NPs (as was discussed in Chapters 1 and 3), it was therefore appropriate to determine if polynuclear iron complexes could also be as precursors to synthesise iron oxide NPs. Preliminary results showed that it is possible to synthesise magnetite NPs using iron complexes of the general formula [Fe₃O(O₂CR)₆L₃], where R = acetate, pivalate, benzoate and 2-phenoxybenzoate. Representative TEM images from a sample of typical Fe₃O₄ particles are given in Fig. 5.23. There is significant scope for further work in optimising the synthesis of magnetite NPs using these precursors, and for investigating more thoroughly the contributions that each carboxylate ligand has on magnetite nanoparticle growth kinetics. We will discuss the role of iron-containing polynuclear precursors in magnetite NP synthesis in more detail in the following Chapter,

which looks at the synthesis of doped magnetite particles.

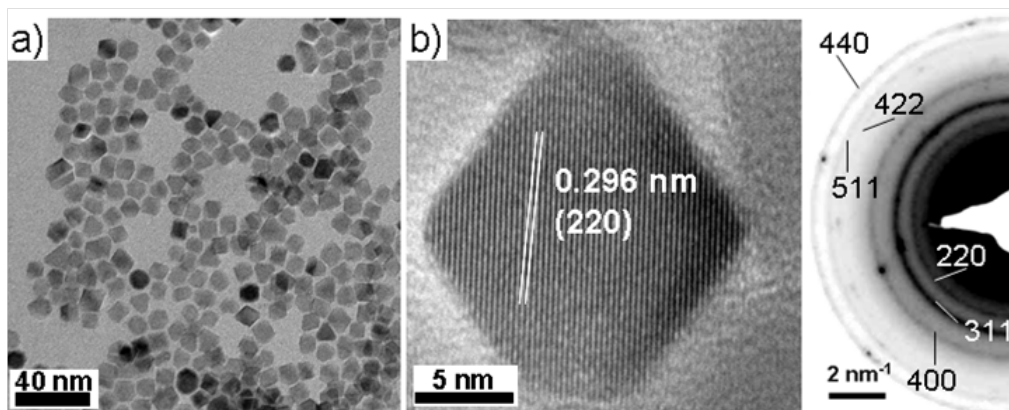


Figure 5.23: a) Representative TEM image of truncated octahedral particles obtained from the $[\text{Fe}_3\text{O}(\text{benz})_6(\text{H}_2\text{O})_3]$ precursor. b) HRTEM image and c) SAED pattern confirm the particles to be magnetite.

5.5.2 Conclusions

In this chapter a series of polynuclear carboxylate precursors were synthesised to be used as precursors for metal oxide NPs. The motivation for this was to see what effect the ligands present in the precursor had on the particle formation mechanisms, and in turn how the ligand effected the final morphology of the particle. A number of precursors with the general formula $[\text{M}_3\text{O}(\text{O}_2\text{CR})_6\text{L}_3]$ ($\text{M} = \text{Mn}, \text{Fe}$) were prepared, which incorporated a variety of different ligands ($\text{R}, =$ acetate, benzoate and pivalate, $\text{L} =$ pyridine and imidazole). Precursors were chosen so that different combinations of ligands could be used, and hence the impact of each ligand on particle morphology could be systematically varied. For the manganese precursors it was found that a variety of NP shapes including spherical, rounded cube, octahedral, porous and octapod were obtainable, depending on the precursor used. A number of larger manganese-containing compounds were also used as precursors for metal oxide NPs; the hexanuclear complex Mn_6 -pivalate and the well-known dodecanuclear complex Mn_{12} -acetate were used, in each case particles were formed, indicating that the nuclearity of a NP precursor can be increased without detriment to the outcome of NP formation.

The decomposition characteristics of the manganese precursors were assessed using

TGA. The TGA data were used to determine the temperatures where the precursors decomposed, these temperatures were then chosen as hold temperatures in the NP synthesis. The inclusion or exclusion of a hold step in MnO NP synthesis dictated if the particles grew under thermodynamic or kinetic conditions respectively. Under kinetic (no hold-step) conditions, octapod particles were predominant. Octapod formation was rationalised in terms of the rapid precursor decomposition supplying a high influx of monomers to the {111} surfaces, which resulted in rapid particle growth in the $\langle 111 \rangle$ directions. When a hold step was used, monomer influx was reduced and the particle grew under equilibrium conditions, which usually resulted in the formation of isotropic shapes, such as spheres and rounded cubes. The ligands present in each precursor were found to influence the adsorption of OA and OAm surfactant molecules on the particle surface. Bulky ligands like pivalate are thought to hinder particle stabilisation by disrupting packing of OA and OAm on the particle surface, which results in inadequately stabilised particles. Poorly-stabilised particles are more likely to coalesce, forming large and poorly-defined particles — as was observed when pivalate was used.

Given the biological applications of magnetic manganese oxide particles, there is scope for further research to assess the biological compatibility of these particles and their potential uses as MRI contrast agents, for example. Furthermore, the array of interesting shapes that are readily attainable means that investigation into the cellular uptake of particles as a function of particle morphology can be investigated, as a very recent study of silver NPs of various shapes showed that particle toxicity was dependent on particle morphology.[219] Preliminary investigations into the cellular uptake of MnO particles as a function of shape are currently in progress at the Centre for Cell Engineering at the University of Glasgow. The porous particles obtained using the pivalate precursor are also of interest as potential drug storage/delivery materials, or for potential applications in catalysis.

This chapter has demonstrated the significant contribution that the metal containing precursor can have during NP synthesis, in terms of determining the product size and shape. By altering the nature of the ligands that surround the metal centre, specific particle morphologies can be obtained — meaning that rational design of precursors could lead to products with pre-determined characteristics. It was envisaged that rational design of

precursors could not only determine particle morphologies, but also their compositions — if heterometallic precursors were used, for example. This idea of using heterometallic precursors as potential precursors to bimetallic particles will be explored in further detail in the next chapter, in which various synthetic approaches to obtain bimetallic particles are investigated.

Chapter 6

Synthesis of bimetallic magnetic nanoparticles

The term ‘composite’ and its derivatives are generalisations used to describe a sample which contains two or more distinct materials. For example, core-shell particles are considered composite NPs, as are particles which contain dopant ions. In this Chapter two main strategies will be employed to obtain composite nanoparticles, these are the ‘multi-source’ and ‘single-source’ approaches. In the multi-source approach, a composite material is obtained by the reaction of two (or more) precursors, with each precursor supplying just one type of metal to the final product. In the single-source approach, a molecule that contains more than one type of metal atom is used as a precursor, and both metal atoms in the precursor are incorporated into the resulting composite material.

Composite nanomaterials are of interest to researchers as their unique and tunable properties have a range of applications across many fields. This Chapter relates to the synthesis of gadolinium oxide-iron oxide core-shell particles (denoted $\text{Gd}_2\text{O}_3\text{-Fe}_3\text{O}_4$) and also to gadolinium-doped metal oxide particles (denoted $\text{Gd:Fe}_3\text{O}_4$). These magnetic composites have applications both as magnetic resonance imaging (MRI) contrast agents and in magnetic fluid hyperthermia (MFH), the physical processes of which were described back in Chapter 1. It is clear that the magnetic properties of magnetic nanoparticles (MNPs) coupled with their small size that places them on the same scale as biological structures has been the main driver for research in the nano-medicine field, and the biocompatibility of iron oxide means that iron oxide particles are excellent candidates as

potential host materials for dopant ions or as the biocompatible ‘shell’ of a core-shell particle.

Magnetic ion doping can exploit the magnetic characteristics of the dopant ion, or rely on a structural change caused by doping which results in new magnetic phenomena. For example, Selinsky et al. recently showed that the Curie temperature (T_C) of $\text{Eu}_{1-x}\text{Gd}_x\text{S}$ nanoparticles could be controlled by varying the amount of Gd^{3+} present as a dopant. A maximum T_C of 29.4 K was observed for Gd dopant levels of 5.3%. [59] Developing NP synthesis which can control the Curie temperature is an intensively studied field, especially for MFH applications. MFH treatment requires precise control over the localised heating caused by MNPs in an alternating magnetic field. The ideal operating temperature for MFH is $\sim 45^\circ\text{C}$, as above this temperature healthy tissue may be harmed. It would therefore be desirable to develop MFH materials that had a T_C of 46°C , which would become paramagnetic should accidental over-heating occur. In this way the heating capabilities of a MFH agent can effectively be ‘switched off’ above a certain temperature — meaning the material has a built-in safety mechanism. [220] At present there are numerous potential candidate materials that may be used for MFH and MRI applications.

One such category of potential materials for MRI and MFH applications are ferromagnetic perovskites, in which cation doping can convert normally antiferromagnetic perovskites into ferromagnetic materials. For example, the LaMnO_3 perovskite is a monovalent (Mn^{3+}) antiferromagnetic insulator, yet by replacing La^{3+} ions for Sr^{2+} ions, the magnetic properties can be altered. This is due to a change in structure from orthorhombic ($Pbnm$) to rhombohedral ($R\bar{3}c$) symmetry, and a change in valence of manganese ($\text{Mn}^{3+} \rightarrow \text{Mn}^{4+}$). A combination of both of these effects results in an antiferromagnetic to ferromagnetic transition in $\text{La}_{1-x}\text{Sr}_x\text{MnO}_3$ for $x \approx 0.1$. [221]

Nanoparticles of MnZn ferrites are another material that has been widely studied for MRI and MFH applications. MnZn ferrites have the general formula $(\text{Mn}_a\text{Zn}_b\text{O}_{a+b})(\text{Fe}_c\text{O}_{3c/2})$ and are normally prepared by the co-precipitation method, which allows for variation of a, b and c simply by varying the amount of the relevant metal precursor used in the reaction mixture. [222] Recently, the effect of doping Ln^{3+} ions into Mn-Zn ferrites was investigated. From the resulting $(\text{Mn}_{1-x}\text{Zn}_x)(\text{Fe}_{2-y}\text{L}_y)\text{O}_4$ species it was found that Ln^{3+} substitution into MnZn ferrites resulted in higher magnetisation values

and lower Curie temperatures.[223]

This chapter will primarily discuss synthetic approaches to create gadolinium and iron oxide composite materials, either as Gd_2O_3 - Fe_3O_4 core-shell particles or gadolinium doped magnetite particles. For core-shell particles iron oxide was chosen as the shell material given its biocompatibility and to limit leaking of Gd^{3+} ions from the particle into the bloodstream, as gadolinium ions are known to be toxic.[110] Gadolinium and iron oxide composite systems have the potential to act as MRI contrast agents due to the large magnetic moments of the Gd^{3+} and Fe^{3+} ions, which have been shown to improve contrast in T_1 and T_2 weighted MRI scans respectively.[124, 224] Furthermore, lanthanide-doped ferrite materials show increased magnetocrystalline anisotropy due to lattice strain caused by the differences in ionic radii between Ln^{3+} and iron ions. For $Gd:Fe_3O_4$ particles, this increase in magnetic anisotropy has been shown to improve performance in MFH experiments.[225] Initial attempts to synthesise composite particles utilised a two-precursor, multi source approach, and will be described in more detail in the following section.

6.1 Bimetallic Particles by the Multi-Source Approach

Initially, it was decided that the effect of the structure of metal precursor and the order of precursor addition on the morphologies and composition of bimetallic iron and gadolinium NPs would be investigated. It was thought that the order of reagent addition could dictate the morphology of the product, with simultaneous decomposition of gadolinium and iron containing precursors potentially leading to doped particles and subsequent, step-wise decomposition of gadolinium then iron precursors potentially leading to core-shell morphologies.

A paper published during this Ph.D project described a similar route to obtain lanthanide doped magnetite particles.[67] In this paper $Fe(acac)_3$ was refluxed in phenyl ether with $Ln(acac)_3$ (where $Ln = Sm, Eu$ and Gd) for 22 hours in the presence of OA, OAm and HDD. The simultaneous decomposition of iron and lanthanide acetylacetonates yielded $Ln:Fe_3O_4$ particles. However, there was little discussion of the $Gd:Fe_3O_4$ particles and only the Sm doped magnetite particles were characterised in any detail. STEM EDX

measurements appeared to confirm the presence of Sm in the particles, though no quantitative discussion was provided. Despite these limitations, this publication proved that doped particles could be obtained by simultaneous decomposition of iron and lanthanide carboxylate precursors.

In contrast to the synthesis of doped particles, particles with a core-shell morphology require the decomposition of metal containing precursors onto pre-formed nanoparticles. This can be achieved using a multi-pot process, whereby particles are isolated from one reaction mixture and added into another vessel to act as seeds for shell growth.[226] An alternative method for core-shell growth is the one-pot processes, in which the core particles are formed in-situ before the shell components are added separately, usually via hot-injection. The one-pot approach has been used to synthesise a range of particles such as Au-Fe₃O₄ ‘dumbbell’ composites[43] and well defined FePt-CdSe core-shell particles.[227] At the time of writing there were no published methods to synthesise Gd₂O₃-Fe₃O₄ or Fe₃O₄-Gd₂O₃ core-shell particles, though a few reports did exist which described iron oxide and gadolinium composites. For example, Choi et al. described the synthesis of a MnFe₂O₄-SiO₂ core-shell system where the SiO₂ shell was further functionalised with amorphous gadolinium oxide carbonate (Gd₂O(CO₃)₂).[228] The combination of Mn-ferrite core and Gd³⁺ embedded in the particle shell enabled these particles to work as ‘multimodal’ MRI contrast agents, enhancing contrast in both T₁ and T₂ weighted scans. We decided to synthesise core-shell particles in which the gadolinium core was coated with an iron oxide shell and not the other way around for two reasons: iron oxide has excellent biocompatibility; and to minimise the leakage of free Gd³⁺ from the particles. If a particle is to be used in a physiological system, toxicity has to be considered and the Gd³⁺ ion is considered especially toxic due to the similarity of ionic radii between the Ca²⁺ ion (114 pm) and the Gd³⁺ ion (107.8 pm). The similarity between ionic radii means that Gd³⁺ is able to disrupt the ion channels used by Ca²⁺, impeding calcium-mediated physiological processes.[229] For this reason Gd³⁺ is currently only approved for clinical use in stable chelated forms.[110]

To attempt to synthesise Gd:Fe₃O₄ and Gd₂O₃-Fe₃O₄ core-shell particles, a series of reaction conditions were devised, which varied both the metal precursor and the order of reagent addition. The experimental details are provided in the following section.

Precursor	Condition	
	Simultaneous	Subsequent
Gd(acac) ₃	Fe(CO) ₅	Fe(CO) ₅
	Fe(acac) ₃	Fe(acac) ₃
Gd(OAc) ₃	Fe(CO) ₅	Fe(CO) ₅
	Fe(acac) ₃	Fe(acac) ₃

Table 6.1: The eight reactions performed to investigate the effect of precursor on iron and gadolinium bimetallic particles.

6.1.1 Experimental

A series of reactions were performed to investigate the effect of the structure of the metal precursor and the order of precursor addition on the morphologies and compositions of bimetallic iron and gadolinium NPs. Four precursors were chosen, two for each metal. Fe(CO)₅ and Fe(acac)₃ were chosen as the iron sources, with Gd(OAc)₃ and Gd(acac)₃ chosen as the gadolinium sources. These precursors were used as they have been previously shown to be versatile precursors in the synthesis of oxide NPs. For each reaction an identical solvent / surfactant mixture was used, consisting of OAm : OA : BE in the ratio 4.5 : 3 : 2.5 mL. These ratios were chosen as they have been used previously to synthesise Gd₂O₃ particles[119] and we have seen in Chapters 4 and 5 that the above solvent ratios can be used to synthesise rare-earth and iron oxide particles. For each of the two gadolinium containing precursors (Gd(acac)₃ and Gd(OAc)₃) an iron containing precursor (either Fe(acac)₃ or Fe(CO)₅) was decomposed in the reaction vessel at the same time as the gadolinium precursor (to create gadolinium doped iron oxide, referred to as *simultaneous* decomposition) or after the gadolinium precursor (to create Gd₂O₃-Fe₃O₄ core-shell particles, referred to as *subsequent* decomposition). This gave a total of eight possible reactions, as described in Table 6.1. In addition, four control reactions were performed using just one of each of the precursors.

Gd₂O₃-Fe₃O₄ Core-shell Synthesis

For the *subsequent* reactions the iron precursor was added to the mixture after Gd₂O₃ particles had been formed. Briefly, gadolinium precursor (0.1 mmol) was dissolved by heating the mixture to 110 °C under a nitrogen flow for 30 minutes, resulting in a pale yellow solution. The nitrogen flow was reduced and the mixture was then rapidly heated to 310 °C for 30 minutes, during which time the mixture darkened to pale brown, indicating particle formation had occurred. The mixture was then cooled to one of two temperatures, depending on the iron precursor that was to be added.

In reactions where Fe(CO)₅ was added, the mixture was cooled to 110 °C and 0.15 mL Fe(CO)₅ was rapidly injected into the flask before the mixture was slowly heated to 310 °C for 30 minutes, during which time the colour changed from pale yellow to black, indicating the formation of particles. In the case of Fe(acac)₃, the mixture was cooled to room temperature and 0.5 mmol Fe(acac)₃ and 1.5 mmol HDD were added. The mixture was then slowly heated under a nitrogen flow to 110 °C for 30 minutes, then the flow was reduced and the mixture was further heated to 200 °C for 60 minutes then finally 310 °C for 30 minutes, during which time the reaction darkened from orange through brown before becoming black on reflux. The 200 °C hold-step was included to encourage the nucleation of monodisperse particles, and is common in syntheses using metal acetylacetonate compounds.[23] After the reactions had finished, the mixtures were cooled to room temperature. The Fe(CO)₅ mixture was opened to air and vigorously stirred for a further hour to allow complete conversion of Fe to Fe₃O₄. The particles were then precipitated with ethanol and collected via centrifugation.

Gd:Fe₃O₄ Doped Particle Synthesis

For doped particles, the iron and gadolinium precursors were heated to reflux together. In the case of Fe(CO)₅, the gadolinium precursor (0.1 mmol) was heated to 110 °C under a nitrogen flow for 30 minutes, giving a clear yellow solution. The flow was reduced, 0.15 mL Fe(CO)₅ was rapidly injected and the mixture slowly heated to 310 °C for 30 minutes. For Fe(acac)₃, 0.1 mmol of the gadolinium precursor, 0.5 mmol Fe(acac)₃ and 1.5 mmol HDD were mixed and then slowly heated under a nitrogen flow to 110 °C for 30 minutes, then the flow was reduced and the mixture was further heated to 200 °C for

60 minutes then finally to 310 °C for 30 minutes. The NPs were precipitated with excess ethanol and collected via centrifugation.

Control Reactions

For the control reactions, only one precursor was added to the reaction mixture. The control reactions served to prove that Gd_2O_3 or Fe_3O_4 particles could be obtained using the reaction conditions described above, but also to give an indication of the size and shape of particle that would be obtained for each precursor.

6.1.2 Results and Discussion

Control Reactions.

TGA analysis of the gadolinium-containing precursors was performed to compare their decomposition characteristics, as we have seen in the previous chapter that TGA can provide valuable insight into precursor decomposition and hence NP formation mechanisms. The TGA plots for each precursor are given in Fig. 6.1.

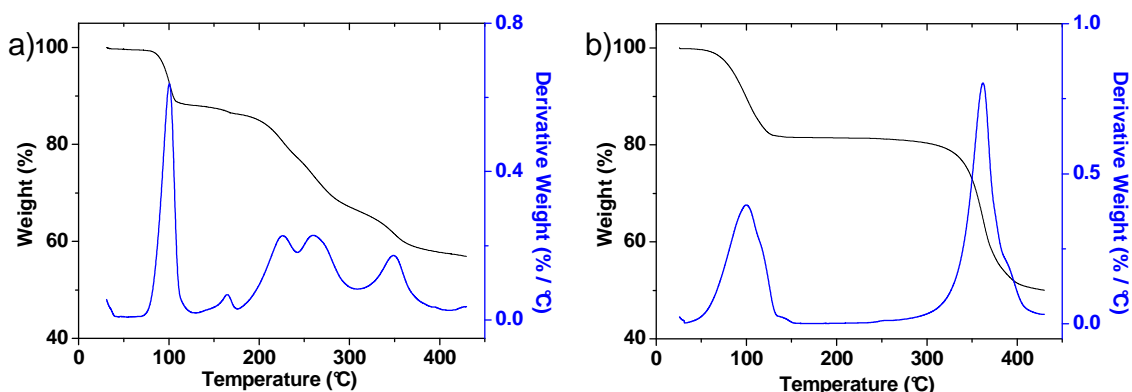


Figure 6.1: TGA data (black) and corresponding derivative weight-loss plots (blue) for a) $\text{Gd}(\text{acac})_3$ and b) $\text{Gd}(\text{OAc})_3$.

Losses of 13% and 19% for $\text{Gd}(\text{acac})_3$ and $\text{Gd}(\text{OAc})_3$ respectively occur around 100 °C, corresponding to the loss of 4 water molecules from each precursor (each precursor is sold as a hydrate, with an unspecified number of coordinated water molecules). Beyond 100 °C, the decomposition profiles of each precursor are quite different. $\text{Gd}(\text{acac})_3$ shows steady gradual decomposition with minor peaks in the derivative weight loss plot, which

can be assigned to the decomposition of an (acac^-) ligand to an (OAc^-) ligand, which occurs at ~ 150 , 235 and 270 °C for each subsequent (acac^-) ligand.[230] On the other hand, $\text{Gd}(\text{OAc})_3$ remains stable until ~ 310 °C then there is sudden onset of decomposition, which is presumably due to the decomposition of acetate ligands and the formation of intermediate gadolinium oxides and hydroxides. The chosen reaction temperature of 310 °C is therefore high enough to ensure decomposition of both $\text{Gd}(\text{acac})_3$ and $\text{Gd}(\text{OAc})_3$ precursors occurs and Gd_2O_3 NPs form. The TEM images of the Gd_2O_3 particles obtained from the gadolinium control reactions are given in Fig. 6.2, which confirm that NPs can be formed under the chosen reaction conditions.

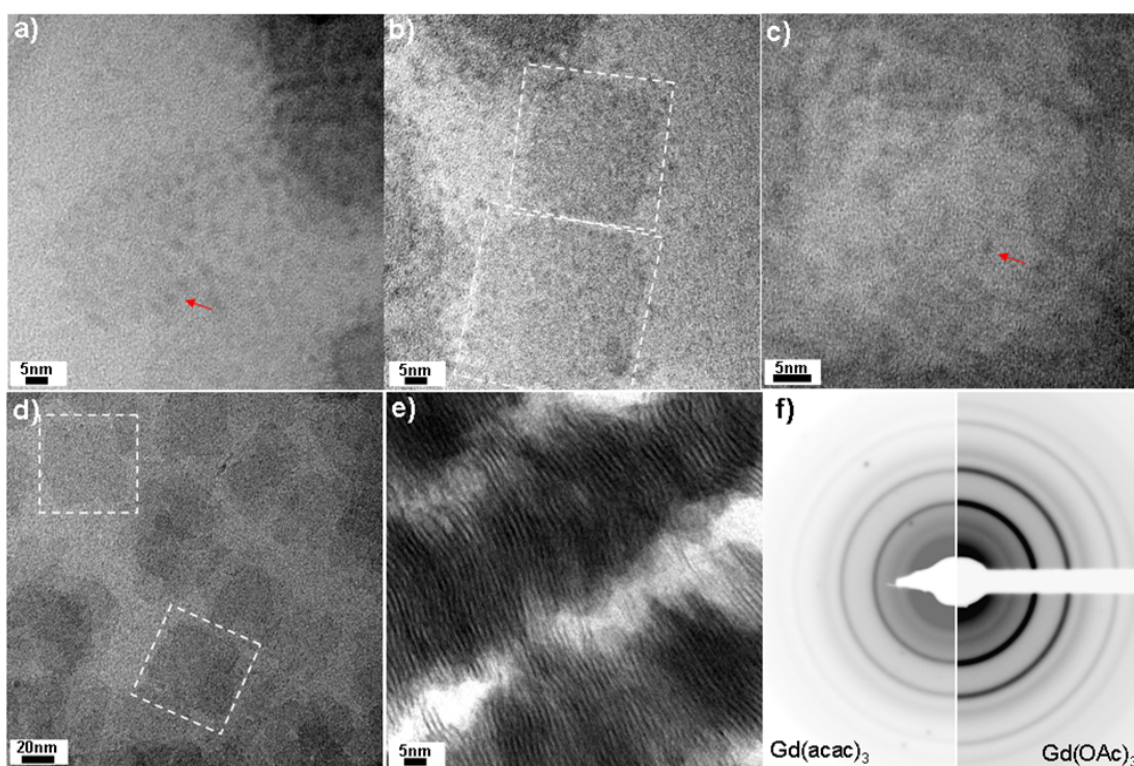


Figure 6.2: TEM images from a,b) $\text{Gd}(\text{acac})_3$ and c,d) $\text{Gd}(\text{OAc})_3$ control reactions. For each precursor the presence of both small 3 nm particles (red arrows) and thin square nanoplates (white boxes) can be seen. e) Face to face self assembly of nanoplates obtained using $\text{Gd}(\text{OAc})_3$. f) SAED patterns, showing an identical pattern for each precursor which agrees with the expected Gd_2O_3 pattern.

The TEM images of the particles obtained using $\text{Gd}(\text{acac})_3$ and $\text{Gd}(\text{OAc})_3$ (Fig. 6.2), show that under these reaction conditions it is possible to form Gd_2O_3 particles. For each

precursor, two distinct species formed. The first species are small ~ 3 nm particles, which are poorly defined and lack any visible shape preference (indicated by red arrow in Fig. 6.2a,c). These small particles are similar to the ‘sub-unit’ particles that formed the basic building blocks of the Ln_2O_3 nanowires seen in Chapter 4. The second species are thin nanoplates, with edge sizes 32 ± 3 nm (9%) and 40 ± 8 nm (20%) for $\text{Gd}(\text{acac})_3$ and $\text{Gd}(\text{OAc})_3$, respectively. These nanoplates are very thin, as can be seen by their poor contrast variation with the carbon support of the TEM grid. Face-to-face self assembly of these thin plates into arrays was also seen as shown in Figure 6.2e), from which a plate thickness of ~ 1.3 nm was estimated. This is close to the unit cell parameter of Gd_2O_3 , which is 1.1 nm. The formation of thin Gd_2O_3 nanoplates is consistent with previous reports using similar three-solvent systems.[119] Electron diffraction confirmed that the particles were Gd_2O_3 , although the smaller particles were too small and the thin nanoplates too thin to obtain images suitable to perform lattice spacing analysis.

We will now turn our attention to the iron oxide NPs obtained from the control reactions using $\text{Fe}(\text{acac})_3$ and $\text{Fe}(\text{CO})_5$. TEM images from these reactions are given in Fig. 6.3.

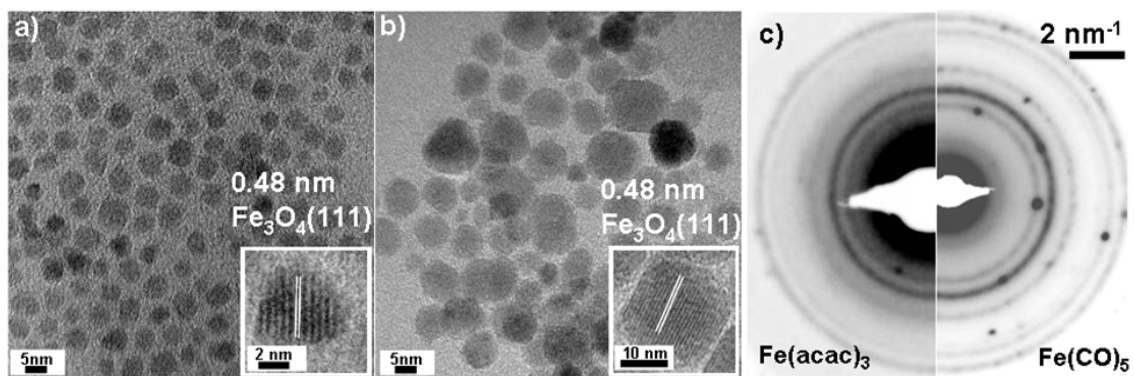


Figure 6.3: TEM images showing the particles obtained using a) $\text{Fe}(\text{acac})_3$ and b) $\text{Fe}(\text{CO})_5$. Inset for each is a HRTEM image showing the lattice fringes. c) SAED patterns, showing that magnetite particles are obtained in each instance.

Figure 6.3 shows that the morphology of the magnetite particle depends on the precursor chosen. Using $\text{Fe}(\text{acac})_3$ resulted in smaller and more uniform particles than using $\text{Fe}(\text{CO})_5$. The sizes of the obtained particles were 4.9 ± 1.0 nm (19 %) and 8.2 ± 2.2 nm (27 %) respectively. The particles obtained using $\text{Fe}(\text{acac})_3$ have narrow size distributions

and have a pseudo-spherical shape. The narrow size distribution is a result of controlled particle nucleation and growth, enforced by using a hold step in the heating regime at 200 °C. The use of heating hold steps is an established way to achieve high quality particles using metal acetylacetonate complexes,[21, 23] as was discussed previously in Chapter 3.

The difference in morphologies observed for these precursors will be due to their different reaction rates and nucleation habits. It is understood that the NP formation mechanism of $\text{Fe}(\text{CO})_5$ in a solution of oleic acid or oleylamine proceeds via the in-situ formation of an iron-oleate/iron-oleylamine complex which decomposes to give metallic Fe^0 NPs, that can be further oxidised to iron oxide.[30, 100] $\text{Fe}(\text{acac})_3$, on the other hand, does not produce metallic Fe^0 particles, giving instead Fe_3O_4 particles that can be converted to other forms of iron oxide (such as α or γ - Fe_2O_3) through controlled annealing. [23] From the above series of control reactions it is possible to conclude that the iron and gadolinium precursors are able to form iron oxide and gadolinium oxide nanoparticles under the chosen reaction conditions. This observation provides the basis for performing the simultaneous and subsequent decomposition reactions, the results of which are given in the following section.

$\text{Gd}(\text{acac})_3$ Reactions

$\text{Gd}:\text{Fe}_3\text{O}_4$ Particles by Simultaneous Decomposition

The TEM images for the particles obtained by simultaneous decomposition of $\text{Gd}(\text{acac})_3$ with either $\text{Fe}(\text{CO})_5$ or $\text{Fe}(\text{acac})_3$ are given in Fig. 6.4.

Gd_2O_3 - Fe_3O_4 Particles by Subsequent Decomposition

The TEM images for the particles obtained by decomposition of $\text{Gd}(\text{acac})_3$ followed by subsequent decomposition of either $\text{Fe}(\text{CO})_5$ or $\text{Fe}(\text{acac})_3$ are given in Fig. 6.5.

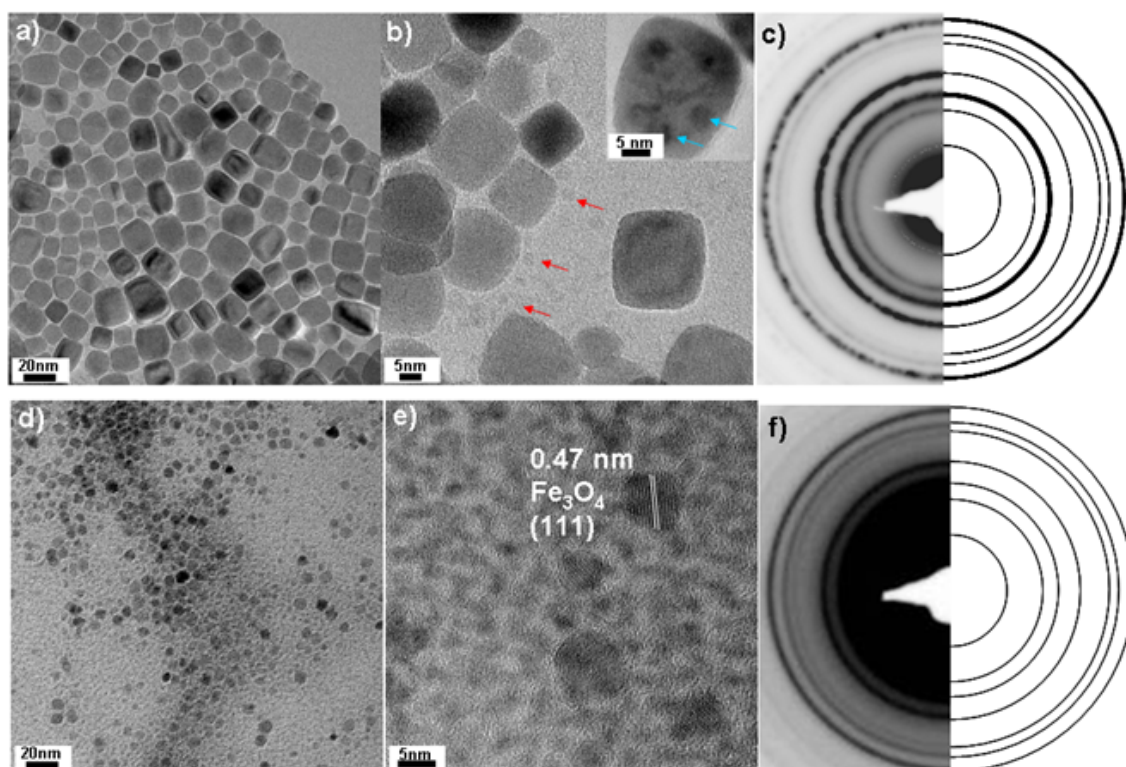


Figure 6.4: a,b) TEM images of the particles obtained by reaction between $\text{Gd}(\text{acac})_3$ and $\text{Fe}(\text{CO})_5$. Two species are visible: pseudo-cubic iron oxide particles and smaller Gd_2O_3 particles (indicated by red arrows). Inset is an image of a single magnetite particle, showing contrast variations. c) SAED of particles, showing agreement with simulated magnetite pattern. d,e) TEM images of particles obtained by reaction between $\text{Gd}(\text{acac})_3$ and $\text{Fe}(\text{acac})_3$, showing separate nucleation of Fe_3O_4 and Gd_2O_3 particles. d) Clustering of Gd_2O_3 particles. e) HRTEM image showing the magnetite particles alongside ~ 3 nm poorly defined Gd_2O_3 particles. f) SAED of particles, showing agreement with the expected magnetite pattern.

$\text{Gd}(\text{OAc})_3$ Reactions

$\text{Gd}:\text{Fe}_3\text{O}_4$ Particles by Simultaneous Decomposition

The TEM images for the particles obtained by simultaneous decomposition of $\text{Gd}(\text{OAc})_3$ with either $\text{Fe}(\text{CO})_5$ or $\text{Fe}(\text{acac})_3$ are given in Fig. 6.6.

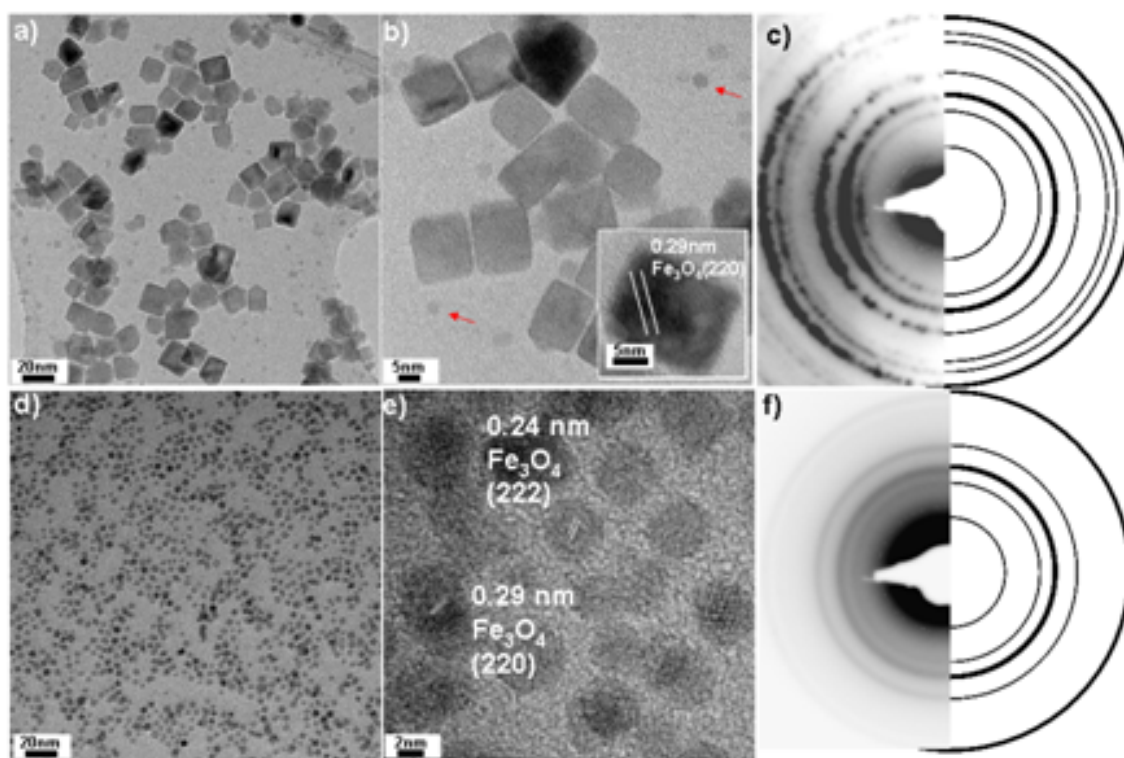


Figure 6.5: a,b) TEM images of the particles obtained by decomposition of $\text{Gd}(\text{acac})_3$ followed by $\text{Fe}(\text{CO})_5$. Two species are visible, pseudo-cubic iron oxide particles and smaller Gd_2O_3 NPs (indicated by red arrows). Inset is an image of a single Fe_3O_4 particle, showing contrast variations. c) SAED of particles, indexed to magnetite. d,e) TEM images of particles obtained by decomposition of $\text{Gd}(\text{acac})_3$ followed by $\text{Fe}(\text{acac})_3$. Only one species of particle was visible, which HRTEM and SAED imaging revealed to be monodisperse Fe_3O_4 NPs.

Gd_2O_3 - Fe_3O_4 Particles by Subsequent Decomposition

The TEM images for the particles obtained by decomposition of $\text{Gd}(\text{OAc})_3$ followed by subsequent decomposition of either $\text{Fe}(\text{CO})_5$ or $\text{Fe}(\text{acac})_3$ are given in Fig. 6.7.

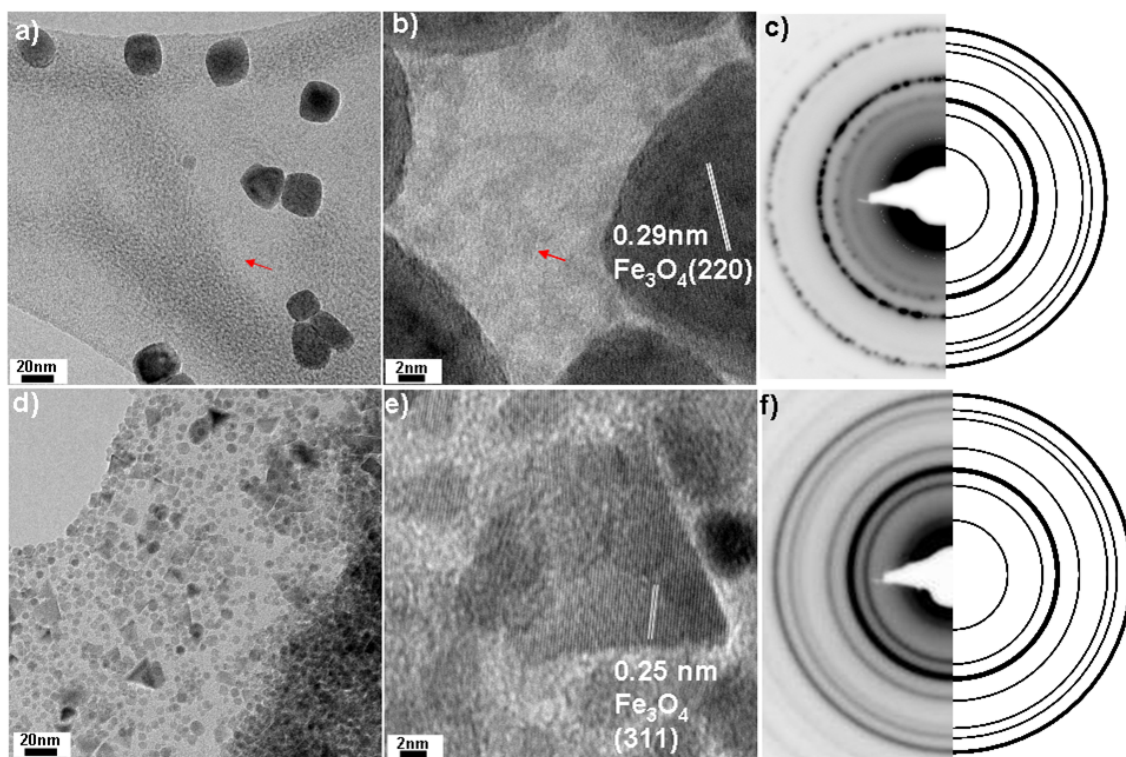


Figure 6.6: a,b) TEM images of the particles obtained by reaction between $\text{Gd}(\text{OAc})_3$ and $\text{Fe}(\text{CO})_5$. Two species are visible, pseudo-cubic iron oxide particles and smaller Gd_2O_3 particles (indicated by red arrows). A clump of small Gd_2O_3 NPs is visible as a region of darker contrast on the holey carbon support in (a), and small Gd_2O_3 particles are visible amongst the larger magnetite particles visible in (b). c) SAED of particles, indexed to magnetite. d,e) TEM images of particles obtained by reaction between $\text{Gd}(\text{OAc})_3$ and $\text{Fe}(\text{acac})_3$, showing the poor shape control of the magnetite NPs. A mixture of small spherical particles and larger triangular particles is visible. f) SAED of particles, showing agreement with the expected magnetite pattern.

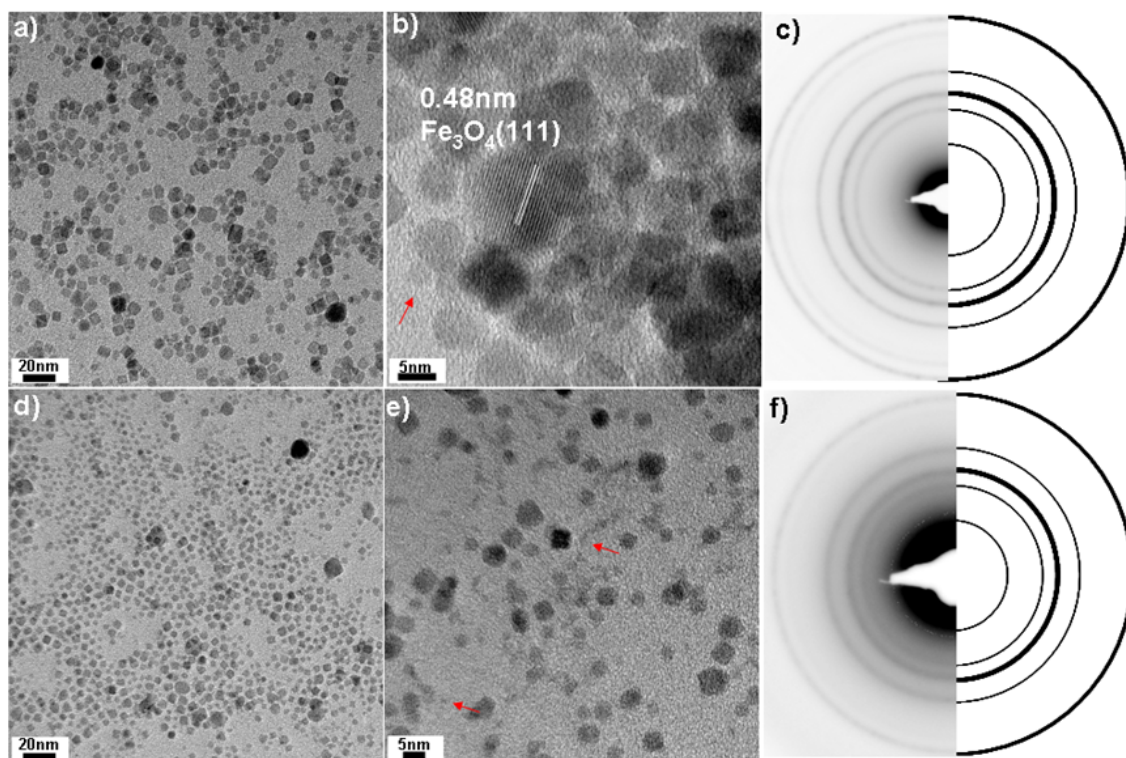


Figure 6.7: a,b) TEM images of the particles obtained by subsequent decomposition of $\text{Gd}(\text{OAc})_3$ then $\text{Fe}(\text{CO})_5$. A mixture of larger spherical particles were obtained alongside some smaller particles which may be Gd_2O_3 (indicated by the red arrow.) c) SAED of particles, indexed to magnetite. d,e) TEM images of particles obtained by subsequent decomposition of $\text{Gd}(\text{OAc})_3$ then $\text{Fe}(\text{acac})_3$, showing worsened size control of magnetite particles. e) reveals poorly defined Gd_2O_3 particles amongst the larger magnetite NPs. f) SAED of particles, showing agreement with the expected magnetite pattern.

Precursor	Condition & Outcome	
	Simultaneous	Subsequent
Gd(acac) ₃	Fe(CO) ₅ – separate nucleation	Fe(CO) ₅ – separate nucleation
	Fe(acac) ₃ – separate nucleation	Fe(acac) ₃ – apparent single nucleation
Gd(OAc) ₃	Fe(CO) ₅ – separate nucleation	Fe(CO) ₅ – apparent single nucleation
	Fe(acac) ₃ – apparent single nucleation	Fe(acac) ₃ – separate nucleation

Table 6.2: Summary table showing the outcomes of the eight reactions performed to investigate the effect of precursor and reaction order on iron and gadolinium bimetallic particles.

Discussion of the Simultaneous/Subsequent Reactions

The results of the simultaneous/subsequent reactions (as determined by bright-field TEM imaging) are summarised in Table 6.2. For the majority of the reaction conditions it is quite clear that two separate species of particle can be seen on the TEM grid. These reaction conditions are denoted ‘separate nucleation’ in the table. There were fewer reaction conditions where it appeared that only one species of particle was visible on the TEM grid, these conditions are denoted by ‘apparent single nucleation’ in the table.

It is not easy to accurately identify the species present when separate nucleation has occurred. The larger particles were easily identified as magnetite, as they were large enough to allow HRTEM imaging of lattice planes. When present, the secondary, smaller particles were so small that it was impossible to perform successful HRTEM imaging. The magnetite particles were large enough to be strongly diffracting, producing clear ring patterns. The strength of diffraction from the magnetite particles was such that the diffraction pattern from the small particles (which are assumed to be Gd₂O₃) could easily be obscured. Furthermore, some of the diffraction rings expected from cubic $Ia\bar{3}$ Gd₂O₃ are concurrent with those expected from cubic $Fm\bar{3}m$ magnetite, which makes conclusive phase identification difficult. However, the appearance of the small particles on the TEM grid is consistent with the appearance of small Gd₂O₃ particles obtained from other reactions performed during this thesis and observed in the literature (such as in Fig. 6.2a and Fig. 4.1b), and so the small particles are assumed to be Gd₂O₃.

It should be noted that separate nucleation of Fe_3O_4 and Gd_2O_3 particles does not necessarily mean that gadolinium doping of magnetite has not occurred — it could mean that the solubility limit of gadolinium in the magnetite lattice has been reached, and that the excess gadolinium nucleated as gadolinium oxide particles. Similarly, the presence of one only species on the TEM grid does not imply that gadolinium doping was successful, it could simply be the case that the small Gd_2O_3 particles indicative of separate nucleation went undetected. This could be the case if the concentration of magnetite particles on the grid was so high that the small Gd_2O_3 particles were obscured, or that there were no Gd_2O_3 particles in the area of the grid that was imaged. The latter is unlikely, as numerous squares of the TEM grid were thoroughly searched prior to imaging.

In the subsequent reactions (those which were anticipated to yield Gd_2O_3 - Fe_3O_4 core-shell particles) no intra-particle contrast variation was seen in the TEM investigations. If a core-shell morphology was present, the Gd_2O_3 core would be expected to show up much darker in a TEM image than the Fe_3O_4 shell. However, there was no evidence of core-shell morphology for the reactions where $\text{Fe}(\text{acac})_3$ was used. On the other hand, when $\text{Fe}(\text{CO})_5$ was the iron source used then the magnetite particles could occasionally be seen to comprise regions of increased contrast with respect to the rest of the particle, such as the inset of Fig. 6.4b). However, a recent report by Shavel et al. described darker regions within iron oxide nanocubes, which were determined to be regions of Fe^0 .^[203] When $\text{Fe}(\text{CO})_5$ is used as a precursor, the particles nucleate initially as metallic iron particles, which require subsequent oxidation to convert them into iron oxide particles. In the current system, the as-prepared Fe particles were oxidised to Fe_3O_4 by ambient oxidation for 1 hour, a procedure based on a previous report.^[43] (Complete oxidation of Fe particles to γ - Fe_2O_3 requires oxidation by $(\text{CH}_3)_3\text{NO}$ at reflux temperatures.^[30]) It is possible that the 1 hour ambient oxidation step was not long enough to completely convert the as-prepared Fe particles into Fe_3O_4 . EELS could be used to unambiguously determine the oxidation state of iron in these particles but has not been attempted here.

To determine the composition of the particles, elemental specific characterisation was performed. EDX measurements (not shown) from both the single and separate nucleation samples did indeed show the presence of both iron and gadolinium within the sample, although EDX is a non-specific technique and does not allow one to say unambiguously

if bimetallic particles have been prepared or not, as secondary scattering of X-rays may occur causing erroneous peaks in the EDX spectrum. The presence of gadolinium in the magnetite particles is best confirmed using STEM EELS techniques, which allow the measurement of elemental compositions from a precise area of a nanoparticle. Unfortunately, STEM EELS analysis did not detect any gadolinium in the particles from any of the 8 samples prepared. Representative EELS data from the decomposition of $\text{Gd}(\text{OAc})_3$ followed by the subsequent decomposition of $\text{Fe}(\text{CO})_5$ is given in Fig. 6.8. EELS data was collected by hopping the beam across individual particles, the dwell time was ~ 3 seconds per particle for a total acquisition time of 50 seconds.

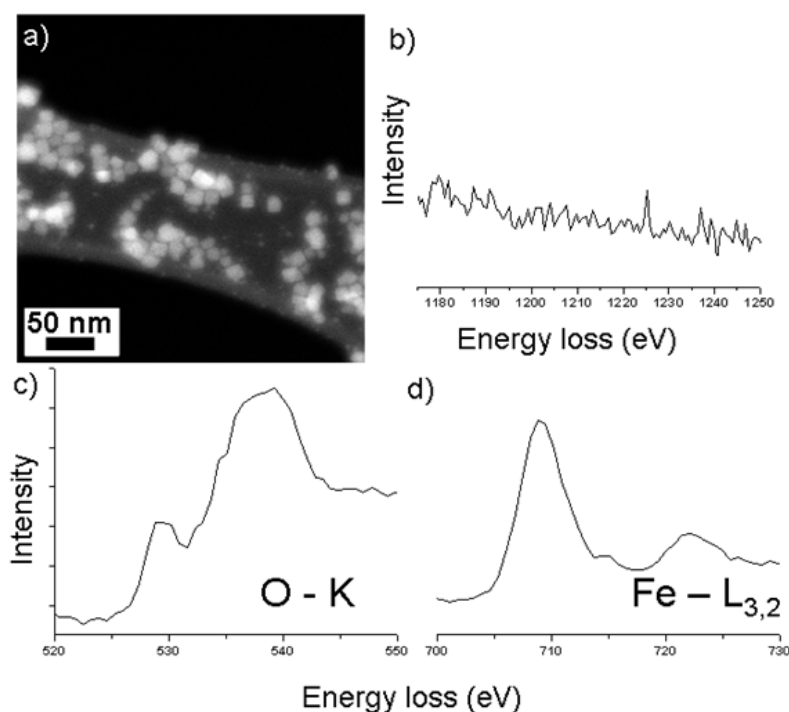


Figure 6.8: STEM EELS data for a multi source iron and gadolinium reaction. a) DF-STEM image of particles suspended on holey carbon film. b) Region of EELS spectra where gadolinium $M_{5,4}$ edges are expected. The lack of defined gadolinium edges confirms the particles are un-doped iron oxide, as confirmed by the presence of the c) oxygen and d) iron edges.

The failure to produce $\text{Gd}:\text{Fe}_3\text{O}_4$ particles indicates the two-precursor approach is not suited to synthesising either $\text{Gd}_2\text{O}_3\text{-Fe}_3\text{O}_4$ or $\text{Gd}:\text{Fe}_3\text{O}_4$ particles. The fact that bimetallic particles were not created indicates there is an incompatibility between the precursors that were chosen. As we saw in Fig. 6.1, both the gadolinium precursors are relatively

stable, especially when compared to the $\text{Fe}(\text{acac})_3$ and $\text{Fe}(\text{CO})_5$ precursors (the volatility of $\text{Fe}(\text{CO})_5$ is especially well known) — meaning that iron oxide particles are likely to form in advance (or at a lower temperature) of gadolinium oxide particles.

To attempt to overcome the separate nucleation problem the hot injection method was used, in which precursors are injected into a hot solution, the temperature of which is above the decomposition temperature of the precursors. A reaction mixture containing the standard 4.5:3:2.5 mL OA:OAm:BE mixture was heated to 310 °C, at which point iron (0.5 mmol) and gadolinium (0.1 mmol) precursors in 2 mL of hot OAm were rapidly injected into the reaction vessel via a syringe. A number of different iron precursors were used, including $\text{Fe}(\text{acac})_3$, $\text{Fe}(\text{CO})_5$, $\text{Fe}(\text{oleate})_3$, $\text{FeCl}_3/\text{FeCl}_2$ and $\text{Fe}(\text{NO}_3)_3$. The gadolinium precursor was also varied, including $\text{Gd}(\text{acac})_3$, $\text{Gd}(\text{OAc})_3$, $\text{Gd}(\text{oleate})_3$, GdCl_3 and $\text{Gd}(\text{NO}_3)_3$. TEM investigations showed that the hot-injection method was capable of producing particles, although separate nucleation was still an issue and EELS measurements showed that the iron particles were undoped magnetite. Variations on the hot injection protocol whereby a hot OAm solution containing gadolinium precursor was injected into a refluxing OA:OAm:BE mixture containing $\text{Fe}(\text{acac})_3$ were also unsuccessful, as again undoped magnetite was obtained.

6.1.3 Conclusions

The above results highlight the difficulties in obtaining gadolinium doped magnetite particles by the multi source approach. Despite a range of reaction conditions being used (simultaneous and subsequent decomposition, hot-injection using different precursors) separate nucleation of particles frequently occurred, and the magnetite particles were found not to contain gadolinium. It seems that the current two-precursor solution-based approach is simply not an appropriate way of obtaining particles, ostensibly due to a combination of factors: the difference in reaction rates of the two precursors (which is a challenge in the synthesis of any doped material) and the difference in ionic radii between the iron and gadolinium ions.

Given the difficulties experienced with separate nucleation using the multi source protocol, a new approach was taken in which a new, single source precursor would be used as a starting material to synthesise iron and gadolinium particles.

6.2 Bimetallic Particles by the Single Source Approach

As we have seen in the previous section, using separate precursors to obtain bimetallic particles is difficult, especially for $\text{Gd}_2\text{O}_3/\text{Fe}_3\text{O}_4$ and $\text{Gd}:\text{Fe}_3\text{O}_4$ particles. Part of the difficulty is finding precursors which will decompose simultaneously, to minimise the amount of separate nucleation that occurs. Even when relatively rapidly-decomposing precursors such as $\text{Gd}(\text{OAc})_3$ are hot-injected above their decomposition temperatures this is no guarantee that incorporation of Gd^{3+} into the Fe_3O_4 lattice will occur. To circumvent the separate nucleation problem, a different approach was adopted whereby a new carboxylate precursor, containing both iron and gadolinium was synthesised. Starting materials which contain two or more metal atoms that are intended to feature in the product are named ‘single source’ precursors. The advantage of using single source precursors over the multi source approach is that there is no associated difficulty in finding two precursors with similar decomposition habits as metal centres are in close proximity to one another, and would therefore be more likely to form a bimetallic product as opposed to two separate species.

At present there are few literature reports that use single source precursors to make doped particles, and even fewer reports of using bimetallic precursors to make bimetallic metal oxide particles. Single source precursors are most commonly used in the synthesis of rare-earth and halogen containing particles, for example Du et al. employed $\text{Eu}(\text{CF}_3\text{COO})_3$ as a starting material to create EuOF nanowires.[130] The same group used an analogous approach with $\text{La}(\text{CCl}_3\text{COO})_3 \cdot \text{H}_2\text{O}$ as the starting material to create LaOCl nanoplates.[129] Recently, Mirsha et al. synthesised novel heterobimetallic trifluoroacetate derivatives as precursors to create $\text{NaY}(\text{Ln})\text{F}_4$ ($\text{Ln} = \text{Yb}, \text{Er}, \text{Tm}$) particles.[231] Other examples where single source precursors have been used to synthesise complex products include the formation of bismuthinite (Bi_2S_3) nanoflowers using $\text{Bi}(\text{SCOPh})_3$ [232] and the formation of $\text{CuInS}_2/\text{CuInSe}_2$ semiconductor films by decomposition of $[(\text{Ph}_3\text{P})_2\text{CuIn}(\text{QEt})_4]$ (where $\text{Q} = \text{S}, \text{Se}$).[233]

Whilst the above examples show single source precursors can be used to synthesise a range of materials, examples of bimetallic precursors being used to create bimetallic metal oxide particles are rare. During the course of this Ph.D a few reports were published which discussed the possibility of using single-source precursors as starting materials in

the synthesis of mixed ferrite particles. For example, Chen et al. described the synthesis of MFe_2O_4 ($M = Ni, Co, Mn, \text{ and } Zn$) particles by the solid state thermolysis of the single-source precursor $[MFe_2O(OAc)_6(H_2O)_3] \cdot nH_2O$.^[234] These acetate precursors are similar to the polynuclear carboxylate precursors we saw in the previous chapter to synthesise MnO and Fe_3O_4 particles, yet the solid-state approach used by Chen et al. results in poorly defined and agglomerated particles.^[234] Shortly after Chen's publication, Mathur et al. published a report describing the solution-based synthesis of $CoFe_2O_4$ particles using a $CoFe_2(O^tBu)_8$ precursor.^[235] Mathur showed that the 1:2 Co:Fe stoichiometry in the precursor resulted in the formation of $CoFe_2O_4$ particles, and that careful consideration of the precursor decomposition characteristics (as determined by TGA) facilitated the synthesis of monodisperse spherical NPs. The above examples show that bimetallic polynuclear precursors can be used to synthesise bimetallic particles, and confirm that doped iron oxide particles can be synthesised using this method. We saw in the previous chapter that polynuclear carboxylate complexes containing either manganese or iron can be used to synthesise MnO or Fe_3O_4 nanoparticles, hence it was decided that a new precursor containing both iron and gadolinium would be synthesised as a potential single-source precursor to obtain $Gd:Fe_3O_4$ particles. The strategies employed for designing and synthesising the bimetallic iron and gadolinium precursor are given in the following section. Additionally, within the Murrie research group synthetic methodologies for other polynuclear bimetallic carboxylate complexes are known, and it was decided that one such compound, $[Mn_2Gd_2O_2(piv)_8(Hpiv)_2(MeOH)_2]$ would be synthesised as potential precursor for $Gd:MnO$ particles.

6.2.1 Experimental

Systematic Approaches to a Novel Iron and Gadolinium Precursor

Two systematic approaches were undertaken to attempt to synthesise a new iron and gadolinium containing precursor, based around the reaction of iron and gadolinium containing precursors in the presence of various ligands.

The first approach involved reacting different gadolinium salts with pre-formed iron complexes, varying the ratio of iron complex to gadolinium salt. The iron complexes used were those briefly mentioned in the previous chapter as potential precursors for magnetite

NPs, namely Fe₃O-pivalate, Fe₃O-phenoxybenzoate, Fe₃O-acetate and Fe₃O-benzoate. Both gadolinium nitrate (Gd(NO₃)₃ · 6 H₂O) and gadolinium acetate (Gd(OAc)₃ · 4 H₂O) were used as the gadolinium source. In a typical synthesis, the required amount of iron-containing precursor was dissolved with stirring in MeCN (40 mL) for five minutes. To this solution gadolinium precursor in MeOH (5 mL) was added dropwise. This solution was stirred for 24 hours, filtered and the resultant deep red solutions were allowed to slowly evaporate at room temperature to promote crystallisation of the product.

The second systematic approach involved modifying an existing report by Ako et al., who described the synthesis of a [Fe₅Gd₈] carboxylate cluster by reaction of iron-pivalate with Gd(NO₃)₃ · 6 H₂O in the presence of N-butyldiethanolamine (B-DEA) and NaOAc · 3 H₂O.[236] In the original communication very little detail was included in the experimental section, and no information regarding reagent ratios, heating regimes, reaction times or solvent volumes was provided. Attempts to repeat the synthesis of the Fe₅Gd₈ precursor were unsuccessful, despite trying a range of different reaction conditions as it was found that the only crystals that were obtained from the reaction mixture were of the Fe₃O-pivalate starting material. It seemed that the stability of the Fe₃O-pivalate complex was such that it readily crystallised out of the reaction mixture. It was decided that the protocol would be varied, to include a larger number of ligands and use iron nitrate and gadolinium nitrate as the source of metal ions. The original publication used B-DEA as the polyol ligand, this ligand was used again in addition to 6 others, whose structures are given in Fig. 6.9. The ratios of iron nitrate, gadolinium nitrate, sodium acetate and polyol ligand were systematically varied for each reaction.

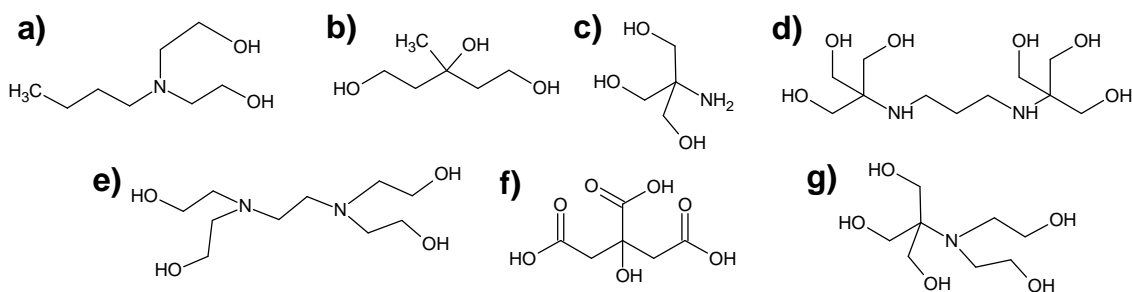


Figure 6.9: Structures of each of the ligands used; a) B-DEA, b) MPT, c) tris, d) bis-tris propane, e) tetrakis, f) citric acid and g) bis-tris.

At the time of writing, unfortunately no crystals of new bimetallic compounds had

been obtained from any of the reaction mixtures, either from the reactions using the pre-formed iron carboxylate clusters, or the iron nitrate and gadolinium nitrate reactions with polyol ligands. With the systematic approach it is very difficult to predict which reagent ratios or reaction conditions will yield a novel product, and the crystallisation of molecules from solution is not trivial. Furthermore, the long time-scales that are often required for crystals to grow out of solution mean that this approach is not an entirely practical method of synthesising precursors in suitable quantities for NP synthesis.

For the above reasons another approach was taken, in which the synthesis of a known bimetallic complex containing iron and copper was altered to include gadolinium. In the Murrie research group the benzoate carboxylate complex $[\text{Fe}_2\text{CuO}(\text{OBz})_6(\text{H}_2\text{O})_3] \cdot 8\text{H}_2\text{O}$ ($\text{Fe}_2\text{Cu-benz}$) was previously synthesised and used as a starting material in the synthesis of larger iron and copper containing molecules.[237] This mixed-metal benzoate is an ideal precursor for bimetallic nanoparticles, as it can easily be synthesised in good yields using cheap precursors. It was thought that by simple modification of the $\text{Fe}_2\text{Cu-benz}$ synthesis, an analogous $\text{Fe}_2\text{Gd-benz}$ complex could be obtained. The procedures for the synthesis of the iron and gadolinium benzoate complexes are given in the following section. Additionally, a mixed metal manganese and gadolinium complex $[\text{Mn}_2\text{Gd}_2\text{O}_2(\text{piv})_8(\text{Hpiv})_2(\text{MeOH})_2]$ was prepared and trialled as a potential precursor to gadolinium-doped manganese oxide particles.[238]

Synthesis of the $[\text{Fe}_2\text{GdO}(\text{benz})_6(\text{H}_2\text{O})_3]$ Precursor

$[\text{Fe}_2\text{GdO}(\text{benz})_6(\text{H}_2\text{O})_3]$ was prepared in an analogous way to the previously reported iron and copper complex.[237] To a stirred solution of $\text{FeCl}_2 \cdot 4\text{H}_2\text{O}$ (0.5 g, 2.5 mmol) and $\text{GdCl}_3 \cdot 2\text{H}_2\text{O}$ (0.46 g, 1.25 mmol) in H_2O (50 mL) was added a solution of sodium benzoate (1.88 g, 13 mmol) in H_2O (100 mL). To this solution MeCN (25 mL) was added, and the reaction mixture was stirred overnight to give a light brown, tan-coloured precipitate. This precipitate was collected by filtration and washed with Et_2O .

The air-dried precipitate analyses as $[\text{Fe}_2\text{GdO}(\text{benz})_6(\text{H}_2\text{O})_3]$, analysis (%) calculated (found): C, 46.55 (46.46); H, 3.53 (3.07); N, 0 (0).

Synthesis of $[\text{Mn}_2\text{Gd}_2\text{O}_2(\text{piv})_8(\text{Hpiv})_2(\text{MeOH})_2]$ ($\text{Mn}_2\text{Gd}_2\text{-piv}$)

The $\text{Mn}_2\text{Gd}_2\text{-piv}$ precursor was prepared by reaction of $\text{Mn}_6\text{-pivalate}$ (synthesised as described in the previous chapter) with $\text{Gd}(\text{NO}_3)_3 \cdot 6\text{H}_2\text{O}$. Briefly, $\text{Mn}_6\text{-pivalate}$ (0.316 mmol) was dissolved in CH_2Cl_2 (40 mL). To this solution $\text{Gd}(\text{NO}_3)_3 \cdot 6\text{H}_2\text{O}$ (1.26 mmol) in MeOH (5 mL) was added slowly, with stirring. The reaction mixture was stirred for 24 h, then the solvent volume was reduced to ~ 15 mL. After standing for a week a small quantity of orange microcrystalline material was obtained. Unfortunately the crystals were too small to perform single-crystal X-ray diffraction, and not enough material was obtained to perform CHN analysis. However, the colour of the crystals (orange) agreed with the expected colour of the product and was different to the colour of the $\text{Mn}_6\text{-pivalate}$ starting material (brown). Hence it was assumed that the microcrystalline product was in fact the target complex.[238]

Synthesis of Nanoparticles Using Bimetallic Starting Materials.

Nanoparticles were synthesised using a method similar to that which was used in the subsequent/simultaneous reactions given in Section 6.1.1. Briefly, 0.2 g of precursor was added to a reaction mixture consisting of OAm:OA:BE in the ratio 4.5:3:2.5 mL. The mixture was then heated to 110 °C under a nitrogen flow for 30 minutes. The nitrogen flow was reduced and the mixture was then slowly heated to 310 °C for 30 minutes. The mixture was then cooled to room temperature and the particles were precipitated with excess ethanol and washed as described earlier.

6.2.2 Results and Discussion**Bimetallic Iron-Containing Precursors**

Whilst the CHN data for $[\text{Fe}_2\text{GdO}(\text{benz})_6(\text{H}_2\text{O})_3]$ agrees with the indicated stoichiometry, further attempts to characterise the precursor were made. Attempts to recrystallise the as-obtained powder by slow evaporation of a concentrated THF or MeCN solution proved unsuccessful, as larger complexes containing only iron were obtained. These complexes $[\text{Fe}_{11}\text{O}_6(\text{OH})_6(\text{O}_2\text{CPh})_{15}] \cdot 6\text{THF}$ and $[\text{Fe}_{17}\text{O}_{10}(\text{OH})_{10}(\text{O}_2\text{CPh})_{20}] \cdot 8\text{MeCN}$ were isolated as orange-brown blocks and were identical to those which had been described

previously.[239, 240] The formation of these larger species is attributed to the use of THF and MeCN, which are strongly-coordinating solvents and are capable of disrupting the bonds present within the 'Fe₂GdO' core of the [Fe₂GdO(benz)₆(H₂O)₃] cluster. Attempts were then made to recrystallise the compound using a non-coordinating solvent system. Layering of a dichloromethane (DCM) solution of the complex with toluene or hexane resulted in the formation of microcrystalline pale yellow-orange needles. Attempts to determine the structure of these crystals by single-crystal X-ray diffraction were unsuccessful, as the crystals were simply too small to obtain usable diffraction data. Given the difficulties in obtaining single crystal structures of the iron and gadolinium benzoate precursor, powder XRD was performed to further investigate the crystal structure.

To determine if Fe₂GdO-benzoate was actually a new complex, powder XRD patterns were obtained from the analogous iron-only benzoate complex (Fe₃O-benzoate) and from the gadolinium-only benzoate, prepared by reaction between gadolinium chloride and sodium benzoate (compound analyses as Gd(benz)₃ · 3 H₂O, in agreement with previous reports[241]). Comparing the XRD patterns from the mixed metal precursor with the analogous iron-only and gadolinium-only complexes would enable us to see if the Fe₂GdO-benzoate precursor was in fact a new compound or just a binary mixture of the two single-metal benzoate precursors. Comparison between the patterns (which are given in Fig. 6.10) confirms that the [Fe₂GdO(benz)₆(H₂O)₃] powder contained unique peaks not seen in the iron-only and gadolinium-only powders (between 7.5–10 degrees, as indicated by ★). Whilst the XRD from the Fe₂GdO-benzoate precursor is quite different from the iron only precursor, there are some peaks (denoted by ■) that appear in both the Fe₂GdO and Gd-benzoate starting materials, which would imply that these compounds bear structural similarities.

Given the differences between the mixed-metal and the single-metal precursors it was assumed that the Fe₂GdO-benzoate complex was indeed a new compound, and not a binary mixture of two individual complexes. IR characterisation was performed on each precursor, as any structural differences would yield noticeable differences in the IR spectra. The IR spectra for each precursor are given in Fig. 6.11. Whilst there are similarities between each precursor and the sodium benzoate ligand, it is possible to see that a new peak has emerged in the Fe₂GdO-benzoate complex at ~1325 wavenumbers. This peak

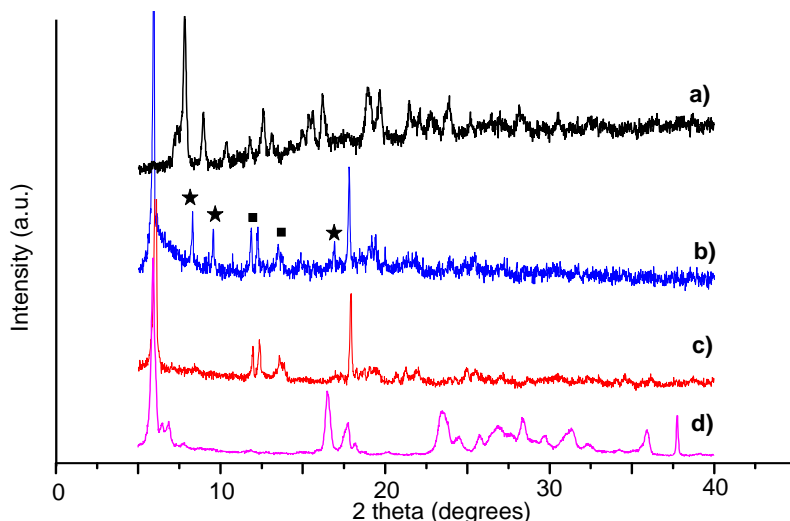


Figure 6.10: Powder XRD patterns of a) Fe_3O -benzoate, b) Fe_2GdO -benzoate, c) Gd-benzoate and d) sodium benzoate starting material. The XRD pattern of the Fe_2GdO -benzoate starting material (blue spectrum, b) contains unique peaks (denoted by ★) that are not visible for either the iron-only (a) or gadolinium only (c) precursors. Whilst the XRD from the Fe_2GdO -benzoate precursor is quite different from the iron only precursor, there are some peaks (denoted ■) that appear in both the Fe_2GdO and Gd-benzoate starting materials, which would imply that these compounds bear structural similarities. There are no similarities between any of the precursor patterns and the sodium benzoate starting material, implying that ‘free’ benzoate was not found in any of the complexes.

cannot be seen in any of the other IR spectra and again provides evidence that there are subtle differences between the Fe_2GdO -benzoate complex and the other single-metal precursors. Unfortunately without a single-crystal X-ray structure is difficult to comment unambiguously on the origins of this new peak.

Finally, TGA plots for each precursor were recorded. Differences in the decomposition profiles of each precursor would provide further evidence for structural differences between complexes, as well as providing insight into the decomposition characteristics for each precursor, which would allow for logical placements of hold steps in the nanoparticle formation reaction. The TGA data for each precursor are given in Fig. 6.12.

The TGA data shows that the decomposition profiles of the Fe_3O -benzoate and Fe_2GdO -benzoate are remarkably similar in shape, save for subtle differences in the temperatures

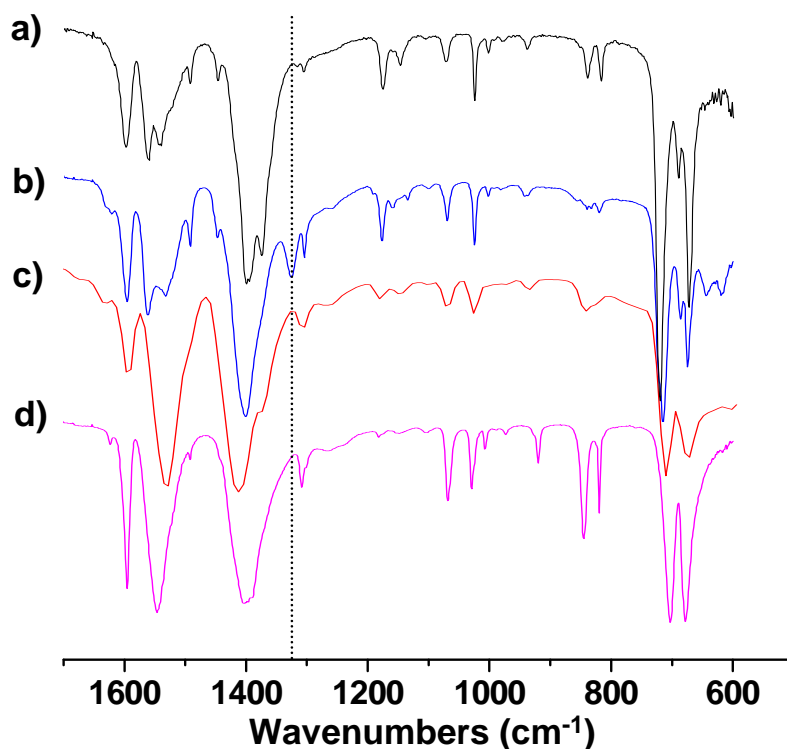


Figure 6.11: IR spectra of the a) Fe_3O -benzoate, b) Fe_2GdO -benzoate, c) Gd-benzoate and d) sodium benzoate precursors. The new peak at $\sim 1325\text{ cm}^{-1}$ in the Fe_2GdO -benzoate precursor is indicated.

and rates at which decomposition occurs. For example, both the iron-only and iron-gadolinium precursors exhibit $\sim 5\%$ weight losses in the $\text{RT} \rightarrow 100\text{ }^\circ\text{C}$ region, attributable to water loss. For both of these precursors no sudden and rapid weight loss was observed, and complex decomposition was instead more gradual, with steady decomposition occurring right up to the $320\text{--}340\text{ }^\circ\text{C}$ region, whereupon a change in decomposition rate was observed at $337\text{ }^\circ\text{C}$ for Fe_3O -benzoate and $322\text{ }^\circ\text{C}$ for Fe_2GdO -benzoate. The decomposition rate is seen to increase for both complexes at around $380\text{--}390\text{ }^\circ\text{C}$. In contrast, the behaviour of the Gd-benzoate precursor is quite different. Apart from an initial $\sim 10\%$ weight loss in the $\text{RT} \rightarrow 100\text{ }^\circ\text{C}$ region, the Gd-only precursor is very stable, and a near-zero derivative weight loss is observed until $250\text{ }^\circ\text{C}$ whereupon marginal decomposition is observed. Indeed, from $100\text{ }^\circ\text{C}$ to the end temperature of $450\text{ }^\circ\text{C}$ the Gd-benzoate precursor only loses 7% of weight. The stability of the Gd-benzoate precursor is such that no particles were obtained even at high temperature reactions heated to $350\text{ }^\circ\text{C}$. The decomposition seen for the Fe_3O -benzoate and Fe_2GdO -benzoate complexes near typical

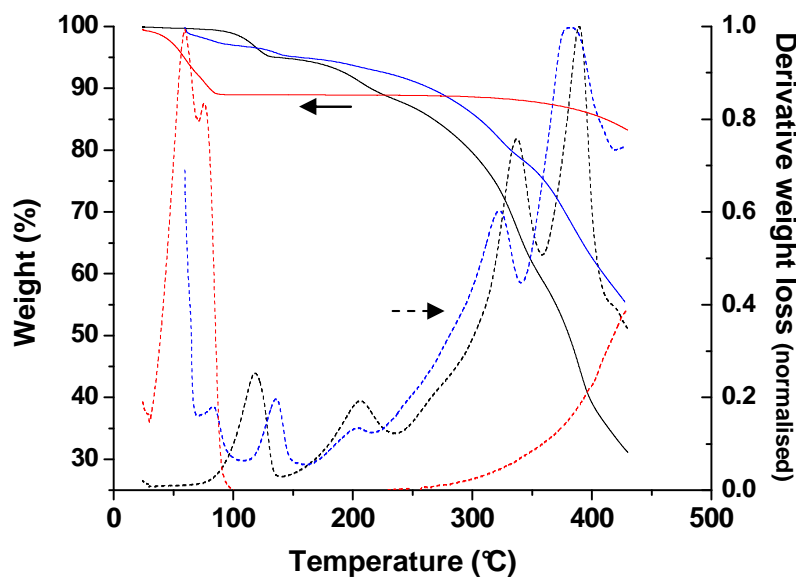


Figure 6.12: TGA weight-loss plots (solid lines) and corresponding derivative weight loss plots (dotted lines) for Fe_3O -benzoate (black), Fe_2GdO -benzoate (blue) and Gd -benzoate (red).

reaction temperatures indicates that NP formation is expected using these complexes. Indeed, we have seen in the previous chapter that Fe_3O -benzoate can be used to synthesise high quality particles.

The above discussions show that although the structure of the ‘ Fe_2GdO -benzoate’ precursor is not presently known, we can infer that the complex is not a simple binary mixture of the corresponding iron-only and gadolinium-only complexes. IR spectrometry also indicates that subtle differences between these complexes exist, as although the spectra from each precursor were similar a new peak was observed in the Fe_2GdO -benzoate spectra (Fig. 6.11). Finally, TGA data (Fig. 6.12) showed that the Fe_3O -benzoate and Fe_2GdO -benzoate complexes have similar decomposition characteristics though slight variations exist with respect to the temperatures and rates at which decomposition occurs. Furthermore, TGA data showed that the Gd -benzoate precursor is exceptionally stable up to even $450\text{ }^\circ\text{C}$, and this stability explains why no particles were obtained under standard particle-forming conditions. Whilst efforts to determine the structure of the mixed metal iron-gadolinium precursor were met with varying degrees of success, TEM analysis confirms Fe_2GdO -benzoate is capable of producing nanoparticles when reacted under the conditions described in section 6.2.1. TEM images of these particles are given

in Fig. 6.13.

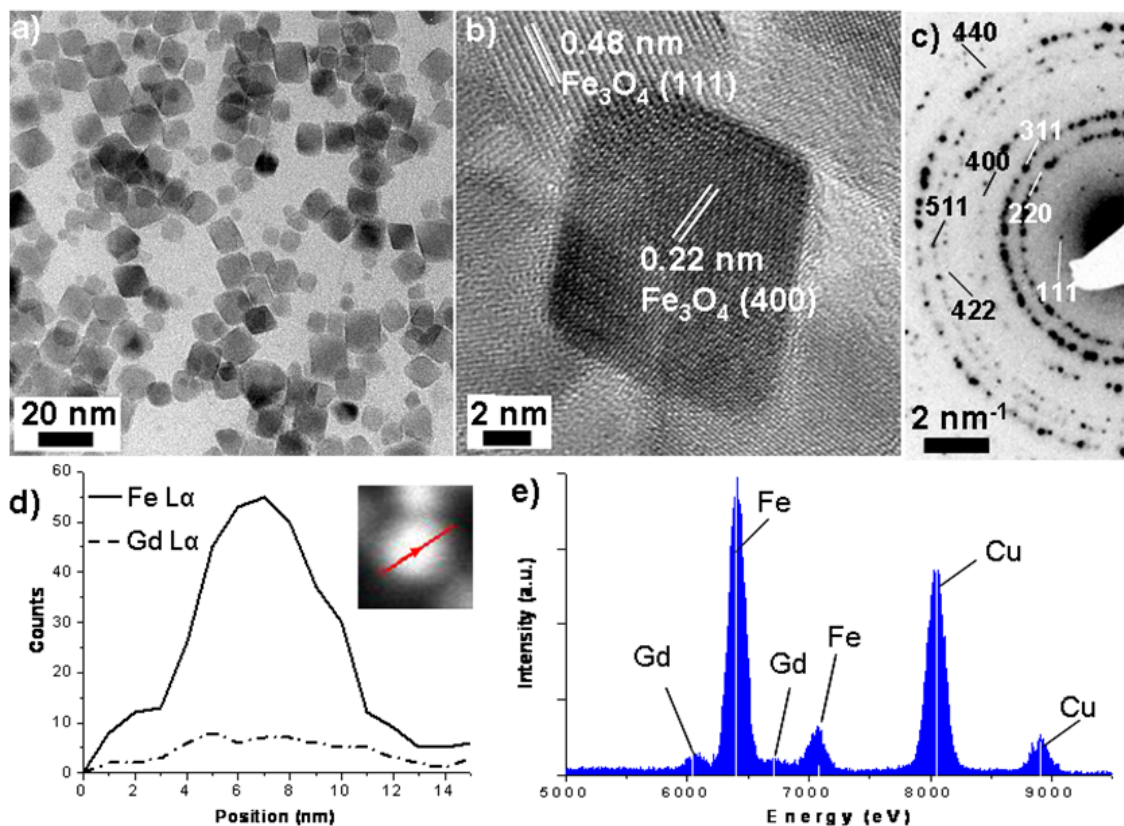


Figure 6.13: TEM images of the particles obtained by decomposition of Fe_2GdO -benzoate, showing a) overview of particles, with a clear prevalence of octahedral particles. b) HRTEM of a single octahedral particle, and c) SAED, confirming the particles to be magnetite (Fe_3O_4). d) STEM EDX line trace across an individual particle, showing the rise and fall of the Fe L_α and Gd L_α signals as the beam is scanned across a single particle. e) Bright field EDX spectrum obtained from a clump of particles, showing the presence of iron and gadolinium. The Cu peaks are from the TEM grid.

TEM characterisation shows the particles are octahedral and reasonably monodisperse, with sizes 12.0 ± 2.6 nm (21%). Lattice fringe analysis and electron diffraction confirms the particles to be Fe_3O_4 . Crucially, the poorly defined 3 nm Gd_2O_3 particles which were prevalent across the grid in the simultaneous/subsequent reactions described in section 6.1 were not visible when using Fe_2GdO -benzoate as a single-source precursor. Elemental characterisations were performed using EDX and EELS. Bright-field EDX

characterisation was performed on a clump of particles and confirms the presence of both iron and gadolinium in the particles, (Fig. 6.13e). To determine the compositions of specific particles, STEM EELS measurements were performed. The STEM-DF images for these measurements are given in Fig.6.14.

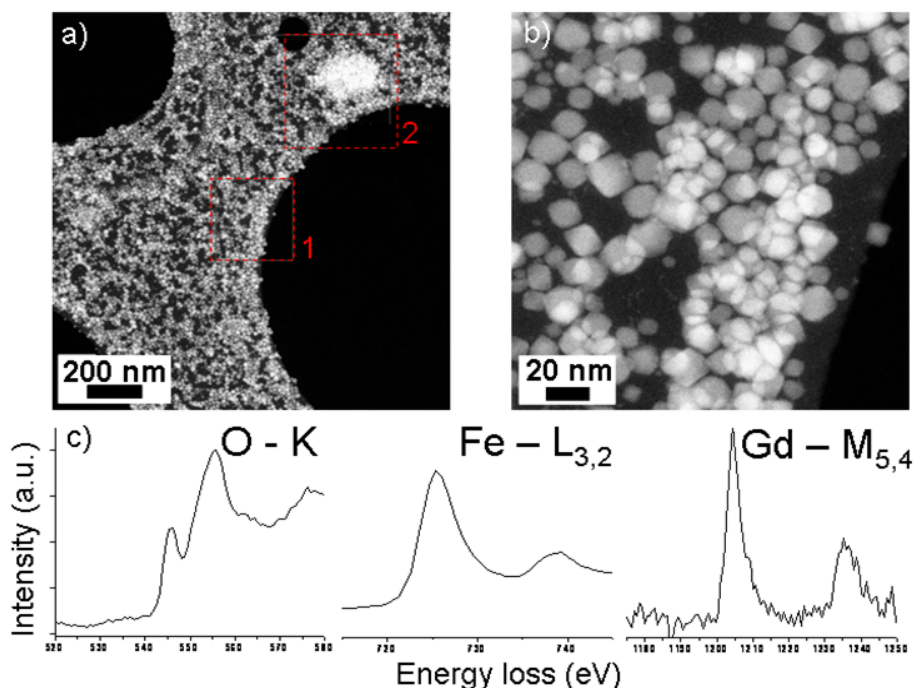


Figure 6.14: a) STEM-DF images of the $\text{Gd}:\text{Fe}_3\text{O}_4$ particles. the two highlighted regions 1 and 2 indicate areas where EELS scans were taken. b) Expansion of region 1 from which an EELS spectrum was collected by dwelling the beam on 35 particles to minimise contamination during collection. c) The resulting EELS edges, showing the presence of O, Fe and Gd in the particles.

It was found that the sample began to contaminate upon prolonged exposure to the electron beam. To counteract this, data were acquired by ‘hopping’ the electron beam from particle to particle, dwelling on each particle for 5 seconds. The particles chosen for this measurement are those from region 1 in Fig.6.14a), which is shown in more detail in Fig.6.14b). The EELS spectra obtained from roughly 35 particles is presented in Fig. 6.14c), which shows well defined edges for oxygen- K and iron- $L_{2,3}$ edges, in addition to a faint signal from the gadolinium- $M_{5,4}$ edges. The calculated elemental composition was determined to be Fe: 47.6%, O: 50.8% and Gd: 1.6%. It should be noted that the expected Fe:O ratio for magnetite (Fe_3O_4) is Fe:O 42.9:57.1. The obtained ratios of

47.6:50.8 with 1.6% Gd are more consistent with gadolinium-doped FeO particles. However, we know this not to be the case as the SAED pattern was in good agreement with the magnetite pattern.

There are a number of reasons why the expected Fe:O ratio was not obtained. It could be that during EELS acquisition the Fe³⁺ ions in magnetite are directly reduced to Fe²⁺ by the electron beam, which would give rise to a Fe:O stoichiometry. However, this is unlikely as the acquisition times were kept short and dwell times on individual particles were only a few seconds at most. A more likely explanation is that the oxygen signal is obscured during acquisition by the increasing background signal that is caused by carbon deposition during sample contamination. The build-up of carbon during contamination will obscure the edges at the lower energy losses the worst, meaning the oxygen edge will become obscured by an increasing background signal. To overcome this, a second EELS spectra was collected from region 2 of Fig. 6.14a), though this time an average EELS spectra was collected over the whole field of view. This approach has the advantage of reducing the beam dosage to individual particles though has the disadvantage of not permitting precise placement of the electron beam. This is not a real disadvantage in the current sample, where the NP population is uniform and we can be confident that there is only one type of particle present. The elemental composition obtained from the average field-of-view EELS spectrum was Fe: 43.3%, O: 54.2% and Gd: 2.5%. This ratio is closer to the expected Fe:O ratio for magnetite (42.9:57.1) though still indicates that mild contamination of the TEM grid is occurring during acquisition.

The relatively low levels of gadolinium doping (1.6–2.5%) suggest that the solubility limit of Gd³⁺ ions in the magnetite lattice is low, which is not surprising given the difference in ionic radii between Gd³⁺ (107.8 pm), Fe²⁺ (78 pm) and Fe³⁺ (65 pm).[242] Low dopant levels have been reported elsewhere, for example by Drake et al. who previously synthesised Gd_{0.02}Fe_{2.98}O₄ particles by a co-precipitation method.[225] Furthermore, the observed gadolinium levels (1.6–2.5 mol%) are similar to previously reported levels for other non-magnetite ferrite particles. For example, Wang et al. reported a maximum Gd³⁺ dopant level of 2.85 mol% in cobalt-ferrite microparticles.[243] Above this level, the nucleation of a separate GdFeO₃ perovskite phase was observed. SAED measurements confirmed that the magnetite structure had been retained upon gadolinium doping (and no

other gadolinium ferrite phases such as perovskite GdFeO_3 and garnet $\text{Gd}_3\text{Fe}_5\text{O}_{12}$ were formed [244]). The $\text{Gd}:\text{Fe}_3\text{O}_4$ particles showed a $\sim 2\%$ reduction in lattice parameter (as calculated from the SAED pattern) compared to undoped Fe_3O_4 , with a equal to 8.397 and 8.210 Å for the undoped and doped samples respectively. Interestingly, there are a few reports which mention a reduction in lattice parameter upon Ln^{3+} ion doping into ferrite lattices.[243, 245–247] The reduction in lattice parameter is often accompanied by a reduction in grain size, due to the increased grain stress associated with the doping of large ions into the lattice, which reduces grain growth.[243, 247] This is interesting as the $\text{Gd}:\text{Fe}_3\text{O}_4$ particles were slightly smaller than the analogous Fe_3O -benzoate Fe_3O_4 particles (12.0 ± 2.6 nm and 16.5 ± 2.8 nm respectively). Both particle samples were made under identical reaction conditions so it is possible that the presence of Gd in the particles (as confirmed by EELS) may inhibit the growth of larger particles, due to the strain involved with increasing the grain size.

The successful synthesis of $\text{Gd}:\text{Fe}_3\text{O}_4$ particles is a promising result as it means that the chosen ‘single source’ route is a viable and easy way to produce doped magnetite nanoparticles. The obtained $\text{Gd}:\text{Fe}_3\text{O}_4$ composites are exciting as they have potential applications as MRI contrast agents or for use in magnetic fluid hyperthermia. To determine the magnetic properties of the $\text{Gd}:\text{Fe}_3\text{O}_4$ particles SQUID measurements were performed. Hysteresis loops were recorded at 5 K, 100 K and 300 K. These measurements are provided in Fig.6.15 and summarised in Table 6.3. Field-cooled (FC) and zero field-cooled (ZFC) measurements were also performed in the 2 K \rightarrow RT region at 100 Oe and are shown in Fig. 6.16.

Temperature (K)	M_r (emu/g)	M_s (emu/g)	H_c (T)
5 K	12.20	82.50	0.05
100 K	0.00	41.20	0.00
300 K	0.00	33.19	0.00

Table 6.3: M_r (remnant magnetisation), M_s (saturation magnetisation), and H_c (coercivity) values of $\text{Gd}:\text{Fe}_3\text{O}_4$ nanoparticles recorded at 5, 100 and 300 K.

The hysteresis loops in Fig. 6.15 clearly show the superparamagnetic behaviour of

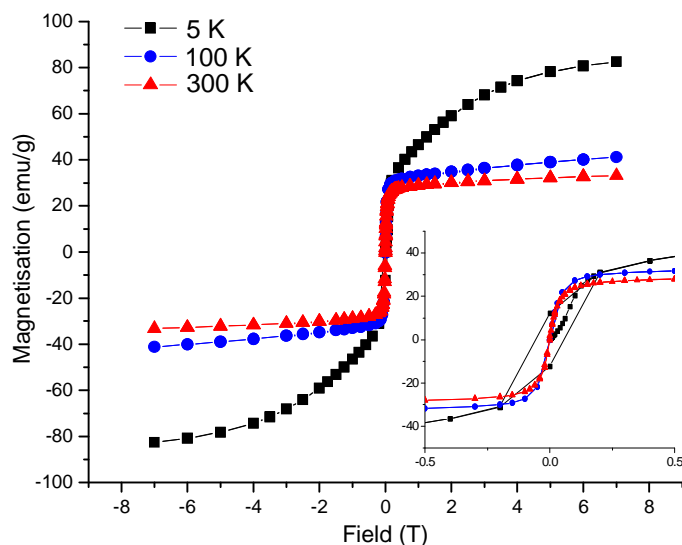


Figure 6.15: Hysteresis loops for Gd:Fe₃O₄ particles recorded at 5, 100 and 300 K. Inset is an expansion of the region near the origin.

the particles. A very small coercive field of 0.05 T was observed at 5 K, and no coercive field was observed at 100 K or 300 K. Interestingly, the M_s values were lower than the value expected for bulk magnetite (which is 96.4 emu/g).[105] This follows similar trends for lanthanide doped magnetite, as Drake et al. reported M_s values of 65.67 emu/g for superparamagnetic Gd_{0.02}Fe_{2.98}O₄ nanoparticles, synthesised by the co-precipitation method.[225] Liang et al. also prepared lanthanide-doped magnetite particles using the co-precipitation method, of these the gadolinium doped particles showed the highest M_s values of 45.9 emu/g although no attempt was made by the authors to quantify the level of gadolinium doping, and no STEM analytical measurements were taken to confirm that successful Ln³⁺ doping (and not separate nucleation) had occurred.[248] As previously mentioned, De Silva et al. published a high temperature thermolysis route to Ln:Fe₃O₄ (Ln = Sm, Eu, and Gd) particles.[67] In this report the authors show the M_s values for Sm:Fe₃O₄ and Eu:Fe₃O₄ particles are 31.3 and 23.6 emu/g respectively. No comment is made regarding the M_s values of the Gd:Fe₃O₄ particles. Looking outwith doped magnetite nanoparticles, decreasing M_s values with increasing levels of Ln³⁺ doping has also been observed for other ferrite systems. Nikumbh reported decreasing M_s values with increasing gadolinium doping in γ -Fe₂O₃ powders.[249] Wang et al. showed that M_s for cobalt-ferrite microparticles with the general formula Co_yGd_zFe_{3-y-z}O₄ decreased steadily from 91 emu/g to 73 emu/g as the value of z was increased from 0 to 0.4.[243] A sim-

ilar trend was observed by Sattar et al. who synthesised $\text{Cu}_{0.5}\text{Zn}_{0.5}\text{Fe}_{2-x}\text{Ln}_x\text{O}_4$ powders, where a decrease in magnetisation upon Ln^{3+} doping (increasing x from 0.0 to 0.02) was observed.[246]

The most common explanation for the decrease in magnetisation upon doping is that Ln^{3+} ions cause an increase in the magnetic anisotropy of the host particles.[67, 225] As was mentioned previously, the difference in ionic radii between gadolinium(III) and iron(II)/(III) ions is in the order of 30 pm (for Fe^{2+}) and 43 pm (for Fe^{3+}). In lanthanide-doped magnetite, the large Gd^{3+} ion will go into the octahedral B sites of the lattice, increasing strain in the lattice and therefore reducing the overall crystalline symmetry, which will increase the magneto crystalline anisotropy.[243, 250] Reducing the overall crystalline symmetry will also disrupt the ferrimagnetic ordering within the magnetite lattice, which could contribute to the lower overall magnetisation of the particle.

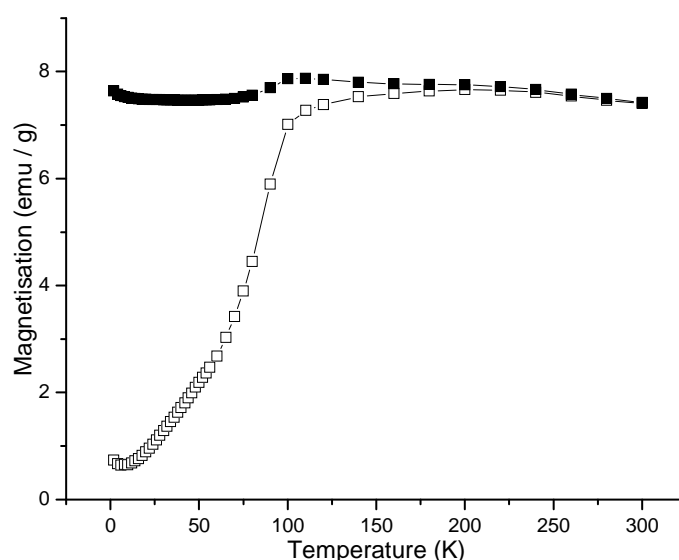


Figure 6.16: Zero field cooled (open symbols) and field-cooled (closed symbols) magnetisation of octahedral 12 nm $\text{Gd}:\text{Fe}_3\text{O}_4$ particles in an applied field of 100 Oe. The blocking temperature was determined to be ~ 200 K.

Field cooled (FC) and zero field cooled scans (ZFC) were recorded for the $\text{Gd}:\text{Fe}_3\text{O}_4$ NPs, this data is presented in Fig. 6.16, from which a blocking temperature (T_B) of ~ 200 K was extracted. This value of T_B is in agreement with previously reported values for undoped magnetite NPs of similar sizes. For example, Park et al. reported T_B values of ~ 110 K and ~ 225 K for 12 and 16 nm particles respectively.[31] The current

12.0 ± 2.6 nm Gd:Fe₃O₄ particles with a T_B of 200 K are (as expected) in between the values reported by Park et al. Whilst Gd³⁺ doping was seen to have a detrimental effect on the M_S values of Gd:Fe₃O₄ particles, there does not appear to have been a noticeable effect on the T_B values of the doped particles. This implies that doping does not affect the energy required to overcome the energy barrier for the reversal of magnetisation.

Whilst it may initially appear that there is no immediate advantage to synthesising Gd:Fe₃O₄ particles (as M_S values are lower than undoped magnetite and there no significant increase to either H_C or T_B), it is possible that the doped particles could have potential applications as agents in magnetic fluid hyperthermia (MFH). The physical processes by which particles generate heat in alternating magnetic field were described in Chapter 1. MFH is an area of significant interest to the nanomaterials community as the localised heating produced by particles is capable of killing cancerous cells, such as tumours. The ‘effectiveness’ of a NP sample as a heat transfer agent in MFH is described in terms of its specific adsorption rate (SAR). The SAR value provides an efficient numerical way to compare the heating potential of different NPs under different conditions. Literature SAR values are usually normalised to 1 MHz and 100 Oe, and are usually quoted in Watts per gram of iron (W/g [Fe]). Normalising the data in this way allows easy comparison between data published by different research groups.

As was mentioned previously, a recent report by Drake et al. (which is to date the only published report which examines the magnetic properties of Gd:Fe₃O₄ nanoparticles) described the increased performance of Gd:Fe₃O₄ versus undoped Fe₃O₄ particles as localised heating agents in MFH.[225] In this report, the 12 nm Gd:Fe₃O₄ NPs were superparamagnetic, with zero H_C and M_R values and a reduced saturation magnetisation of 65.67 emu/g (much like the Gd:Fe₃O₄ particles synthesised in this chapter). Despite the apparent limitations in NP magnetic properties, the SAR values of the doped particles were twice that of similarly-sized undoped particles (115 and 59 W/g [Fe] respectively).[225]

The improved SAR value of the doped particles is explained in terms of the effect that gadolinium has on the anisotropy constant of the material. As was described in Chapter 1, heat generation by NPs in MFH occurs two main relaxation processes, Brownian and Néel, with characteristic relation times τ_B and τ_N . Brownian motion is associated with

the thermal fluctuations and the rotation of the whole particle, whereas Néel relaxation is associated with the relaxation of the magnetic moment of the particle. τ_N is determined by the following relationship

$$\tau_N = \tau_0 \exp\left(\frac{KV_M}{k_B T}\right), \quad (6.1)$$

where τ_0 is 10^{-9} s, V_M the particle volume, K is the magnetic anisotropy constant, k_B is the Boltzmann constant and T is the temperature.[55, 225] In the report of Drake et al. the SAR values of similarly sized doped and undoped particles were recorded under identical conditions, and it was concluded that the only variable that changed between samples was the magnetic anisotropy constant, K . The increase in K associated with the strain caused by fitting a Gd^{3+} ion into the magnetite lattice was therefore believed to be responsible for the observed increase in SAR value. This is consistent with the literature discussed above, which described the increase in strain associated with doping large lanthanide ions (not just gadolinium) for a range of ferrite systems. This suggests that the current $Gd:Fe_3O_4$ particles are exciting candidates for MFH applications. Before being used for any biological applications, NPs obtained by the thermolysis method (which are usually stabilised by hydrocarbons) must first undergo ligand exchange to replace the hydrophobic hydrocarbon ligand with a hydrophilic one, to allow NP dispersion in physiological conditions. This process will be described in more detail in section 6.3, but first we still have to discuss the gadolinium-doped manganese oxide species obtained by decomposition of the $[Mn_2Gd_2O_2(piv)_8(Hpiv)_2(MeOH)_2]$ complex, the synthesis of which was given in section 6.2.1. Details of the particles obtained using this species are given below.

Bimetallic Manganese-Containing Precursors

TEM images of the particles obtained using the $[Mn_2Gd_2O_2(piv)_8(Hpiv)_2(MeOH)_2]$ precursor are given in Fig. 6.17. Unlike the samples obtained using the $[Fe_2GdO(benz)_6(L)_3]$ precursor, it is quite clear that separate nucleation has occurred. Small Gd_2O_3 particles can be seen in abundance on the TEM grid, Fig. 6.17a–c), in addition to larger agglomerated particles which comprise numerous cubic subunits Fig. 6.17d–f).

Unusually, the Gd_2O_3 particles are remarkably well defined monodisperse spheres, with an average diameter of 2.6 ± 0.2 nm (8%) and large arrays were readily found on the grid. This is contrast to the Gd_2O_3 particles observed when separate nucleation

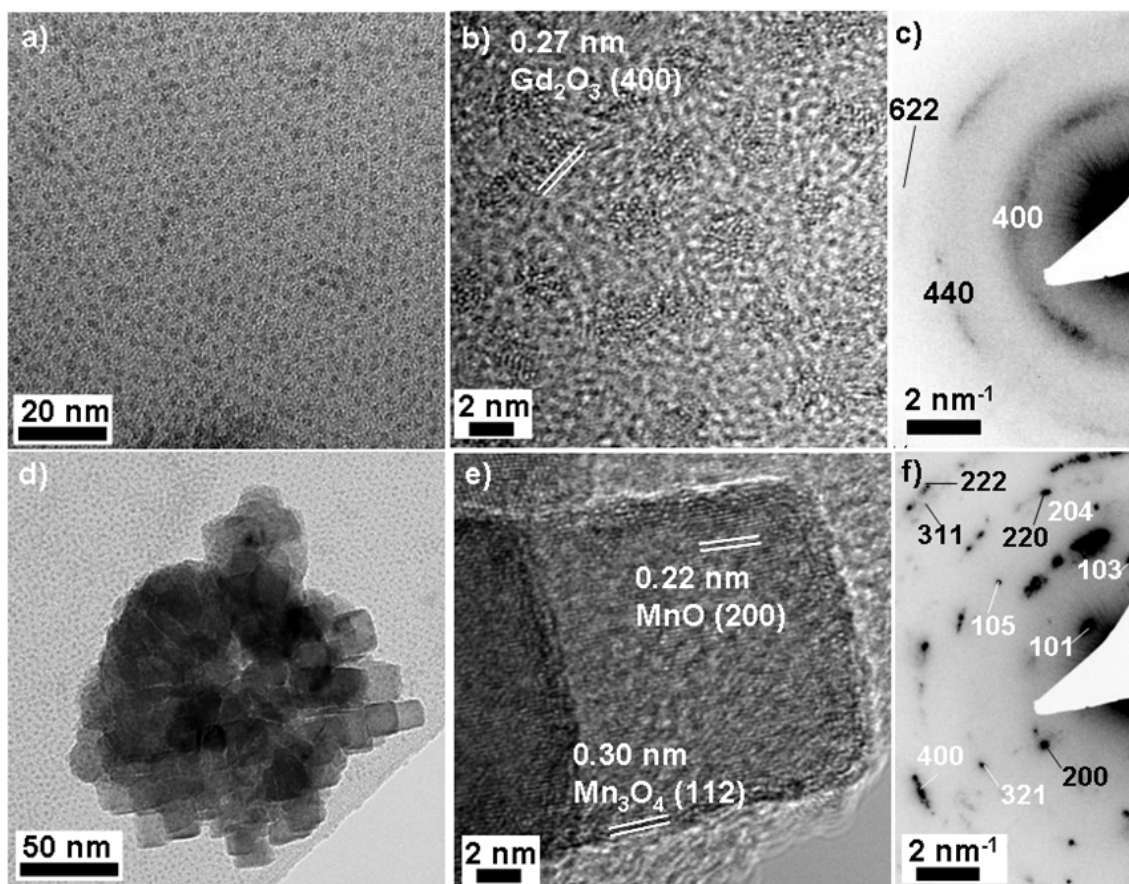


Figure 6.17: TEM and electron diffraction data from the Gd-Mn bimetallic precursor. a–c) Data from the Gd_2O_3 sample, showing the narrow size distribution of the obtained particles. The SAED pattern has been indexed with respect to cubic ($Ia\bar{3}$) Gd_2O_3 . d–f) Images showing a larger agglomerate, the cubic subunits clearly visible. e) HRTEM from a single cubic subunit, showing MnO fringes in addition to a thin layer of Mn_3O_4 on the subunit edge. f) SAED from a single agglomerate showed reflections from both MnO (black numbers) and Mn_3O_4 (white numbers).

occurred in the multi source reactions, which were poorly defined and did not form extended lattices (as in Fig. 6.4, for example). Selected area electron diffraction (Fig. 6.17f) from a lattice of small particles confirms the Gd_2O_3 composition. The larger agglomerated species, however, are not as well-defined. Lattice fringe analysis and selected area diffraction confirms these larger agglomerates to be a mixture of cubic MnO and tetragonal Mn_3O_4 , which is a similar composition to the manganese oxide particles discussed in the previous chapter. HRTEM of a cubic ‘sub-unit’ of an agglomerate shows the particle

to be a mixture of MnO in the particle core, with a thin layer of Mn₃O₄ at the particle edge. This is consistent with the observation that a thin outer layer of Mn₃O₄ forms upon exposure of the sample to air.

These MnO/Mn₃O₄ agglomerated particles bear a morphological resemblance to the ‘compound cube’ magnetite particles we previously encountered in section 3.3.4, when M-DEA was used as a solvent in the autoclave decomposition of Fe(acac)₃. However, unlike the compound cube magnetite particles the MnO/Mn₃O₄ particles do not possess a uniform crystal orientation, as was confirmed by the formation of a ring pattern (as opposed to a spot pattern) during selected area electron diffraction studies of a single agglomerate, Fig. 6.17f). The large size of the agglomerates (which are ~180 nm in diameter) is consistent with the MnO/Mn₃O₄ particles synthesised using the pivalate-containing precursors seen in chapter 5, which were larger than MnO particles prepared using non pivalate-containing precursors. The large and often irregular shaped particles obtained using pivalate as a coordinating ligand/surfactant are explained in terms of the steric bulk of the pivalate group ((CH₃)₃CCOO⁻) which can inhibit the adequate stabilisation of particles by blocking the long-chain surfactants from reaching the particle surface. Inadequate particle stabilisation results in the observed agglomerated forms, in a similar fashion to the agglomerated particles obtained using polyol solvents in the autoclave synthesis of Fe₃O₄ particles (Chapter 3).

Elemental specific measurements were acquired using EDX and EELS. The bright-field EDX spectrum (Fig. 6.18c) confirms the presence of both Mn and Gd in the sample, as was expected given the fact that separate nucleation has occurred. To probe the precise composition of the observed species, STEM EELS measurements were performed of both the small Gd₂O₃ particles and the larger MnO/Mn₃O₄ particles, as shown in Fig. 6.18.

Firstly, an average EELS spectra was obtained from an area containing only the small Gd₂O₃ particles. The EELS spectra was found to contain only the O-*K* and Gd-*M*_{5,4} edges, confirming that the small particles are pure Gd₂O₃, and do not contain any manganese. To investigate the composition of the larger MnO/Mn₃O₄ agglomerates, STEM EELS data was collected from an agglomerate straddling a hole. The DF-TEM image and corresponding EELS spectra obtained by hopping the electron beam across one such particle are given in Fig. 6.18a,b), which confirms the presence of O, Mn *and* Gd in the

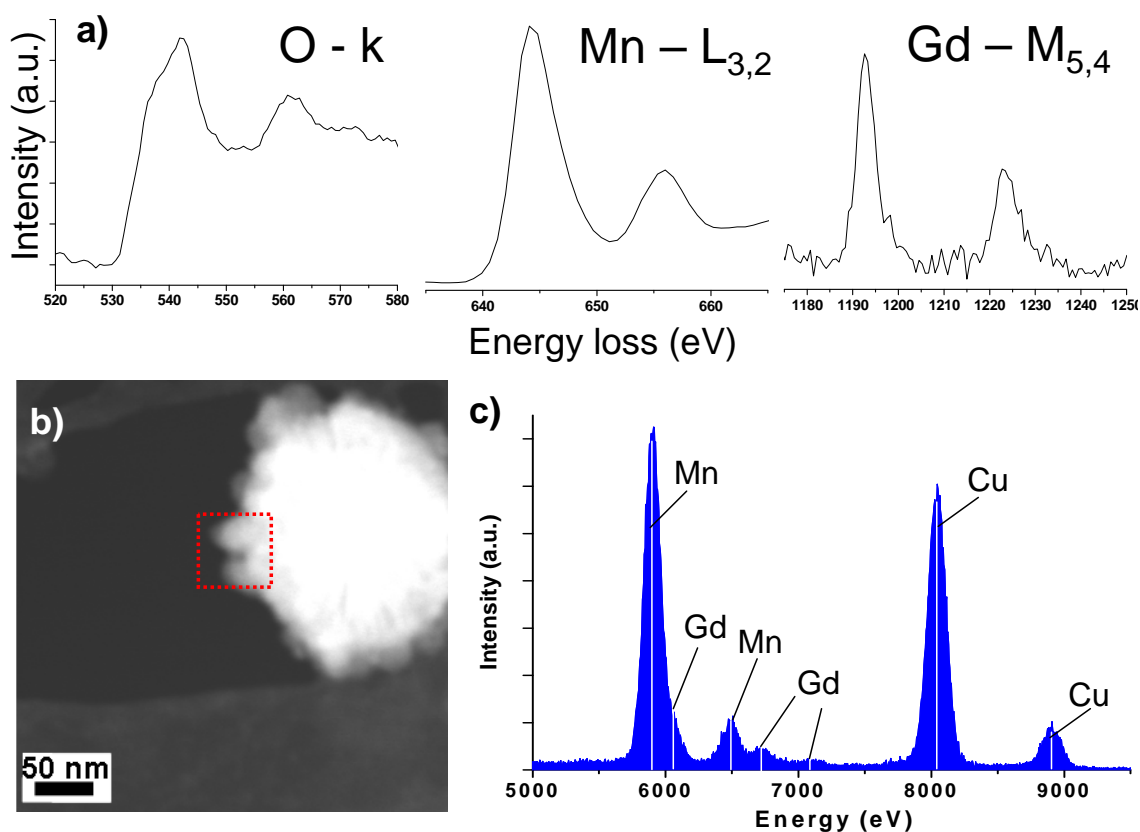


Figure 6.18: a) O, Mn and Gd EELS edges from the agglomerated Gd:Mn₃O₄ particles. The edges shown in a) were collected by moving the beam within the area indicated by the red box in b), which shows a dark field image of an agglomerate straddling a hole in the TEM grid. The contrast has been enhanced in this image to better identify the carbon support. c) EDX spectra obtained by condensing the beam on one such agglomerate, showing the presence of both manganese and gadolinium. The Cu peaks arise from the TEM grid.

particle. The elemental composition from this particular agglomerate was Mn: 40.23%, O: 55.6% and Gd: 4.21%, which is consistent with the values expected for replacement of manganese ions with Gd³⁺ ions in a mixed MnO/Mn₃O₄ system, which would have a metal content between 50% and 42% (for MnO and Mn₃O₄ respectively).

This result confirms that although using [Mn₂Gd₂O₂(piv)₈(Hpiv)₂(MeOH)₂] as a bimetallic NP precursor causes separate nucleation of Gd₂O₃ and MnO/Mn₃O₄ particles to occur, it is possible to incorporate some of the gadolinium present in the precursor into the MnO/Mn₃O₄ lattice. It is not possible to comment on the similarity of the ~4% Gd-dopant levels to other gadolinium-doped manganese oxide nanoparticles in the literature,

as at the time of writing no such reports could be found, and only a recent report relating to the surface functionalisation of Gd_2O_3 NPs with MnO existed.[251] Other reports in the literature show that it is possible to form the stoichiometric phases GdMnO_3 and GdMn_2O_5 , though these phases are only obtainable using a solid state ‘shake and bake’ reaction between bulk Gd_2O_3 and MnO powders at 1100 °C, which is far outwith the current 310 °C, solution based approach.[252] However, given the difference in ionic radii between the Mn^{2+} ion (83 pm) and the Gd^{3+} ion (107.8 pm), dopant levels of only a few percent are to be expected, due to the strain that will be placed on the MnO lattice. This is consistent with what we have seen in earlier in this Chapter, where dopant levels of between 1.6–2.5 mol% were seen for the $\text{Gd}:\text{Fe}_3\text{O}_4$ particles. The higher levels seen in the $\text{Gd}:\text{MnO}_x$ system may be due to the larger ionic radii of $\text{Mn}^{2+/3+}$ compared to $\text{Fe}^{2+/3+}$ ions, meaning that less strain is experienced by the MnO_x lattice upon Gd^{3+} doping, hence doping occurs to a greater extent. Separate nucleation in this instance may simply be a consequence of the solubility limit of Gd^{3+} in the MnO lattice being reached, i.e: the residual gadolinium that is not incorporated in the MnO lattice simply forms discrete Gd_2O_3 particles (as both manganese and gadolinium are present in the precursor in a 1:1 ratio). Attempts were made to measure the lattice constant using SAED measurements, the lattice parameter shift (if present) was too small to be visible.

Overall, using Mn_2Gd_2 -piv is not necessarily the most efficient method of preparing $\text{Gd}:\text{MnO}$ NPs, although the formation of doped particles does mean that the single-source method is indeed a viable method of obtaining bimetallic particles.

6.2.3 Conclusions

In this section we have seen that bimetallic single source precursors provide a means to create bimetallic composite species. Whilst separate nucleation was seen to occur for the Mn_2Gd_2 -piv precursor, EELS analysis confirmed that the larger agglomerated particles were in fact gadolinium doped $\text{MnO}/\text{Mn}_3\text{O}_4$ particles. It was also found that simple variations to an existing $\text{Fe}_3\text{O}(\text{benz})_6(\text{L})_3$ synthesis protocol enabled the formation of heterobimetallic iron-gadolinium precursors. This precursor could be decomposed to yield $\text{Gd}:\text{Fe}_3\text{O}_4$ NPs. The small size and narrow size distribution of the $\text{Gd}:\text{Fe}_3\text{O}_4$ particles makes them promising candidates for further biological studies and the increase in mag-

netic anisotropy associated with the doping of large Gd^{3+} ions into the magnetite lattice may improve their performance as MFH agents.

6.3 Biological Studies Using $\text{Gd}:\text{Fe}_3\text{O}_4$ Particles

In the last section of this Chapter the $\text{Gd}:\text{Fe}_3\text{O}_4$ particles are prepared for biological study by rendering them water soluble by ligand exchange with a polyethylene glycol based ligand. The suitability of the water-soluble NPs for biological applications was determined by preliminary investigations including cell uptake studies and toxicity tests. The methodologies for ligand exchange and the biological investigations are described below.

The potential biological applications of magnetic nanoparticles (MNPs) have undoubtedly driven the recent surge of research interest in these materials. As was discussed in Chapter 1, MNPs have applications in MRI and MFH, and as such are considered ‘theranostic’ materials which can function as both therapeutic and diagnostic agents.[54] Because of this dual modality researchers from a range of disciplines have studied MNPs, from materials scientists looking to improve the physical properties of the particles[53] to biologists who are keen to exploit the labelling, imaging, tracking and drug-delivery properties of MNPs to better understand cellular processes and develop medicinal applications.[253] The aim of this section is to determine if the $\text{Gd}:\text{Fe}_3\text{O}_4$ particles can be used for biological applications, by testing their uptake into cells and subsequent toxicity. These tests are important as any particle to be used in a nanomedicinal application it must be able to enter and remain in a cell without any detrimental side-effects.

In order for MNPs to be used in nanomedicinal applications, they first have to be coated in a water-dispersible material, so that they can persist in physiological conditions without agglomeration. As the $\text{Gd}:\text{Fe}_3\text{O}_4$ particles (and indeed all the particles in this thesis) were synthesised using a non-aqueous thermolysis route, the hydrophobic hydrocarbon surfactants (oleic acid and oleylamine) must be replaced with hydrophilic molecules. There are two approaches that can render a particle suitable for physiological conditions. The first is direct surfactant exchange, in which the hydrophobic molecules which stabilise a particle are replaced by hydrophilic ligands which bind covalently to the particle surface. The second approach is surfactant addition, whereby an amphiphilic ligand (con-

taining both a hydrophilic polar head group and a lipophilic tail, such as a hydrocarbon chain) is added to a solution containing hydrocarbon-stabilised particles. The lipophilic tail of the amphiphilic surfactant will form a double-layer with the hydrocarbons present on the particle surface. The polar head groups of the amphiphilic surfactant render the whole particle hydrophilic.

For biological applications, the stability of MNP dispersions is crucial. If agglomeration between particles occurs the macrophage system will recognise the large agglomerate as a foreign body, and the agglomerate will be phagocytosed by macrophage cells.[254] It is therefore important to choose a surfactant that will provide excellent particle stability and ensure long blood circulation times. In the current study, the direct ligand exchange protocol was adopted and the oleate surfactant covering the Gd:Fe₃O₄ particles was replaced with a modified polyethylene glycol (PEG) derivative. PEG is a common ligand used to render particles water-soluble, and the long length of its polyethylene backbone ensures that agglomeration of particles is minimised. Once functionalised, the uptake and subsequent toxicity of the particles to fibroblast cells was assessed by standard methods.

6.3.1 Experimental

Ligand Exchange Protocol

The PEG ligand was modified using DCC/NHS conjugate chemistry to include a dopamine derivative (DPA) on one end, as the hydroxyl groups of dopamine were shown to act as a robust 'linker' molecule to attach PEG ligands to the surface of particles.[255] The PEG-DPA surfactant was synthesised and attached to the particle surface according to a previously published method.[254] Both Gd:Fe₃O₄ and a control batch of similarly sized undoped Fe₃O₄ particles were prepared for biological studies. Briefly, PEG diacid 600 (200 mg) was mixed with N-hydroxysuccinimide (NHS, 4 mg), N,N'-dicyclohexylcarbodiimide (DCC, 6 mg) and dopamine hydrochloride (DPA, 3 mg) in a solution containing CHCl₃ (4 mL), DMF (1 mL), and anhydrous Na₂CO₃ (20 mg). This mixture was then stirred for two hours at room temperature to ensure complete formation of the PEG-DPA ligand. 15 mg of oleate-coated particles was then added and the resultant mixture was left to stir for 24 hours under N₂ protection. The modified particles were precipitated by adding hexane and collected via centrifugation for 5 minutes at 4,000 r.p.m before be-

ing dried under a gentle N₂ flow. The particles can then be dispersed in water, giving a pale-brown dispersion. The aqueous particle dispersion was purified by dialysis against DI water using SnakeSkin™ dialysis tubing (Thermo-Scientific, MWCO = 7,000) for 24 hours, changing the water 3 times during the 24 hour period. Finally the particles were filtered through a 200 nm syringe filter to remove any large aggregates or biological contaminants.

Cell Culture Protocol

Infinity™ Telomerase Immortalised primary human fibroblasts (h-TERT BJ1, Clontech Laboratories Inc., CA, USA) were seeded onto ethanol sterilised 13 mm diameter coverslips at a density of 1×10^4 cells per disc in 1 ml of medium and permitted 24 h for cell attachment prior to incubation with particles, cultured at 37 °C, 5% CO₂. The medium used was 71% Dulbeccos Modified Eagles Medium (Sigma Aldrich, MO, USA), 18% medium 199, 10% fetal calf serum (Invitrogen, UK), 0.9% 100 mM sodium pyruvate (Sigma Aldrich). After 24 h cells were incubated with either Gd:Fe₃O₄ or Fe₃O₄ NPs for 60 min at 37 °C, 5% CO₂. For the MTT assay, cells were incubated with particles at 3 different concentrations; 0.1, 0.01 and 0.001 mg/mL. For fluorescence microscopy, SEM and TEM, cells were incubated with particles at 0.1 mg/mL. Control cells were cultured in the absence of particles.

MTT Assay Protocol

The enzymes present in a healthy cell can convert yellow MTT (a triazole dye) to purple formazan. The MTT assay technique optically measures the conversion of MTT to formazan, with greater conversion indicative of greater numbers of healthy cells. To assess the toxicity of the particles, particle suspensions at the required concentrations were incubated with cells in a 96 well plate for 1 hour at 37 °C. The particle suspension was then removed and 5 µL of MTT dye (5 mg/mL in phosphate buffer pH 7.4, Sigma-Aldrich) was added to each well. After 1.5 h of incubation at 37 °C, the medium was removed and any formazan crystals produced were dissolved in 100 µL of DMSO. The absorbance of each well was read on a microplate reader (Dynatech MR7000 instruments) at 550 nm, calibrated to zero absorbance using culture medium without cells.

Immunofluorescence Microscopy

Fluorescence microscopy was used to investigate how cells respond to the nanoparticles. In the current study, cells from each of the three samples were stained with 3 different fluorescent stains. Each stain binds to a specific part of the cell and fluoresces at a different wavelength. The stains used were rhodamine-conjugated phalloidin, anti- β -tubulin and 4',6-diamidino-2-phenylindole (DAPI) which image the cell F-actin, β -tubulin and nucleus respectively. By imaging cells using the different wavelengths of light for each stain a false-coloured composite image can be created, showing the morphology of the structures in the cell. Fluorescence imaging therefore allows us to see the morphology of the cell and its organelles, which is useful as the cell morphology is dependent on the health of the cell and can be affected by external stimuli, such as nanoparticles.

Cells were incubated with 0.1 mg/mL NP dispersions for 1 hour at 37 °C and mounted in a 96 well plate as previously described. The medium was then removed and 4% formaldehyde/PBS was added to fix the cells (15 mins, 37 °C). The fixative was removed and permeabilising buffer was added for 5 mins at 4 °C. Permeabilising buffer is added to permeate the cell membrane. The buffer was removed and 1% bovine serum albumin (BSA) in PBS was added (5 mins, 37 °C). A solution containing phalloidin and the primary antibody anti- β -tubulin in a 1:50 ratio with PBS/BSA was prepared. The BSA was removed from the wells and 200 μ L of the phalloidin/anti- β -tubulin solution was added to each well (1 hour, 37 °C). The stains were removed and the cells were washed gently with a PBS/0.5% Tween (detergent) solution three times. The Tween solution was removed and 200 μ L of the secondary antibody anti- β -tubulin in a 1:50 PBS/BSA solution was added (1 hour, 37 °C). The stain was removed and the cells were gently washed again with PBS/0.5% Tween. Finally, the tertiary streptavidin component was added (30 minutes, 4 °C). The coverslips were then removed from the wells and a drop of fluorescent mountant that contains DAPI was added to the cell area. The coverslip was then stored between two microscope slides until required for imaging. A control sample was prepared in analogous way though in the absence of particles.

Electron Microscopy

Electron Microscopy (EM) was performed to compliment the fluorescence microscopy studies. Both scanning electron microscopy (SEM) and transmission electron microscopy (TEM) were performed to examine the cells after incubation with particles. SEM provides a good overview of the morphologies of a sample of cells, whilst TEM allows us to see a cross-section through a sample of cells, to see if particles were present inside the cells. EM was performed at the Integrated Microscopy Facility, University of Glasgow.

The cells were cultured and incubated with particles as described in the cell culture protocol section. The cells were fixed with 1.5% glutaraldehyde (Sigma, UK) buffered in 0.1 M sodium cacodylate (Agar, UK) for 1 h at 4 °C. The cells were then postfixed in 1% osmium tetroxide for 1 h (Agar, UK) and 1% tannic acid (Agar, UK) was used as a mordant. Samples were stained in 0.5% uranyl acetate, then dehydrated using a series of increasing methanol concentrations (30, 50, 70 and 90%), followed by a final step using 100% ethanol). The final dehydration was in hexamethyl-disilazane (Sigma, UK), followed by air-drying. Once dry, the samples were sputter-coated with gold before examination with a JEOL JSM6400 Digital SEM at an accelerating voltage of 6 kV.

For TEM, the cells were cultured and incubated with particles as described in the cell culture protocol section and fixed and stained as for SEM. The coverslips were then treated with (1:1) dried absolute alcohol:resin over night to evaporate the alcohol. The cells were then embedded in Spur's resin and ultra thin sections were cut. Images were taken on a Leo 912AB TEM operated at 120 kV.

6.3.2 Results and Discussion

The reaction scheme for ligand synthesis and for the ligand exchange protocol are given in Figs. 6.19 and 6.20, respectively. The ligand exchange protocol was successful for both the doped and undoped Fe_3O_4 particles, as the nanoparticle-PEG powders were found to be dispersible in water, giving a pale brown suspension. TEM imaging of the $\text{Gd}:\text{Fe}_3\text{O}_4$ and Fe_3O_4 particles showed that the particles remain un-agglomerated after PEG functionalisation and that the core shape and size of the particles has not been altered during the functionalisation process, as shown in Fig. 6.21. The exchange of oleate to PEG was seen in dynamic light scattering (DLS) measurements, which showed an increase in the

hydrodynamic radius of particles after ligand exchange. This increase is consistent with the replacement of the short oleate surfactant with the long PEG ligand, Fig. 6.21d).

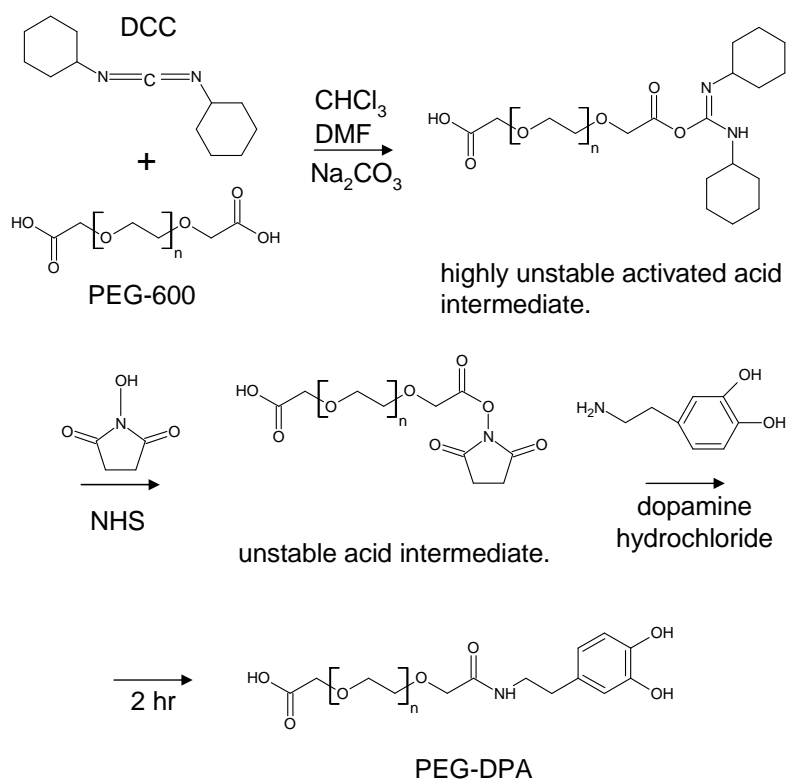


Figure 6.19: Reaction scheme showing the synthesis of the PEG-DPA ligand by the DCC/NHS mediated coupling between PEG 600 and dopamine hydrochloride (DPA).

An MTT assay was performed to determine the toxicity of particles towards cells. It allows a quantitative measurement of cell viability upon exposure to particles to be obtained and the results are given in Fig. 6.22, which shows good overall cell viability for both the Fe_3O_4 and $\text{Gd}:\text{Fe}_3\text{O}_4$ particles. For the Fe_3O_4 particles, the cell viabilities (\pm standard deviation) were 110.3 (24.8), 94.9 (11.8) and 97.4 (17.8) percent, for 0.1 mg/mL, 0.01 mg/mL and 0.001 mg/mL particle dispersions respectively. For the doped $\text{Gd}:\text{Fe}_3\text{O}_4$ particles, the cell viabilities (\pm standard deviation) were 75.7 (28.4), 79.5.9 (24.8) and 82.0 (29.1) percent, for 0.1 mg/mL, 0.01 mg/mL and 0.001 mg/mL particle dispersions respectively. It is clear that the doped particles show slightly lower cell viabilities. This could be due to the minor ‘leakage’ of gadolinium ions from the particles, as free Gd^{3+} is known to be toxic. If gadolinium ions are diffusing from the particles then

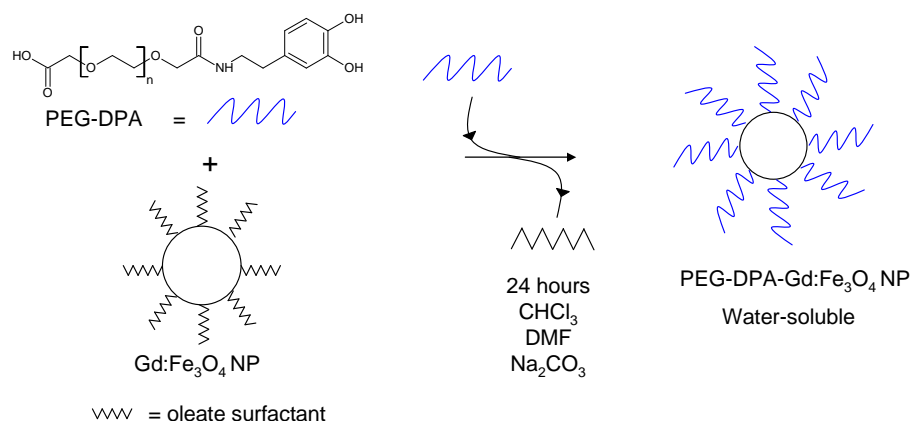


Figure 6.20: Schematic for the exchange between oleate ligand and the PEG-DPA ligand.

it could be that the PEG surfactant does not provide adequate stabilisation of the particle surface.

As the MTT assay showed that the cells were still alive after incubation with particles, immunofluorescence microscopy was performed to determine if the morphology of the cell cytoskeletal structure (i.e.: the F-actin and tubulin) was affected after exposure to particles. Immunofluorescence microscopy is a powerful technique as it enables different organelles within a cell to be labelled with a different fluorophore and imaged independently. A false-coloured composite image can therefore provide a great deal of information from each cell. The fluorescence microscopy pictures for a control sample (with no particles added) and the Fe_3O_4 and $\text{Gd:Fe}_3\text{O}_4$ particles are given in Fig. 6.23.

For the control cells (Fig. 6.23a) the fluorescence microscopy pictures show the elongated and well-spread cells (upper and lower pictures) that would be expected for a typical healthy cell sample on a flat surface (like a coverslip). The nucleus of each cell is visible in blue (due to DAPI staining) and each nucleus appears spherical, indicating no abnormalities. The F-actin (stained red) is filamentous and provides the main structural support to the cell cytoskeleton. In a control cell this typically appears along the cell periphery and throughout a cell spread on a flat surface in the form of stress fibres across the cell. The β -tubulin, visible in green is an additional part of the cell cytoskeleton and is involved in cell trafficking (i.e.: movement of endocytosed material through the cell to storage by the nucleus). In a healthy cell, β -tubulin should be evenly dispersed throughout the cell, so Fig. 6.23a) indicates that normal β -tubulin distribution is observed in the control cells.

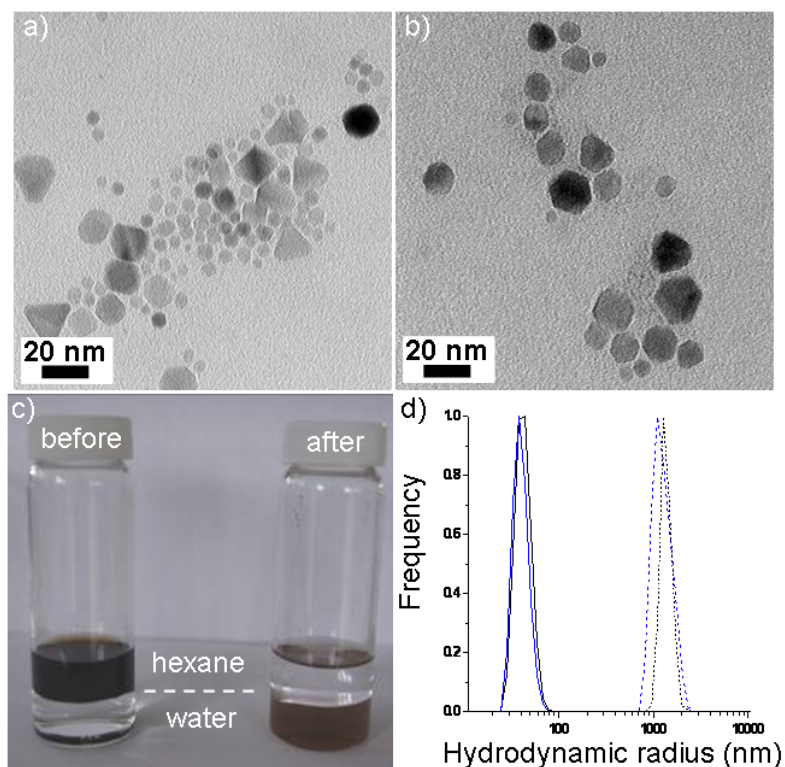


Figure 6.21: TEM images of a) Fe₃O₄ and b) Gd:Fe₃O₄ PEG functionalised NPs deposited from their aqueous dispersions. c) Photograph showing dispersion of doped particles in hexane and water before and after ligand exchange respectively. d) Hydrodynamic radii of undoped (black) and doped (blue) particles before and after functionalisation (solid and dotted lines respectively).

The micrographs of the cells which have been exposed to particles (Fig. 6.23b,c) for the undoped and doped particles respectively) show that there is a difference in cell morphology when compared to the control cells. The elongated cells seen in the control sample were not as prevalent in the particle samples, and instead the cells appear to have adopted a more rounded shape — although elongated cells were still visible in some areas of the coverslip. The long strands of actin (stained red) that were visible in the control cells are not as apparent in the cells that have been incubated with particles, and only small amounts of actin are visible at the cell edge. This implies that the introduction of particles has altered the cell cytoskeleton, perhaps as the cells change to uptake particles. Interestingly, the DAPI staining of the Fe₃O₄ and Gd:Fe₃O₄ samples reveals that some of the nuclei of the rounded up cells are in fact dividing, and the cells were in the process of cell division when they were fixed. It is not currently clear why the cells incubated with

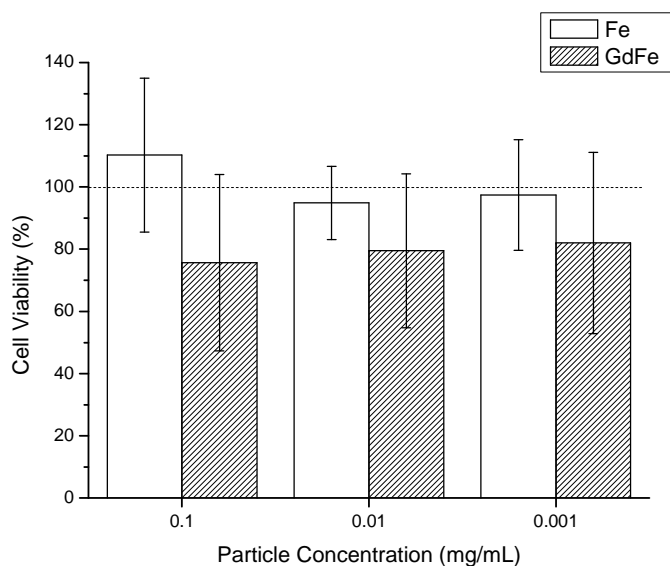


Figure 6.22: MTT toxicity assays of Fe_3O_4 and $\text{Gd}:\text{Fe}_3\text{O}_4$ particles, showing good cell viability for the undoped Fe_3O_4 NPs and a moderate cell viability for the $\text{Gd}:\text{Fe}_3\text{O}_4$ particles.

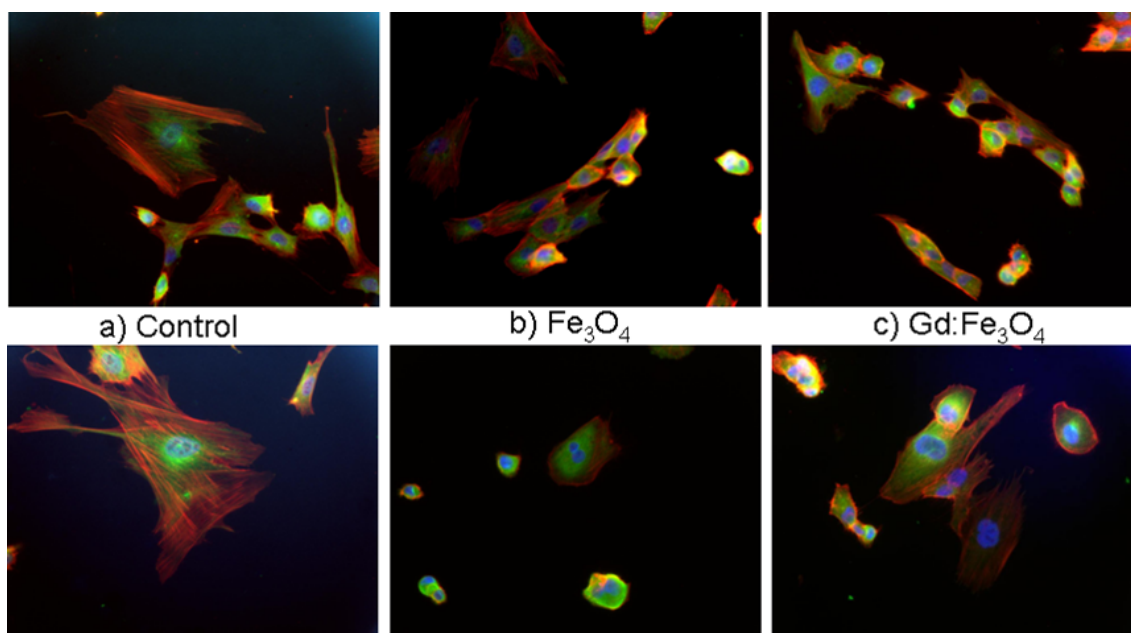


Figure 6.23: Optical fluorescence microscopy of the three stained cell samples a) control, b) incubated with Fe_3O_4 NPs and c) incubated with $\text{Gd}:\text{Fe}_3\text{O}_4$ NPs.

particles would undergo the cell division process, though cell division would explain the rounded-up shape of the cells, which is normal for a dividing cell.

As the fluorescence images show that cells are healthy and their organelles are intact after incubation to particles, electron microscopy (EM) was performed to obtain additional information regarding the uptake of particles into the cells. With SEM, the surface of the cells can be imaged, enabling us to see the cell protrusions associated with cellular uptake. TEM, on the other hand, allows imaging of cell cross-sections, meaning that

the distribution of particles within a cell can be seen. The results of the EM imaging are shown in Fig. 6.24.

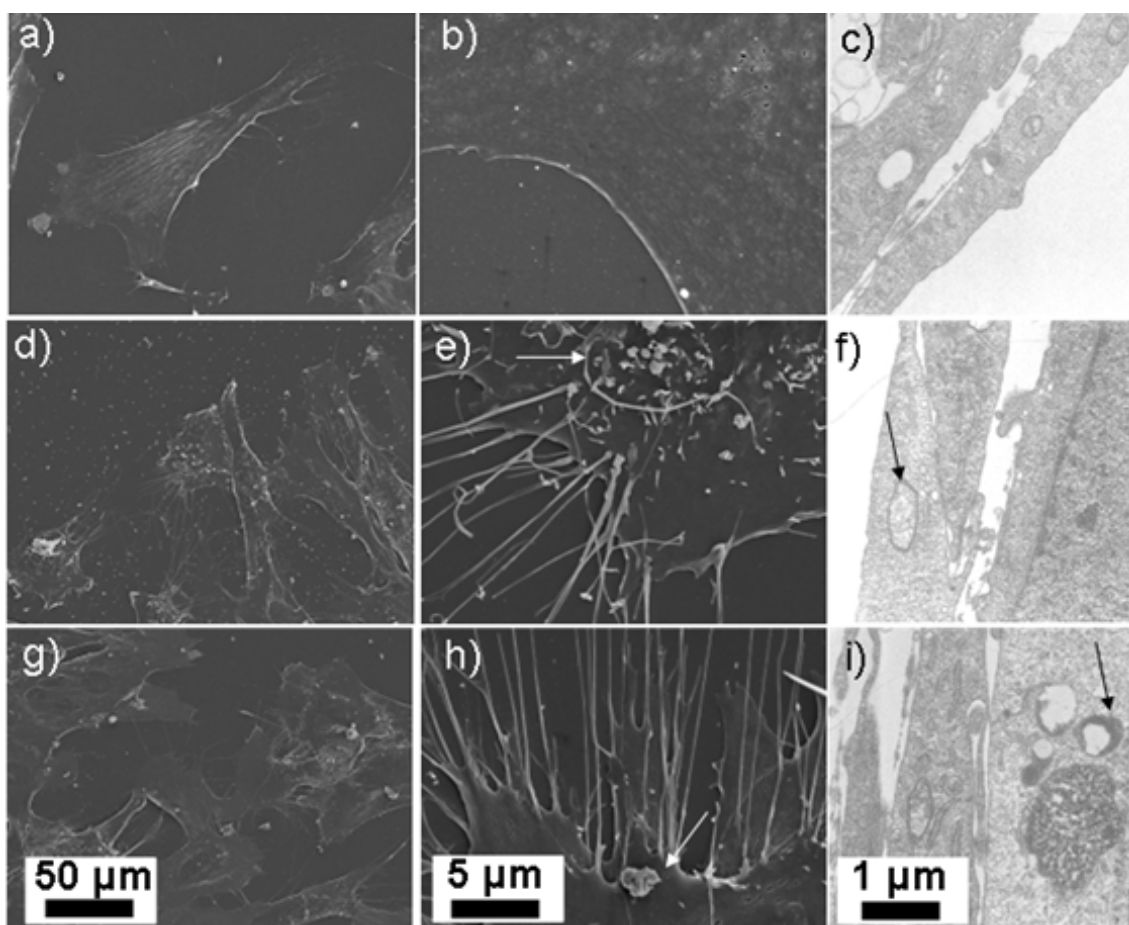


Figure 6.24: Low magnification SEM (left column), high magnification SEM (middle column) and TEM images (right column) of a–c) Control cells incubated in the absence of particles, d–f) Cells incubated with Fe_3O_4 particles and g–i) Cells incubated with $\text{Gd}:\text{Fe}_3\text{O}_4$ particles. White arrows in the SEM images are actin protrusions, which form on the cell surface during uptake of material. Black arrows in the TEM images show uptake of particles into vesicles.

The EM images of the control cells (which have not been exposed to particles) show how a typical healthy cell should look. The SEM images (a,b) show the cell is flat on the coverslip surface and that the edges are smooth. The TEM image c) reveals the vacuoles of the control cells to not contain any discernible high-contrast material. The cells obtained from the undoped (d–f) and doped (g–i) particles are quite different in comparison to the control cells. The SEM images show that after exposure to particles the cells

are flat on the surface and appear healthy, implying no adverse reaction upon exposure to particles has occurred. Furthermore, the surfaces of the cells are seen to be covered with actin protrusions (indicated by white arrows), which are the structures that form during the cellular uptake of material in a process known as pinocytosis. The edges of the cells incubated with particles also show more filopodia than the control cells, which are the long, spindle-like protrusions the cell uses to sense its surroundings and feel its way around a surface. This indicates that the cells are responding to presence of the nanoparticles. TEM images (right column of Fig.6.24) show that the vesicles of cells incubated with particles (indicated by black arrows in images f,i) contain more material than the vesicles of the control cells. Given the small particle size and the reduced contrast of the particles against the cell structures (which have been stained with osmium and uranium) it is difficult to get a clear view of the particles within the cell vesicles.

6.3.3 Conclusions

In this section we have seen that the $\text{Gd:Fe}_3\text{O}_4$ particles obtained in section 6.2.2 are readily made water soluble through a simple surfactant exchange mechanism. The water-dispersible $\text{Gd:Fe}_3\text{O}_4$ NPs and similarly-sized undoped Fe_3O_4 particles were incubated with fibroblast cells, and their uptake into the cells and subsequent toxicity was assessed. The MTT toxicity assay showed good cell viability for both the doped and undoped particles, with a marginally higher cell viability seen for the undoped particles than the doped particles. Fluorescence microscopy showed that some of the cells incubated with particles (either the doped or undoped NPs) had a different morphology to cells from a control sample which had not been incubated with particles. The cells incubated with NPs were generally more rounded (although some normal-looking cells were present), and the nuclei of the rounded cells suggested that the cells were undergoing cell division. At the moment it is not clear why exposure to NPs would cause cell division to occur, and repeat experiments would be required. SEM confirmed that the cells were responding to the presence of both the doped and undoped particles, and the actin protrusions associated with pinocytosis (the cellular uptake mechanism) were visible. TEM measurements showed that the cells were healthy, although it was hard to comment unambiguously on the particle distribution within the cell, given the small size of the iron oxide particles and

their comparatively poor contrast with the uranium and osmium stained cells. However, the vacuoles of the cells incubated with particles appeared to contain more material than the vacuoles of the control cells.

From the above studies it is clear that the PEG-functionalised Gd:Fe₃O₄ particles are not toxic and are readily taken up by cells. This is a promising result as it means these particles can be used in further MFH and MRI studies.

6.4 Chapter Conclusions and Further Work

In this chapter various approaches to synthesising bimetallic metal oxide-dopant particles were investigated. An emphasis was placed on developing a synthetic protocol to incorporate the Gd³⁺ ion into the magnetite lattice (to create Gd:Fe₃O₄ particles), although Gd:MnO_x particles were also investigated.

Initially, the multi source precursor approach was studied. In this approach two separate precursors (either Gd(OAc)₃ or Gd(acac)₃ and Fe(acac)₃ or Fe(CO)₅) are reacted together, in the hope that upon precursor decomposition a bimetallic particle will form. Using the multi source approach the synthesis of both Gd:Fe₃O₄ and Gd₂O₃/Fe₃O₄ (core/shell) particles was attempted by varying the order of reagent addition; for core/shell particles the gadolinium precursor was reacted first then the iron precursor was added subsequently, whereas for Gd:Fe₃O₄ particles both the gadolinium precursor and the iron precursor were reacted simultaneously. A range of reactions were performed, in which combinations of the nanoparticle precursors were reacted employing either subsequent or simultaneous particle decomposition. TEM investigation of these particles revealed that in most cases separate nucleation of Gd₂O₃ and Fe₃O₄ particles had occurred and STEM EELS studies showed that in all cases there was no uptake of gadolinium into the magnetite particles.

Given the difficulty in overcoming the separate nucleation problem using the multi source approach, the single source approach was adopted. In addition to a known bimetallic manganese and gadolinium compound, a new iron and gadolinium compound was synthesised by slight modification of the synthesis for a previously reported iron and copper compound. This new compound was characterised by IR, TGA, and powder-XRD.

Nanoparticles were synthesised using the bimetallic precursors, and HRTEM/STEM-EELS investigations confirmed that bimetallic nanoparticles (both Gd:Fe₃O₄ and Gd:MnO) had been created. Magnetic properties of the gadolinium-doped magnetite particles were measured, and revealed the particles to be superparamagnetic, with a saturation magnetisation of 33.19 emu/g at 300 K. This value is far below the saturation magnetisation value of bulk magnetite and is indicative of a decrease in crystal symmetry, which is consistent with the doping of a large lanthanide ion into the magnetite matrix. Despite the reduced saturation magnetisation, the enhanced magnetic anisotropy afforded by the lanthanide doping means that the Gd:Fe₃O₄ particles represent promising potential candidates for applications in magnetic fluid hyperthermia.

Further studies were performed to test the suitability of these Gd:Fe₃O₄ particles for biological applications. A simple ligand exchange protocol was employed to render the particles water soluble. Uptake of these particles by fibroblast cells was confirmed through TEM and it was found that the cells incubated with Gd:Fe₃O₄ particles had good overall viability, with slightly lower viabilities than cells incubated with similarly sized undoped Fe₃O₄ particles. The biological studies confirm that the Gd:Fe₃O₄ particles are stable and non-toxic under physiological conditions and are therefore suitable for further testing as MFH agents.

Furthermore, the formation of Gd:MnO_x bimetallic particles using the Mn₂Gd₂-piv bimetallic precursor proves the single source precursor approach to be a versatile and straightforward way of producing new nanocomposite materials. Given the wealth of polynuclear complexes that are known in the literature, there is considerable scope for the synthesis of more complicated composite particles using novel heterometallic polynuclear compounds.

Chapter 7

Conclusions and future work

In this thesis a number of different solution-based approaches to synthesising magnetic nanoparticles have been studied. Principally, two main strategies (the autoclave and reflux protocols) were adopted, and in each Chapter a different aspect of NP synthesis was investigated.

In Chapter 3 the role of solvent on the morphology of magnetite NPs obtained by the autoclave method was investigated. For this investigation, a number of solvents were chosen so that the contributions of different physical and chemical properties of each solvent could be studied. A range of polyol solvents were chosen, which contained different numbers and types of functional groups (such as alcohols) as the hydroxyl functionality of polyol solvents has previously been shown to be capable of chelating to iron which can help stabilise particles during particle nucleation and growth. Furthermore, subtle structural changes between each solvent enabled the effect of alkyl side-arm length on surfactant packing at the particle to be investigated. From these experiments it was possible to draw a number of conclusions.

Firstly, in the autoclave synthesis of magnetite particles, control over NP morphology is generally improved if a solvent with functionality (preferably a primary alcohol group) is used. This was evident in comparison between the particles obtained using a solvent with limited functionality (BE) and a solvent containing two primary alcohols (DEG). BE produced large and inhomogeneous NPs and platelets, whereas the use of DEG resulted in the formation of monodisperse particles.

Secondly, the structure of the polyol ligand will also influence the particle morphol-

ogy, by disrupting the packing of surfactant molecules on the particle surface. The adsorption of surfactants on a particle surface is a key driver for NP shape selectivity, and the alkyl side-arms of the polyol solvents used in Chapter 3 could destabilise the surfactants immediately surrounding the NP surface. Disrupted stabilisation of NPs has two effects: firstly, the reduced stabilisation of particles will render them more susceptible to coalescence and will therefore facilitate the formation of compound particles, which were observed for M-DEA and E-DEA. Secondly, the alkyl side arms of these polyol solvents will also alter the competitive adsorption kinetics of surfactants — which is believed to be responsible for the formation of cuboidal particles when M-DEA was used.

Magnetic characterisation of these particles showed that the NPs obtained exhibited superparamagnetic behaviour, with high saturation magnetisations that were slightly lower than the bulk value. The reduced saturation magnetisation values are believed to be a consequence of the increased number of surface spins present in nanoparticles compared to bulk materials. Surface spins are magnetically disordered with respect to the spins present in the particle core.

There is scope for future work in the autoclave synthesis of iron oxide particles using the current autoclave route. For one, an in-depth investigation of the factors that influence particle growth when the alkyl side-arm length is varied is warranted, as it is obvious from comparison of the particles obtained using DEA, M-DEA and E-DEA that there is no obvious trend and that particle growth is a result of a delicate balance between several competing factors. Additionally, it is anticipated that this method could be extended to other transition metal oxides, simply by varying the acetylacetonate precursor. Indeed, it may be possible to synthesise mixed metal particles simply by using the appropriate mixture of transition metal acetylacetonate starting materials in the synthesis.

The autoclave approach was again used in Chapter 4, which set out to investigate possible methods to synthesise lanthanide oxide (LnO_x) nanoparticles. For this Chapter the polyol solvent was replaced with a mixture of DOE, OA and OAm molecules, a solvent mixture which was previously shown to result in the synthesis of Ln_2O_3 particles from $\text{Ln}(\text{acac})_3$ starting materials. In Chapter 4 it was discovered that the autoclave decomposition of $\text{Ln}(\text{oleate})_3$ in the DOE:OA:OAm solvent mixture resulted in the formation of remarkable, high-aspect ratio CeO_2 and Ln_2O_3 nanowires (for Ce, Nd, Eu, Gd and Yb

oleates) and ribbons (for Dy oleate). Interestingly, HRTEM investigation revealed that the nanowires and ribbons are not single crystalline. The wires and ribbons were found to comprise many randomly orientated individual Ln_2O_3 crystalline regions, the size of which depended on the lanthanide oleate used and was found to decrease with increasing atomic number. The production of discrete and small Ln_2O_3 NPs by decomposition of a lanthanide oleate has been reported previously, though the oriented assembly of small Ln_2O_3 particles into wires and ribbons is unprecedented.

It was found that the thickness of the nanowires decreased across the lanthanide series, from ~ 5 nm for CeO_2 to ~ 2 nm for Yb_2O_3 . The decrease in wire thickness was attributed to an increase in stability of the $\text{Ln}(\text{oleate})_3$ precursor with increasing atomic number across the lanthanide series. It is postulated that an increase in precursor stability reduces the number of NP monomers that are formed and hence results in smaller particles/thinner wires.

To determine the wire formation mechanisms, time dependent reactions were performed using the CeO_2 wires as a model system. Reducing the reaction time from 24 hours to 4 hours resulted in the formation of shorter wires which were ~ 100 nm in length, compared with the wires from the 24 hour reaction which were microns in length. HRTEM investigation of the short wires revealed that they consisted of numerous, randomly aligned small nanoparticles — which were much smaller than the individual crystalline regions that constituted the CeO_2 wires obtained from the 24 hour reaction. The time dependent reactions afforded sufficient insight such that a 3-stage growth mechanism can be proposed. The first stage is the formation of discrete oleate-stabilised LnOx nanoparticles upon $\text{Ln}(\text{oleate})_3$ decomposition. In the second stage these individual particles undergo oriented assembly and align end-to-end, which forms 1D chains of particles. During the third stage, the adjacent particles will recrystallise, forming regions of extended crystallinity within the wires. The rate of recrystallisation is dependent on the stability of the oleate precursor, which also determines the thickness of the wires.

It is postulated that the ‘oriented assembly’ or ‘imperfect oriented attachment’ mechanism by which the wires grew was facilitated by the growth of material within a constrained reaction environment, which consists of ordered assemblies of surfactant molecules and are formed in-situ, in the autoclave. These assemblies (which are com-

monly referred to as mesophases, liquid crystals or organic superstructures) consist of ordered arrays of surfactant molecules, and feature channels between arrays in which it is postulated that the oriented assembly of discrete LnOx nanoparticles into nanowires occurs. It was found that replacing DOE with the bulkier solvent BE in the reaction mixture resulted in the formation of discontinuous nanowires, presumably since the steric bulk of BE hindered the formation of extended channels within the surfactant mesophases. Conversely, DOE (which has a similar length $C_{16}H_{34}O$ backbone as OA and OAm) can easily assemble into mesophases with the surfactant molecules, resulting in continuous nanowires.

The magnetic properties of Gd_2O_3 nanowires and Dy_2O_3 nanoribbons are very similar to those of discrete particles, implying that no long-range ordering exists in the nanowires. Optical characterisation of the Eu_2O_3 nanowires showed that there is an increase in fluorescence lifetime going from bulk Eu_2O_3 to the nanoscale.

There is considerable scope for further work in the CeO_2 and Ln_2O_3 nanowire and ribbon system. Firstly, whilst some experiments were performed to investigate the effect of reaction time on particle morphology, these reactions only studied the effect of reducing the reaction time (from 24 hours to 4 hours), so it is possible that by *increasing* the reaction time beyond 24 hours, it may be possible to synthesise even longer nanowires. Secondly, it is feasible that by finely tuning the deposition of wires onto substrates it may be possible to form larger assemblies of wires. In this thesis the nanowires and ribbons were deposited from hexane onto TEM grids, and it is anticipated that by using a less volatile hydrocarbon (such as octane or decane) as a dispersant it may be possible to slow the rate of solvent evaporation and therefore yield larger assemblies of wires. Controlled assembly of nanomaterials is important for device fabrication, for example.

With regards the physical properties of the nanowires and ribbons, it is anticipated that it will be possible to synthesise doped Ln_2O_3 nanowires and ribbons, simply by utilising a mixture of different $Ln(oleate)_3$ starting materials. As the optical properties of Ln^{3+} ions are susceptible to the nature of their surrounding matrix, it may be possible to tailor the optical properties of the nanowires simply by doping various levels of Eu^{3+} into different Ln_2O_3 host nanowires. The magnetic measurements of the Gd_2O_3 and Dy_2O_3 wires showed them to be superparamagnetic, with similar properties to similarly-sized discrete

nanoparticles. It was therefore possible to conclude that there is no short nor long-range ordering present in the nanowires and ribbons. It is possible that increasing the reaction time or including a post-processing annealing step may improve the crystallinity of the nanowires. With an increase in crystal domain size it is possible that the magnetic properties may be altered.

In Chapter 5 the reflux protocol was introduced as a versatile method of synthesising MNPs. In this Chapter the use of polynuclear carboxylate precursors in the synthesis of MnO NPs was investigated, and it was found that simple variations to the structure of the precursor (such as the structures of the carboxylate ligands and secondary ligands, and the number of metal centres in the complex) resulted in changes to the final morphologies of the particle. The most important contributing factor was the nature of the carboxylate ligand, as these ligands could influence the packing of OA and OAm surfactant molecules on the particle surface (analogous to the adsorption of polyol solvent molecules that was seen in Chapter 3). For example, it was shown that the steric bulk of strongly-binding pivalate molecules was capable of blocking OA and OAm from the particle surface, which lead to inadequately stabilised particles. Larger, poorly-defined particles formed as a consequence of this poor stabilisation, due to the increased level of inter-particle collisions and Ostwald ripening that was occurring. Precursors which featured smaller ligands (such as acetate) generally produced higher quality particles, since stabilisation by OA/OAm was not hindered by large molecules on the NP surface.

The heating regime was also important in the synthesis of MnO NPs using polynuclear carboxylate precursors, with the inclusion or exclusion of a heating step in the reaction heating profile capable of producing particles with two distinct morphologies. Bypassing the heating regime resulted in particles which exhibited complex shapes associated with kinetic growth, such as octapod particles. The formation of octapod particles was rationalised in terms of a high influx of monomers to the $\{111\}$ particle surfaces, which resulted in growth in the $\langle 111 \rangle$ directions. The reaction heating profile was also shown to determine the size of particles obtained using Mn_{12} -acetate as a precursor; with temperatures of 290 °C, 300 °C and 310 °C yielding 7 nm, 11 nm and 17 nm particles respectively.

Magnetic measurements were performed for the spherical and octapod MnO particles. MnO MNPs are interesting as bulk MnO is antiferromagnetic, yet the MnO MNPs were

seen to exhibit weakly ferromagnetic properties, with the ferromagnetic properties (such as M_s , M_r and H_c) of the spherical particles increasing as the particle size decreased. The increase in magnetisation was explained in terms of the increased number of surface spins present in smaller particles, which are magnetically misaligned with the antiferromagnetic spins of the particle core. As the particle size decreased, the ratio of surface spins to core spins increased and the magnetic contribution of the surface spins became more substantial. The significance of misaligned surface spins was seen in the magnetic measurements of the 85 nm octapod particles, which exhibited magnetic properties very similar to the 7 nm and 11 nm spherical particles. Despite the large size of the 85 nm octapod particles, the high number of surface spins arising from the branched octapod structure rendered them more magnetic than the largest of the spherical particles (17 nm), due to the significantly lower number of surface spins of large spherical particles compared with larger octapod particles.

The results obtained in Chapter 5 imply that there is significant scope for further work using carboxylate precursors as precursors in MNP synthesis. There are two main studies that would appear pertinent. Firstly, it would be interesting to systematically alter the structure of the carboxylate derivative used as a ligand, to see precisely what the steric contributions from the ligand are. For example, it would be interesting to compare the particles obtained from Mn_{12} -acetate with those obtained using Mn_{12} -propanoate, Mn_{12} -butanoate and so on. Secondly, it would be interesting to see if other metal carboxylate complexes could be used to obtain nanoparticles. It was shown that high-quality magnetite particles were obtained when $[Fe_3O(O_2CR)_6L_3]$ precursors were used, and hence using polynuclear carboxylate precursors of other transition metals may lead to the formation of high-quality metal oxide NPs. Similarly, the use of bimetallic polynuclear complexes as precursors to bimetallic particles could be investigated.

In Chapter 6 potential routes to gadolinium-doped magnetite particles were investigated. The motivation for this study was to determine if the presence of gadolinium in iron oxide particles could increase their effectiveness as potential agents for MRI and MFH applications. Initial experiments sought to create doped ($Gd:Fe_3O_4$) or core-shell ($Gd_2O_3-Fe_3O_4$) particles by varying the order of reaction between an iron-containing and gadolinium-containing precursor (known as the multi-source approach). Unfortunately,

the multi-source method failed to produce doped particles, and instead separate nucleation of two populations of particles (Gd_2O_3 and Fe_3O_4) was observed. To circumvent the separate nucleation problem, a new single-source precursor that contained both gadolinium and iron was synthesised. Decomposition of the single-source precursor produced a uniform population of magnetite particles, and EELS analysis confirmed that the magnetite particles contained small levels of Gd^{3+} as a dopant (2–4%). Magnetic characterisation of these particles showed them to be superparamagnetic at room temperature, with a reduced saturation magnetisation (M_s) of 33.2 emu/g (compared to bulk magnetite, which is 96.4 emu/g). The reduced M_s value was consistent with the decrease in crystalline symmetry with the insertion of Gd^{3+} ions into the magnetite lattice.

To test the potential applications of these particles as agents for MRI and MFH, preliminary biological studies were performed. The particles were rendered biologically compatible by a ligand exchange protocol with a modified polyethylene glycol (PEG) based ligand. The PEG coated $\text{Gd}:\text{Fe}_3\text{O}_4$ particles were found to be readily uptaken by human fibroblast cells, and exhibited a low toxicity. The gadolinium doped magnetite particles represent a very interesting material, and the observed biological compatibility and low toxicity of these particles means that there is considerable scope for assessing the potential applications of these particles as contrast agents for MRI scans or for use in MFH therapies. Despite the reduced saturation magnetisation, the enhanced magnetic anisotropy afforded by the lanthanide doping means that the $\text{Gd}:\text{Fe}_3\text{O}_4$ particles represent promising potential candidates for applications in MFH.

Bibliography

- [1] D. Gatteschi, R. Sessoli and J. Villain, *Molecular Nanomagnets*, Oxford University Press, 2006, p. 124.
- [2] ISI Web of Knowledge search for keyword 'nano*' for years 2000 and 2010 . Retrieved 13th February 2012.
- [3] E. T. Thostenson, Z. Ren and T.-W. Chou, *Compos. Sci. Technol.*, 2001, **61**, 1899–1912.
- [4] P. Serp, M. Corrias and P. Kalck, *Appl. Catal. A-Gen.*, 2003, **253**, 337–358.
- [5] J. Wang, *Electroanalysis*, 2005, **17**, 7–14.
- [6] J. N. Coleman, U. Khan, W. J. Blau and Y. K. Gun'ko, *Carbon*, 2006, **44**, 1624–1652.
- [7] A. Shields, M. O'Sullivan, I. Farrer, D. Ritchie, R. Hogg, M. Leadbeater, C. Norman and M. Pepper, *Appl. Phys. Lett.*, 2000, **76**, 3673–3675.
- [8] D. Loss and D. P. DiVincenzo, *Phys. Rev. A*, 1998, **57**, 120–126.
- [9] P. Reiss, M. Protiere and L. Li, *Small*, 2009, **5**, 154–168.
- [10] X. Michalet, F. F. Pinaud, L. A. Bentolila, J. M. Tsay, S. Doose, J. J. Li, G. Sundaresan, A. M. Wu, S. S. Gambhir and S. Weiss, *Science*, 2005, **307**, 538–544.
- [11] C. Wang, H. Yin, S. Dai and S. Sun, *Chem. Mater.*, 2010, **22**, 3277–3282.
- [12] V. Mazumder, Y. Lee and S. Sun, *Adv. Funct. Mater.*, 2010, **20**, 1224–1231.
- [13] Y. Li and M. A. El-Sayed, *J. Phys. Chem. B*, 2001, **105**, 8938–8943.
- [14] T. Choudhary and D. Goodman, *Appl. Catal. A-Gen.*, 2005, **291**, 32 – 36.
- [15] H. Fecht, E. Hellstern, Z. Fu and W. Johnson, *Metall. Mater. Trans. A.*, 1990, **21**, 2333–2337.
- [16] R. Massart, *IEEE T. Magn.*, 1981, **17**, 1247–1248.
- [17] D. Kim, Y. Zhang, W. Voit, K. Rao and M. Muhammed, *J. Magn. Magn. Mater.*, 2001, **225**, 30–36.
- [18] S. Laurent, D. Forge, M. Port, A. Roch, C. Robic, L. Vander Elst and R. N. Muller, *Chem. Rev.*, 2008, **108**, 2064–2110.
- [19] Y. Lee, J. Lee, C. Bae, J.-G. Park, H.-J. Noh, J.-H. Park and T. Hyeon, *Adv. Funct. Mater.*, 2005, **15**, 503–509.
- [20] J. Rockenberger, E. C. Scher and A. P. Alivisatos, *J. Am. Chem. Soc.*, 1999, **121**, 11595–11596.
- [21] S. Sun and H. Zeng, *J. Am. Chem. Soc.*, 2002, **124**, 8204–8205.
- [22] S. Sun, C. B. Murray, D. Weller, L. Folks and A. Moser, *Science*, 2000, **287**, 1989–1992.
- [23] S. Sun, H. Zeng, D. B. Robinson, S. Raoux, P. M. Rice, S. X. Wang and G. Li, *J. Am. Chem. Soc.*, 2004, **126**, 273–279.

- [24] S. G. Kwon, Y. Piao, J. Park, S. Angappane, Y. Jo, N.-M. Hwang, J.-G. Park and T. Hyeon, *J. Am. Chem. Soc.*, 2007, **129**, 12571–12584.
- [25] J. Park, J. Joo, S. Kwon, Y. Jang and T. Hyeon, *Angew. Chem., Int. Ed.*, 2007, **46**, 4630–4660.
- [26] V. LaMer and R. Dinegar, *J. Am. Chem. Soc.*, 1950, **72**, 4847–4854.
- [27] Y. Xia, Y. Xiong, B. Lim and S. E. Skrabalak, *Angew. Chem., Int. Ed.*, 2008, **47**, 2–46.
- [28] C. Murray, D. Norris and M. Bawendi, *J. Am. Chem. Soc.*, 1993, **115**, 8706–8715.
- [29] C. Donega, P. Liljeroth and D. Vanmaekelbergh, *Small*, 2005, **1**, 1152–1162.
- [30] T. Hyeon, S. S. Lee, J. Park, Y. Chung and H. B. Na, *J. Am. Chem. Soc.*, 2001, **123**, 12798–12801.
- [31] J. Park, K. An, Y. Hwang, J. Park, H. Noh, J. Kim, J. Park, N. Hwang and T. Hyeon, *Nat. Mater.*, 2004, **3**, 891–895.
- [32] L. M. Bronstein, X. Huang, J. Retrum, A. Schmucker, M. Pink, B. D. Stein and B. Draznea, *Chem. Mater.*, 2007, **19**, 3624–3632.
- [33] D. V. Talapin, A. L. Rogach, M. Haase and H. Weller, *J. Phys. Chem. B*, 2001, **105**, 12278–12285.
- [34] P. Dagtepe and V. Chikan, *J. Phys. Chem. C*, 2010, **114**, 16263–16269.
- [35] R. Penn and J. F. Banfield, *Geochim. Cosmochim. Acta*, 1999, **63**, 1549 – 1557.
- [36] Y.-w. Jun, M. F. Casula, J.-H. Sim, S. Y. Kim, J. Cheon and A. P. Alivisatos, *J. Am. Chem. Soc.*, 2003, **125**, 15981–15985.
- [37] D. Zitoun, N. Pinna, N. Frolet and C. Belin, *J. Am. Chem. Soc.*, 2005, **127**, 15034–15035.
- [38] K. Cho, D. Talapin, W. Gaschler and C. Murray, *J. Am. Chem. Soc.*, 2005, **127**, 7140–7147.
- [39] C. Pacholski, A. Kornowski and H. Weller, *Angew. Chem., Int. Ed.*, 2002, **41**, 1188–1191.
- [40] Z. Tang, N. A. Kotov and M. Giersig, *Science*, 2002, **297**, 237–240.
- [41] G. A. Rance, D. H. Marsh, S. J. Bourne, T. J. Reade and A. N. Khlobystov, *ACS Nano*, 2010, **4**, 4920–4928.
- [42] J.-H. Lee, J.-t. Jang, J.-s. Choi, S. H. Moon, S.-h. Noh, J.-w. Kim, J.-G. Kim, I.-S. Kim, K. I. Park and J. Cheon, *Nat. Nano.*, 2011, **6**, 418–422.
- [43] H. Yu, M. Chen, P. M. Rice, S. X. Wang, R. L. White and S. Sun, *Nano Lett.*, 2005, **5**, 379–382.
- [44] L. E. Greene, M. Law, D. H. Tan, M. Montano, J. Goldberger, G. Somorjai and P. Yang, *Nano Lett.*, 2005, **5**, 1231–1236.
- [45] X. Wang and Y. Li, *Angew. Chem., Int. Ed.*, 2002, **41**, 4790–4793.
- [46] Z. L. Wang, *J. Phys. Chem. B*, 2000, **104**, 1153–1175.
- [47] A. R. Tao, S. Habas and P. Yang, *Small*, 2008, **4**, 310–325.
- [48] H. Yang, T. Ogawa, D. Hasegawa and M. Takahashi, *J. Appl. Phys.*, 2008, **103**, 07D526.
- [49] Y. Hou, Z. Xu and S. Sun, *Angew. Chem., Int. Ed.*, 2007, **46**, 6329–6332.
- [50] K. An, M. Park, J. H. Yu, H. B. Na, N. Lee, J. Park, S. H. Choi, I. C. Song, W. K. Moon and T. Hyeon, *Eur. J. Inorg. Chem.*, 2012, **2012**, 2148–2155.
- [51] M. Chen, T. Pica, Y.-B. Jiang, P. Li, K. Yano, J. P. Liu, A. K. Datye and H. Fan, *J. Am. Chem. Soc.*, 2007, **129**, 6348–6349.
- [52] M. J. Bonder, S. Cardoso, S. van Dijken, R. Dittrich, R. E. Dunin-Borkowski, . Ertl, H. Ferreira,

- R. Ferreira, J. Fidler, P. P. Freitas, D. Givord, J. Gregg, G. C. Hadjipanayis, G. Herzer, G. Hrkac, Y. Huang, S. S. Jaswal, A. Kashyap, M. Kirschner, J. R. H. Kraus, V. Labhasetwar, D. L. Leslie-Pelecky, J. C. Lodder, M. R. McCartney, T. McDaniel, S. Rivoirard, R. Sabirianov, T. Schrefl, D. J. Sellmyer, R. Skomski, D. J. Smith, D. Suess, S. Sun, K. Suzuki, D. Weller, W. Wemsdorfer, Y. F. Xu, M. L. Yan and J. Zhou, *Advanced Magnetic Nanostructures*, Springer, 2006.
- [53] N. A. Frey, S. Peng, K. Cheng and S. Sun, *Chem. Soc. Rev.*, 2009, **38**, 2532–2542.
- [54] K. Krishnan, *IEEE Trans. Magn.*, 2010, **46**, 2523–2558.
- [55] I. Sharifi, H. Shokrollahi and S. Amiri, *J. Magn. Magn. Mater.*, 2012, **324**, 903–915.
- [56] H. B. Na, I. C. Song and T. Hyeon, *Adv. Mater.*, 2009, **21**, 2133–2148.
- [57] H. Na, J. Lee, K. An, Y. Park, M. Park, I. Lee, D.-H. Nam, S. Kim, S.-H. Kim, S.-W. Kim, K.-H. Lim, K.-S. Kim, S.-O. Kim and T. Hyeon, *Angew. Chem., Int. Ed.*, 2007, **46**, 5397–5401.
- [58] S. Laurent, S. Dutz, U. O. Häfeli and M. Mahmoudi, *Adv. Colloid Interface Sci.*, 2011, **166**, 8–23.
- [59] R. S. Selinsky, J. H. Han, E. A. Morales Perez, I. A. Guzei and S. Jin, *J. Am. Chem. Soc.*, 2010, **132**, 15997–16005.
- [60] D. B. Williams and B. C. Carter, *Transmission Electron Microscopy: A Textbook for Materials Science*, Springer, 2nd edn, 2009.
- [61] L. de Broglie, *Ann. Phys.*, 1925, **3**, 22–128.
- [62] C. Davisson and L. H. Germer, *Phys. Rev.*, 1927, **30**, 705–740.
- [63] G. Thomson, *Proc. R. Soc. A*, 1928, **117**, 600–609.
- [64] M. Knoll and E. Ruska, *Z. Phys.*, 1932, **78**, 318–339.
- [65] H. Busch, *Arch. Elektrotech.*, 1927, **18**, 583–594.
- [66] N. R. Wilson, P. A. Pandey, R. Beanland, R. J. Young, I. A. Kinloch, L. Gong, Z. Liu, K. Suenaga, J. P. Rourke, S. J. York and J. Sloan, *ACS Nano*, 2009, **3**, 2547–2556.
- [67] C. R. D. Silva, S. Smith, I. Shim, J. Pyun, T. Gutu, J. Jiao and Z. Zheng, *J. Am. Chem. Soc.*, 2009, **131**, 6336–6337.
- [68] R. J. Hickey, A. S. Haynes, J. M. Kikkawa and S.-J. Park, *J. Am. Chem. Soc.*, 2011, **133**, 1517–1525.
- [69] V. Mazumder, M. Chi, K. L. More and S. Sun, *J. Am. Chem. Soc.*, 2010, **132**, 7848–7849.
- [70] K. Byrappa and M. Yoshimura, *Handbook of Hydrothermal Technology: A technology for crystal growth and materials processing*, Noyes Publications, 2001, p. 891.
- [71] R. Riman, W. Suchanek and M. Lencka, *Ann. Chim. Sci. Mat.*, 2002, **27**, 15–36.
- [72] R. H. Laye, M. Murrie, S. Ochsenein, A. R. Bell, S. J. Teat, J. Raftery, H.-U. Güdel and E. J. L. McInnes, *Chem.–Eur. J.*, 2003, **9**, 6215–6220.
- [73] Y. Xing, M. Li, S. A. Davis and S. Mann, *J. Phys. Chem. B*, 2006, **110**, 1111–1113.
- [74] S. Peng, Y. Lee, C. Wang, H. Yin, S. Dai and S. Sun, *Nano Res.*, 2008, **1**, 229–234.
- [75] W. Wang, S. Kunwar, J. Y. Huang, D. Z. Wang and Z. F. Ren, *Nanotechnology*, 2005, **16**, 21.
- [76] W. Yue, S. Han, R. Peng, W. Shen, H. Geng, F. Wu, S. Tao and M. Wang, *J. Mater. Chem.*, 2010, **20**, 7570–7578.
- [77] R. K. Wahi, Y. Liu, J. C. Falkner and V. L. Colvin, *J. Colloid Interface Sci.*, 2006, **302**, 530–536.

- [78] G. Gao, R. Shi, W. Qin, Y. Shi, G. Xu, G. Qiu and X. Liu, *J. Mater. Sci.*, 2010, **45**, 3483–3489.
- [79] S.-B. Wang, Y.-L. Min and S.-H. Yu, *J. Phys. Chem. C*, 2007, **111**, 3551–3554.
- [80] C.-J. Jia, L.-D. Sun, F. Luo, X.-D. Han, L. J. Heyderman, Z.-G. Yan, C.-H. Yan, K. Zheng, Z. Zhang, M. Takano, N. Hayashi, M. Eltschka, M. Klauui, U. Ruediger, T. Kasama, L. Cervera-Gontard, R. E. Dunin-Borkowski, G. Tzvetkov and J. Raabe, *J. Am. Chem. Soc.*, 2008, **130**, 16968–16977.
- [81] N. K. Chaudhari, H. C. Kim, D. Son and J.-S. Yu, *CrystEngComm*, 2009, **11**, 2264–2267.
- [82] L.-P. Zhu, H.-M. Xiao, W.-D. Zhang, G. Yang and S.-Y. Fu, *Cryst. Growth Des.*, 2008, **8**, 957–963.
- [83] J. Wang, M. Yao, G. Xu, P. Cui and J. Zhao, *Mater. Chem. Phys.*, 2009, **113**, 6 – 9.
- [84] C. Gotaas, P. Havelka, H. A. Jakobsen, H. F. Svendsen, M. Hase, N. Roth and B. Weigand, *Phys. Fluids*, 2007, **19**, 102106.
- [85] R. M. DiGuilio, R. J. Lee, S. T. Schaeffer, L. L. Brasher and A. S. Teja, *J. Chem. Eng. Data*, 1992, **37**, 239–242.
- [86] D. Zhang, X. Zhang, X. Ni and H. Zheng, *Mater. Lett.*, 2006, **60**, 1915–1917.
- [87] R. D. Rodriguez, D. Demaille, E. Lacaze, J. Jupille, C. Chaneac and J.-P. Jolivet, *J. Phys. Chem. C*, 2007, **111**, 16866–16870.
- [88] Z. Li, J. F. Godsell, J. P. O’Byrne, N. Petkov, M. A. Morris, S. Roy and J. D. Holmes, *J. Am. Chem. Soc.*, 2010, **132**, 12540–12541.
- [89] J. Wan, W. Cai, X. Meng and E. Liu, *Chem. Commun.*, 2007, **47**, 5004–5006.
- [90] A. Naravanaswamy, H. Xu, N. Pradhan and X. Peng, *Angew. Chem., Int. Ed.*, 2006, **45**, 5361–5364.
- [91] Y.-L. Chen, Z.-A. Hu, Y.-Q. Chang, H.-W. Wang, Z.-Y. Zhang, Y.-Y. Yang and H.-Y. Wu, *J. Phys. Chem. C*, 2011, **115**, 2563–2571.
- [92] M. A. van Huis, L. T. Kunneman, K. Overgaag, Q. Xu, G. Pandraud, H. W. Zandbergen and D. Vanmaekelbergh, *Nano Lett.*, 2008, **8**, 3959–3963.
- [93] C. Colliex, T. Manoubi and C. Ortiz, *Phys. Rev. B*, 1991, **44**, 11402–11411.
- [94] L. Cavé, T. Al, D. Loomer, S. Cogswell and L. Weaver, *Micron*, 2006, **37**, 301 – 309.
- [95] A. Corrias, G. Mountjoy, D. Loche, V. Puentes, A. Falqui, M. Zanella, W. J. Parak and M. F. Casula, *J. Phys. Chem. C*, 2009, **113**, 18667–18675.
- [96] L.-M. Lacroix, S. Lachaize, A. Falqui, M. Respaud and B. Chaudret, *J. Am. Chem. Soc.*, 2009, **131**, 549–557.
- [97] A. Demortiere, P. Launois, N. Goubet, P. A. Albouy and C. Petit, *J. Phys. Chem. B*, 2008, **112**, 14583–14592.
- [98] L. Guo, F. Liang, X. Wen, S. Yang, L. He, W. Zheng, C. Chen and Q. Zhong, *Adv. Funct. Mater.*, 2007, **17**, 425–430.
- [99] H. Bi, X. Wang, H. Li, B. Xi, Y. Zhu and Y. Qian, *Solid State Commun.*, 2009, **149**, 2115–2119.
- [100] S.-H. Choi, H. Bin Na, Y. I. Park, K. An, S. G. Kwon, Y. Jang, M.-h. Park, J. Moon, J. S. Son, I. C. Song, W. K. Moon and T. Hyeon, *J. Am. Chem. Soc.*, 2008, **130**, 15573–15580.
- [101] F. Song, J. Guan, X. Fan and G. Yan, *J. Alloys Compd.*, 2009, **485**, 753–758.
- [102] D. Caruntu, G. Caruntu and C. J. O’Connor, *J. Phys. D: Appl. Phys.*, 2007, **40**, 5801.

- [103] N. Pinna, S. Grancharov, P. Beato, P. Bonville, M. Antonietti and M. Niederberger, *Chem. Mater.*, 2005, **17**, 3044–3049.
- [104] W. Cai and J. Wan, *J. Colloid Interface Sci.*, 2007, **305**, 366–370.
- [105] A. Angermann and J. Töpfer, *J. Mater. Sci.*, 2008, **43**, 5123–5130.
- [106] M. P. Morales, S. Veintemillas-Verdaguer, M. I. Montero, C. J. Serna, A. Roig, L. Casas, B. Martínez and F. Sandiumenge, *Chem. Mater.*, 1999, **11**, 3058–3064.
- [107] Y. Jun, Y. Huh, J. Choi, J. Lee, H. Song, S. Kim, S. Yoon, K. Kim, J. Shin, J. Suh and J. Cheon, *J. Am. Chem. Soc.*, 2005, **127**, 5732–5733.
- [108] J.-H. Lee, Y.-M. Huh, Y.-w. Jun, J.-w. Seo, J.-t. Jang, H.-T. Song, S. Kim, E.-J. Cho, H.-G. Yoon, J.-S. Suh and J. Cheon, *Nat. Med.*, 2007, **13**, 95–99.
- [109] M. Opel, *J. Phys. D: Appl. Phys.*, 2012, **45**, 033001.
- [110] J.-M. Idée, M. Port, I. Raynal, M. Schaefer, S. Le Greneur and C. Corot, *Fundam. Clin. Pharm.*, 2006, **20**, 563–576.
- [111] R. Bazzi, M. Flores, C. Louis, K. Lebbou, W. Zhang, C. Dujardin, S. Roux, B. Mercier, G. Ledoux, E. Bernstein, P. Perriat and O. Tillement, *J. Colloid Interface Sci.*, 2004, **273**, 191–197.
- [112] M.-A. Fortin, R. M. P. Jr, F. Söderlind, A. Klasson, M. Engström, T. Veres, P.-O. Käll and K. Uvdal, *Nanotechnology*, 2007, **18**, 395501.
- [113] J. Y. Park, M. J. Baek, E. S. Choi, S. Woo, J. H. Kim, T. J. Kim, J. C. Jung, K. S. Chae, Y. Chang and G. H. Lee, *ACS Nano*, 2009, **3**, 3663–3669.
- [114] K. Kattel, J. Y. Park, W. Xu, H. G. Kim, E. J. Lee, B. A. Bony, W. C. Heo, J. J. Lee, S. Jin, J. S. Baeck, Y. Chang, T. J. Kim, J. E. Bae, K. S. Chae and G. H. Lee, *ACS Appl. Mater. Interfaces*, 2011, **3**, 3325–3334.
- [115] K. Ai, B. Zhang and L. Lu, *Angew. Chem., Int. Ed.*, 2009, **48**, 304–308.
- [116] C. Bouzigues, T. Gacoin and A. Alexandrou, *ACS Nano*, 2011, **5**, 8488–8505.
- [117] E. Hemmer, Y. Kohl, V. Colquhoun, H. Thielecke, K. Soga and S. Mathur, *J. Phys. Chem. B*, 2010, **114**, 4358–4365.
- [118] J. Shen, L.-D. Sun and C.-H. Yan, *Dalton Trans.*, 2008, 5687–5697.
- [119] Y. C. Cao, *J. Am. Chem. Soc.*, 2004, **126**, 7456–7457.
- [120] H.-X. Mai, Y.-W. Zhang, R. Si, Z.-G. Yan, L.-d. Sun, L.-P. You and C.-H. Yan, *J. Am. Chem. Soc.*, 2006, **128**, 6426–6436.
- [121] F. Pandozzi, F. Vetrone, J.-C. Boyer, R. Naccache, J. A. Capobianco, A. Speghini and M. Bettinelli, *J. Phys. Chem. B*, 2005, **109**, 17400–17405.
- [122] F. Söderlind, M. A. Fortin, R. M. P. Jr, A. Klasson, T. Veres, M. Engström, K. Uvdal and P.-O. Käll, *Nanotechnology*, 2008, **19**, 085608.
- [123] C.-J. Jia, L.-D. Sun, F. Luo, X.-C. Jiang, L.-H. Wei and C.-H. Yan, *Appl. Phys. Lett.*, 2004, **84**, 5305–5307.
- [124] M. Ahrén, L. Selegård, A. Klasson, F. Söderlind, N. Abrikosova, C. Skoglund, T. Bengtsson, M. Engström, P.-O. Käll and K. Uvdal, *Langmuir*, 2010, **26**, 5753–5762.

- [125] R. Bazzi, M. A. Flores-Gonzalez, C. Louis, K. Lebbou, C. Dujardin, A. Brenier, W. Zhang, O. Tillement, E. Bernstein and P. Perriat, *J. Lumin.*, 2003, **102-103**, 445–450.
- [126] R. Si, Y.-W. Zhang, H.-P. Zhou, L.-D. Sun and C.-H. Yan, *Chem. Mater.*, 2007, **19**, 18–27.
- [127] R. Si, Y.-W. Zhang, L.-P. You and C.-H. Yan, *Angew. Chem., Int. Ed.*, 2005, **44**, 3256–3260.
- [128] S. V. Mahajan and J. H. Dickerson, *J. Alloys Compd.*, 2009, **488**, 574 – 577.
- [129] Y.-P. Du, Y.-W. Zhang, L.-D. Sun and C.-H. Yan, *J. Am. Chem. Soc.*, 2009, **131**, 3162–3163.
- [130] Y.-P. Du, Y.-W. Zhang, Z.-G. Yan, L.-D. Sun and C.-H. Yan, *J. Am. Chem. Soc.*, 2009, **131**, 16364.
- [131] T. Yu, J. Joo, Y. I. Park and T. Hyeon, *J. Am. Chem. Soc.*, 2006, **128**, 1786—1787.
- [132] S. V. Mahajan and J. H. Dickerson, *Nanotechnology*, 2007, **18**, 325605.
- [133] M. Zinkevich, *Prog. Mater. Sci.*, 2007, **52**, 597–647.
- [134] K. Nakamoto, *Infrared and Raman Spectra of Inorganic and Coordination Compounds*, John Wiley & Sons, Ltd, 5th edn, 1997, p. 59.
- [135] F. Söderlind, H. Pedersen, R. M. P. Jr., P.-O. Käll and K. Uvdal, *J. Colloid Interface Sci.*, 2005, **288**, 140–148.
- [136] Z. Xu, C. Shen, Y. Hou, H. Gao and S. Sun, *Chem. Mater.*, 2009, **21**, 1778–1780.
- [137] V. Perrichon, A. Laachir, G. Bergeret, R. Frety, L. Tournayan and O. Touret, *J. Chem. Soc., Faraday Trans.*, 1994, **90**, 773–781.
- [138] S. Tsunekawa, R. Sivamohan, S. Ito, A. Kasuya and T. Fukuda, *Nanostructured Materials*, 1999, **11**, 141 – 147.
- [139] L. Wu, H. Wiesmann, A. Moodenbaugh, R. Klie, Y. Zhu, D. Welch and M. Suenaga, *Phys. Rev. B*, 2004, **69**, 125415.
- [140] J. Conesa, *Surf. Sci.*, 1995, **339**, 337 – 352.
- [141] J. A. Fortner, E. C. Buck, A. J. Ellison and J. K. Bates, *Ultramicroscopy*, 1997, **67**, 77–81.
- [142] F. Xu and Y. Bando, *J. Appl. Phys.*, 2001, **89**, 5469–5472.
- [143] C. Ribeiro, E. Longo and E. R. Leite, *Appl. Phys. Lett.*, 2007, **91**, 103105.
- [144] H.-P. Zhou, Y.-W. Zhang, H.-X. Mai, X. Sun, Q. Liu, W.-G. Song and C.-H. Yan, *Chem.–Eur. J.*, 2008, **14**, 3380–3390.
- [145] F. Bao, Y. Wang, Y. Cheng and Y. Zheng, *Mater. Lett.*, 2006, **60**, 389 – 392.
- [146] R. L. Penn and J. F. Banfield, *Science*, 1998, **281**, 969–971.
- [147] J. Zhang, F. Huang and Z. Lin, *Nanoscale*, 2010, **2**, 18–34.
- [148] D. V. Sastri, D. J.-C. Bünzli, D. V. R. Rao, D. G. Rayudu and D. J. Perumareddi, *Modern aspects of rare earths and their complexes*, Elsevier, Amsterdam, 2003, pp. 127–257.
- [149] D. Wang, Z. Wang, P. Zhao, W. Zheng, Q. Peng, L. Liu, X. Chen and Y. Li, *Chem. Asian J.*, 2010, **5**, 925–931.
- [150] C. Hu, H. Liu, W. Dong, Y. Zhang, G. Bao, C. Lao and Z. Wang, *Adv. Mater.*, 2007, **19**, 470–474.
- [151] M. Han, N.-E. Shi, W.-L. Zhang, B.-J. Li, J.-H. Sun, K.-J. Chen, J.-M. Zhu, X. Wang and Z. Xu, *Chem.–Eur. J.*, 2008, **14**, 1615–1620.
- [152] Z. Deng, D. Chen, F. Tang, X. Meng, J. Ren and L. Zhang, *J. Phys. Chem. C*, 2007, **111**, 5325–5330.

- [153] D. Chen, T. Li, L. Yin, X. Hou, X. Yu, Y. Zhang, B. Fan, H. Wang, X. Li, R. Zhang, T. Hou, H. Lu, H. Xu, J. Sun and L. Gao, *Mater. Chem. Phys.*, 2011, **125**, 838 – 845.
- [154] M.-R. Gao, W.-T. Yao, H.-B. Yao and S.-H. Yu, *J. Am. Chem. Soc.*, 2009, **131**, 7486–7487.
- [155] M. H. Huang, S. Mao, H. Feick, H. Yan, Y. Wu, H. Kind, E. Weber, R. Russo and P. Yang, *Science*, 2001, **292**, 1897–1899.
- [156] N. Zhang, R. Yi, L. Zhou, G. Gao, R. Shi, G. Qiu and X. Liu, *Mater. Chem. Phys.*, 2009, **114**, 160–167.
- [157] Z. Huo, C.-k. Tsung, W. Huang, X. Zhang and P. Yang, *Nano Lett.*, 2008, **8**, 2041–2044.
- [158] X. Lu, M. S. Yavuz, H.-Y. Tuan, B. A. Korgel and Y. Xia, *J. Am. Chem. Soc.*, 2008, **130**, 8900–8901.
- [159] Y. Chen, E. Johnson and X. Peng, *J. Am. Chem. Soc.*, 2007, **129**, 10937–10947.
- [160] R. Guo and Q. Fu, *Chin. J. Chem.*, 2000, **18**, 13–17.
- [161] G. Liu, C. E. Conn and C. J. Drummond, *J. Phys. Chem. B*, 2009, **113**, 15949–15959.
- [162] H. Wu, Y. Yang and Y. C. Cao, *J. Am. Chem. Soc.*, 2006, **128**, 16522–16523.
- [163] B. Mutelet, N. Keller, S. Roux, M. Flores-Gonzales, F. Lux, M. Martini, O. Tillement, C. Billotey, M. Janier, C. Villiers, G. Novitchi, D. Luneau and P. Perriat, *Appl. Phys. A.*, 2011, **105**, 215–219.
- [164] C.-C. Huang, T.-Y. Liu, C.-H. Su, Y.-W. Lo, J.-H. Chen and C.-S. Yeh, *Chem. Mater.*, 2008, **20**, 3840–3848.
- [165] H. Gustafsson, M. Ahrén, F. Söderlind, J. M. Córdoba Gallego, P.-O. Käll, P. Nordblad, P.-O. Westlund, K. Uvdal and M. Engström, *J. Phys. Chem. C*, 2011, **115**, 5469–5477.
- [166] S. L. Bud'ko and P. C. Canfield, *J. Magn. Magn. Mater.*, 2006, **299**, 281–287.
- [167] K. Kattel, J. Y. Park, W. Xu, H. G. Kim, E. J. Lee, B. A. Bony, W. C. Heo, S. Jin, J. S. Baeck, Y. Chang, T. J. Kim, J. E. Bae, K. S. Chae and G. H. Lee, *Biomaterials*, 2012, **33**, 3254–3261.
- [168] M. Norek, E. Kampert, U. Zeitler and J. A. Peters, *J. Am. Chem. Soc.*, 2008, **130**, 5335–5340.
- [169] M. Norek, G. A. Pereira, C. F. G. C. Geraldés, A. Denkova, W. Zhou and J. A. Peters, *J. Phys. Chem. C*, 2007, **111**, 10240–10246.
- [170] P. Si, E. Bruck, Z. Zhang, I. Skorvanek, J. Kovac and M. Zhang, *Mater. Res. Bull.*, 2004, **39**, 1005–1012.
- [171] U. Köbler, A. Zaker and J. Hauck, *J. Magn. Magn. Mater.*, 1980, **15**, 315–316.
- [172] D.-X. Chen, V. Skumryev and B. Bozzo, *Rev. Sci. Instrum.*, 2011, **82**, 045112.
- [173] J. Feng, G. Shan, A. Maquieira, M. E. Koivunen, B. Guo, B. D. Hammock and I. M. Kennedy, *Anal. Chem.*, 2003, **75**, 5282–5286.
- [174] V. Gueu, H. You, T. Hayakawa and M. Nogami, *J. Sol-Gel Sci. Technol.*, 2007, **41**, 231–236.
- [175] C.-S. Park, M.-G. Kwak, S.-S. Choi, Y.-S. Song, S.-J. Hong, J.-I. Han and D. Y. Lee, *J. Lumin.*, 2006, **118**, 199–204.
- [176] G. Wakefield, H. Keron, P. Dobson and J. Hutchison, *J. Colloid Interface Sci.*, 1999, **215**, 179–182.
- [177] R. Meltzer, S. Feofilov, B. Tissue and H. Yuan, *Phys. Rev. B*, 1999, **60**, 14012–14015.
- [178] W. Chen, A. Joly, C. Kowalchuk, J. Malm, Y. Huang and J. Bovin, *J. Phys. Chem. B*, 2002, **106**, 7034–7041.

- [179] B. Bihari, H. Eilers and B. Tissue, *J. Lumin.*, 1997, **75**, 1–10.
- [180] M. Buijs, A. Meyerink and G. Blasse, *J. Lumin.*, 1987, **37**, 9–20.
- [181] G. Blasse and B. Grabmaier, *Luminescent materials*, Springer-Verlag, 1997.
- [182] X. Zhong, R. Xie, L. Sun, I. Lieberwirth and W. Knoll, *J. Phys. Chem. B*, 2006, **110**, 2–4.
- [183] W. S. Seo, H. H. Jo, K. Lee, B. Kim, S. J. Oh and J. T. Park, *Angew. Chem., Int. Ed.*, 2004, **43**, 1521–3773.
- [184] D. Kim, N. Lee, M. Park, B. H. Kim, K. An and T. Hyeon, *J. Am. Chem. Soc.*, 2009, **131**, 454–455.
- [185] Z.-R. Tian, W. Tong, J.-Y. Wang, N.-G. Duan, V. V. Krishnan and S. L. Suib, *Science*, 1997, **276**, 926–930.
- [186] X.-W. Liu, X.-F. Sun, Y.-X. Huang, G.-P. Sheng, K. Zhou, R. J. Zeng, F. Dong, S.-G. Wang, A.-W. Xu, Z.-H. Tong and H.-Q. Yu, *Water Res.*, 2010, **44**, 5298 – 5305.
- [187] G. Salazar-Alvarez, J. Sort, S. Suriñach, M. D. Baró and J. Nogués, *J. Am. Chem. Soc.*, 2007, **129**, 9102–9108.
- [188] A. E. Berkowitz, G. F. Rodriguez, J. I. Hong, K. An, T. Hyeon, N. Agarwal, D. J. Smith and E. E. Fullerton, *Phys. Rev. B*, 2008, **77**, 024403.
- [189] T. Ould-Ely, D. Prieto-Centurion, A. Kumar, W. Guo, W. V. Knowles, S. Asokan, M. S. Wong, I. Rusakova, A. Lüttge and K. H. Whitmire, *Chem. Mater.*, 2006, **18**, 1821–1829.
- [190] M. Yin and S. O'Brien, *J. Am. Chem. Soc.*, 2003, **125**, 10180–10181.
- [191] R. Bagai and G. Christou, *Chem. Soc. Rev.*, 2009, **38**, 1011–1026.
- [192] L. Chen, H. Xing, Y. Shen, J. Bai and G. Jiang, *J. Solid State Chem.*, 2009, **182**, 1387 – 1395.
- [193] B. Folch, J. Larionova, Y. Guari, C. Guerin, A. Mehdi and C. Reye, *J. Mater. Chem.*, 2004, **14**, 2703–2711.
- [194] B. Folch, J. Larionova, Y. Guari, C. Guérin and C. Reibel, *J. Solid State Chem.*, 2005, **178**, 2368 – 2375.
- [195] J. B. Vincent, H. R. Chang, K. Folting, J. C. Huffman, G. Christou and D. N. Hendrickson, *J. Am. Chem. Soc.*, 1987, **109**, 5703–5711.
- [196] R. Wu, M. Poyraz, F. E. Sowrey, C. E. Anson, S. Wocadlo, A. K. Powell, U. A. Jayasooriya, R. D. Cannon, T. Nakamoto, M. Katada and H. Sano, *Inorg. Chem.*, 1998, **37**, 1913–1921.
- [197] M. Murrie, S. Parsons and R. Winpenny, *Dalton Trans.*, 1998, 1423–1424.
- [198] T. Lis, *Acta Crystallogr., Sect. B: Struct. Sci.*, 1980, **36**, 2042–2046.
- [199] J. Larionova, R. Clerac, B. Boury, J. Le Bideau, L. Lecren and S. Willemin, *J. Mater. Chem.*, 2003, **13**, 795–799.
- [200] M. Gonzales and K. M. Krishnan, *J. Magn. Magn. Mater.*, 2005, **293**, 265 – 270.
- [201] O. Chen, X. Chen, Y. Yang, J. Lynch, H. Wu, J. Zhuang and Y. Cao, *Angew. Chem., Int. Ed.*, 2008, **47**, 8638–8641.
- [202] J. Park, E. Kang, C. Bae, J. Park, H. Noh, J. Kim, J. Park, J. Park and T. Hyeon, *J. Phys. Chem. B*, 2004, **108**, 13594–13598.
- [203] A. Shavel, B. Rodriguez-Gonzalez, M. Spasova, M. Farle and L. Liz-Marzin, *Adv. Funct. Mater.*,

- 2007, **17**, 3870–3876.
- [204] C.-C. Lin, C.-J. Chen and R.-K. Chiang, *J. Cryst. Growth*, 2012, **338**, 152 – 156.
- [205] Q. Li, J. Wang, Y. He, W. Liu and X. Qiu, *Cryst. Growth Des.*, 2009, **9**, 3100–3103.
- [206] H. Kurata and C. Colliex, *Phys. Rev. B*, 1993, **48**, 2102–2108.
- [207] B. Gilbert, B. H. Frazer, A. Belz, P. G. Conrad, K. H. Neelson, D. Haskel, J. C. Lang, G. Srajer and G. De Stasio, *J. Phys. Chem. A*, 2003, **107**, 2839–2847.
- [208] T. E. Furia, *CRC Handbook of Food Additives — Chapter 6, Sequestrants in Foods*, CRC Press, 1972, vol. 1.
- [209] J. R. Kanicky and D. O. Shah, *J. Colloid Interface Sci.*, 2002, **256**, 201–207.
- [210] J. Shin, R. Anisur, M. Ko, G. Im, J. Lee and I. Lee, *Angew. Chem., Int. Ed.*, 2009, **48**, 321–324.
- [211] X.-F. Shen, Y.-S. Ding, J. Liu, J. Cai, K. Laubernds, R. Zerger, A. Vasiliev, M. Aindow and S. Suib, *Adv. Mater.*, 2005, **17**, 805–809.
- [212] K. Miszta, J. de Graaf, G. Bertoni, D. Dorfs, R. Brescia, S. Marras, L. Ceseracciu, R. Cingolani, R. van Roij, M. Dijkstra and L. Manna, *Nat. Mater.*, 2011, **10**, 872–876.
- [213] S.-M. Lee, Y.-w. Jun, S.-N. Cho and J. Cheon, *J. Am. Chem. Soc.*, 2002, **124**, 11244–11245.
- [214] T. Mandal, G. Piburn, V. Stavila, I. Rusakova, T. Ould-Ely, A. C. Colson and K. H. Whitmire, *Chem. Mater.*, 2011, **23**, 4158–4169.
- [215] X. Wang, J. Qiu, J. Qu, Z. Wang and D. Su, *RSC Adv.*, 2012, **2**, 4329–4334.
- [216] Y.-w. Jun, J.-s. Choi and J. Cheon, *Angew. Chem., Int. Ed.*, 2006, **45**, 3414–3439.
- [217] H. Zhang, W. Li, M. Jin, J. Zeng, T. Yu, D. Yang and Y. Xia, *Nano Lett.*, 2011, **11**, 898–903.
- [218] K. J. Klabunde, J. Stark, O. Koper, C. Mohs, D. G. Park, S. Decker, Y. Jiang, I. Lagadic and D. Zhang, *J. Phys. Chem.*, 1996, **100**, 12142–12153.
- [219] S. George, S. Lin, Z. Ji, C. R. Thomas, L. Li, M. Mecklenburg, H. Meng, X. Wang, H. Zhang, T. Xia, J. N. Hohman, S. Lin, J. I. Zink, P. S. Weiss and A. E. Nel, *ACS Nano*, 2012, **6**, 3745.
- [220] I. Apostolova and J. Wesselinowa, *Solid State Commun.*, 2009, **149**, 986 – 990.
- [221] E. Pollert, P. Veverka, M. Veverka, O. Kaman, K. Závěta, S. Vasseur, R. Epherre, G. Goglio and E. Duguet, *Prog. Solid State Chem.*, 2009, **37**, 1–14.
- [222] E. Auzans, D. Zins, E. Blums and R. Massart, *J. Mater. Sci.*, 1999, **34**, 1253–1260.
- [223] T. Brusentsova and V. Kuznetsov, *J. Magn. Magn. Mater.*, 2007, **311**, 22–25.
- [224] Y. Huh, Y. Jun, H. Song, S. Kim, J. Choi, J. Lee, S. Yoon, K. Kim, J. Shin, J. Suh and J. Cheon, *J. Am. Chem. Soc.*, 2005, **127**, 12387–12391.
- [225] P. Drake, H.-J. Cho, P.-S. Shih, C.-H. Kao, K.-F. Lee, C.-H. Kuo, X.-Z. Lin and Y.-J. Lin, *J. Mater. Chem.*, 2007, **17**, 4914–4918.
- [226] H. Zeng, J. Li, Z. L. Wang, J. P. Liu and S. Sun, *Nano Lett.*, 2004, **4**, 187–190.
- [227] T. T. Trinh, D. Mott, N. T. K. Thanh and S. Maenosono, *RSC Adv.*, 2011, **1**, 100–108.
- [228] J.-s. Choi, J.-H. Lee, T.-H. Shin, H.-T. Song, E. Y. Kim and J. Cheon, *J. Am. Chem. Soc.*, 2010, **132**, 11015–11017.
- [229] J. Lansman, *J. Gen. Physiol.*, 1990, **95**, 679–696.

- [230] H. M. Ismail, *Colloid. Surface. A*, 1995, **97**, 247 – 254.
- [231] S. Mishra, G. Ledoux, E. Jeanneau, S. Daniele and M.-F. Joubert, *Dalton Trans.*, 2012, **4**, 1490–1502.
- [232] L. Tian, H. Yao Tan and J. J. Vittal, *Cryst. Growth Des.*, 2008, **8**, 734–738.
- [233] W. Hirpo, S. Dhingra, A. C. Sutorik and M. G. Kanatzidis, *J. Am. Chem. Soc.*, 1993, **115**, 1597–1599.
- [234] L. Chen, Y. Shen and J. Bai, *Mater. Lett.*, 2009, **63**, 1099 – 1101.
- [235] S. Mathur, C. Cavelius, K. Moh, H. Shen and J. Bauer, *Z. Anorg. Allg. Chem.*, 2009, **635**, 898–902.
- [236] A. M. Ako, V. Mereacre, R. Clerac, I. J. Hewitt, Y. Lan, C. E. Anson and A. K. Powell, *Dalton Trans.*, 2007, 5245–5247.
- [237] A. Ferguson, J. McGregor, E. K. Brechin, L. H. Thomas and M. Murrie, *Dalton Trans.*, 2009, 9395–9397.
- [238] C. Benelli, M. Murrie, S. Parsons and R. E. P. Winpenny, *J. Chem. Soc., Dalton Trans.*, 1999, 4125–4126.
- [239] S. Gorun and S. Lippard, *Nature*, 1986, **319**, 666–668.
- [240] W. Micklitz, V. Mckee, R. Rardin, L. Pence, G. Papaefthymiou, S. Bott and S. Lippard, *J. Am. Chem. Soc.*, 1994, **116**, 8061–8069.
- [241] M. Taylor, C. Carter and C. Wynter, *Journal of Inorganic and Nuclear Chemistry*, 1968, **30**, 1503 – 1511.
- [242] C. E. Housecroft and A. G. Sharpe, *Inorganic Chemistry*, Pearson Education, 2001, p. 745.
- [243] Q. Wang, S. Li, A. Wu and H. Yang, *J. Magn. Magn. Mater.*, 2009, **321**, 2622 – 2626.
- [244] F. Söderlind, L. Selegård, P. Nordblad, K. Uvdal and P.-O. Käll, *J. Sol-Gel Sci. Technol.*, 2009, **49**, 253–259.
- [245] A. Samy, *J. Mater. Eng. Perform.*, 2003, **12**, 569–572.
- [246] A. A. Sattar, A. H. Wafik, K. M. El-Shokrofy and M. M. El-Tabby, *Phys. Stat. Sol. A*, 1999, **171**, 563–569.
- [247] N. Rezlescu, E. Rezlescu, C. Pasnicu and M. Craus, *J. Phys.: Condens. Matter*, 1994, **6**, 5707–5716.
- [248] X. Liang, X. Wang, J. Zhuang, Y. Chen, D. Wang and Y. Li, *Adv. Funct. Mater.*, 2006, **16**, 1805–1813.
- [249] A. Nikumbh, *J. Mater. Sci.*, 1990, **25**, 3773–3779.
- [250] Y.-I. Kim, W. B. Im, M. K. Jeon, Y.-H. Lee, K.-B. Kim and K.-S. Ryu, *J. Nanosci. Nanotechnol.*, 2011, **11**, 810–814.
- [251] E. Sook Choi, J. Young Park, M. Ju Baek, W. Xu, K. Kattel, J. Hyun Kim, J. Jun Lee, Y. Chang, T. Jeong Kim, J. Eun Bae, K. Seok Chae, K. Jin Suh and G. Ho Lee, *Eur. J. Inorg. Chem.*, 2010, **2010**, 4555–4560.
- [252] K. Kitayama, H. Ohno, Y. Ide, K. Satoh and S. Murakami, *J. Solid State Chem.*, 2002, **166**, 285 – 291.
- [253] C. C. Berry, *J. Phys. D: Appl. Phys.*, 2009, **42**, 224003.
- [254] J. Xie, C. Xu, N. Kohler, Y. Hou and S. Sun, *Adv. Mater.*, 2007, **19**, 3163–3166.
- [255] C. Xu, K. Xu, H. Gu, R. Zheng, H. Liu, X. Zhang, Z. Guo and B. Xu, *J. Am. Chem. Soc.*, 2004, **126**,

9938–9939.